

Optofluidic devices integrated with micro/nanochannels

Xiong, Sha

2014

Xiong, S. (2014). Optofluidic devices integrated with micro/nanochannels. Doctoral thesis, Nanyang Technological University, Singapore.

<https://hdl.handle.net/10356/61027>

<https://doi.org/10.32657/10356/61027>



**NANYANG
TECHNOLOGICAL
UNIVERSITY**

OPTOFLUIDIC DEVICES INTEGRATED
WITH MICRO/NANOCHANNELS

**OPTOFLUIDIC DEVICES INTEGRATED
WITH MICRO/NANOCHANNELS**

XIONG SHA

**XIONG SHA
SCHOOL OF ELECTRICAL AND ELECTRONIC
ENGINEERING
2014**

2014

OPTOFLUIDIC DEVICES INTEGRATED WITH MICRO/NANOCHANNELS

XIONG SHA

School of Electrical and Electronic Engineering

A thesis submitted to the Nanyang Technological University
in partial fulfillment of the requirement for the degree of
Doctor of Philosophy

2014

ACKNOWLEDGEMENTS

Foremost, I would like to express my sincere gratitude to my supervisor, Professor Liu Ai Qun, for his guidance, encouragement and confidence in my ability, which have been crucial motivators throughout my research. He has not only provided me the inspiration for my research, but also helped me in personality development, which will affect me for a life time.

I take this opportunity to express my gratitude to Professor Claus-Dieter Ohl who introduced me into the world of bubble. His enthusiasm for the research inspired me to push myself in overcoming the difficulties I faced in the project. Without his guidance and tremendous support, this thesis would not have been possible.

In particular, I am grateful to Dr Chin Lip Ket, Dr Yang Yi, Dr Keita Ando and Dr Tandiono for the knowledge and effects they have imparted for the complement of this work. I would like to thank Dr Lei Lei, Dr Shui Lingling, Mr Shahnawaz Pukkeyil Shamsuddin, Mr Goh Jun Hui for helping me in the fabrication. My thanks go to Dr Silvestre Roberto Gonzalez Avila, Ms Li Fenfang and Mr Chan Chon U for their help in the cavitation experiment setups. I would also like to take this opportunity to appreciate Dr Yu Yefeng, Dr Fu Yuan Hsing, Dr Huang Hungji and Mr Li Zhenguo for their enlightening discussions.

I would also like to extend my thanks to the technicians of the Photonics lab I, Photonics lab II, Valens Centre and Nanyang NanoFabrication Centre for their

help in offering the resources and technical supports in the fabrication process and experiment setups.

Last but not least, I would like to thank my parents for supporting me spiritually throughout my life.

Xiong Sha

SUMMARY

Optofluidics uses optics and fluidics synergistically to synthesize novel functionalities. It is a burgeoning field with important applications in areas such as biotechnology, chemical synthesis and analytical chemistry. This doctorate thesis focuses on the theoretical and experimental studies of optofluidic devices, which can be integrated on the lab-on-a-chip and micro/nanofluidic systems. Specifically, two aspects of this subject have been investigated: using liquid as the optical medium to manipulate the transfer of light, i.e. tunable optofluidic prism; and using the focused energy of light to control the fluid motion, i.e. laser induced micro/nano-bubbles and jets generated by two bubble interactions.

A tunable optofluidic prism is developed based on the configuration of two laminar flow streams in a microfluidic system. A theoretical model including the hydrodynamic control and optical analysis is established. The prism shape is tuned by the variation of the flow rates, and the deviation angle and the position of the output light beam is predicted accordingly. A study with simulation on the geometry of the microfluidic channel is used to optimize the chip design. Then, the fabrication processes and experimental setups for the optofluidic prism are illustrated. Experimental results demonstrate the tunability of the optofluidic prism by varying the flow rates and refractive indices of the liquids. The apex angle of the prism and the deviation angle of the output light beam can be tuned continuously with a larger variation range than the previous methods. By precise control of the asymmetric prism shape, parallel light beam scanning was achieved. In addition, the dispersion of light with different wavelengths has been demonstrated. The experimental results are also illustrated the possibility to use the optofluidic prism

as an on-chip refractometer. The optofluidic prism has potential applications in building up the on-chip optical circuits and promising for the optical detection and biochemical analysis.

Study of laser induced micro/nano-bubble is focused on its dynamics in a confined environment: from micro to nanochannels. The theoretical analysis investigates the radial motion of a cylindrical vapor bubble starting from the Navier-Stokes equation. A Rayleigh-Plesset-type equation that accounts for the shear stress from channel walls and surface tension is derived. Moreover, the dynamics of a cylindrical gas bubble due to mass diffusion is explored. The theoretical models are verified in a micro/nanofluidic chip, which is designed and fabricated by using borosilicate glass. Experimental results demonstrate that the viscosity and surface tension play important roles on the bubble dynamics in the confined channels. With the decreasing of channel height, the bubble life time is prolonged. This study provides new insights in the cavitation dynamics especially for these practical situations in optofluidic systems where the fluid dynamics is severely affected by confinement.

The laser induced micro/nano-bubble accelerates surrounded liquid molecules and forms jetting flow when it is near a boundary. Here, the dynamics of jets is studied when a static gas bubble is impacted by a laser induced bubble. The theoretical analysis indicates the dependence of the jet velocity on the laser energy and the distance between the two bubbles. In a microchannel, the jetting process is sufficiently long to obtain a thorough analysis, and an empirical equation is derived. In a nanochannel, fast jets with a thickness of hundreds of nanometers are obtained within 300 ns following the cavitation event. The experimental results demonstrate that inertia dominated dynamics is still possible for sufficiently short times in the

extremely confined environment. The study of fluidic instability is emphasized, since it plays an important role in the bubble pinch-off and shattering during the micro-jetting and breakup of thin film during the nano-jetting.

The successful implementation of the new optofluidic components improves the performance of the same type devices and the integration of diverse functionalities on a lab-on-chip system. At the same time, the development of the fundamental concepts and new phenomena, especially on the nanoscale, gain a deeper insight and opens intriguing possibilities for optofluidic applications.

TABLE OF CONTENTS

Acknowledgement	i
Summary	iii
Table of Contents	vi
List of Figures	x
Nomenclature	xviii
1. Introduction	1
1.1 Motivation	1
1.2 Objectives	8
1.3 Major contributions	10
1.4 Organization.....	12
2. Literature Survey	14
2.1 Optofluidics	15
2.1.1 Optofluidic analysis.....	15
2.1.2 Tunable optofluidic components.....	18
2.1.3 Optofluidics prism.....	23
2.1.4 Optically driven fluid.....	25
2.2 Bubbles	29
2.2.1 Methods for bubble formation.....	30
2.2.2 Bubble nucleation.....	31

2.2.3	Bubble dynamics.....	34
2.2.4	Research on nanobubbles.....	36
2.3	Jets.....	41
2.3.1	Jets from bubbles.....	41
2.3.2	Jet breakup.....	45
2.3.3	Breakup of liquid sheet.....	47
2.4	Summary	50
3.	Tunable Optofluidic Prism	51
3.1	Design of the tunable optofluidic prism	52
3.1.1	Hydrodynamic control of the prism	53
3.1.2	Optical deviation on the prism.....	57
3.1.3	Dispersion effect.....	60
3.1.4	Design of the triangular chamber.....	63
3.2	Fabrication processes and experimental setups.....	67
3.2.1	Polymer soft lithography fabrication flow.....	67
3.2.2	Optofluidic prism fabrication.....	69
3.2.3	Preparation of fluids.....	70
3.2.4	Experimental setup.....	71
3.3	Experimental results and discussions	73
3.3.1	Control of the prism shape.....	73
3.3.2	Tunable deviation angle of output light.....	77

3.3.3	Parallel light scanning with constant deviation angle	82
3.3.4	Light dispersion.....	85
3.3.5	On-chip refractometer.....	87
3.4	Summary	92
4.	Laser-Induced Micro/Nano-Bubble	94
4.1	Theoretical modeling.....	95
4.1.1	2D viscous Rayleigh-Plesset-type model.....	95
4.1.2	Mass diffusion on bubble surface.....	102
4.2	Fabrication processes and experimental setups.....	105
4.2.1	Glass chip fabrication process flow.....	105
4.2.2	Surface treatment of the glass channel	108
4.2.3	Experimental setup.....	109
4.3	Experimental results of microbubble.....	112
4.3.1	Microbubble in a 1D confined channel	113
4.3.2	Microbubble in a 2D confined channel	120
4.3.3	Microbubble near an elastic surface.....	125
4.4	Experimental results of nanobubble	131
4.4.1	Effect of channel height.....	132
4.4.2	Effect of surface hydrophilicity.....	136
4.5	Summary	140

5. Jets Penetration by Two Bubble Interaction	142
5.1 Theoretical modeling	143
5.1.1 Cavitation induced jet.....	143
5.1.2 Transient plane Poiseuille flow.....	151
5.1.3 Jet breakup and instability.....	153
5.2 Experimental results of microjet.....	156
5.2.1 Jetting process.....	157
5.2.2 Shattered bubbles.....	164
5.3 Experimental results of nanojet	170
5.3.1 Jetting process	170
5.3.2 Breaking pattern and surface instability	174
5.3.3 “Soap bubble” in nanochannel.....	176
5.4 Summary	181
6. Conclusions	183
6.1 Conclusions	183
6.2 Recommendations	188
Author’s Publications	190
Bibliography	191

LIST OF FIGURES

Fig. 3.1	(a) Schematics of the optofluidic prism. The shape is tuned by the ratio of two flow rates: (b) symmetric prism, (c) right-shifting asymmetric prism, and (d) left-shifting asymmetric prism	52
Fig. 3.2	(a) Two laminar flows in a microchannel. (b) Dimensionless model of two streams for estimating the velocity distribution inside the channel.....	54
Fig. 3.3	Hydrodynamic model of the optofluidic prism.....	55
Fig. 3.4	Vertex of the prism shifts as a function of the flow rate Q_3 while Q_1 and Q_2 are fixed.....	56
Fig. 3.5	Optical model of the optofluidic prism.....	57
Fig. 3.6	Illustration of the width variation of a light beam when it passes through a prism	59
Fig. 3.7	Refractive indices of ethylene glycol, water and an optofluidic prism constructed by the two fluids at different wavelengths.....	61
Fig. 3.8	Relationship between the deviation angle and the wavelength of light with different apex angles	62
Fig. 3.9	Relationship between the apex angle of the prism and the flow rate ratio with different chamber shapes.....	64
Fig. 3.10	Simulation results of the flow streams with different chamber shapes...	65

Fig. 3.11	Simulation results of the diffusion with different ratios of width of inlet to the length of the base of the triangular chamber.....	66
Fig. 3.12	Simulation results of the flow streams with different ratios of width of inlet to the length of the base of the triangular chamber. The line with arrows shows the effective working length for each chamber when the prism has a fixed height	66
Fig. 3.13	Fabrication process flow of PDMS chip.....	68
Fig. 3.14	Photograph of the optofluidic prism.....	70
Fig. 3.15	Experimental setup of the optofluidic prism.....	72
Fig. 3.16	Relationship between the apex angle of the prism and the flow rate Q_1 when Q_2 is fixed at 10 ml/min.....	74
Fig. 3.17	Relationship between the apex angle of the prism and the flow rate Q_3 when Q_2 is maintained at 120 μ l/min and Q_1 is maintained at 10 μ l/min (solid line) and 70 μ l/min (dash line).....	75
Fig. 3.18	Relationship between the deviation angle, apex angle and the flow rate Q_1 with chambers of 70° (solid line) and 90° (dash line). The inner liquid is benzyl alcohol ($n = 1.540$).....	78
Fig. 3.19	Relationship between the deviation angle, apex angle and the flow rate Q_1 with chambers of 70° (solid line) and 90° (dash line). The inner liquid is DI water ($n = 1.332$).....	79
Fig. 3.20	Relationship between the beam expansion factor and the flow rate Q_1 with chamber of 90°. The inner liquid is benzyl alcohol ($n = 1.540$)....	81

Fig. 3.21	Deviation angle as a function of the flow rate Q_2 and Q_3 while the flow rate Q_1 is fixed at $10 \mu\text{l min}^{-1}$	82
Fig. 3.22	Light scanning controlled by Q_2 and Q_3 , when Q_1 is kept at $100 \mu\text{l/min}$. The output light position (solid line) and Q_3 (dashed line) are both plotted as the functions of Q_2	83
Fig. 3.23	Adjustment of the detected light intensity by tuning the output position.....	84
Fig. 3.24	Optical dispersion caused by different apex angles of the optofluidic prism.....	86
Fig. 3.25	Schematics of the on-chip refractometer.....	88
Fig. 3.26	Photography of the on-chip refractometer filled by samples with different refractive indices.....	89
Fig. 3.27	Output light intensity profile shifts with the refractive index of sample.....	90
Fig. 3.28	Position of light beam is plot as a function of the refractive index.....	90
Fig. 4.1	Schematic of a cylindrical bubble of radius R confined in a channel of height h	95
Fig. 4.2	Fabrication process flow of glass chip.....	106
Fig. 4.3	Photograph of the water droplet on a glass substrate (a) before the surface treatment and (b) after the surface treatment.....	109
Fig. 4.4	Schematics of the experimental setup for laser-induced bubbles.....	110

Fig. 4.5	Schematic of the laser-induced microbubble on different boundary conditions: (a) 1D confined channel, (b) 2D confined channel, and (c) near an elastic surface.....	112
Fig. 4.6	Photographs of microbubble evolution in a 1D confined channel.....	114
Fig. 4.7	Comparison of the measured bubble radii (square) and the model predictions for the 3D Rayleigh collapse (dashed line) and 2D inviscid Rayleigh type collapse (solid line). The dash-dot line is used to illustrate the bubble expansion tendency.....	115
Fig. 4.8	Comparison of the bubble dynamics for different sized bubbles with a 2D inviscid (solid line) and 3D Rayleigh model (dashed line).....	116
Fig. 4.9	Simulation results for 2D viscous Rayleigh-Plesset-type model with different viscosity in a microchannel ($h = 8 \mu\text{m}$).....	117
Fig. 4.10	Simulation results for 2D viscous Rayleigh-Plesset-type model with different gas pressure in a microchannel ($h = 8 \mu\text{m}$)	118
Fig. 4.11	Bubble dynamics for 2D viscous Rayleigh-Plesset-type model with simulation results in different channel heights: $10 \mu\text{m}$ (solid), $8 \mu\text{m}$ (dash), $6 \mu\text{m}$ (dot), $4 \mu\text{m}$ (dash dot) and $2 \mu\text{m}$ (dash dot dot), and experiments results in $8 \mu\text{m}$ and $4 \mu\text{m}$ channel.....	119
Fig. 4.12	Sequential snapshots of a bubble in a tube microchannel with height of $4 \mu\text{m}$ and width of $140 \mu\text{m}$	121
Fig. 4.13	Distances between the right and left edges (L_x), and upper and lower edges (L_y) of the bubble in the 2D confined microchannel are depicted as a function of time, and compared with the radial revolution of a 1D confined bubble (R_0).....	123

Fig. 4.14	Volumes evolution of a 2D confined bubble at laser energies of 1.7, 5.8 and 14 μJ	124
Fig. 4.15	Sequential snapshots of a bubble in a tube microchannel with a distance of 85 μm away from a gas/liquid surface.....	125
Fig. 4.16	Evolution of the length between the laser spot and the bubble edges...	126
Fig. 4.17	Maximum length of L_l and L_r with different distances when $E = 5.2$ and 3.4 μJ	127
Fig. 4.18	Evolution of laser induced bubble with different laser energies when $D = 64 \pm 3 \mu\text{m}$	129
Fig. 4.19	Evolution of laser induced bubble with different distances when $E = 5 \pm 0.4 \mu\text{J}$	129
Fig. 4.20	(a) Schematics of the laser-induced nanobubble in the micro-nanofluidic channel. Side view of the nanobubble in the (b) hydrophilic and (c) hydrophobic channel.....	131
Fig. 4.21	Cavitation bubble evolution in (a) microchannel ($h = 8 \mu\text{m}$) and (b) nanochannel ($h = 700 \text{ nm}$).....	133
Fig. 4.22	Comparing the radial dynamics of a bubble in nanochannel with $h = 700 \text{ nm}$ (circle) and microchannel with $h = 8 \mu\text{m}$ (hollow square) with a viscid 2D model (solid line) and inviscid 2D model (dashed line). Left axis is for the bubble in nanochannel and right one is for the bubble in microchannel.....	134
Fig. 4.23	Dynamics of cavitation bubble in nanochannels of variable heights: 700 nm (circle), 500 nm (triangle) and 300 nm (square).....	135

Fig. 4.24	Collapse time as a function of the maximum radius of bubble in a hydrophilic (square) and hydrophobic (circle) nanochannel. The lines show the predicted effective viscosities as $0.4 \times 10^{-6} \text{ m}^2\text{s}^{-1}$ (solid line), $0.5 \times 10^{-6} \text{ m}^2\text{s}^{-1}$ (dashed line) and $0.6 \times 10^{-6} \text{ m}^2\text{s}^{-1}$ (dashed-dotted line).....	136
Fig. 4.25	Comparison of the bubble dynamics in the hydrophilic and hydrophobic nanochannel and the model predictions.....	138
Fig. 4.26	Simulation of the collapse time as a function of the maximum radius for varying contact angles in an 800-nm high extended nanochannel and viscosity of $\nu = 0.5 \times 10^{-6} \text{ m}^2 \text{ s}^{-1}$	139
Fig. 5.1	Schematic illustration of the jet formation induced by a laser bubble in a microchannel.....	144
Fig. 5.2	Schematic of flow focusing on the target bubble surface that is impacted by the pressure wave generated from the laser induced bubble.....	147
Fig. 5.3	Simulation of shape change of the target bubble due to the flow focusing. The bubble surface is concaved from point <i>A</i> to <i>B</i>	147
Fig. 5.4	Schematic geometry of the liquid jet, which is the zoom-in view of the framed part in the inset.....	149
Fig. 5.5	Velocity profile of Poiseuille flow in a microchannel.....	152
Fig. 5.6	Schematics of the cylindrical column in (a) steady state and (b) perturbed state.....	154
Fig. 5.7	Sequential snapshots showing the interaction between a laser-induced cavitation bubble and a nearby gas bubble.	156

Fig. 5.8	Sequential snapshots showing evolution of the gas bubble when a cavitation bubble is generated nearby at $t = 0$	158
Fig. 5.9	Evolution of the jet length (blue line) and jet velocity (red line). The inset is definition of the parameter.....	159
Fig. 5.10	Photographs of the microjets with varied laser energies E : (a) $1.7 \mu\text{J}$, (b) $3.6 \mu\text{J}$, (c) $5.4 \mu\text{J}$ and (d) $6.5 \mu\text{J}$, when $D = 90 \pm 3 \mu\text{m}$ at $t = 3.3 \mu\text{s}$	161
Fig. 5.11	Photographs of the microjets with varied distances D : (a) $55 \mu\text{m}$, (b) $90 \mu\text{m}$, (c) $130 \mu\text{m}$ and (d) $158 \mu\text{m}$, when $E = 6.0 \pm 0.4 \mu\text{J}$ at $t = 3.3 \mu\text{s}$..	162
Fig. 5.12	Jet velocity as a function of the laser energy with different distances.....	163
Fig. 5.13	Jet velocity as a function of the distance with different laser energy.....	163
Fig. 5.14	Typical sequence snapshots with (a) $E = 4.9 \pm 0.5 \mu\text{J}$, (b) $E = 6.0 \pm 0.5 \mu\text{J}$ and (c) $E = 7.1 \pm 0.5 \mu\text{J}$, when $D = 64 \pm 3 \mu\text{m}$	165
Fig. 5.15	Sketch for breaking up of the gas cylinders with different number of shattered bubble.....	167
Fig. 5.16	Histogram of the number of shattered bubbles for different energies with $D = 64 \pm 3 \mu\text{m}$	168
Fig. 5.17	Photographs of nanojet in a nanochannel ($h = 550 \text{ nm}$).....	170
Fig. 5.18	Sketches for the typical evolution of the thin liquid film generated in the nanojetting process.....	171
Fig. 5.19	Nanojet velocity as a function of the distances between the laser focus and bubble surface when the laser energy is $6 \mu\text{J}$	173

Fig. 5.20	Nanojet velocity as a function of the laser energy with different distances between the laser focus and bubble surface.....	173
Fig. 5.21	Photographs showing different breakup pattern of the nanojets.....	174
Fig. 5.22	Photographs showing a soap bubble formed in the gas phase accompanied with the nanojet. Dot line highlights the thin liquid layer that forms the soap bubble.....	177
Fig. 5.23	Photographs showing a soap bubble formed with thick wall accompanied with the nanojet. Dot line highlights the thin liquid layer that is critical for forming the soap bubble.....	178
Fig. 5.24	Schematics of the soap bubble in a nanochannel.....	179

NOMENCLATURE

AFM	Atomic force microscope
BL	Boundary layer
CaCl₂	Calcium chloride solution
CCD	Charge coupled device
DEP	Dielectrophoretic
DI	Deionized
DNA	Deoxyribonucleic acid
FDTS	1H,1H,2H,2H- perfluorodecyltrichlorosilane
FP	Fabry-Pérot
IPA	Isopropanol solution
LEDs	Light-emitting diodes
LOC	Lab-on-a-chip
MEMS	Micro-electro-mechanical system
PDMS	Polydimethylsiloxane
RIU	Refractive index unit
TIRF	Total internal reflection fluorescence

CHAPTER 1

INTRODUCTION

1.1 Motivation

This PhD research topic is motivated by the potential of optofluidic technology in exploring new solutions and opportunities to add novel and sophisticated functionalities for a wide range of traditional optical components and integrated devices with potential applications in chemistry, biology, medicine, display technology and energy generation.

Optofluidics aims at manipulating fluids and light at microscale and exploiting their interaction to create highly versatile systems [1]. It has attracted wide research interests in multi-disciplinary areas for their unique advantages. First, the sophisticated microfluidic networks allow several chemical analysis and biological diagnosis to be conducted with precise control [2]. Since the microfluidic network has a significant advantage in fluid handling at the micron scale, samples for optical analysis can be delivered, manipulated and tested within one compact chip [3]. For example, the optofluidic flow cytometer uses flow focusing technology to arrange cells, and collects the scattering and fluorescent signals as each cell passes the laser beam [4]. The information obtained from the optical signals including both physical properties (e.g. shape, size) and biochemical

properties (e.g. protein contents, cycle distribution) of the cells. It greatly facilitates the rapid and quantitative analysis of biological samples. In addition, the microfluidic networks allow the analysis to be conducted in parallel [5]. Second, optofluidics contributes tremendous effort for integrating the optical components that are usually reconfigurable and adjustable [6, 7]. Fluid can be used as a tunable part in an optofluidic device due to its mobile nature. The smooth boundaries formed by fluids are also favored for low-loss optical components. In addition, liquids with large variety of refractive indices can be used to interact with light. Optical properties of these components can be dynamically modified through variations in the refractive index. Some optofluidic components have already been demonstrated, such as waveguide [8], microlens [9], dye laser [10] and interferometer [11]. Third, the adaptation mechanisms of optofluidic components are often used as micro-sensors with high sensitivity. For instance, the optofluidic interferometer uses a fluid–air interface to provide an optical path difference, which can be adapted for biosensing or chemical analysis [12]. Other optofluidic sensors can be found in the optofluidic resonator [13], optofluidic microscope [14] and Bragg grating refractive-index sensors [15]. Fourth, the optofluidic systems can efficiently convert optical energy to mechanical, thermal or chemical energy for facilitating the hydrodynamic control, medical treatment and biochemical analysis [16]. Fluids can incorporate with a variety of optically attractive elements, such as gold nanoparticles, silica microspheres and cells. Optical forces are used to manipulate and trap particles and target cells [17]. Light can even be utilized for flow manipulation by optically controlling micropumps [18] or generating cavitation bubble [19]. Optofluidic planar reactors uses TiO_2 coated micro-chamber

for photocatalytic water treatment which overcome the limitations of mass transfer and photon transfer in traditional photocatalytic reactors [20]. Finally, optofluidic system operates in a closed miniaturized chip for small sample volumes at low concentrations, which subsequently lower the costs, reduce the running time, and offer a safer platform for biochemical studies. The increasing portability and sensitivity of the optofluidic devices are also expected in the environmental monitoring and clinic diagnostics.

A major challenge for the development of optofluidics is the improvement of control approaches, which are mainly twofold. On one hand, fluids are exploited to control light through constructing versatile optical devices, making them tunable, reconfigurable and adaptive. It is expected to develop more types of optofluidic devices with larger tunability. On the other hand, light not only can offer the optical signal for analysis, but also is an effective method to control the fluid motion. The improvement in controlling optics combined with the capability to manipulate small amounts of fluidics can be a major step towards the implementation of optofluidic devices in the robust and highly automated applications.

Optofluidic devices are attractive for their abilities in precisely adjusting the optical path among multiple integrated components. The most common one is optofluidic lens [21]. The curvatures of the lenses are fine tuned to achieve optimal finesse and minimal propagation losses. However, the lenses have limited ability in beam steering. In traditional optical systems, a prism is a critical component to change the optical path of a collimated light beam or perform light dispersion. Therefore, realizing a tunable optofluidic prism that can precisely adjust the optical path in an integrated on-chip system is one of the requests in the development of

lab-on-a-chip systems. Conventional solid prisms have a fixed geometrical shape, so one cannot show the continuous change of the light path with the variation of the refraction angle. In order to overcome this difficulty, variable-angle prisms have been constructed. Liquid prisms have been reported in which liquid is enclosed in a trough or bag [22, 23]. The refraction angle could be varied by mechanically changing the shape of the container. These prisms are large due to the limitation of the fabrication techniques. Recently, prisms have been fabricated at the microscale. A micro-liquid prism was fabricated by putting two transparent plates on a liquid droplet and encapsulating the structure with parylene [24]. Unfortunately, once the shape of the prism is retained by the encapsulation, the refraction angle is unchangeable. Another small prism consisting of two plates and a sandwiched liquid layer was developed to be wedge angle tunable by electrowetting [25]. However, the prism is not in a sealed environment, thus may face the evaporation problem. On-chip micro-prisms are usually fabricated by PDMS with or without liquid filling in the hollow prism. These prisms can be designed on the microchip with a high degree of monolithic integration, but the rigid geometry provides a hindrance in the developing route of the optofluidic systems. Recently, a tunable symmetrical prism based on the liquid-core liquid-cladding structure has been formed in a sector-shape chamber [26]. This prism is constructed by three laminar flows and the light deviation with single wavelength is investigated. The prism has a tunable apex angle with limited tuning range ($20^{\circ}\sim 70^{\circ}$), which leads to the deviation angle of output light beam to be smaller than 12° . As one of the critical component, optofluidic prism requires better solutions to improve tunability and stability. For example, the prism can be designed with a larger apex angle that will

result in a larger deviation angle. In addition, the two-laminar-flow optofluidic components are more favorable in simplifying the fluidic control and make their performance more stable.

Current study on optofluidic devices is still in a formative stage. Most researches thus far have approached optofluidics from constructing tunable optical components by liquids, such as optofluidic waveguide and lens [8, 9]. On the contrary, only few works have been done on using light to actuate liquids. For instance, a focused light beam with photothermal particles have been demonstrated to drive liquid flow moving at controlled speeds and directions [27]. Laser-induced cavitation bubbles have been reported for generating transient flows in confined regions [28-30]. In addition, an optical force can provide pumping action by manipulating particles dispersed in liquid [31, 32]. Among those innovative methods for optically driving liquid, laser-induced cavitation is the most favorable one due to its distinctive advantages. First, the optical energy is directly transferred to the liquid without other medium (e.g. particles) in the cavitation driven fluidic system. It is more efficient for the conversion from optical to hydrodynamic energy. Second, the cavitation method is more flexible in the location selection. The photothermal method only works at the liquid/air interface, while the optical force method is depending on the position of the particles or micro rotator. Third, the whole cavitation process is only within tens of microseconds, which causes fast flow motion (the flow velocity can be as high as 100 m/s). The other methods can only drive the flow with a velocity below 50 $\mu\text{m/s}$. Therefore, it has tremendous potential to optically drive flows through generating cavitation bubbles.

Inspired by the blooming of nanotechnology, the extension of microfluidic systems into nanofluidics becomes an attractive goal. In the context of biotechnology, decreasing the scales considerably increases the sensitivity and specificity of analytical techniques in order to meet the requirement for a wide range of application fields from medical diagnostics to pathogen detection [33]. Single cell and single molecule detection and analyses also need techniques to work with small volumes of sample [34-36]. In addition, nanofluidics is a way of increasing the density of fluidic operations on a chip, thus improving the large scale integration for the optofluidic devices. Nanofluidics also carries the hope that new properties will emerge by benefiting from the specific phenomena occurring with the reducing scales. Hence, there are many attractive motivations to foster researches on optofluidic devices towards the nanoscales. From the point of view of fluidic operations, nanostructures allow new fluidic functionalities to be developed, using the explicit benefit of the surface, such as the near-surface water, ion and electrolyte transport at this interface [37]. However, the surface and boundary effect will hinder the cavitation process. To obtain fast flows in the nanochannels is a critical challenge for further applications. Fundamental researches on the cavitation bubble dynamic and bubble caused liquid jet in the micro/nanochannels are necessary for creating bubble based optofluidic devices. So far, most works on nanobubble and nanojet are still mainly focused on simulations. It is eagerly expected to demonstrate the nanobubble and nanojet dynamics through experiments.

Many opportunities exist across the field of optofluidics. Further researches on the fundamental physics are necessary to offer a solid theoretical support for the

sustainable development of optofluidics. Optofluidic devices obtain novel functions from the physical properties and further exploit new phenomena from light and fluid interaction. Therefore, the research of the optofluidic devices can be approached from two sides: either light is tuned by liquid or liquid is driven by light. As critical components, optofluidic prism, laser-induced bubble and jets are chosen to be studied.

1.2 Objectives

The main objective of this research is to innovate and develop novel optofluidic devices, which can be integrated on the lab-on-a-chip and micro/nanofluidic systems. Specifically, two aspects of this subject are investigated. First, tunable optofluidic prism uses liquid as the optical medium to manipulate the transfer of light. Second, the laser-induced cavitation bubble and jet use the focused energy of light to control the fluid motion. Both research investigations include theoretical analyses, chip designs, fabrication process developments and experimental studies.

An optofluidic prism is developed based on the configuration of two laminar flows in a microfluidic system. The optofluidic prism is capable of transforming from a symmetric to an asymmetric prism with the assistance of a third flow. The prism shape is tuned by the variation of the flow rates, and the deviation angle and the position of the output light beam is adjusted accordingly. The theoretical models guide the design of the optofluidic prism, including the optical design and hydrodynamic control. The chip design is conducted to increase the tuning range of light beam and keep the stability of the flow. A soft-lithography process is developed for fabricating the PDMS chip. The tunability of the prism is demonstrated experimentally with different liquids and chambers. Some applications are discussed, including parallel light beam scanning, light dispersion and on-chip refractometer.

Laser-induced micro/nano-bubbles are studied, which are generated by focusing a pulsed laser into the micro/nanochannels filled with liquid. A theoretical

model is derived to describe the bubble dynamics in the confined environment, which accounts for the wall shear stress, capillary forces, wetting properties of the channel, and gas diffusion. A glass fabrication process is developed for realizing nanofluidics on the chip. The bubble dynamics are experimentally investigated with different channel heights, boundary conditions and surface hydrophobicities. The discussions are focused on effect of the surface forces on the bubble dynamics, such as the maximum radius and collapse time.

Micro/nano-jets during bubble-bubble interaction are studied as well. Liquid surrounded the cavitation bubble is accelerated and forms a focusing flow when it is near another static gas bubble. The theoretical model is studied, which analyzes the dependence of the jet velocity on the laser energy and the distance between the two bubbles. The model is verified in a micro/nanofluidic chip, which is designed and fabricated by using glass. The micro/nano-jets dynamics are experimentally studied and compared with the theoretical analyses. An empirical equation can be derived to express the relationship between the laser energy, distance and jet velocity. It aims to investigate whether inertia dominated dynamics is still possible for sufficiently short times in the extremely confined environment. Jet breakup process is also discussed based on the fluidic instability.

1.3 Major contributions

The major contributions of this PhD thesis lie in various aspects of the theoretical analyses, designs, fabrications, and experiments of the optofluidic devices integrated with micro/nanochannels. The details are listed below:

- 1) An optofluidics prism is designed, fabricated and experimented. Particularly, the apex angle of the prism, the output position and deviation angle of the light beam are studied. The parallel light beam scanning and light dispersion are demonstrated by using the optofluidic prism. (See Chapter 3)
- 2) An on-chip refractometer is proposed and experimented. It utilizes the optofluidic prism to measure the refractive index of small quantity of liquid by detecting the output beam position. (See Chapter 3)
- 3) Fabrication process for the optofluidic system is developed using polydimethylsiloxane (PDMS) as the chip material. SU8 is used as the mold and patterned on a silicon wafer by lithography. PDMS chip can fast replicate the patterns from molding. (See Chapter 3)
- 4) A theoretical model is derived to describe the dynamics of a confined cavitation bubble. It is applicable for both microchannel and nanochannel, overcoming the shortages of other models which diverge from the experimental data when the channel dimension decreases. (See Chapter 4)

- 5) Fabrication process for the opto-nanofluidic system is developed using borosilicate glass as the chip material. The fabrication techniques including lithography, chemical etching and thermal bonding. (See Chapter 4)
- 6) Nanobubbles are experimentally studied by directly optical observation. The nanofluidic dynamics is approached by using an extended nanochannel, which has only one dimension in the nanometer scale. (See Chapter 4)
- 7) Nanojets in the form of ultrathin liquid sheets are obtained by creating laser-induced nanobubbles. It is demonstrated that inertia dominated dynamics is still possible for sufficiently short times (< 300 ns). (See Chapter 5)
- 8) New phenomena related with the fluidic instability in a confined geometry are studied. Particularly, the pinch-off of microbubbles during fast microjetting, thin film break patterns and “soap bubbles” during the nanojets are discussed. (See Chapter 5)

1.4 Organization

The thesis is organized into six chapters. The introduction of the thesis covers the motivation, objective, and major contributions as presented in this chapter. The motivation section explains why the PhD research is carried out. The objective states the main focus of this thesis, and the contribution section lists the innovations and important findings in both the theoretical and technological aspects.

In Chapter 2, literatures of optofluidic technology, cavitation bubble and jet study are reviewed. This chapter reviews the background and state-of-art for optofluidic technology. The significance of tunable optofluidic devices are discussed as well as their applications in biochemical analysis. Optofluidic prism and optically driven fluid are reviewed as emphasis in the optofluidics. Then, the dynamics of cavitation bubble and bubble generated jet are introduced, which is the basic technology employed in the thesis to realize optical control over fluids. All such important background work provides the guidance and impetus for the research, and also lays the technological foundations on which the work of this thesis is built.

In Chapter 3, the design, fabrication and experiments of optofluidic prism are presented. A hydrodynamic model has been developed to predict the tuning of the prisms by the variation of the flow rates. The optical analysis including the deviation angle and the position of the output light beam are presented accordingly. The chip design is aimed to provide optimum working range and avoid recirculating flows. The tunability and the optical characteristics of the optofluidic prism are

experimentally studied and discussed. Some application cases are discussed, including the parallel light scanning, light dispersion and on-chip refractometer.

In Chapter 4, the theoretical modeling, fabrication and experiments for laser-induced micro/nano-bubbles are presented. A theoretical model of a cylindrical cavitation bubble in reduced scale (from several micrometers to nanometers) is proposed. The bubble dynamics is examined with different channel heights, boundary conditions and surface hydrophobicities. Experimental results are discussed and compared with the theoretical models.

In Chapter 5, the theoretical analysis, fabrication and experiments for micro/nanojets generated during two-bubble interaction are presented. In the jetting process, the emphasis is the dependence of the jet velocity on the laser energy and the distance between the two bubbles, and an empirical equation is derived. Instability induced shattered bubbles and thin film breakup pattern are discussed and statistically analysed. The experimental results of the micro/nanojets with novel instability phenomena are discussed.

Chapter 6 concludes the major contributions of this thesis, and follows by the recommendations for future work.

CHAPTER 2

LITERATURE SURVEY

This chapter is divided into three parts. The first part presents an overview on the optofluidic technology that consists of the optofluidic analysis, tunable optofluidic components, optofluidic prism and optically driven fluid. The second part presents the bubble studies including the methods for bubble formation, bubble nucleation and bubble dynamics. The state-of-art for nanobubble research is discussed as an emphasis. The third part is focused on the study of jets, especially the jets generated from bubbles. The works on breakup mechanism of liquid jets and thin sheets are discussed as well. All these works lay the foundation for contributions of this thesis on the study and development of optofluidic devices integrated with micro/nanochannels.

2.1 Optofluidics

Optofluidics refers to a class of technology that aims to manipulate light and fluids at the micro/nanoscale, exploiting their interaction to create highly versatile devices and integrated systems. The lab-on-a-chip technology has known for a broad success, which exploits the microfluidic systems for biomedical and chemical analysis. Integration of optical components into the microfluidic systems helps to increase portability and sensitivity, and avoid the limitation from free space optical elements. In some situations, the implemented components are even constructed by the liquids that offer remarkable flexibility and unique properties to these systems and cannot be found in solid equivalents.

Optofluidics has emerged from the development of microelectromechanical systems (MEMS), which are conventionally fabricated in silicon based micromachining processes. In the early stage researches on optofluidic systems, the devices are all based on the MEMS fabrication techniques [38]. Recently, cheaper polymeric materials such as polydimethylsiloxane (PDMS) and polymethylmethacrylate (PMMA) have been employed in the microfluidic systems. PDMS is the most commonly used polymeric materials due to its attractive properties such as optical transparency, biocompatibility, elasticity and air permeability [39, 40]. PDMS chip are fabricated by soft lithography techniques that allow replicating the identical devices in a fast and cheap way. Glass is another popular microchip material due to its chemical inertness, thermal stability and physical robustness. The technology of glass nanochannel fabrication has been well established with high resolution and reproducibility. Currently, glass became the

ideal and most used substrate in the fabrication of nanofluidic chips [41, 42]. Paper-based microfluidic device is a new rising techniques using pattern papers which have the capacity to split a single, low-volume ($<40\ \mu\text{l}$) sample into multiple separate portions that can be assayed in parallel [43, 44]. They do not need any external instrumentation and power during operation. Moreover, they are portable and disposable. So far, the paper-based microfluidic devices have been reported for clinical chemistry, enzymatic, immunoassay test, but no optical detection is involved. With the development of fabrication technology, sophisticated optofluidic platforms have been achieved with a complex microfluidic network. Optofluidic components can even be directly fabricated from the same materials using the same processes, which significantly improved the compatibility, integration and efficiency of the system.

2.1.1 Optofluidic analysis

Optical detection methods are among the most widely used for chemical and biomedical analysis, which have extremely low detection limits and the capability to obtain tremendous information from the samples. The optical detection for biochemical analysis in microfluidic systems is usually based on measuring some parameters in a particular optical phenomenon, such as scattering, absorption, fluorescence and refractive index.

Scattering pattern is a function of scattering angle at certain wavelength on a particular sample medium. Therefore, detailed information can be obtained from the angular scattering spectrum, such as the particle size, surface roughness and internal

structures. Scattering is probably the simplest method for cell/particle counting in a microchannel [45-47]. With the development of techniques and integration of optical components, higher resolution and frequency are expected with more information on cells.

Optical absorption as a non-labeling method is widely used in the conventional detections. Precise measurements of the absorbance at different wavelengths allow the identification of a substance via absorption spectroscopy. Extending the physical path-length is a direct way to enhance absorption. For instance, a planar U-shaped or multi-reflection cell can increase the absorbance more than 10 times [48]. Instead of sensing through bulk flow, some special waveguides achieves higher sensitivity by using evanescent wave in absorption detection [49].

Fluorescence technique is commonly used for biomolecular analysis for its high sensitivity and capability for single molecule detection. It is feasible for detecting autofluorescent species, e.g. molecules or cells, and those attached to a fluorophore or quantum dot, such as bacteria, virus and DNA [50-53]. For example, encoded particles are created with a spatial fluorescent pattern including one million possible codes [54]. After incubation with the target, the code is read by analyzing the fluorescent intensity, and the target is identified.

Refractive index based techniques is another attractive field in the chemical and biomedical sensing. Refractive index is a dimensionless number that describe how fast the light propagates through the medium. The refractive index is not only depending on the species, but also changed with the concentration of solute in the

solvent. The concentration of protein in a cell can be determined by the refractive index of the cell [55, 56]. The refractive index is an indicator for monitoring the cell status. The difference of refractive index between cancer cell and normal cell can be taken advantages in the diagnoses of cancer [57].

Optical resonators are also widely developed for measuring refractive indices of molecules or living cells. It can be classified into standing wave resonator, i.e. Fabry-Pérot (FP) resonator [58-60], and travelling wave resonator, i.e. ring resonator [61-63]. The resonant conditions for the light waves are affected by the refractive index of the medium, which can be measured from the spectra shift [64]. In addition to resonators, interferometers such as Mach-Zehnder interferometer [65-69] and Young interferometer [70, 71] are high sensitive waveguide devices for refractive index measurement.

2.1.2 Tunable optofluidic components

The majority functions in the optofluidic analysis system are realized by external optical systems. Recently, incorporating optical components on the microfluidic chips has been demonstrated as an efficient means to improving the robustness, flexibility and operator-independence of the system. In addition, it has potential for mass manufacture of fully integrated approaches.

The fluid-configured optical components benefit from three key features of microfluidics. First, the flexible interfaces with sharp index contrast ensure the devices have the same function as their solid counterparts with highly adaptivity.

Second, the index contrast can be adjusted by changing the fluid composition. The range of refractive index modulation provided by microfluidics ($\Delta n \approx 0.5-1$) is much higher than those offered by electro-optic ($\Delta n \approx 10^{-3}$) or thermal effects ($\Delta n \approx 10^{-2}$) [1]. Third, fluid mobility makes the interface shape and location to be readily controlled at the micro scale, and the devices are reconfigurable.

The simplest application of laminar flow is the liquid-liquid waveguide, in which the light is guided and confined in a liquid core with a higher refractive index than that of the surrounding liquid cladding [8]. The refractive-index gradients can be generated by changing the concentration of solutions [72], dispersing particles in the core stream [73], or using thermal gradients [74]. Hydrodynamic control of the liquid streams has been used to define the optical path. By decreasing the flow rate ratio of core to cladding, the width of the core decreased, consequently the waveguide was changed from multimode to single mode. An optical switch was demonstrated by pushing the core stream into different outlets [8]. The liquid waveguide can also be used as an optical splitter and a wavelength filter by control the diffusion [75]. Recently, a controllable transformation optics device is realized based on an optofluidic waveguide, which achieved chirped focusing of light and strong interference effect with analogous discrete diffraction [76].

Integrated microlenses are the most studied optical components. In-plane PDMS lenses are used to collimate light beams and increase the incident light intensity for optical detection in neighbouring microfluidic channels and chambers [77-79]. These lenses can be easily integrated on a microfluidic chip, but the geometries of them are permanently fixed. Liquid lenses with tunable focal length offer significant advantages in terms of functionality and versatility. Most out-of-

plane lenses, i.e. manipulating light paths perpendicular to the plane of substrate, are designed as a liquid filling chamber covered by a thin membrane. The radius of curvature is controlled by the membrane deflection when a pressure is applied to the liquid [9, 80]. Although the out-of-plane microlenses could replace conventional lens in applications such as cell phones or digital cameras, the fabrication is complex and precise alignment is required. In-plane microlenses are more suitable for lab-on-a-chip applications, because they can be integrated with the microfluidic network on the same substrate. In plane lenses utilize the curvature formed by the interface between two immiscible fluids, i.e. liquid/liquid or liquid/gas. Dynamically reconfigurable liquid-core liquid-cladding lens are reported by using the curved interfaces in rectangular chamber [81, 82] or circular chamber [83]. Liquid lens can also achieve the curved interface between two flow streams in a curved channel [84, 85]. Another type of liquid microlens is demonstrated using the liquid waveguide structure but operated in extremely low flow rate to achieve the desired refractive index gradient [86, 87]. With the transversely variable refractive index, a liquid gradient refractive index lens is formed. Light travelling along the optical axis of the gradient index lens is deviated gradually toward the optical axis to become a focused or collimated beam.

Optofluidic gratings attract increasing interest for its applications in filters and interferometers. They can be the periodic structures of liquid-solid, liquid-liquid or liquid-gas. A transmission grating has been constructed by an array of evenly spaced straight microchannels [88]. Each grating line is formed by a flowing stream in a microchannel. The tunability of the grating diffraction pattern can be achieved by dynamically modulating the refractive index of all the microflows at the same

time. A diffraction grating has been constructed by uniform gas bubbles, which forms ordered 2D lattices by self-assembly [89]. In other reported works, 1D grating has been demonstrated by aligning a stream of uniform droplets into a microfluidic channel [90-92]. The bubble/droplet arrays are formed at a constant period, which can be tuned by changing the ratio of the flow rates of the two fluids.

Besides those basic optical components for tuning the optical path, light sources are required to be integrated into a microfluidic system. Firstly, micro-cavity liquid dye lasers have been fabricated, whose cavity size is comparable to the wavelength of spontaneous emission [93-95]. After that, various configurations have been explored in the optofluidic light sources. The mirroring-based laser demonstrates a switchable output with a highly multimode integrated waveguide, whose wavelength is tunable by changing the dye/solvent properties [96]. The distributed-feedback dye lasers are based on higher order Bragg grating embedded in the liquid, which displays narrowband laser by exploiting antiguiding effects and achieved single-mode operation [97, 98]. Another class of microfluidic light sources relies on liquid-liquid waveguides, which is constructed by two immiscible liquid streams with different indices [10, 99]. The liquid core is filled with laser dye and used for light emission and guiding. The laser beam size and intensity are varied by adjusting the flow rate, while the emission wavelength is tuned by changing the composition of the liquid core. Moreover, a broadband light source can be achieved by constructing waveguide arrays and cascades [100]. A 3D liquid waveguide dye laser is reported to take the advantage of centrifugal Dean flow to increase the light confinement [101]. The efficiency of 3D optofluidic laser is at least 3-fold higher than its traditional 2D equivalent. Dye laser can also be realized using droplet

microfluidics [102, 103]. Lasing occurs when the emitted light has a wavelength in which coincides with the whispering gallery mode of the droplet cavity. The fast-switching dye lasers are based on a stream of droplets with different laser dyes, which are capable of switching the lasing wavelength between 580 nm to 680 nm at frequencies up to 3.6 kHz [104]. Optofluidic ring resonator lasers based on micro-bubbles have been demonstrated [105]. The micro-bubbles are filled in liquid gain medium, which have 3-dimensional optical confinement, extremely high Q-factors, and versatility in handling liquids of different refractive index.

With the development of a wide range of integrated optical elements, several optofluidic devices have been developed, e.g. interferometers, optical switches and attenuator. These optofluidic devices are essential to integrate optical detection and analytical techniques into the microfluidic system for biological and biomedical research such as on-chip spectrometer, refractometer and biomaterial concentration sensor. For instance, optofluidic microscope has been demonstrated, which successfully replace a bulky laboratory microscopic system with a compact and portable imaging chip [14]. The image of the sample is obtained by compiling the time-dependent changes of the optical transmission, when the sample flows across the microchannel.

2.1.3 Optofluidic prism

Prism is another critical component for optic path adjustment, such as steering light beam and controlling dispersion. It is widely used in the optical analysis system.

Liquid prism has been developed since 1938. When a rectangular trough containing liquid is rotated around one of its lower edges, the liquid forms a prism whose angle varies with the rotation [22]. The liquid prism is used to construct an auto-collimating microscope, which greatly increases the accuracy for the measurement of refractive indices. Another type of liquid prism is made of liquid or gas enclosed in a sector-shape bag with two transparent and stiffened side walls (120×80 mm) [23]. The apex angle of the prism is changed by adjusting the distance between the bases of the two walls. The refractive index of the prism can also be varied by changing the medium in the bag.

Recently, the prism size is decreasing with the miniaturization of optical systems. A micro-liquid prism has been fabricated by putting two transparent plates on a liquid droplet and encapsulating the structure with parylene [24]. Surface tension is used to automatically position the two plates (400 ~1200 μm in diameter). Once the shape of the prism is retained by the encapsulation, the refraction angle is unchangeable. The prism with an apex angle of 118.5° has been verified in surface plasmon resonance (SPR) measurement. Another small prism consisting of two plates (2~4 mm in diameter) and a sandwiched liquid layer (1.5-mm high) is developed to be wedge angle tunable by electrowetting [25]. The wedge angle is increased with the applied voltage, and shows a maximum value of 13° with 100 V.

The prism is capable to shift the light path by 8° and the field of view by 3° . However, the prism cannot be kept for a long time, because its volume changes due to evaporation. Those micro-prisms are all out-of-plane optical components.

On-chip micro-prisms are usually fabricated by PDMS without or with liquid filling in the hollow prism [106-108]. Early work demonstrates that the light beam was shifted before and after oil filling in prism chamber [106]. Later, the optofluidic prisms are used for on-chip detection. A hollow Abbe prism has been used for absorption detection and refractive index measurement of chemical species that filling in it [107]. The shift of wavelength collected by the output optical fiber can be used to calculate the variation of the refractive index. The total volume of the prism is $1.579\ \mu\text{L}$. The minimum fluorescein concentration detectable is $112.5\ \mu\text{M}$. By modifying the volumes and geometries, optimization of the prism performance has been obtained. The limit of detection is achieved as $1.83\ \mu\text{M}$ for fluorescein by using a prism with a total deviation angle of 90° [108]. These prisms can be designed on the microchip with a high degree of monolithic integration, but the rigid geometry provides a hindrance in the developing route of the optofluidic systems.

Recently, a tunable symmetrical prism based on the liquid-core liquid-cladding structure has been formed in a sector-shape chamber [26]. This prism is constructed by three laminar flows and its apex angle is tuned by the flow rates. The chamber acts as a source-sink pair bounded within a divergent boundary with a 90° opening angle. As a result, the prism demonstrated a tunable apex angle always smaller than 90° . When the chamber is fully occupied by the core liquid (the apex

angle is 90°), the deviation angle achieves a maximum value of 11.4° . If the tuning range of the apex angle can be expanded, large deviation angle can be achieved.

2.1.4 Optically driven fluid

The previous sections demonstrate that laser plays important roles in optical detection and analysis, especially the applications requiring highly spatial or temporal coherence of light, such as the interferometers [11, 71]. The laser is indispensable in surface plasmonic resonance related techniques, because the couplings are highly wavelength-dependent and incident-angle-dependent. The fluorescence and scattering detections are preferred to employ laser due to diffraction-limited focusing.

Besides illumination and excitation, lasers are utilized for particle manipulation. Recently, optical forces attract increasing attentions as a non-contact approach for particle trapping and separation. The optical forces are mainly separated into the propagation force and gradient force. When photons are absorbed or scattered by the particles, they impart momentum to the particles and the propagation force drive the particles in the direction of light propagation. On the contrary, particles are attracted along the gradient to the region of strongest electric field. Hence, the gradient force drives particles to the region of maximum optical intensity [109, 110].

Weakly focused beams combination with opposing fluid flows in microfluidic systems led to demonstration of optical separation and sorting [111-

113]. Tightly-focused single beam is designed for submicron particles [114, 115] and exploited for investigating the weak signals of individual particles or cells, such as scattering spectra [116] and Raman spectra [117], because of the improved noise reduction. Dual-beam demonstrates great advances in cell manipulation [118-120]. The divergent fields can not only generate a large area trap for relative large targets (e.g. cells), but also offers greater positional control and reduced risk of damage by high energy laser. Beam arrays offer larger flexibility in tuning the potential barriers and the interconnection of optical traps for particle sorting [121-124]. Beside focused beams, evanescent field was exploited to guide and trap particles and cells [125-127]. The evanescent approach provides convenient manipulation, improved stability and greater spatial localization through the near-field. However, working zone is restricted within a few hundred nanometers to the surface.

Besides directly manipulating particles through optical force, the laser can manipulate fluids themselves through controlling pumps and mixers. Colloidal particles are reported to be assembled into a microfluidic channel and manipulated using optical forces to provide pump action [31, 32]. Rotation of a microgear [128] or rotors [18, 129], using optical forces have also been demonstrated. Optically actuated pumps have the advantages of simple reconfigurability, integration, small size, few constraints compared to other micropumps.

Photothermal effect is an attractive phenomenon, which can convert optical energy to hydrodynamic energy for optofluidic applications [130, 131]. Using focused laser beams with photothermal nanoparticles (e.g. gold nanoparticle), liquid flows can be driven and guided in microfluidic channels to transport biomolecules and cells at controlled velocities and directions. When the photothermal particle

suspended liquid is illuminated by the laser spot near the liquid-air interface, heat is generated and transferred from the particles to the surrounded liquid, which significantly accelerates the liquid evaporation at the interface and produces vapor. The vapor in the cold air condenses immediately after the evaporation and droplets form close to the contact line. The droplets eventually merge into the bulk liquid, and thus the contact line is expended. It is found that the optofluidic flow speed in a channel with the width of 10 μm can be as high as 500 $\mu\text{m/s}$ using a 20-mW, 785-nm laser [27].

It has been reported that light scattering by inhomogeneities in the refractive index of a fluid can drive a large-scale flow [132]. A liquid jet can be formed, when a laser beam traversing the liquid produces an interface deformation. Light scattering can produce an upwards body force on the liquid, which drives an upwards flow within the laser illuminated region. Thereafter, this flow is refilled by a downward flow and forms a toroidal recirculation. As a result, the interface is deformed by the recirculation associated with the viscous stresses.

Laser-induced cavitation is another way to realize optical-hydrodynamic energy conversation. Because of the rapid expansion/collapse and flow focusing ability of the cavitation bubbles, the liquid can be accelerated to very high speeds. Laser pulses generated cavitation bubbles in a microfluidic channel are utilized to disrupt the laminar flow of two fluids and produce a localized mix zone, which enhances the rapid mixing of chemicals in the lab-on-a-chip devices [133]. A micropump driven by a laser-induced cavitation bubble was reported for repeatable and precise control of picolitre volumes [19]. The transient radial flow generated by the laser-induced bubble was utilized to manipulate the microsize particles [134]

and nanowires [135]. The cavitation are also facilitating many cell operations, such as cell surgery, lysis [136-139]. The detailed discussion on the laser-induced cavitation is presented in the following section.

2.2 Bubbles

The early stage of bubble research is motivated by the problems they caused in the marine and hydraulic system. Researchers tried to reduce the damages caused by the violent collapse of cavitation bubble and investigated its dynamics with surrounding flows. Nowadays, bubbles occupy an important place in contemporary science and technology, due to their frequently appearance in the fluid systems and their applications in multi-disciplinary area, such as biology, chemistry, physics, engineering and medical field. The fascinating properties of the bubbles, such as nucleation, oscillation and sonoluminescence, are also attractive to researchers.

The best known application of the cavitation bubble is ultrasonic cleaning [140-142]. Micro-streaming will form during the bubble collapse and flush away the dirt particles attached on the surface. Another frequently mentioned technique is sonochemistry [143, 144]. A high temperature zone is created at the center of a collapsing bubble, which acts as a catalyst that enhances the reaction rate to several orders of magnitude [145, 146]. Cavitation bubbles can be used as pumps to control microfluidics in miniaturized devices, i.e. lab-on-a-chip, fuel cell, etc. [147, 148]. New progress of bubble in medicine is related to cell operation. Bubbles are capable of passing through the capillaries and releasing drug and gene incorporated onto their surface [149]. Cavitation bubbles have been used in Lab-on-a-chip systems for cell stretch, lysis and membrane poration [150-152]. The deformability of red blood cells during a transient cavitation bubble event in microchamber has been recorded and analyzed, that can be used as an indicator for blood disease [153].

2.2.1 Methods for bubble formation

There are two main ways in which the bubble can be generated, depending on the system discussed. In an n -ary system, one or more components may be supersaturated and form bubbles, i.e. carbonated drinks, whereas in a unary system, bubbles are generated by cavitation or boiling [154]. Cavitation is the formation of voids in a liquid where the local pressure falls below the vapor tension of the liquid. Though the basic mechanics of cavitation and boiling are similar, there is essential difference between the thermodynamic paths that precede the formation of vapor [155]. Cavitation is the process of rupturing a liquid by decreasing pressure at constant temperature. Boiling is the process of rupturing a liquid by increasing the temperature at constant pressure.

In the earlier studies, cavitation bubbles occur after a transient stretching of the liquid, for instance, the mechanical motion of pumps and propellers, or the action of an ultrasonic field, or an increase of local flow velocity. According to Bernoulli's law, the local pressure decreases with increasing flow velocity. Cavitation occurs when the pressure drops below the vapor pressure of the liquid. At an ambient pressure of 1 bar and room temperature, a water velocity of 14 m/s is sufficient for bubble formation [156].

Cavitation bubble can also generated by local deposition of energy, such as a focused laser pulse or an electrical discharged spark. The laser-induced bubble is realized by optical breakdown, which is a nonlinear absorption process to form plasma at locations where the threshold irradiance for breakdown is surpassed [157-161]. Whereas the spark-generated bubble is created by converting electrical energy

into a small volume of plasma, which has a temperature of 2×10^4 K, and a pressure of 10^4 atmospheres. The spark generator for creating bubbles is settled under water. When the gap between the electrodes is pulled down by the trigger pulse, current flows between the two electrodes, the plasma followed by the spark is generated [162-166].

Once plasma with a high pressure inside has been created, the surrounding liquid is compressed and starts to flow radically outward, and the inertia of the external liquid will confine it. The compression wave propagates through the liquid and incorporates more and more liquid mass into the radial flow. The acceleration continues after the shockwave has passed, because the pressure within the expanding cavitation bubble is still high. The radial flow at the bubble wall thus reaches a larger velocity than the initial particle velocity behind the shock front. After emission of the shock wave, the pressure in the bubble quickly falls. With increasing bubble radius, the kinetic energy eventually distributes among a larger liquid mass. Therefore, the bubble wall velocity starts to decrease again after about 10 ns, although the bubble pressure is still higher than the hydrostatic pressure and continues to drive the bubble expansion [167]. When the internal pressure is lower than the external pressure, the bubble collapses.

2.2.2 Bubble nucleation

The inception of cavitation bubble is started from nucleation. In a pure liquid, the thermal motions within the liquid form temporary and microscopic voids, which constitute the nuclei for rupture and growth to large bubbles. This is termed

as homogeneous nucleation. However, in practical situation, it is more common to find that rupture occurs near a surface, such as the solid wall of the container, or particles in the liquid. It is generally accepted that hydrophobic surfaces stabilize small bubbles. This kind of on-site rupture is heterogeneous nucleation [155].

Surface tension is the macroscopic expression of the intermolecular forces that hold molecules together and prevent the formation of large holes. The relationship between the liquid pressure, p , external to a bubble of radius R and the internal pressure p_B can be expressed as

$$p_B - p = \frac{2\sigma}{R} , \quad (2.3)$$

where σ is the surface tension. When the temperature T is uniform and the bubble only contains vapor, the internal pressure reaches the saturated vapor pressure $p_v(T)$. When the external liquid pressure is lower than $p_v - \frac{2\sigma}{R}$, the bubble will grow and rupture will occur.

Tensile strength is the maximum stress that a material can withstand while being stretched before breaking or rupture. The tensile strength of the liquid, Δp_c , can be given by

$$\Delta p_c = \frac{2\sigma}{R_c} , \quad (2.4)$$

where R_c is the maximum size of vacancy which may be created by random molecular motions. Supposing R_c is comparable with the intermolecular distance of

10^{-10} m, and σ is 0.05 kg/s^2 (a typical surface tension), the calculated tensile strength is 10^9 kg/m s^2 or 10^4 atm .

The deposition of energy is critical for generating the nucleation. It consists of two parts: the energy stored in the surface of the bubble, and the work done by the liquid to achieve the displacement due to the difference between the pressure inside and outside of the bubble. Thus the total energy can be estimated as

$$E_t = 4\pi R_c^2 \sigma - \frac{4}{3} \pi R_c^3 \Delta p_c. \quad (2.5)$$

Substitution of Eq. (2.4) into Eq. (2.5) yields

$$E_t = \frac{16\pi\sigma^3}{3(\Delta p_c)^2}. \quad (2.6)$$

The total deposited energy can be related to the typical kinetic energy of the molecules (kT , k is Boltzmann's constant) by Gibbs number

$$\text{Gb} = \frac{E_t}{kT}. \quad (2.7)$$

The Gibbs number is proposed as a certain probability of a nucleation event. The nucleation rate J takes the general form as

$$J = J_0 e^{-\text{Gb}}, \quad (2.8)$$

where J_0 is a factor of proportionality and has a number of expressions.

2.2.3 Bubble dynamics

Having considered the initial formation of bubbles, the next topic is the subsequent dynamics of bubble growth and collapse. Lord Rayleigh is the first to mathematically describe the bubble dynamics and lays the foundation of today's research on cavitation bubbles [168]. He solved the problem of the collapse of an empty cavity in a large mass of liquid by only considering the inertia. Since the bubble is assumed to be spherical during the whole process, the dynamics is described by the radius as a function of time

$$R\ddot{R} + \frac{3}{2}\dot{R}^2 = 0, \quad (2.9)$$

where R , \dot{R} and \ddot{R} are the bubble radius and its time derivatives. The time required for complete collapse of the cavity can be estimated as

$$t_0 \approx 0.915 \left(\frac{\rho}{p_\infty - p_v} \right)^{1/2} R_i, \quad (3.0)$$

where R_i is the initial bubble radius. Plesset developed a more generalized equation which is called Rayleigh-Plesset equation and expressed as [169]

$$R\ddot{R} + \frac{3}{2}\dot{R}^2 = \frac{1}{\rho} \left(p_B - p_\infty - \frac{2\sigma}{R} - \frac{4\mu}{R} \dot{R} \right), \quad (3.1)$$

where p_B is the pressure inside the bubble, p_∞ is the pressure infinitely far from the bubble, μ is the dynamic viscosity of the liquid. This equation is derived for Newtonian fluids from the Navier-Stokes equation. It describes the whole evolution of the bubble from onset to expansion and collapse.

Following researchers studied the bubble dynamics in more complex situations. The bubble was discussed from vaporous to gaseous [170], from static to travelling [169], from spherical to arbitrary shape [171-173]. Some practical effects were considered, such as surface tension, liquid viscosity, thermal effect, liquid compressibility, gas compressibility, mass diffusion [174-177].

When a bubble is in a periodic pressure field, the bubble radius oscillates in response to the driving pressure with specific nonlinear phenomena [178, 179]. Once the pressure of an acoustic wave (as a function of time) is considered, the Rayleigh-Plesset equation can also describe the further oscillations after the first collapse.

Another distinctive phenomenon in cavitation physics is sonoluminescence, which was discovered in 1934 [180]. Light emission is observed during a large number of bubble oscillations. After that, single-bubble sonoluminescence was investigated [181, 182]. At the adiabatic collapse, the gas inside the bubble is heated up to 1.5×10^4 K [183]. High temperature causes gas ionization. Subsequently, light emission occurs at recombination. Although the emission only last a short time (i.e. 100-300 ps) in each oscillation cycle, energy can be focused by 12 orders of magnitude [184].

Understanding bubble-bubble and bubble-wall interaction are crucial to many applications, which require focus energy and flow in a small zone. When bubble is near a surface, the asymmetric collapse causes jetting flow and vortices and a sequence of shock waves [185-188].

The group behavior of bubble is also an attractive topic, since bubbles usually appear in large number, e.g. on ship propellers and in cleaning tank. The bubbles arrange in the form of cluster, streamer, clouds and swarms [189]. The bubble distributions, bubble tracks and velocity distributions have been studied [190-192].

2.2.4 Research on nanobubbles

The above theories are developed from macroscopic considerations and the standard continuum fluid mechanics is applied. A perhaps crucial limitation for the continuum mechanical approaches is the assumption of local thermodynamic equilibrium, which assumes the macroscopic fluid variables do not change drastically over the molecular length and time scales. However, it is found that the classical hydrodynamic modeling is different to represent the bubble in the final stages of collapse, when it is on the nanometer scale.

As an alternative approach, the molecular dynamics (MD) simulations are carried out to describe the process of bubble collapse [193]. When the simulations are performed for nanobubbles with radii of 1 nm and 1.5 nm, the collapse time is less than 10 ps and is a function of temperature [194, 195]. A focused jet is observed during shock-induced collapse of nanobubbles with a diameter of 6-8 nm, which is investigated with MD simulations based on a reactive force field [196]. The MD simulations can also be utilized for investigating the formation, stability and breakup of nanojets. Recent development in molecular simulations and

statistical mechanics of inhomogeneous fluids has also attracted new focuses on the study of bubble nucleation [197-199].

Although the nanobubble dynamics are studied in details through simulations, there are just limited ways to experimentally explore the properties of nanobubbles. In 1994, the existence of nanobubbles on the hydrophobic surfaces was firstly reported [200]. A significant development of the researches on nanobubbles comes after the images of surface nanobubbles being obtained by using the Atomic Force Microscope (AFM). Nowadays, surface nanobubbles are widely reported on different material surfaces with various detection mechanisms. Although AFM is the most used techniques, others such as rapid cryofixation/freeze fracture [201], optical scattering [202] and total internal reflection fluorescence (TIRF) [203] are used as well. Typical surface nanobubbles are spherical caps with heights of the order of 10 nm and diameters of the order of 100 nm, which are located at the liquid-solid interface.

The most common way to produce the surface nanobubbles is the solvent exchange method. A solvent miscible with water and with a greater solubility of gases is chosen, e.g. ethanol. The substrate is immersed in ethanol and then the ethanol is displaced by water. Ethanol preferentially wets the hydrophobic surface and is not easy to be replaced. The gas will be released when the ethanol is mixed with water, since the solubility of gas in the aqueous phase is exceeded. Besides, the nanobubbles can also be generated by substrate heating [204, 205].

Surface nanobubbles behave differently as compared with regular macroscopic bubbles. Their contact angle is always smaller than expected from

Young's law, and depends on size [206, 207]. Surface nanobubbles are stable against violent decompression and have remarkable long lifetime. According to classical diffusion theory, a gaseous bubble with the radius of 100 nm should disappear in 1 μ s in degassed water. However, surface nanobubbles have been found to exist for longer than 5 days [208]. Therefore, understanding the super stability becomes the research hot-spot on the surface nanobubbles. A possible explanation is that the diffusive outflux is stably balanced by an influx of gas at the contact line [209]. The most recent research points out that because gas has to diffuse toward the atmosphere and due to the pinned contact lines, the nanobubble dissolve on a much longer time scale than free bubbles in an infinite liquid [210].

Femtosecond laser are capable to generate nanosize cavitation bubbles in water. When the laser pulse duration decreases, the energy required for optical breakdown is decreased accordingly. As a result, the shock wave emission and cavitation bubble expansion are both greatly reduced [211]. Bubbles produced by longer laser pulses, i.e. nanoseconds and picoseconds laser, are usually tens or hundreds of micrometers large [167]. Ultrashort laser pulses are assumed to form nanometer size cavitation bubbles by combining the heat and thermoelastic tensile stress [212]. Early investigations demonstrate the dynamics of bubbles produced by femtosecond laser pulses with the maximum radii of 45-100 μ m, when the energy is 6-10 times above threshold [211, 213]. Recently, works have been done to determine the maximum bubble radius as a function of laser pulse energy for near-UV, visible and IR wavelengths [214]. Scattering of a probe laser beam is used to determine the bubble oscillation time, thus deduce the maximum bubble radius. At

threshold, the maximum bubble radius is smaller than the diffraction-limited focus radius and ranging from 190 nm to 320 nm.

As an alternative way, a strong local heating can create transient nanobubbles around the nanoparticles. Pulsed laser excitation causes a strong nonequilibrium heating of the particle, and subsequently the water shell close to the particle surface. The surface temperature of the particle can easily surpass the boiling point of water. It is suggested that the strong curvature of the interface inhibits vapor formation. For instance, gold nanoparticles with a diameter of 9 nm have been excited by femtosecond laser and produced nanobubbles that have the maximum radius of 20 nm and life time within 1 ns [215]. The threshold for the formation of the nanometer-sized vapor bubbles is around 85% of the critical temperature of water [216]. The laser fluence threshold for bubble formation is not only dependent on the nanoparticle size, but also on the nanoparticle aggregation state [217]. The presence of gold nanoparticles increases local absorption, thereby can strongly reduce the power and energy necessary to achieve the same bubbles without nanoparticles. Larger bubble can be generated for higher power or longer pulse duration. The life time of nanobubble is found to be a function of nanoparticle size, aggregation state and laser fluence, ranging from sub-ns to several hundred ns [218].

The femtosecond laser-induced nanobubbles with/without nanoparticles are small and unstable. They are difficult to be directly detected using microscope or CCD camera due to diffraction limit. X-ray scattering is the mostly used technique to investigate the nanobubbles, which can derive a temporal figure of the structural and thermal dynamics of the nanobubbles, nanoparticles and adjacent medium. In

these works, the bubble dynamics is still described by Rayleigh-Plesset equation using continuum thermodynamics.

Recently, nanobubbles are generated in water-filled hydrophilic nanochannels due to evaporation [219]. These nanochannels are etched on a silica substrate with a length of 120 μm and width of 4 μm , and their depth ranges from 20 nm to 120 nm. The nucleation of the nanobubbles is due to the evaporation-induced negative pressure up to -7 MPa. Because this kind of nanobubbles just has one dimensional on the nanoscales, their behaviors are investigated directly through the microscope system. The vapor bubbles exhibit unusual motion as well as translational stability and symmetry, due to the competition between evaporation-induced hydraulic flow and thermocapillary-driven flow.

2.3 Jets

A jet is a stream of matter having a more or less columnar shape, which occurs from the large scale structure of the universe to subatomic length scales [220]. It has wide applications in manufacturing, agricultural irrigation, military technology, jet engine and ink-jet printing for decades. Nowadays, jets on small scale have attracted attention for their potential applications in medical diagnostics, DNA sampling and nuclear fission. However, the thorough understanding of the dynamics and well control of the parameters still remains a significant challenge. In addition to the basic study of the jet behaviour, there are many works focused on the jet breakup process with the stability analysis.

2.3.1 Jets from bubbles

Jets originate from many different sources, such as liquid burst from nozzle, impact of drops with liquid pools, impact of a liquid container, and violent eruptions. In this thesis, jet produced by cavitation bubbles is the focal topic. The jets typically arise when a bubble collapse in a liquid of anisotropic pressure. At the end of the collapse stage, the bubble surface develops a fast liquid jet directing inwards against the local pressure gradient. Two widely investigated categories are the collapse of a cavitation bubble near a boundary and the shock wave caused compression of a gas bubble [157, 221].

In the early works, the liquid jets were recorded during the asymmetric collapse of an initially spherical vapour bubble near a rigid boundary [222]. The

high-speed liquid jet is directed towards the boundary. The jet formation depends on the motion of the liquid around the cavitation bubble. When a cavitation bubble exists near a boundary, the excluded liquid finally converges on a point and results in the deformation of bubble surface near the point, leading to the jet formation. Later studies suggested that the physical properties of the boundary determined the direction of the movement of the jet [223].

A number of experimental and theoretical studies have been focused on vapor bubble motion near a solid boundary. The bubble migrates towards the boundary with jet forming later in the collapse phase. With sufficiently short distance from the boundary, the jet may strike the boundary after piercing the opposing side of the bubble. There are various works on estimating the liquid jet velocity during bubble collapse. To record the jet development directly, large bubbles (i.e. bubble with a maximum radius of 2 mm) and prolonged collapse is obtained by reducing the collapse pressure. A maximum velocity of 90-120 m/s is calculated by measuring the tip velocity during the protrusion [224, 225]. The discrepancy between measurements reveals that the bubble-boundary interaction during bubble expansion is significantly affecting the subsequent motion [226]. Precise experiments are carried out for studying the bubble behavior as the distance from the bubble to the solid wall surface and the wall shape are changed. The jet strikes the boundary directly only when bubble attaches to the boundary during expansion. With large separation, the bubble becomes toroidal and moves toward the boundary during shrinking. It is reported that the penetration of liquid jet on the concave wall surface may generate extreme high pressure by the shock focusing [227, 228]. There are few investigations on the bubble behavior between two solid

parallel walls. The formation of dumbbell and cone-shaped bubbles are observed when the gap between two parallel walls is shortened [229]. However, the current analytical approach cannot be applied to the bubble motion in the narrow space.

The bubble behavior is totally different when it is near a free surface, although jet is also observed during bubble collapse [230-232]. The free surface provides a constant-pressure boundary in the near vicinity of a pulsating vapour bubble. At large separations and in the absence of buoyance, the bubble moves away from the free surface during collapse and the jet threads the bubble in the direction of bubble migration. The free surface develops a pronounced spike moving away from the bubble when the bubble starts to involute [233]. Studies shows that when the distance between the bubble and the free surface decreases, the liquid jet in the bubble is narrowing and the free-surface spike continues to elongate during collapse [234].

A few studies have been conducted on flexible boundaries [235-237]. It is expected that a response between those of the two extreme conditions, i.e. a rigid boundary and a free surface, can be obtained. Such conditions are often occurred in biomaterials, and the fluidic physics can be very complex. An elastic restoring force can inject momentum back into the liquid. The elasticity of the boundary can be modeled through a pressure term at the interface. The jet direction is found depending on the elasticity as well as the distance of the bubble from the boundary and the density ratio [236]. The normalized jet volume is independent of the liquid density and viscosity, but related to the pressure gradient [238]. These researches are helpful for jets used in biotechnologies. Some bio-applications require a jet towards the tissue or cell, while others are trying to prevent the jets from causing

damage. Because of the similarity to human tissue and cells, some studies focus on the bubble growth and collapse near an elastic material. For instance, the cavitation bubble behavior and bubble-shock wave interaction near a gelatin surface are studied to examine the tissue damage mechanism [239]. Jets with tens of m/s are generated and a penetration depth of a few millimeters is achieved.

In recent years, the considered bubbles are much smaller than those in early researches (i.e. several millimetres in radius). It has been reported that bubbles of the size of a few microns can form a liquid jet in the direction of the propagation shock wave [240]. With increasing bubble radius, the averaged jet velocity increases linearly from 20 to 150 m/s. At a later stage, the jet breaks up and releases micro-sized bubbles. The jets from interaction of multiple bubbles are investigated as well [241, 242]. The fast expansion of a cavitation bubble causes anisotropic compression of an existing stable bubble with a penetrating jet. During the expansion stage of the impacted bubble, the nonuniform surrounding flow field induces a transverse inward jetting, which further interacts with the axial jet and lead to fragmentation into small bubbles. Although the bubbles are generated in a 10- μm high liquid gap, their maximum radius reaches 350 μm [241]. Microjets are also observed from the interaction of tandem microbubbles which are generated by laser in a 25- μm liquid layer [243]. Antiphase and coupled oscillation of the tandem microbubbles (a maximum diameter of 50 μm) lead to the formation of alternating, directional microjets with a maximum velocity of 10 m/s. Cells placed on the axis of the tandem microbubble are deformed by jet impact, and highly localized membrane poration is demonstrated. Recently, a fast liquid microjet from single bubble collapse is utilized for membrane poration of a suspension cell [152]. The

cell is trapped by a converging structure within a microfluidic chip. The strength of the bubble induces strain and the flow is a function of the location and the size of the cavitation bubble (the maximum diameter is approximately 100 μm).

2.3.2 Jet breakup

The earliest study on the behavior of jets is related to the formation of drops. It was thought that a drop falling from the tap was due to the gravity. Until the crucial roles of the mean curvature was exhibited, the surface tension was found to be the governing role in driving the breakup [244]. Surface tension drives the liquid towards a state with smaller surface area, which results in a decreasing jet radius. Faster breakup occurs at greater surface tension. In the early 19th century, a stroboscopic technique was developed, which allowed the breakup of jet being recorded [245]. It is noted that the breakup occurs spontaneously, independent of any external force or the jet direction.

The initial growth of the instability is exponential, in which the breakup length of the jet can be estimated by linear theory [246]. Near the breakup, the processes are always described by the balances between surface tension, viscous and inertial forces [247]. When the neck of the jet reduces to micro scales, the thermal noise drives the radius of neck to zero [248, 249].

The linear theory for jet breakup starts from the random initial perturbations, which are unstable when its wavelength is greater than a critical value. The disturbance amplitude is eventually dominated by the most unstable mode with the

wavelength of λ_{opt} [246]. For inviscid jet dynamics, the optimal wavelength is given as $\lambda_{opt} = 9.01 h_0$, where h_0 is the initial radius of the fluid column [246, 250]. For viscous fluids, the jet behaviour is under the action of interfacial surface tension as well as viscous forces. If a long fluid cylinder of viscosity μ' is in an infinite mass of another viscous fluid of viscosity of μ , the optimal wavelength λ_{opt} increases as the ratio μ'/μ tends to infinity or to zero [251].

The above mentioned models have not introduced any factors from the outside. However, the practical experiments is unavoidable affected by the environmental conditions, such as the turbulence in the bulk liquid or perturbation at the nozzle [252, 253]. With the increasing of the perturbations, non-linear effects eventually dominate the breakup process. The dynamics of the non-linear jet are revealed in increasingly sophisticated experiments [254, 255]. The formation of satellite drops, minimum thread radius and drop shape are studied.

The liquid jets are commonly linked with atomization. During the interpenetration process between two phases, a strong shear destabilizes the central liquid jet, which further fragments into a more or less uniform spray. The development of capillary instabilities can be altered by an extensional motion of the jet. For example, the stretching plays as a damping role for a viscous elongating cylinder [256]. In addition, jet can also subject to axial compression, which blows up the cross-section of jet in a short time. Consequently, the blow-up forms a radial sheet with finite extent due to surface tension [257]. The rim of thin sheet will breakup into small droplet and this part will be discussed in the next section.

Most of the researches focus on the liquid jet forming in a gaseous environment and its breakup process. However, the same concept and similar phenomena should be applied to the opposite situation of hollow (or gas) ligament forming in a continuous liquid phase. The fundamental instability works well on the elongated void structures. For instance, the rippling of the air cavity entrained by a rapidly moving solid object in liquid is experimentally observed [258]. The cavity ripples induce a spectacularly periodic breakup. Breaking waves in the open ocean entrain air bubbles, and the bubble formation mechanisms and size distribution are studied [259]. For larger bubbles (>1 mm), the turbulent fragmentation determines bubble size. Smaller bubbles are created by jet and drop impact on the wave face [260].

2.3.3 Breakup of liquid sheet

The transition from a macroscopic liquid volume to a group of dispersed smaller drops often involves a transient stage, which changes the liquid into a thin sheet. The disintegration of thin sheet usually starts from the destabilization of its edges. A liquid sheet can be formed through a fan spray nozzle [261], air-blast [262], or in the collision of two identical jets [263]. The early works focused on the sheet shape and its spatial extension [264-267]. Then the instability of a plane sheet of a constant thickness in the presence of ambient gas was analyzed [268-270]. They considered the instability with respect to the classical temporal growing single Fourier component of the disturbance. For small Weber number, the sheet is smooth with a radial extension; while for a large Weber number (e.g. above 1000), the sheet

demonstrates a flag-like motion that caused by shear [271]. The quantitative study of the drop-formation process was recently addressed [263]. The sheet fragments are usually caused by the destabilization of its thick rim, which are ejected at the tip of the ligaments. The capillary instability at the early stages of a ligament sets its section corrugations. The drop size is a function of both the Weber number and the collision angle in the case of sheet from two jets impacting each other.

The destabilization of liquid sheet starts from the shear instability, also called Kelvin-Helmholtz instability [272]. When there is velocity shear in a single continuous fluid, or a velocity difference across the interface between two fluids, the shear stability will work on the liquid and gives the liquid a flag-like motion. Subsequently, Rayleigh-Taylor instability is triggered at the rim of the sheet, which results in fragmentation. Rayleigh and Taylor reveals the instability of an interface between two media with density difference, subjects to a constant acceleration normal to the interface, and thus a layer is sandwiched between the two phases of different densities [273, 274]. These situations are always unstable in the absence of surface tension. Later work extended the analysis incorporating surface tension [274-276]. When the layer is much thinner than the capillary length, the amplification rate slows down and the selected mode shifts to larger length scales, which is caused by the coupling between the two interfaces of the layer [277]. Moreover, the destabilization of thin film can also be induced by a sudden acceleration [278]. The film modulates its thickness and is eventually break up by hole nucleation. Subsequently, the holes grow in radius and connect to each other, resulting in a web of liquid ligaments, which is unstable and breaks into droplets.

Similar patterns were observed on the dewetting of thin liquid film (< 100 nm) on solid substrates [279, 280].

2.4 Summary

Based on the literature survey presented, microfluidic systems are promising for automated and parallel processing in chemistry, biology and medicine by integrating entire laboratories in the miniaturized fluidic workstations. Optofluidics combines the merits of both fluids and optics, and generates novel functions for improving the microfluidic systems. For instance, fluids can be utilized to realize tunable optofluidic components such as liquid waveguide and optofluidic lens. Whereas light does not only facilitate the detection and analysis in the microfluidic systems, but can also manipulate the fluids by optical force and photothermal effect et al. Laser-induced cavitation bubble is a remarkable method to generate transient flow for microfluidic control. Although the bubble dynamics for macroscopic conditions are extensively studied, there is still little known about bubbles in an extremely small scale, i.e. nanobubbles. Jets can be generated by asymmetric expansion and collapse of bubbles, which plays a key role in most of bubble related applications. Hence nanojet becomes an attractive topic accompanied with complex nonlinear phenomena. With the current development of optofluidics, the research can be extended to further innovate optofluidic components and study their dynamics theoretically, especially highly flexible prisms, laser-induced micro/nanobubbles and their respective resulting jets.

CHAPTER 3

TUNABLE OPTOFLUIDIC PRISM

This chapter presents a tunable optofluidic prism based on the configuration of two laminar flow streams with different refractive indices in a triangular chamber. A hydrodynamic model has been developed to predict the tuning of the prisms by the variation of the flow rates. The chamber is designed to provide an optimum working range and avoid recirculating flows. Then, the fabrication processes and experimental setups for the optofluidic prism are illustrated. Optical analysis including the deviation angle and the position of the output light beam are presented accordingly. The experimental results prove the tunability of the optofluidic prism including the hydrodynamic and optical parts. Finally, the potential applications are discussed such as the parallel light scanning, light dispersion and on-chip refractometer.

3.1 Design of the tunable optofluidic prism

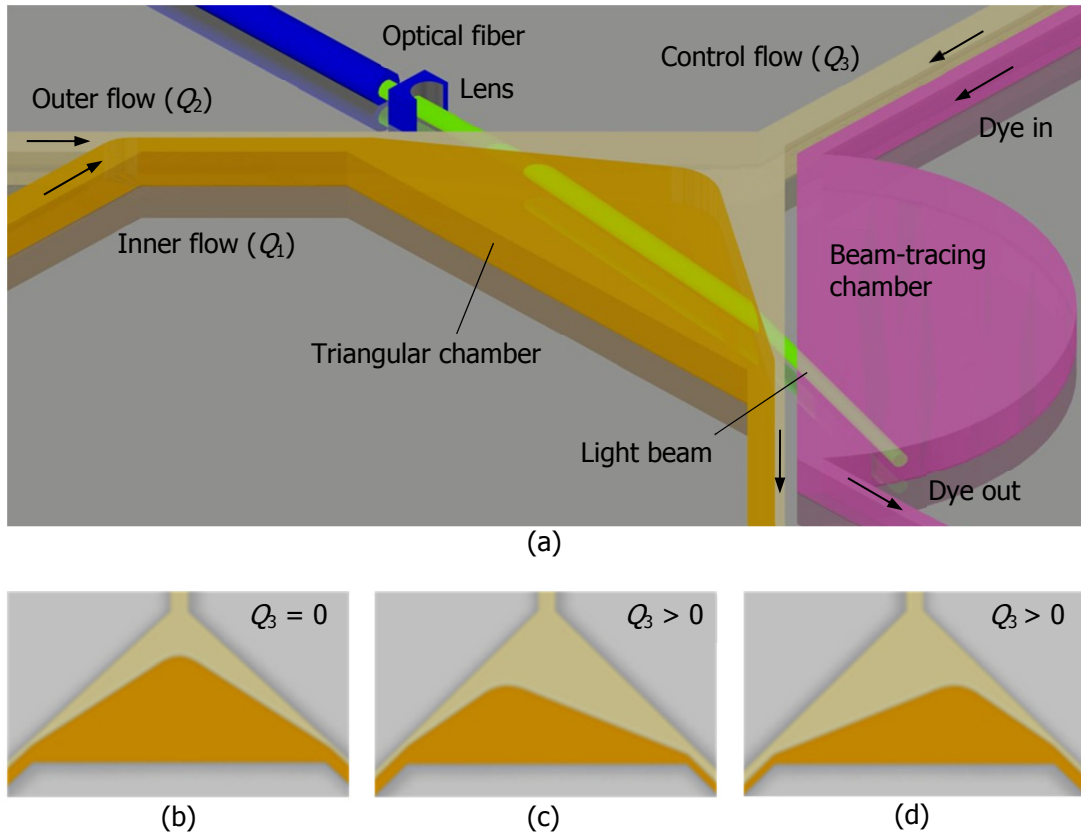


Figure 3.1 (a) Schematics of the optofluidic prism. The shape is tuned by the ratio of two flow rates: (b) symmetric prism, (c) right-shifting asymmetric prism, and (d) left-shifting asymmetric prism.

A tunable optofluidic prism is designed to be realized by two laminar flow streams with different refractive indices as shown in Fig. 3.1. The two laminar flow streams are injected into a triangular chamber. The inlet and outlet are connected to the two base corner of the chamber, separately. The inner flow stream is the main part of the prism, while the outer flow stream is used to adjust the prism shape. Controlling the flow rates of the two flow streams allows the tuning of the apex

angle of the optofluidic prism, and consequently changes the deviation angle of the incident light beam. In addition, a third channel is connected on the vertex of the triangular chamber, which is used to inject the control flow. The same solutions are filled in the outer flow stream and control flow stream. With the help of the control flow stream, the shape of the prism can be changed between symmetrically and asymmetrically as shown in Fig. 3.1 (b)-(d).

The incident light is directed to a single mode optical fiber that is parallel to the base of the prism. A convex lens is placed between the fiber and prism, which allows collimated light beams to be injected into the prism. On the other side of the prism, a semicircular chamber is set close to it and filled with fluorescent dye solution. The dye can be excited by the incident light and used for tracing the output light beams.

This section presents the theoretical model of the hydrodynamic control, optical deviation of the optofluidic prism and dispersion effect. Thereafter, the prism chamber is designed based on these physical models.

3.1.1 Hydrodynamic control of the prism

The position of the interface between two flow streams in a microchannel can be estimated according to the convective-diffusive transport theory [281, 282]. The model consists of two streams in a microchannel as show in Fig. 3.2. For a flat channel ($h \ll w$), the interface position of the two streams can be estimated based on

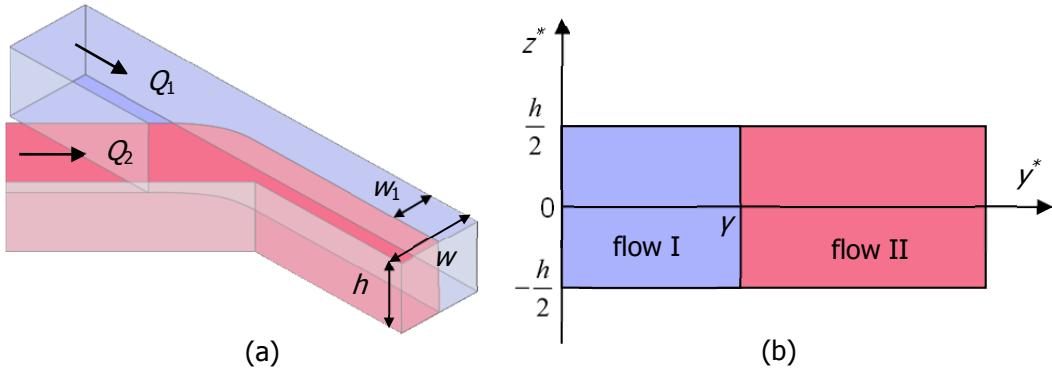


Figure 3.2: (a) Schematic of two laminar flows in a microchannel. (b) Dimensionless model of two streams for estimating the velocity distribution inside the channel.

the mass conservation as

$$\gamma = \frac{w_1}{w} = \frac{1}{1 + \frac{\eta_2}{\eta_1} \cdot \frac{Q_2}{Q_1}} \quad (3.1)$$

where w_1 is the width of the inner flow, w is the width of the channel. η_1 and η_2 are the viscosities of the inner and outer liquids, respectively. Q_1 and Q_2 are the flow rates of the inner and outer flows, respectively.

The hydrodynamic model for an optofluidic prism is shown in Fig. 3.3. The interface of the two flow streams in the chamber is theoretically a straight line from the inlet to the vertex of the chamber and the distribution of the flow flux is proportional to the width ratio of the flow streams. Therefore, a function of the base angle β_1 dealing with the ratio between Q_1 and Q_2 can be derived as

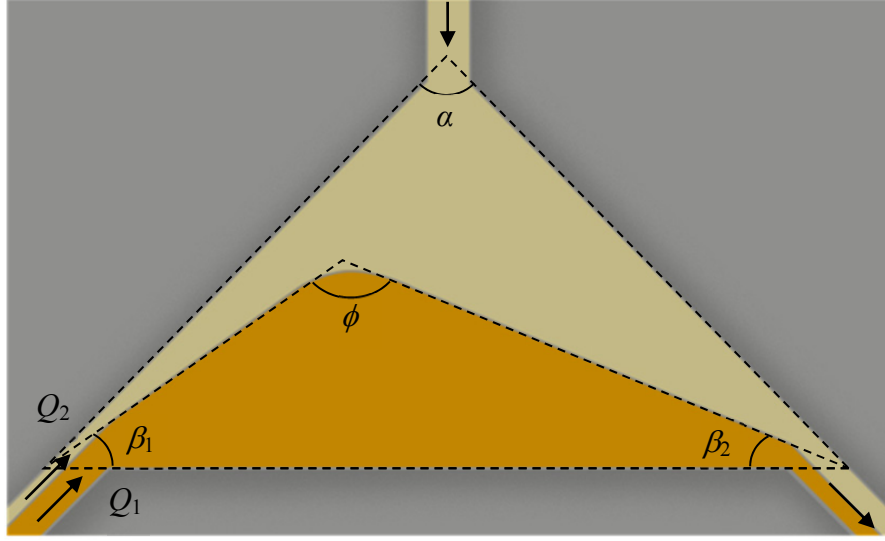


Figure 3.3: Hydrodynamic model of the optofluidic prism.

$$\beta_1 = \frac{90^\circ - \frac{\alpha}{2}}{1 + \frac{\eta_2}{\eta_1} \cdot \frac{Q_2}{Q_1}}, \quad (3.2)$$

where α is the apex angle of the triangular chamber. In this design, a control flow, which consists of the same liquid as the outer flow with the flow rate, Q_3 , is introduced to control the shape of the prism. Therefore, the other base angle β_2 is not merely the function of Q_1 and Q_2 , the effect of Q_3 should be considered. The value of Q_3 is defined as positive when the control flow is injected into the chamber; otherwise, the value of Q_3 is negative. Thus the base angle β_2 can be expressed as

$$\beta_2 = \frac{90^\circ - \frac{\alpha}{2}}{1 + \frac{\eta_2}{\eta_1} \cdot \frac{Q_2 + Q_3}{Q_1}}. \quad (3.3)$$

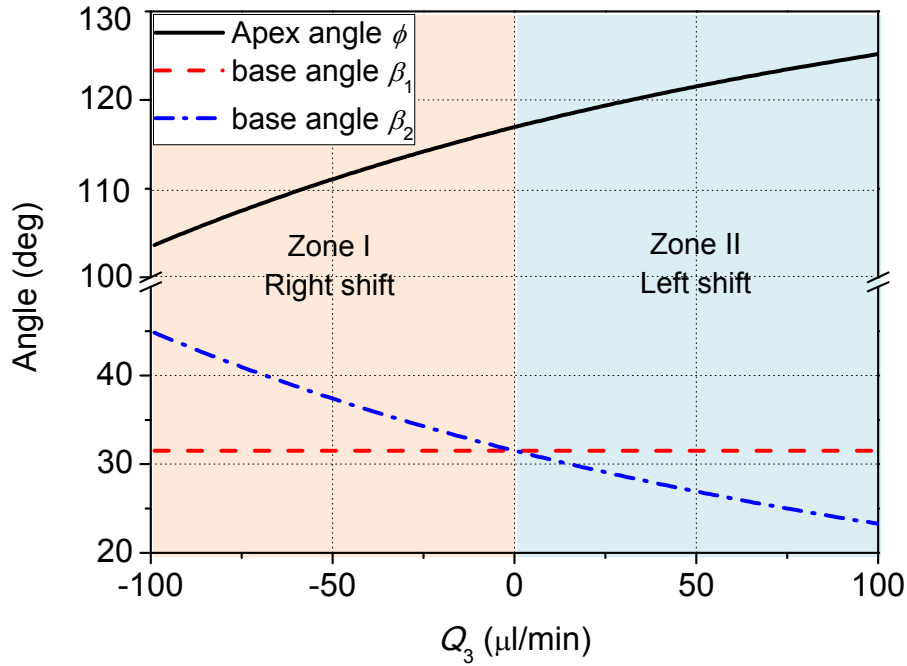


Figure 3.4: Vertex of the prism shifts as a function of the flow rate Q_3 while Q_1 and Q_2 are fixed.

The apex angle of the prism can be written as

$$\phi = 180^\circ - \beta_1 - \beta_2 . \quad (3.4)$$

The shape of the prism can be changed under different flow conditions as shown in Fig. 3.1. When the flow rate Q_3 is zero, the prism is symmetric about the axis of the chamber as shown in Fig. 3.1 (a). The apex angle of the prism increases with the flow rate ratio of Q_2 to Q_1 . When the flow rates Q_1 and Q_2 are kept constant, the apex angle of the prism increases with the flow rate Q_3 and the shape of the prism appears asymmetrical. As shown in Fig. 3.4, the base angle β_1 is fixed when the flow rates Q_1 and Q_2 are constant. The shift of the vertex of the

prism is caused by the difference between the base angle β_1 and β_2 . When the flow rate Q_3 is positive, the base angle β_2 is smaller than β_1 , and consequently the vertex of the prism is on the left side of the chamber as shown in Fig. 3.1(b). On the contrary, when the flow rate Q_3 is negative, the base angle β_2 is larger than β_1 , and consequently the vertex of the prism is on the right side of the chamber as shown in Fig. 3.1 (c).

3.1.2 Optical deviation of the prism

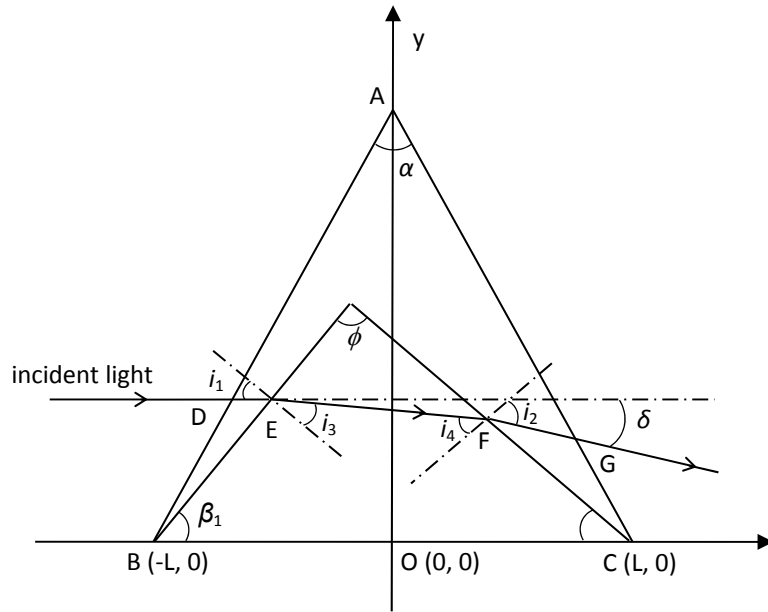


Figure 3.5: Optical model of the optofluidic prism.

When the optofluidic prism is formed in the microchamber, the propagating direction of the light beam is changed after it passes through the prism. Assuming a light beam is horizontally incident on the prism as shown in

Fig. 3.5, the total deviation angle δ of a light beam can be calculated based on Snell's law. The structure can be simply divided into two surfaces A'B and A'C. The total deviation angle is expressed as

$$\delta = (i_1 - i_3) + (i_2 - i_4), \quad (3.5)$$

and

$$\begin{cases} i_1 = 90^\circ - \beta_1, \\ i_2 = \arcsin(n \sin i_4), \\ i_3 = \arcsin(1/n \cos \beta_1), \\ i_4 = 180^\circ - \beta_2 - \beta_1 - i_3, \end{cases} \quad (3.6)$$

where $n = n_1/n_2$, n_1 and n_2 are the refractive index of the inner and outer fluid, respectively. When the prism is symmetric, from Eqs. (3.5) and (3.6), the total deviation angle can be expressed as

$$\delta = i_1 + \arcsin \left\{ \sin(\phi) \sqrt{n^2 - \sin^2(i_1)} - \cos(\phi) \sin(i_1) \right\} - \phi. \quad (3.7)$$

The variation of the output light beam position (point G) can also be estimated from geometrical optics.

The variation of the light beam width for the symmetric prism is discussed here. The model of the asymmetric prism can be analyzed using the similar method. Supposing the light beam has a width of w_{in} before entering the prism, the width of the beam becomes w_{out} after it passes through the prism as shown in Fig. 3.6. Due to the continuity of the light beam on the interfaces, the relationship between w_{in} and w_{out} can be easily determined as

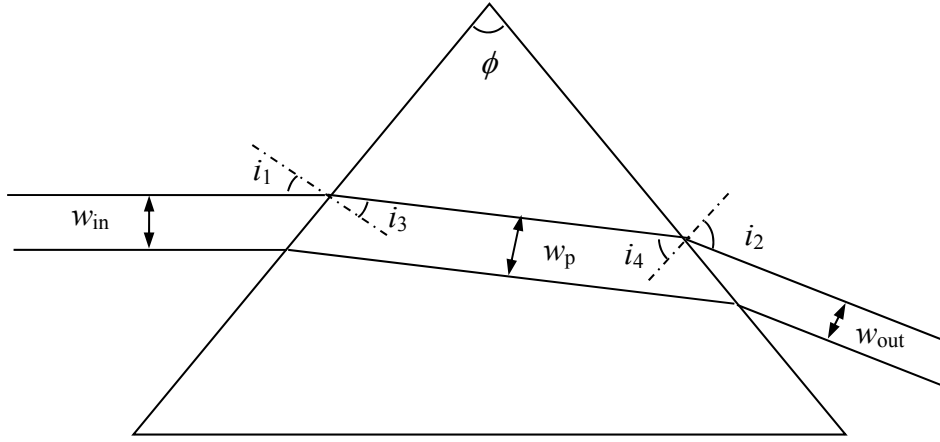


Figure 3.6: Illustration of the width variation of a light beam when it passes through a prism.

$$\frac{w_{in}}{\cos i_1} = \frac{w_p}{\cos i_3}, \quad (3.8)$$

and

$$\frac{w_{out}}{\cos i_2} = \frac{w_p}{\cos i_4}. \quad (3.9)$$

Combining Eqs. (3.8) and (3.9), one can remove w_p , which is the width of beam when the light is propagating in the prism. Using the Snell's law, the angle i_2 , i_3 and i_4 can be described by i_1 . Then the beam width ratio of the symmetric prism can be expressed as

$$M = \frac{w_{out}}{w_{in}} = \left\{ \frac{\left[1 - \left(\frac{n_2}{n_1} \right)^2 \sin^2 i_1 \right] \left[1 - \left(\frac{n_1}{n_2} \right)^2 \sin^2 (\phi - i_3) \right]}{(1 - \sin^2 i_1) [1 - \sin^2 (\phi - i_3)]} \right\}^{1/2}, \quad (3.10)$$

where $i_3 = \arcsin\left(\frac{n_2}{n_1}\sin i_1\right)$. When the light beam is horizontally incident on the prism, i_1 is equal to $\frac{\phi}{2}$. The beam expansion factor is only affected by the apex angle and refractive index of the prism.

3.1.3 Dispersion effect

In optics, dispersion is the phenomenon in which the phase velocity of a wave depends on its frequency, or alternatively when the group velocity depends on the frequency [283]. There are generally two sources of dispersion: material dispersion and waveguide dispersion. Material dispersion comes from a frequency-dependent response of a material to waves. For example, the separation of colors occurs in a prism. Waveguide dispersion happens when the speed of a wave in a waveguide depends on its frequency for geometric reasons. For example, the waves propagate through a photonic crystal.

Material dispersion can be used to construct spectrometers and spectroradiometers. Sometimes a diffraction grating is used in place of the prism for studying optical spectra, because they allow more accurate discrimination of wavelengths. However, a prism refracts the light into a single spectrum, whereas the diffraction grating divides the available light into several spectra. Because of this, slit images formed using a prism are generally brighter than those formed using a grating. Spectral lines that are too dim to be seen with a grating can often be seen using a prism. Therefore, dispersion is important for the study of the optofluidic

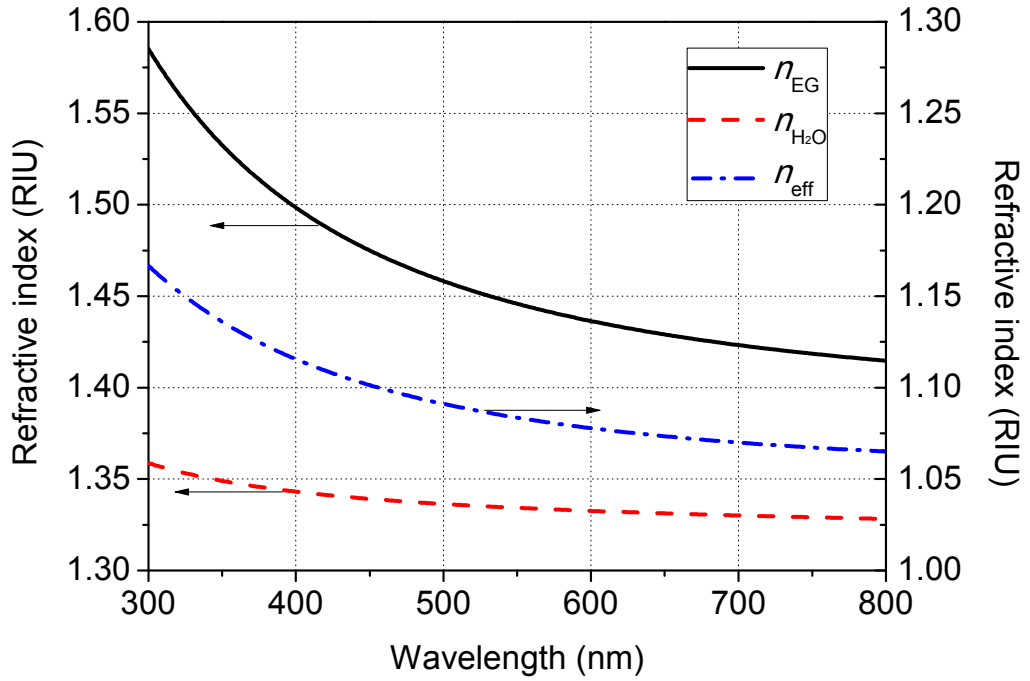


Figure 3.7: Refractive indices of ethylene glycol, water and an optofluidic prism constructed by the two fluids at different wavelengths.

prism.

As discussed in the last section, the deviation angle of the light beam passing through the prism is varied with the refractive index of the prism. However, the refractive index is some function of the light wavelength. For visible light, the refractive indices of most transparent materials (e.g. glass, water) increase with decreasing wavelength. Figure 3.7 shows the refractive indices of water (n_{H_2O}) and ethylene glycol (n_{EG}) [284, 285] at different wavelengths (λ). In general, the dispersion is more obvious with larger value of $\frac{\Delta n}{\Delta \lambda}$. Supposing an optofluidic prism is constructed by water and ethylene glycol flow streams, the effective

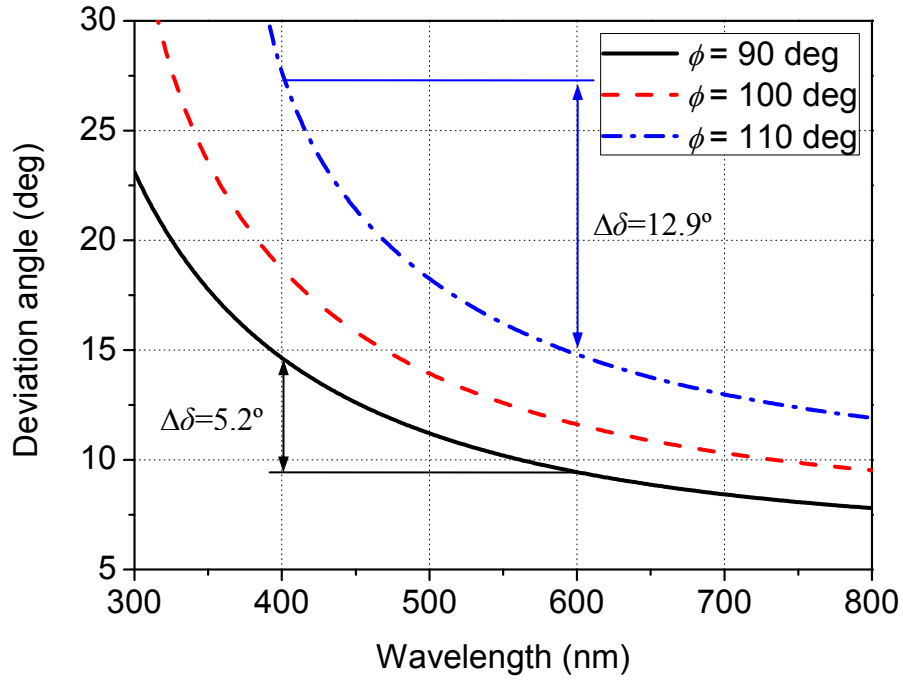


Figure 3.8: Relationship between the deviation angle and the wavelength of light with different apex angles.

refractive index of the prism (n_{eff}) can be calculated as shown in Fig. 3.7. When the wavelength (λ) of the incident light is changed from 300 to 800 nm, the effective refractive index of the prism is decreased from 1.166 to 1.065. The wavelength dependent refractive index can be used to study the dispersion of the prism.

Figure 3.8 plots the relation between the deviation angle and the wavelength of light with different apex angles. When the apex angle is fixed, the deviation angle is increased with the decreasing wavelength. Larger apex angle causes larger deviation difference between lights with varied wavelengths. For example, when the apex angle is 90° , the deviation angle difference between 400 and 600 nm is 5.2° . When the apex angle is 110° , the deviation angle difference

between 400 and 600 nm is increased to 12.9°. It means that large apex angle facilitates light separation with different wavelengths.

Thus the dispersion can be varied by changing the prism shape. In addition, the optofluidic prism can modify the output beam position. Therefore, a tunable optofluidic prism can provide better wavelength selection. The experimental results of the dispersion effect will be discussed in the later section.

3.1.4 Design of the triangular chamber

In order to form an optofluidic prism with optimum optical precision and tuning range, the structure of the chamber has to be optimized. Because the optofluidic prism is constructed by two laminar flow streams, the stability of the flows is important on the performance of the optofluidic prism. Here, COMSOL MultiphysicsTM is used to simulate the fluid behavior with different geometrical designs of different chambers.

The prism shape is studied by simulating the flows of the streams in chambers with different apex angles as shown in Fig. 3.9. Based on the simulation results, a smaller apex angle of the chamber allows a larger variation in the apex angle of the prism. For example, within the same range of flow rate ratio ($Q_2/Q_1 = 0\sim5$), the tuning range of the apex angle is 50° for the chamber with 110° apex angle, while it can be 100° for the chamber with 50° apex angle. However, recirculation zones caused by the turbulence flow occur at the vertex of chamber when the chamber angle is smaller than 90° as shown in Fig. 3.10. This induces the

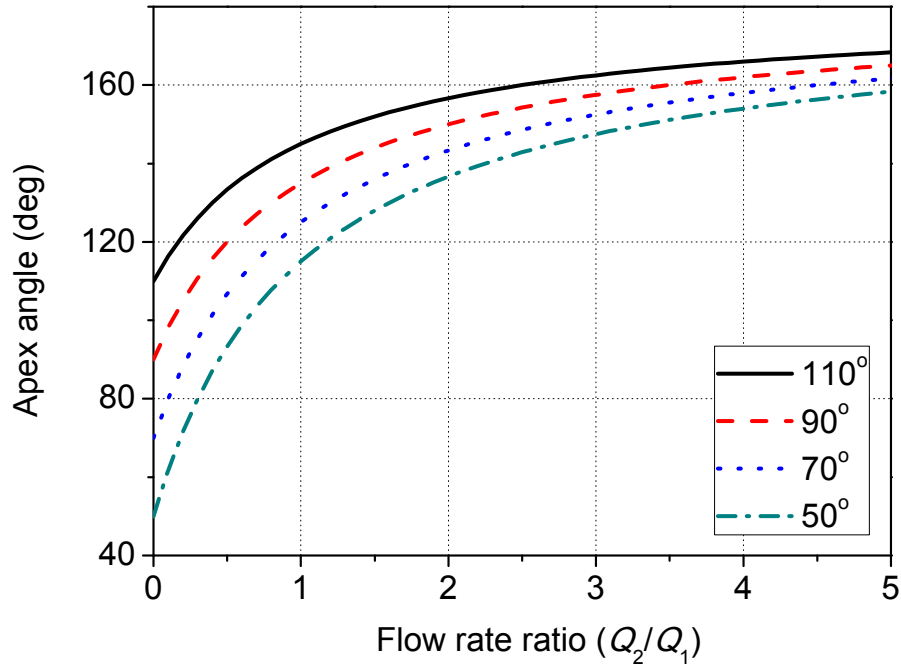


Figure 3.9: Relationship between the apex angle of the prism and the flow rate ratio with different chamber shapes.

top of the optofluidic prism becomes much flatter and reduces the effective working length on the prism. In order to meet the balance between the two requirements, the chambers with apex angle of 70° and 90° are chosen in the experiments.

The influence of width of the inlet is investigated based on the simulation results in the chamber with apex angle of 90°. The inlet width and the length of the base are in a ratio of 1:22 or 1:8. For an optofluidic component, smooth and clear interface between the flows is critical. Figure 3.11 shows that the narrow inlets facilitate the diffusion between the flows. That means too narrow inlets are not good for realizing an optofluidic prism. Here, we also discussed the relationship between the inlet width and the working length which refers to the straight line part of the

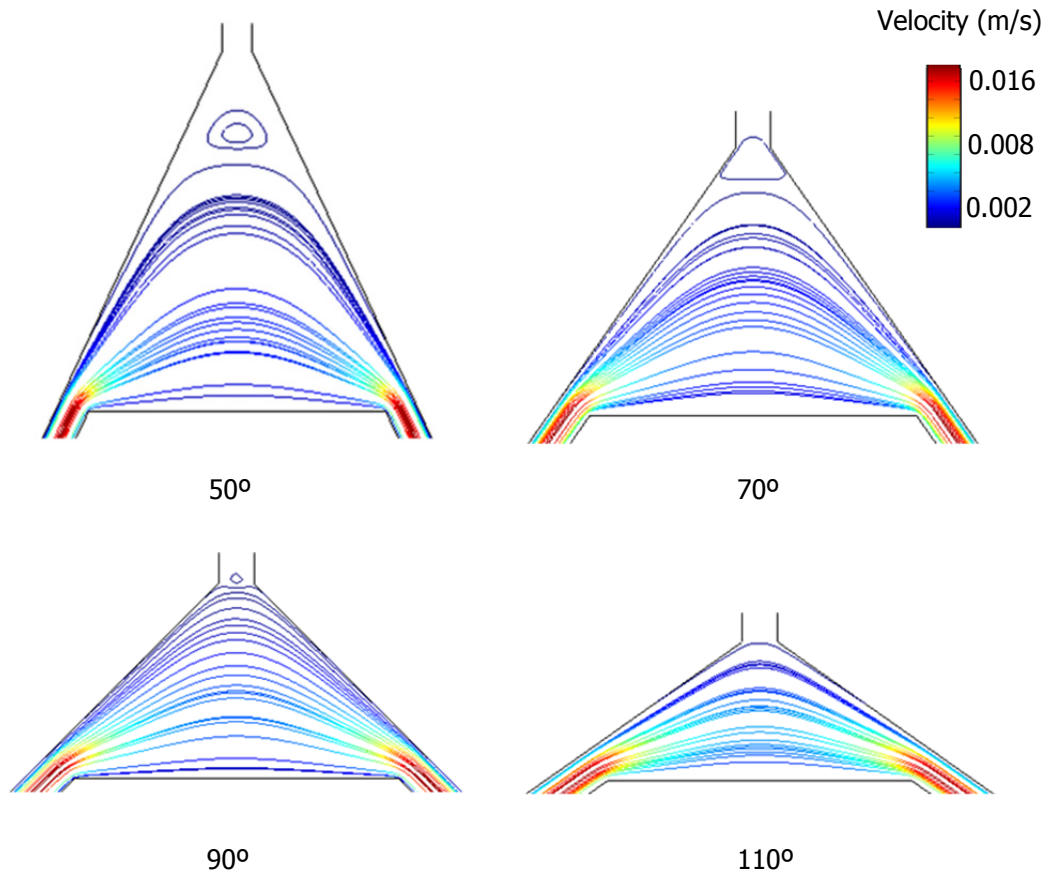


Figure 3.10: Simulation results of the flow streams with different chamber shapes. The streamlines represent the velocity field with different colors.

interface from the inlet to the vertex of the prism. As shown in Fig. 3.12, the working length is shorter for chamber with wider inlets. After making a trade-off between the diffusion and working length, the ratio of the inlet width to the length of the base of the chamber is chosen to be 1:18.

The shape of the prism is based on the laminar flow concept, which is greatly depends on the channel size. As the chamber size increases, the diffusion between the two flows increases. However, the working distance and the length of optical path decreases as the chamber size decreases. Consequently, the tuning range of the optofluidic prism is reduced. For completely recording the

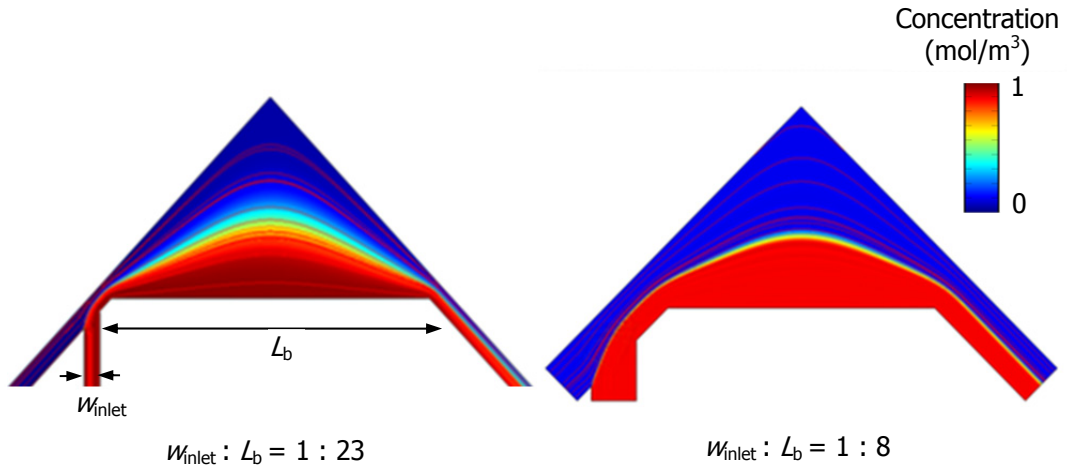


Figure 3.11: Simulation results of the diffusion with different ratios of width of inlet to the length of the base of the triangular chamber. The solutions with concentration of 0 and 1 mol/m³ are injected into the chamber, respectively. The color map represents the concentration distribution.

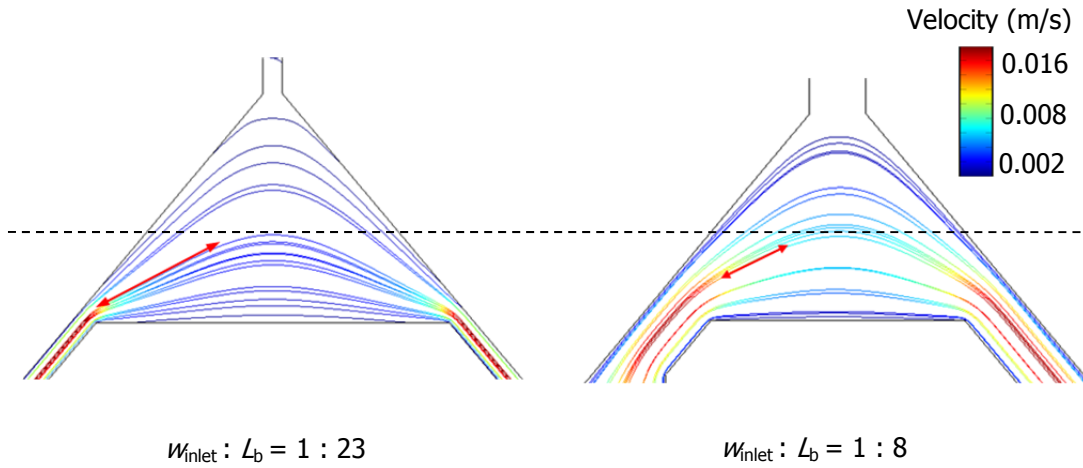


Figure 3.12: Simulation results of the flow streams with different ratios of width of inlet to the length of the base of the triangular chamber. The line with arrows shows the effective working length for each chamber when the height of the prism is fixed. The streamlines represent the velocity field with different colors.

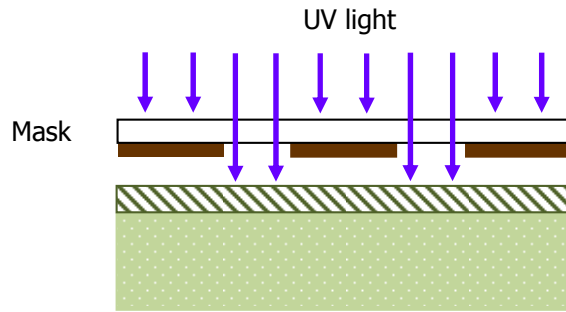
experimental data, the size of the field of view in the microscope system is also need to be considered. Finally, the optimal design is decided on $L_b = 3600 \mu\text{m}$ and $w_{\text{inlet}} = 200 \mu\text{m}$.

3.2 Fabrication processes and experimental setups

3.2.1 Polymer soft lithography fabrication flow

The fabrication of the optofluidic chip is based on the polymer soft lithography fabrication technique. The fabrication process flow consists of patterning, developing, molding and bonding as shown in Fig. 3.13. Polydimethylsiloxane (PDMS) is the most promising material for microfluidic chip because it is biocompatible, inexpensive, easy to fabricate and applicable for mass replication.

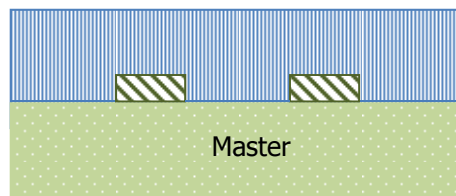
The design layout of the optofluidic chip is drawn using a computer-aided design (CAD) program (L-Edit 12.0). A dark field clear feature chrome mask is commercially fabricated on a piece of sodalime glass based on the CAD drawing. In order to fabricate the master for molding, a 6-inch silicon wafer is cleaned by acetone, isopropyl alcohol (IPA) and DI water, then dried in oven. A layer of SU-8 photoresist (MicroChem, SU-8 50) is spun coated on the wafer at 1800 rpm for 30 s (Spin coater: CEE, 200). Next, the wafer coated with the photoresist is soft baked at 65 °C for 6 min and 95 °C for 20 min to evaporate the solvent and densify the film of the SU-8 layer. After exposed to UV light for 20 s under the soda lime glass mask (Mask aligner: OAI, J500-IR/VIS), the wafer is baked at 65 °C for 1 min and 95 °C for 5 min. Then, it is developed by sinking in the SU-8 developer (MicroChem) for 6 min. The substrate is rinsed with IPA and DI water, and dried with nitrogen. Finally, the wafer is hard baked at 120 °C in an oven for 10 min to further cross-link the SU-8 layer. Thus, the master is fabricated.



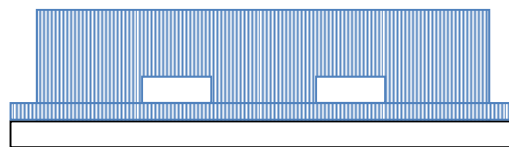
(a) Patterning



(b) Developing



(c) Molding



(d) Bonding

Figure 3.13: Fabrication process flow of PDMS chip.

Replica molding is an efficient method for the duplication of the structure on a mold. A prepolymer of the PDMS elastomer is prepared from the Sylgard 184 silicone elastomer kit (Dow Corning) by mixing the polymer base with the curing agent at a ratio of 10:1 by weight. The pre-cured PDMS is degassed in the vacuum desiccator for 30 min. Then, the mixture is poured on the master and degassed for another 15 min. After curing at 75°C for 1 h, the PDMS is peeled off from the master.

The final step is to bond the PDMS replica on another PDMS substrate to complete a sealed microfluidic channel. A flat layer of PDMS is coated on a glass slide and cured. A through hole is punched at each inlets and outlets of the PDMS replica with a 0.75-mm diameter puncher (Harris Uni-core, 0.75). The two pieces of PDMS are both oxidized by plasma treatment with a handheld corona treater ((Electro-Technic Products, BD-20AC) for 3 mins. The treated surfaces of the two PDMS substrates bond spontaneously when they contact with each other. For a stronger bond, the PDMS chip is put aside to anneal overnight. An irreversible bonding is formed.

3.2.2 Optofluidic prism fabrication

The microfluidic chip is fabricated using PDMS following the steps in the previous section. The base of the chamber has a width of 3600 μm , the inlets and outlets have a width of 200 μm . The height of the channel is approximately 100 μm to accommodate the optical fiber insertion into the device as the light

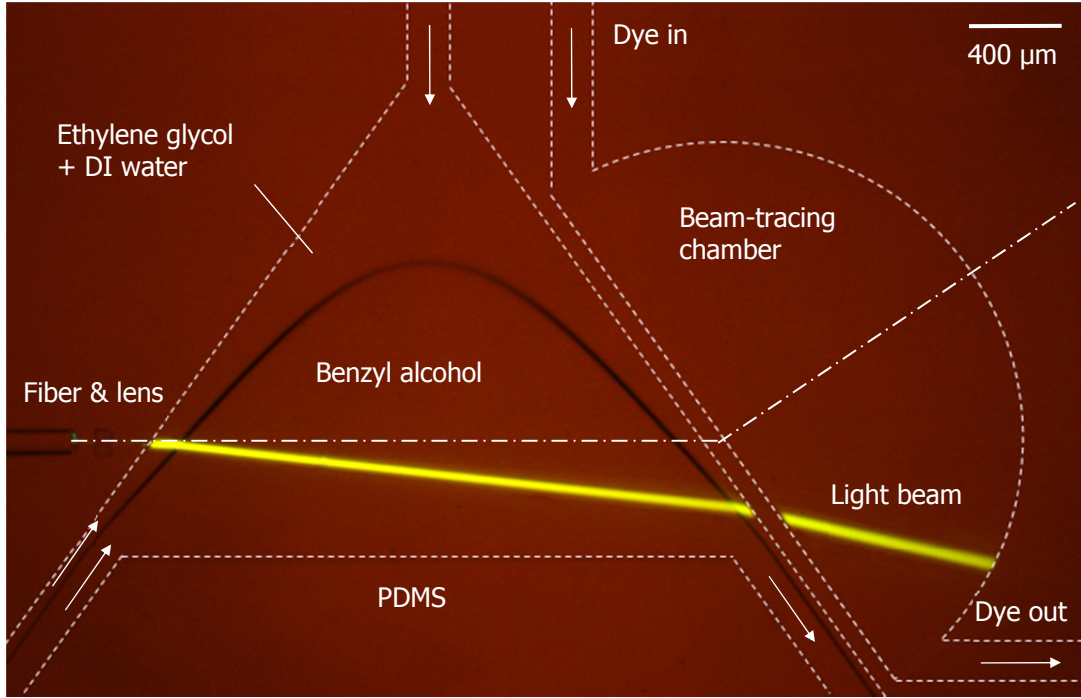


Figure 3.14: Photograph of the optofluidic prism.

source. PDMS lens is built between the fiber insertion channel and the optofluidic prism chamber to collimate the light beam. A semicircular chamber is fabricated on the right side of the prism chamber for output light beam tracing as shown in Fig. 3.14.

3.2.3 Preparation of fluids

Benzyl alcohol ($n = 1.540$, viscosity $\eta = 5.47$ mPa s at 25°C) and DI water ($n = 1.332$, viscosity $\eta = 0.89$ mPa s at 25°C) are used as the inner liquid. A mixture (viscosity $\eta \approx 8$ mPa s at 25°C) of 80% ethylene glycol and 20% DI water with an effective refractive index, which matches to the refractive index of PDMS ($n =$

1.412) is used as outer liquid. Matching the refractive index of the cladding to that of PDMS reduces the scattering of light on the microchannel wall. The light deviation is observed using the combination of inner-outer liquids due to the sufficiently large contrast in refractive indices. The mixture of ethylene glycol and DI water ($n = 1.412$) containing 0.2 mM rhodamine 6G and 0.03 mM fluorescent red 646 is injected into the beam tracing chamber to visualize the optical path. The rhodamine 6G and 0.03 mM fluorescent red 646 are excited by the 488-nm and 633-nm laser, respectively. In order to image the shape of the optofluidic prism easily, rhodamine 6G is doped in the inner liquid and fluorescent image is captured.

3.2.4 Experimental setup

Figure 3.15 shows the experimental setup of the optofluidic prism. The prepared liquids are kept in 20-ml syringes, which are driven by the syringe pumps (NE-1000, New Era Pump System Inc.). The input light from an argon ion laser (Stellar-PRO, Modu-Laser) is coupled into the optofluidic prism using a single-mode optical fiber (NA = 0.22). The intensity of output light is detected by a spectrometer (HR4000, Ocean Optics Inc.). The image acquisition is performed using a microscope (Nikon Eclipse TE2000-E) and a CCD camera (Nikon DS-5M). The Xe lamp and filters mounted on the microscope can offer the excitation light source for fluorescent image.

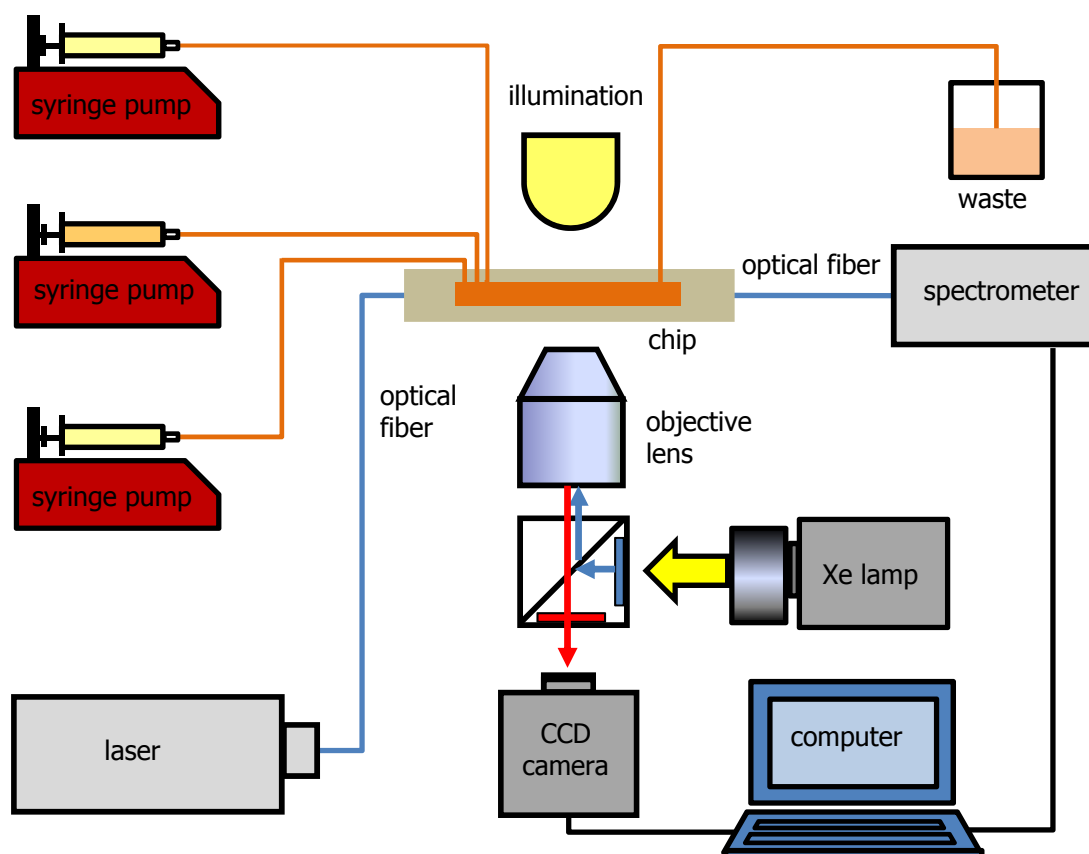


Figure 3.15: Experimental setup of the optofluidic prism.

3.3 Experimental results and discussions

3.3.1 Control of the prism shape

In order to verify the theory in predicting the relationship between the flow rates and the apex angle of the optofluidic prism, the chamber with 70° apex angle is used. The fluorescent dye dissolved in the inner flow, which is benzyl alcohol, is excited and appeared red. The outer flow filled with the ethylene glycol solution ($n = 1.412$) appears black on the image. The interface between the dark and red region is clearly observed.

In the case of a symmetric prism, the flow rate of the control flow is zero. The flow rate of the outer flow is fixed at $10 \mu\text{l/min}$ while the flow rate of the inner flow varied from 10 to $180 \mu\text{l/min}$ to tune the apex angle of the optofluidic prism as shown in Fig. 3.15. The apex angle is changed from 135° to 75° accordingly. When the flow rate of the inner flow increases, the interface of the two liquids approaches the sidewalls of the chamber, and subsequently the apex angle becomes smaller. The relationship between the flow rates and the apex angle of the prism is analytically estimated by using Eqs. (3.2) – (3.4) and depicted as the solid line in the Fig. 3.15, which agrees well with the theoretical prediction. Without the effect of the control flow, a symmetric shape is maintained during the whole flow rate changing process. However, the prism shape is not perfect with the top of the interface being an arc-shape as noted in the simulation results. To avoid the effect of this deviation on the light

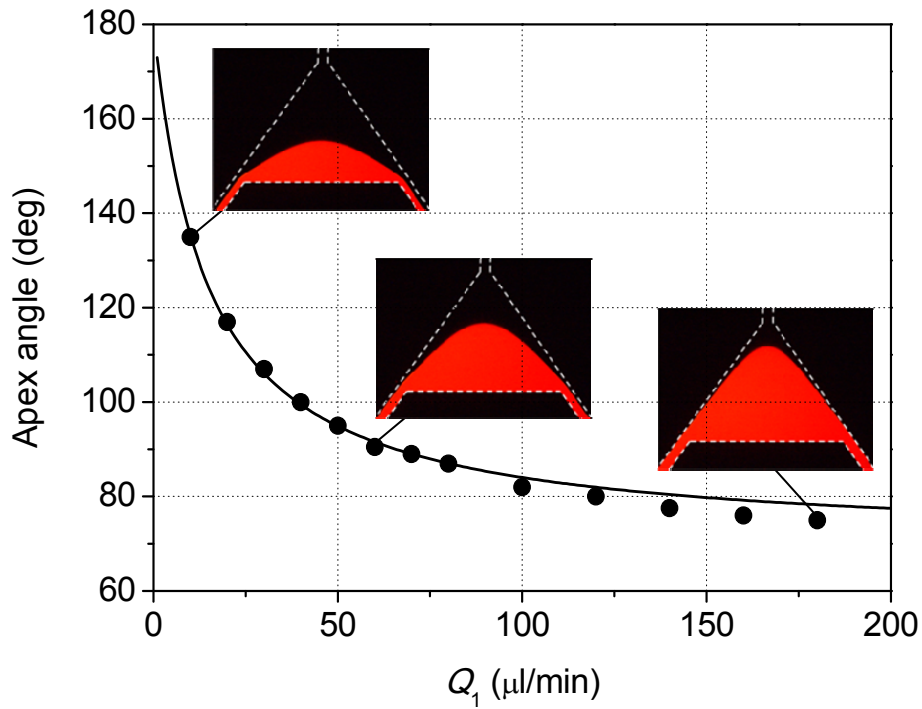


Figure 3.16: Relationship between the apex angle of the prism and the flow rate Q_1 when Q_2 is fixed at 10 ml/min.

propagation, the light insertion is positioned nearer to the lower part of the optofluidic prism.

Asymmetric shapes of the prisms are achieved with the assistance of the control flow. Figure 3.17 shows the shape of the prism obtained as a function of the flow rate of the control flow. The flow rate of the inner flow is fixed at 120 $\mu\text{l/min}$, while the flow rate of the outer flow is chosen as 10 and 70 $\mu\text{l/min}$, respectively. The flow rate of the control flow is varied from -60 to 90 $\mu\text{l/min}$. When the flow rates of the inner and the outer flows are both fixed, the apex angle of the prism is increased with the flow rate of the control flow. Different from the case of a

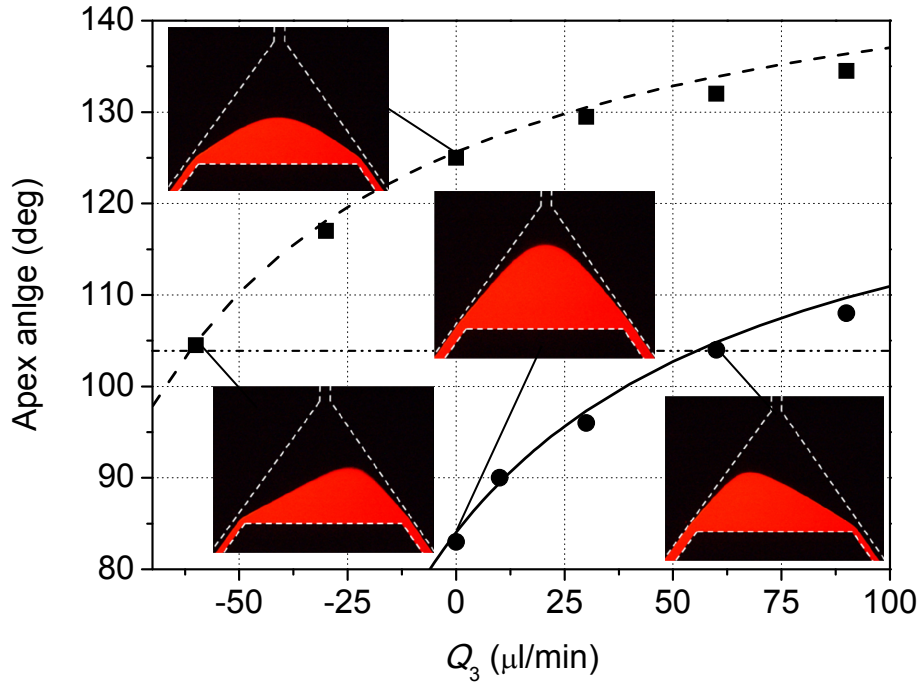


Figure 3.17: Relationship between the apex angle of the prism and the flow rate Q_3 when Q_2 is maintained at 120 $\mu\text{l/min}$ and Q_1 is maintained at 10 $\mu\text{l/min}$ (solid line) and 70 $\mu\text{l/min}$ (dash line).

symmetric prism, the vertex of the prism is no longer fixed in the central line of the chamber. It moves from the right to the left side with the increasing flow rate of control outer flow as shown in Fig. 3.17. The base angle β_1 of the prism is not changed by the control flow when the flow rates of the outer and the inner flows are fixed. The base angle β_2 is varying with the flow rate of the control flow and causes the change of the prism shape. When the control flow is flowing out from the chamber ($Q_3 < 0$), the volume of flow emerging to the original outlet decreases. Subsequently, the flow rate of the outer flow at the outlet side of the chamber is decreased. According to Eqs. (3.2) and (3.3), the base angle β_2 is larger than β_1 .

Hence the vertex of the prism is on the outlet side of the chamber and the right-shifting prism is formed. On the contrary, when the control flow is flowing into the chamber ($Q_3 > 0$), the flow rate of the outer flow is increased at the outlet side of the chamber. Therefore, the base angle β_2 is smaller than β_1 . Hence the vertex of the prism is on the inlet side of the chamber and a left-shifting prism is formed. For example, when the flow rates of the outer flow and the control flow are 10 and 60 $\mu\text{l}/\text{min}$, the base angles β_1 and β_2 are measured as 48° and 27° , respectively. The formed left-shifting prism had an apex angle of 105° . On contrary, when the flow rates of the outer flow and the control flow are 70 and -60 $\mu\text{l}/\text{min}$, the base angles β_1 and β_2 are measured as 27° and 48° , respectively. The formed right-shifting prism has an apex angle of 105° . Therefore, prisms with same apex angle but different shapes can be achieved by tuning the control flow. The tunable optofluidic prism is achieved through the change of shape by controlling the flow rates.

In order to study the stability of the prism, the experiments are repeated for 10 times and 5 experimental data in 30-s interval are measured in each run. The standard deviation of apex angles of the prism is varied from 0.66° to 1.08° . However, when the inner flow is replaced with DI water, the standard deviation is varied from 1.11° to 1.95° . Therefore, the prism made of benzyl alcohol is more stable than that made of DI water. Such difference is caused by the Reynolds number mismatch between the inner and outer flow. For the case of a symmetric prism, the flow rate of outer flow is fixed at 10 $\mu\text{l}/\text{min}$ with Reynolds number of 0.23. When the inner flow is benzyl alcohol, the Reynolds number is changed from 0.64 to 5.73 when the flow rate varies from 20 to 180 $\mu\text{l}/\text{min}$. On the other hand, when the inner flow is DI water, the Reynolds number is changed from 14.98 to

67.42 when the flow rate varies from 80 to 360 $\mu\text{l}/\text{min}$. Since the difference of Reynolds number between the outer mixture and inner DI water flow is much larger, the prism shape is more unstable for the prism constructed by DI water.

3.3.2 Tunable deviation angle of output light

To demonstrate the tunability of the optical path of the optofluidic prism, the beam-tracing experiments for the symmetric prisms are studied. Figure 3.18 and 3.19 show the variation in the deviation angle of the output beam in different flow conditions. The light beam is horizontally incident on the prism. The light path within the beam-tracing chamber shows a green color due to the excited fluorescent dye. The sign of deviation angle is positive (negative) when the output light beam is refracted downwards (upwards). The chambers with 70° and 90° apex angle are both used in the experiments to study the effects of the chamber shape on the prism shape and the tunable deviation angle of the output light. The outer flow is the ethylene glycol solution ($n = 1.412$) at the flow rate of 10 $\mu\text{l}/\text{min}$. The inner flow is DI water or benzyl alcohol at the flow rate varying from 20 to 400 $\mu\text{l}/\text{min}$. Using two types of inner fluids is aimed to expand the tuning range of the deviation angle.

When the refractive index of the inner flow is higher than that of the outer flow (e.g. benzyl alcohol as the inner fluid), the output light beam is refracted downwards as shown in Fig. 3.18. The apex angles of the prisms and the deviation

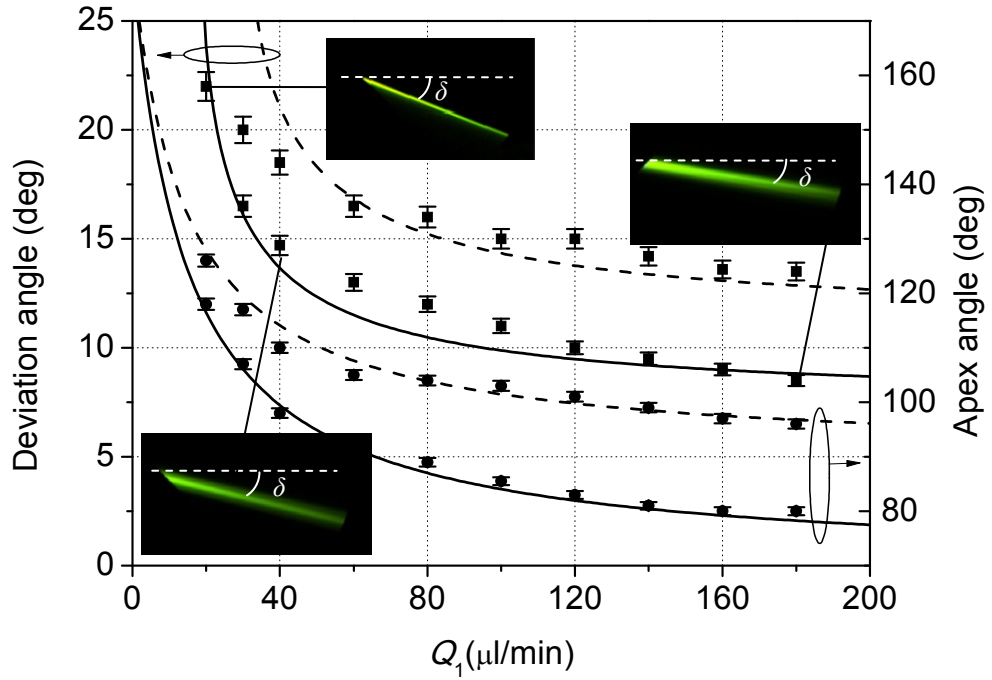


Figure 3.18: Relationship between the deviation angle, apex angle and the flow rate Q_1 with chambers of 70° (solid line) and 90° (dash line). The inner liquid is benzyl alcohol ($n = 1.540$).

angles of the output light beams are plotted as a function of the flow rate of the inner flow which is benzyl alcohol. When the flow rate of the inner flow is varied from 20 to 180 $\mu\text{l/min}$, the apex angle of the prism in 70° chamber is changed from 116.5° to 78° , while the one in 90° chamber is changed from 128° to 97° . Although the apex angle of the prism keeps decreasing when the flow rate increases beyond 180 $\mu\text{l/min}$, the decrease rate becomes much slower. Moreover, the apex angle of the prism will not be smaller than that of its chamber. In addition, when the apex angle of the prism increases, the height of the prism is decreased. Considering the

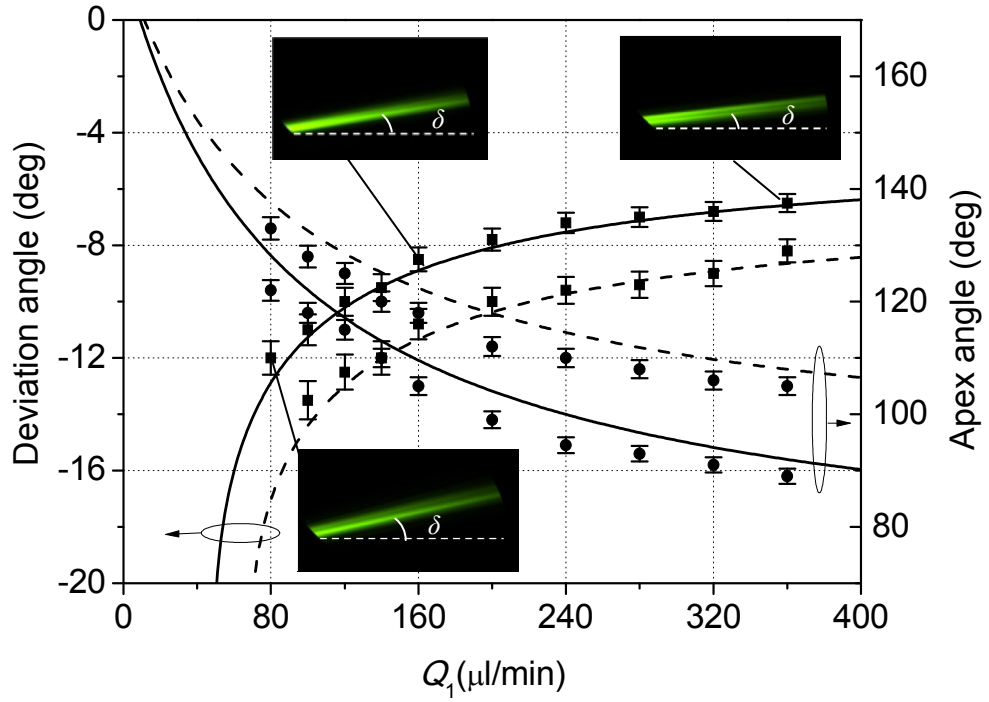


Figure 3.19: Relationship between the deviation angle, apex angle and the flow rate Q_1 with chambers of 70° (solid line) and 90° (dash line). The inner liquid is DI water ($n = 1.332$).

fixed position of the fiber, only the prisms with apex angle smaller than 130° are studied. The corresponding deviation angles are varied from 21° to 8.5° for 70° chamber, and 22° to 11.5° for 90° chamber.

When the refractive index of the inner flow is lower than that of the outer flow (e.g. DI water as the outer fluid), the output light beam is refracted upwards as shown in Fig. 3.19. The apex angle of the prism constructed using DI water is larger than that using benzyl alcohol with the same flow rates because the viscosity of DI water is much lower than that of benzyl alcohol. When the flow rate of the inner flow reaches $200 \mu\text{l/min}$, the apex angle of the prism is only

103° for 70° chamber and 116° for 90° chamber. In order to expand the tuning range of the deviation angle, the flow rate of the inner flow is changed from 40 to 360 $\mu\text{l}/\text{min}$. The deviation angles are varied from -12° to -6.5° for 70° chamber and -13.5° to -8° for 90° chamber.

The variation of the deviation angle follows the variation of the shape of the prism as expected from geometrical optics: a prism with larger apex angle generates a larger deviation angle. In addition, the experimental results also agrees well with the theoretical prediction such that chamber with smaller apex angle can achieve larger tuning range of the prism apex angle. However, the tuning range of the deviation angle is not expanded much in the chamber with smaller apex angle. The distinguished differences exist in the working zone. The chosen of the chamber shape should be based on the specific request of the output light. For the benzyl alcohol and 70° chamber system, the working zone of the deviation angle is 21° to 8.5°. If the requested deviation angle is 7°, the chamber will be designed with smaller apex angle (e.g. 50°) or a liquid with lower refractive index should be chosen. By using the existing design and chosen liquids, the deviation angle can be tuned from -13.5° to 22°. It is possible to achieve a larger deviation angle using other outer and inner liquids with higher refractive index contrast.

The width of the light beam is changed after passing through the prism. In the experiments, the width of the beam entering the prism is approximately 50 μm . The width of the beam exiting the prism is changed from 12 to 50 μm with the tunable prism shape and refractive index.

The changes can be described by the beam expansion factor (M), which is

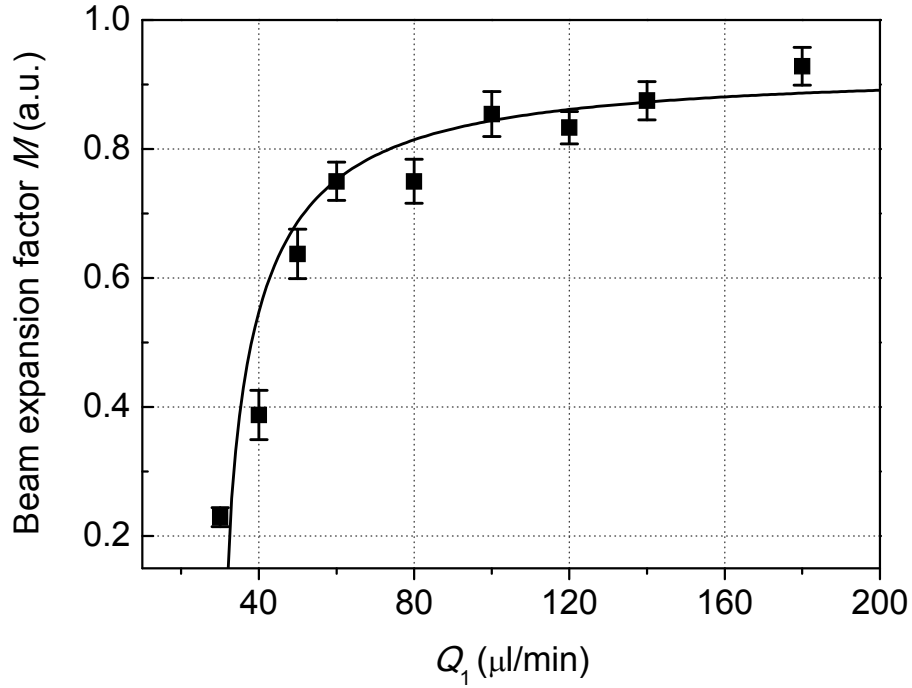


Figure 3.20: Relationship between the beam expansion factor and the flow rate Q_1 with chamber of 90° . The inner liquid is benzyl alcohol ($n = 1.540$).

the ratio of the width of beam exiting the prism (w_{out}) to the width of beam entering the prism (w_{in}). According to Eq. (3.10), the beam expansion factor depends on the incident angle, prism shape and refractive index. Figure 3.20 shows the beam expansion factor varies as a function of the flow rate Q_1 while the flow rate Q_2 is fixed as $10 \mu\text{l/min}$. The experimental results (square) agree well with the calculated results (solid line) estimated from Eq. (3.10). This relationship between the beam expansion factor and the flow rate is not linear. The changing rate slows down when Q_1 is larger than the $80 \mu\text{l/min}$. As shown in Fig. 3.20, the width of the output light beam is always shorter than that of the input light beam, i.e. $M < 1$. Similar results are obtained using water as the inner flow.

3.3.3 Parallel light scanning with constant deviation angle

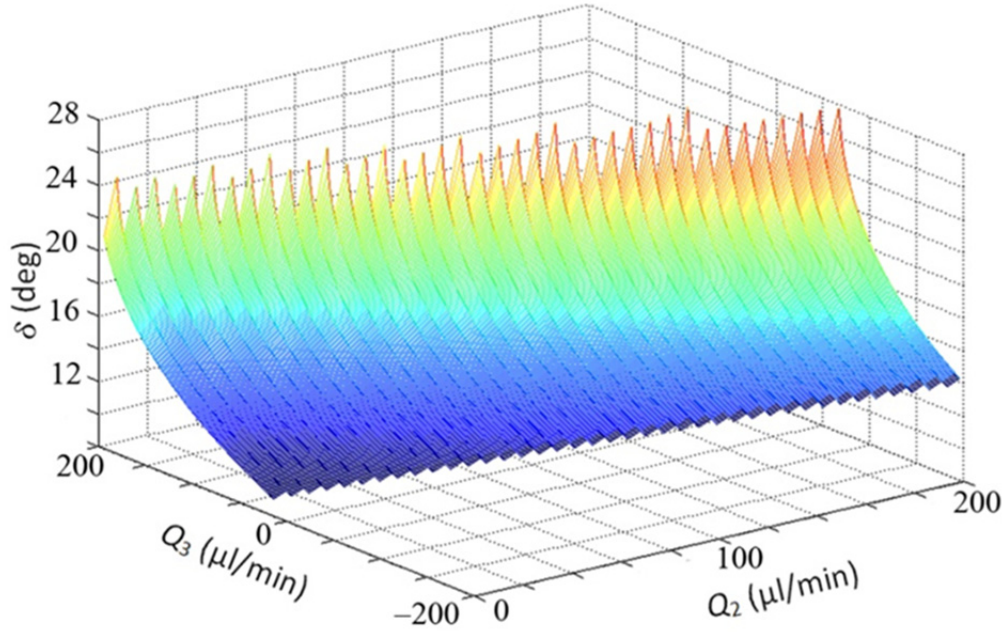


Figure 3.21: Deviation angle as a function of the flow rate Q_2 and Q_3 while the flow rate Q_1 is fixed at 10 $\mu\text{l}/\text{min}$.

For the symmetric prism, when the ratio of the flow rates between the inner flow and the outer flow is changed, the deviation angle of the output light beam is changed accordingly, so as the position of the output light beam (point G in Fig. 3.4). It is hard to control the output position and the propagating direction of the light beam concurrently without changing the properties of the liquids. This limitation will be overcome by asymmetric design of the prism, which offers more precise and flexible control over the optical path. For example, Figure 3.21 shows that the same deviation angle can be obtained by using different combination of flow rate Q_2 and Q_3 . That means one deviation

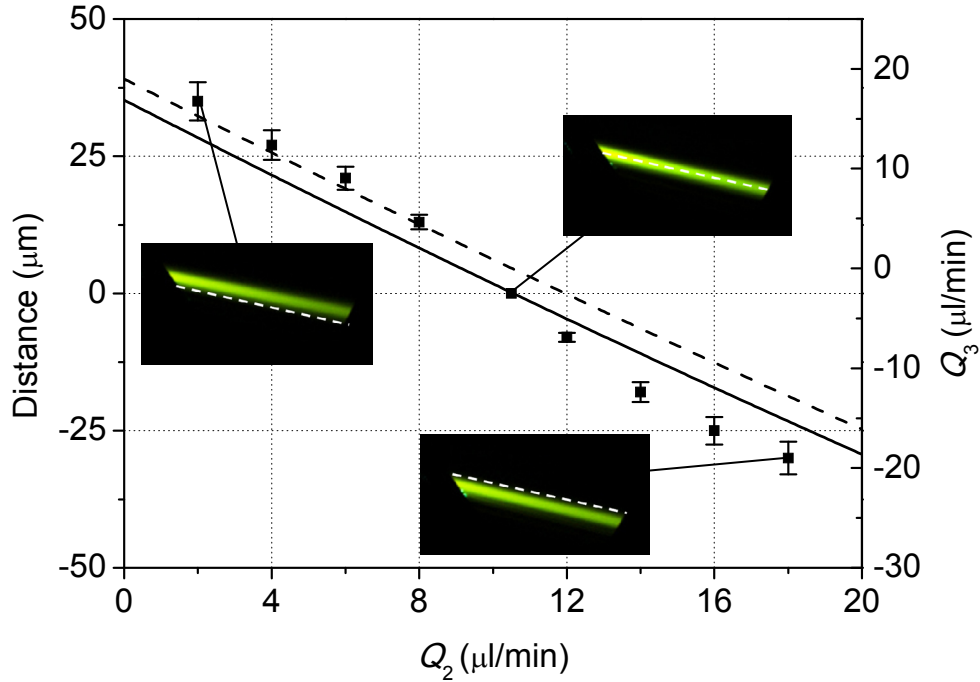


Figure 3.22: Light scanning controlled by Q_2 and Q_3 , when Q_1 is kept at 100 $\mu\text{l}/\text{min}$. The output light position (solid line) and Q_3 (dashed line) are both plotted as the functions of Q_2 .

angle is corresponding to several different positions of the output light beam.

In the experiment, the flow rate of inner flow (Q_1) is kept constant at 100 $\mu\text{l}/\text{min}$. The flow rates of the outer flow (Q_2) and the control flow (Q_3) are adjusted synchronously, while keeping the deviation angle constant at 10° . The relationship between Q_2 and Q_3 is plotted as dashed line in Fig. 3.22. The calculated output positions are changed along with the flow rates and plotted as a function of Q_2 in a solid line. Several typical combinations of Q_2 and Q_3 are experimented, which can generate the refracted light beam with a deviation angle of 10° . The light beams are observed to be parallel shifted down with a

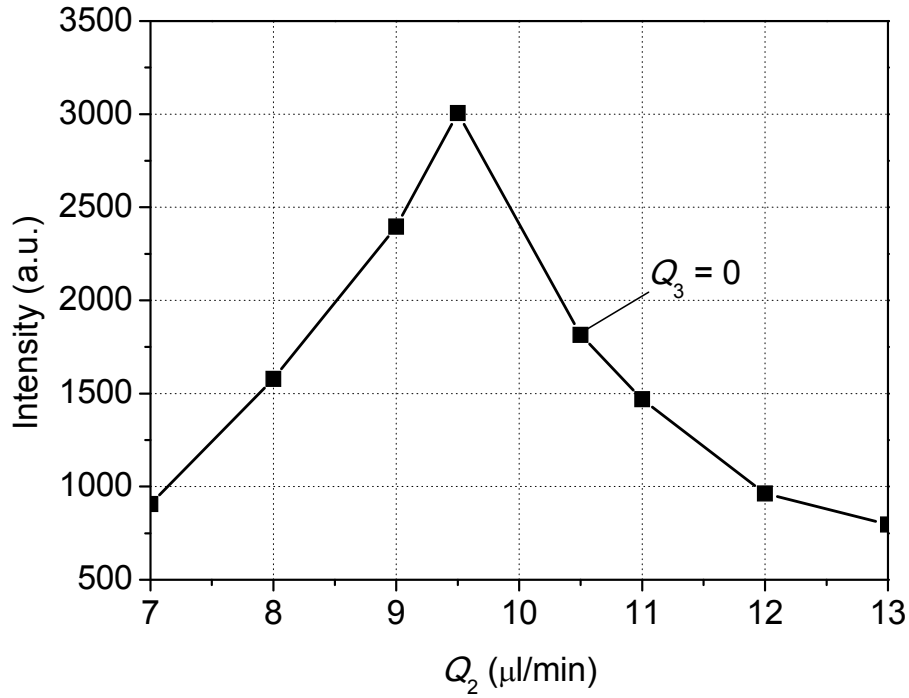


Figure 3.23: Adjustment of the detected light intensity by tuning the output position.

deviation angle of 10° when Q_2 is increased. The position of the output light is measured from the images captured from CCD camera and plotted as a function of Q_2 . The results show a tuning range of approximately $60 \mu\text{m}$. A larger tuning range is possible by further optimizing the refractive indices and the chamber geometries.

In order to demonstrate its potential in adjusting the alignment of the optical path between two components, an optical fiber is fixed while parallel light scanning is performed. Theoretically, the optical fiber is aligned to receive light with a deviation angle of 10° at the optimal position ($Q_2 = 10.5 \mu\text{l/min}$). In the experiment, parallel light scanning is performed and the detected intensity is

plotted in term of Q_2 as shown in Fig. 3.23. The maximum value of the light intensity is not at the predicted position, but in the condition when the asymmetric prism is formed ($Q_2 = 9.5 \mu\text{l/min}$, $Q_3 = 1.7 \mu\text{l/min}$). The light intensity is increased by 65.7% as compared to the theoretically predicted position. This shows the importance of optical path alignment in integrated micro-optical circuits and also the strength of the developed optofluidic prism. To the best of our knowledge, such precise position control of the light beam without changing its propagation direction has never been previously demonstrated in the lab-on-a-chip system. The potential applications for the optical-based lab-on-a-chip such as localized or parallel scanning fluorescent excitation can take great advantages over the tunable optofluidic prism.

3.3.4 Light dispersion

The dispersion of light by glass prisms is used to construct spectrometers and spectroradiometers. Compared with the solid optical components for generating light dispersion, the optofluidic prism provides better flexibility. For example, in order to select a single wavelength light, a fix prism must use additional components such as rotating lens. Whereas the tunable optofluidic prism can change the deviation angle and output position of light by just changing the flow rates. To demonstrate the optical dispersion caused by the optofluidic prism, the argon ion laser (488 nm) and He-Ne laser (633 nm) are used as the light sources. The light beams are visualized by rhodamine 6G and fluorescent red 646, respectively. The refractive index of the optofluidic prism increases with shortening wavelength. As a

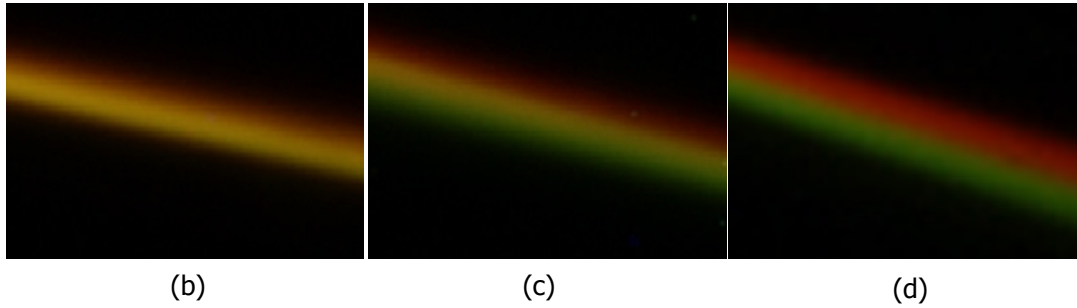
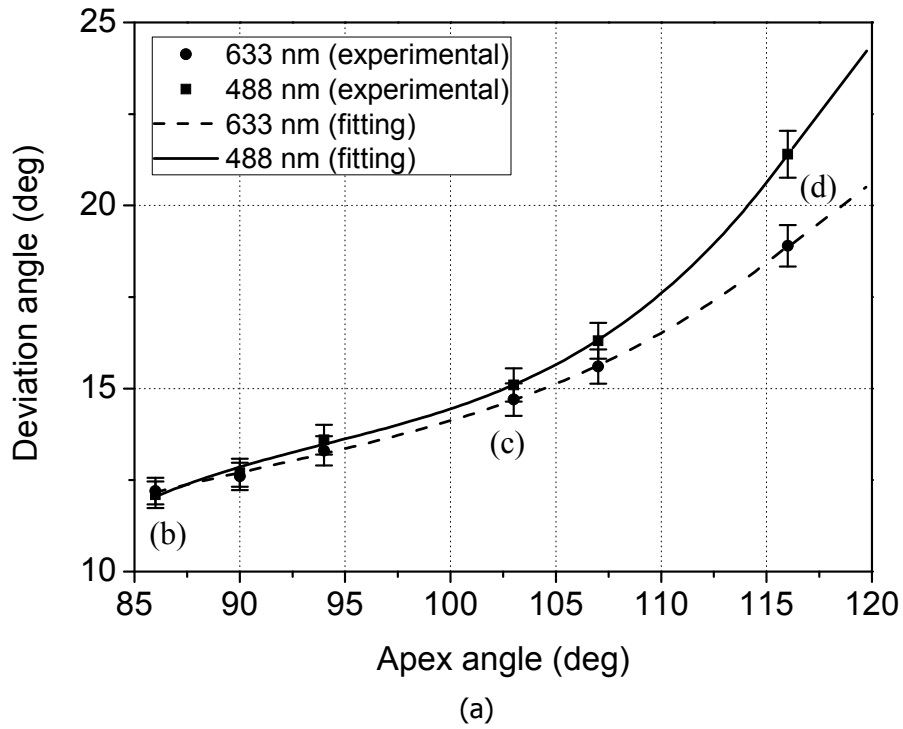


Figure 3.24: Optical dispersion caused by different apex angles of the optofluidic prism.

consequence, when the shape of the prism is fixed, the 488-nm light achieves a larger deviation angle as compared to 633-nm light. When the apex angle is increased, the difference between the two wavelength lights becomes larger. The deviation angle is varied by changing the apex angle of the prism as shown in Fig. 3.24. When the apex angle of the prism is 86° (Fig. 3.24 (a)), the red and green light

beams are mixed and appear as a bright yellow beam. By increasing the apex angle of the prism to 103° , the two-color light beams become distinguishable (Fig. 3.24 (b)). However, the yellow light beam is sandwiched by the red and green light beams, which shows that the two-color beams are still partially overlapped. The difference between the deviation angles of the two light beams is less than 0.5° . When the apex angle reaches 116° , the red and green light beams are separated clearly (Fig. 3.24 (c)). The difference between the deviation angles of two light beams is identified as 2.5° . This shows that the optofluidic prism is promising to separate light with different wavelengths and can be applied for the on-chip spectrometers.

3.3.5 On-chip refractometer

In the previous demonstrated experiments, the output beam is mainly controlled by changing the flow rates of the fluid streams in the optofluidic chip. Besides, the optofluidic prism is also sensitive to the refractive indices of the flows. This property can be used to build an on-chip refractometer as shown in Fig 3.25. The triangular chamber is filled with only one fluid. That means the prism shape is fixed and the deviation angle of the light beam depends the refractive index of the fluid. The chamber with apex angle of 70° is used in this experiment. As the chip is fabricated by PDMS, the reference refractive index (n_2) is 1.412. The tested samples are mixture solution of benzyl alcohol and water whose refractive index (n_1) is changed from 1.332 to 1.540 by varying the mixing ratio. The deviation angle of the output beam shifts with the change of refractive index. The output

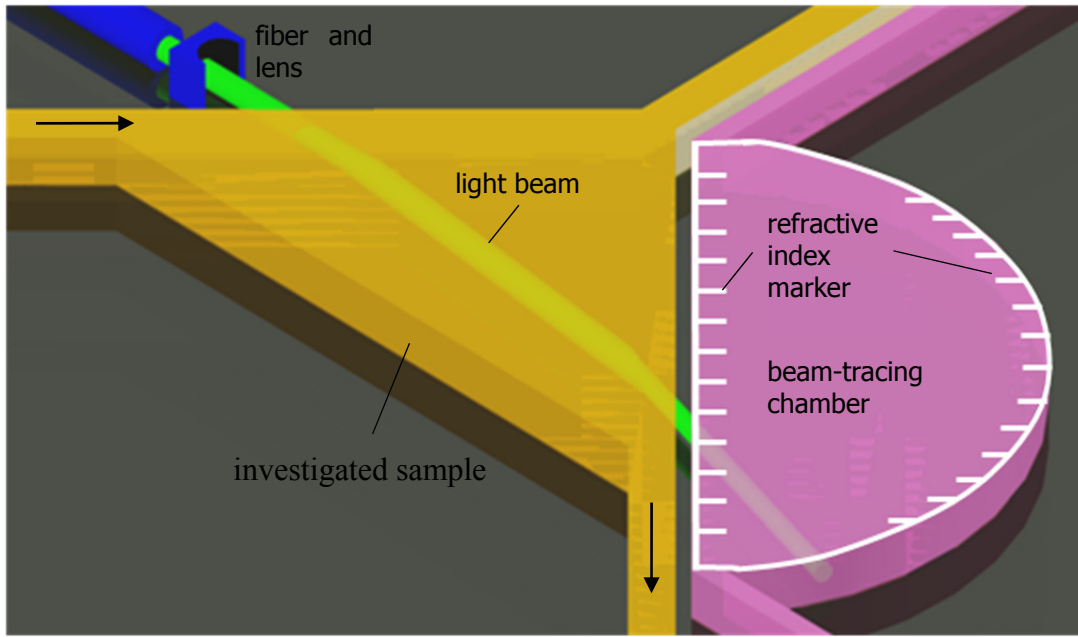


Figure 3.25: Schematics of the on-chip refractometer.

light position can be calculated accordingly. Because the light beam can be traced in the nearby chamber filling with fluorescent dye, the easily identified light beam position can be used to deduce the refractive index of the investigated sample in the prism chamber. Adding markers on the chip can facilitate the usage of the on-chip refractometer.

Figure 3.26 shows the output light position changes with the refractive index of the investigated sample. It is an overlaying image which combines the experimental results with four different solutions ($n_1 = 1.359, 1.412, 1.477$ and 1.540). The experimental results are compared with the simulation results as marked on the beam-tracing chamber in Fig. 3.26. It demonstrates that the output light position agrees well with the estimated one that is calculated from the theoretical model based on Eqs. (3.5)-(3.7).

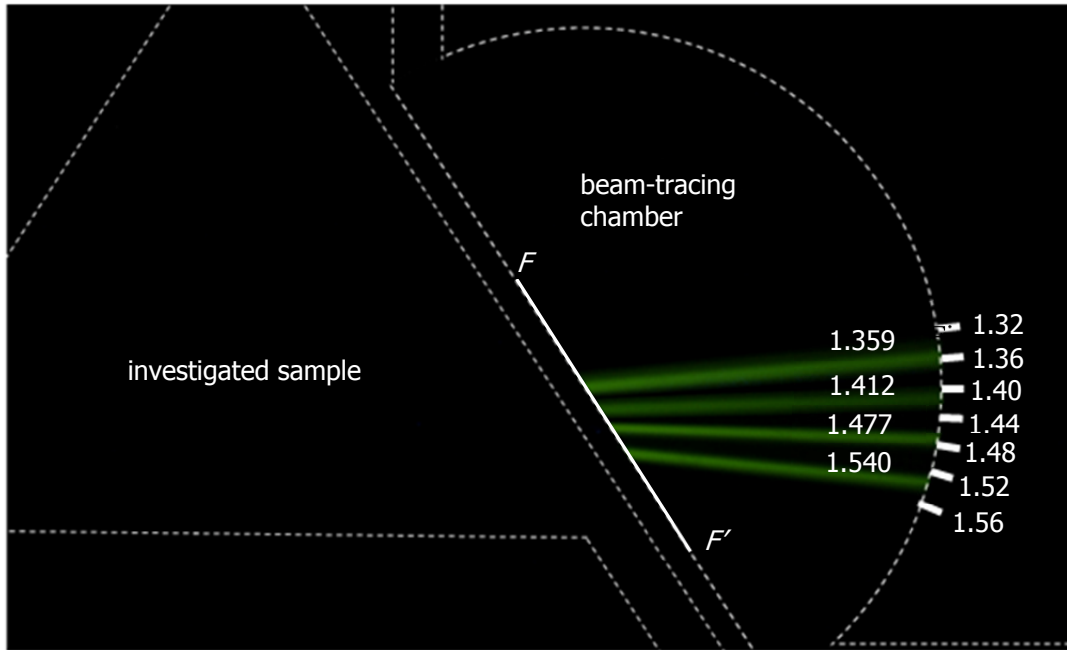


Figure 3.26: Photography of the on-chip refractometer filled by samples with different refractive indices.

Figure 3.27 shows the normalized output light intensity profile shifts with the refractive index of the sample. The light beam profile is obtained along the line FF' as shown in Fig. 3.26. The peak position of the light beam is plotted as a function of the refractive index of the solution. The point $x = 0$ is set at the position when the deviation angle of the light beam is zero. That means the refractive index of the sample is the same as PDMS ($n_1 = n_2 = 1.412$). When the refractive index is changed from 1.358 to 1.540, the light beam is shifted by $320 \mu\text{m}$.

Figure 3.28 shows the position of light beam as a function of the refractive index. The relationship between the two parameters is linear. By using solution with standard refractive index, the experimental data can be used to calibrate the position of markers in the on-chip refractometer. CCD detector (Nikon DS-5M) with a

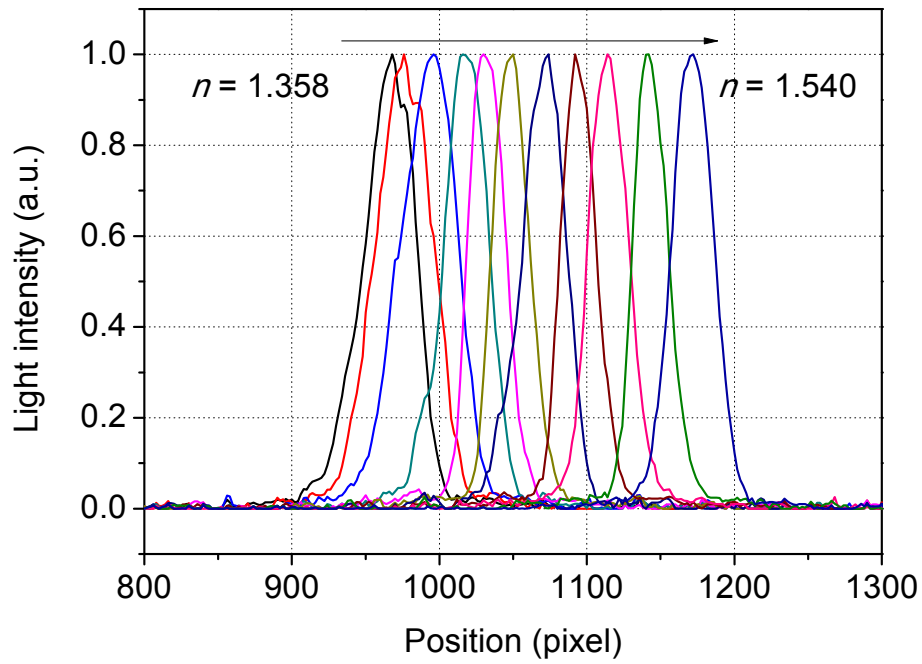


Figure 3.27: Output light intensity profile shifts with the refractive index.

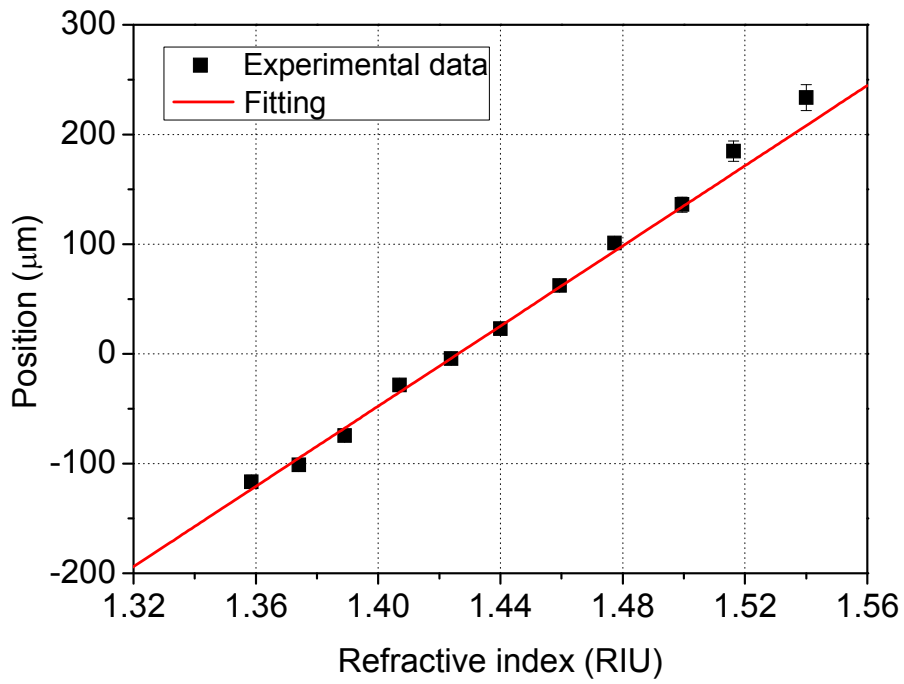


Figure 3.28: Position of light beam is plot as a function of the refractive index.

resolution of $0.339\text{ }\mu\text{m/pixel}$ can obtain a sensitivity of $2\times 10^{-4}\text{ RIU/pixel}$. Moreover, the needed investigated sample volume is only $0.35\text{ }\mu\text{l}$. This on-chip refractometer which is based on the optofluidic prism, offers a new way to do on-chip analysis. It just needs a little quantity of sample and can be easily integrated on lab-on-a-chip systems.

3.4 Summary

This chapter introduces a tunable optofluidic prism via two laminar flows to the microfluidic system. The triangular chamber for the prism configuration has been designed to maintain a stable prism shape and achieve large variation in the apex angle of prism. A simple theoretical model has been used to predict the apex angle of the prism, the deviation angle and the position of the output light beam. The tunability of the optofluidic prism has been experimentally proved. By precise control of the asymmetric prism shape, parallel light beam scanning is achieved. In addition, the dispersion of light with different wavelengths has been demonstrated. The experimental results also illustrate the possibility to use the optofluidic prism as an on-chip refractometer. The optofluidic prism has potential applications in building up on-chip optical circuits and promising for optical detection and biochemical analysis.

The innovation of the tunable optofluidic prism is summarized as follow,

- a) This is the first effort demonstrated to design a prism with two flows in a microfluidic chip. The apex angle of the prism and the deviation angle of the output light beam can be tuned continuously with a larger variation range than the previous methods. The apex angle of the prism was tuned from 75° to 135° . The deviation angle of the output light beam can be tuned by the prism from -13.5° to 22° .
- b) One of the new features of this optofluidic prism is its capability to transform from symmetric to asymmetric prism with the assistance of a third

flow. Parallel light beam scanning is achieved with a constant deviation angle of 10° and tuning range of $60\text{ }\mu\text{m}$ using the asymmetric prism. The maximum intensity obtained by the asymmetric prism is increased by 65.7% compared to that of the symmetric prism.

- c) Light dispersion is experimentally demonstrated using 488-nm and 633-nm laser beams. The two laser beams become distinguishable with a deviation angle difference of 2.5° when the apex angle of the prism reaches 116° .
- d) The optofluidic prism is used to measure the refractive index of a small quantity of liquid by detecting the output beam position. Based on the experimental condition, a sensitivity of 2×10^{-4} RIU/pixel is achieved.

CHAPTER 4

LASER-INDUCED MICRO/NANO-BUBBLE

This chapter presents the study of micro/nano-bubbles created by focusing a pulsed laser into an optofluidic chip filled with a light-absorbing liquid. The resulting bubbles are two-dimensional and sandwiched between the channel walls at the top and bottom. A viscous two-dimensional Rayleigh-Plesset-type model is derived, which accounts for the effect of shear stresses from the channel wall. In addition, the dynamic of a two-dimensional gas bubble due to mass diffusion is explored. Glass chips for both microbubble and nanobubble are designed and fabricated. The bubble dynamics is examined with different channel heights, boundary conditions and surface hydrophobicities. The experimental results are discussed and compared with the theoretical models, which demonstrate that the viscosity and surface tension play important roles on bubble dynamics in the confined channels.

4.1 Theoretical modeling

4.1.1 2D viscous Rayleigh-Plesset-type model

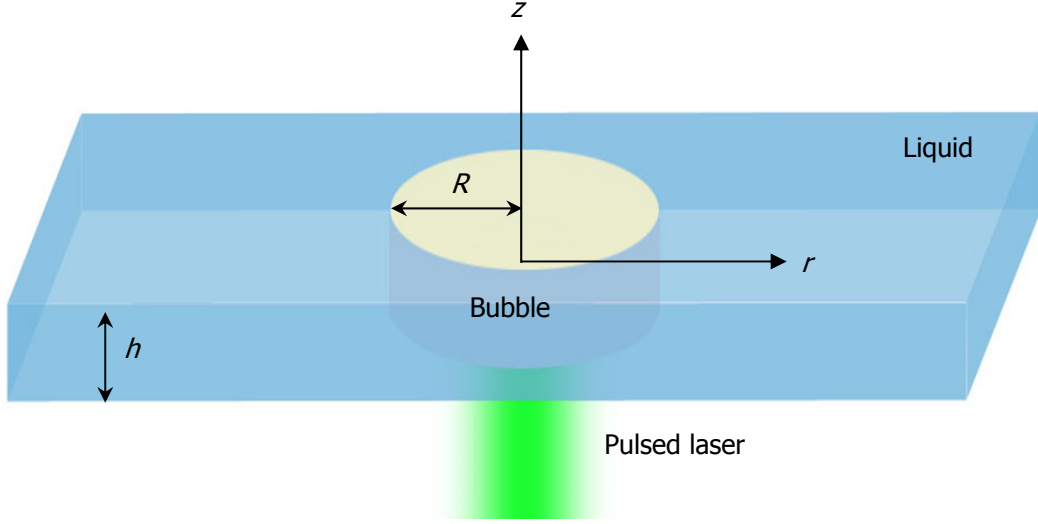


Figure 4.1: Schematic of a cylindrical bubble of radius R confined in a channel of height h .

The incompressible flow around a cylindrical bubble of radius R is in a confined channel of height h . The flow is described in cylindrical coordinates and assumed to be axisymmetric with respect to the z axis (see Fig. 4.1). The translation of the bubble is ignored but its radial motion is considered. The momentum conservation for incompressible flow can be expressed as

$$\frac{\partial \mathbf{u}}{\partial t} + (\mathbf{u} \cdot \nabla) \mathbf{u} = -\frac{1}{\rho} \nabla p + \nu \nabla^2 \mathbf{u} , \quad (4.1)$$

where \mathbf{u} is the velocity vector, ρ is the density, p is the pressure, and ν is the kinematic viscosity ($\nu = \mu/\rho$; μ is dynamic viscosity). Let U be the characteristic

velocity such as bubble wall velocity \dot{R} . For flows with low Reynolds numbers (as in nanochannels), the pressure is normalized by $\rho \nu U/h$. Therefore, the dimensionless form of Eq. (4.1) is given by

$$\frac{\partial \mathbf{u}^*}{\partial t^*} + \text{Re}(\mathbf{u}^* \cdot \nabla^*) \mathbf{u}^* = -\nabla^* p^* + \nu \nabla^{*2} \mathbf{u}^*, \quad (4.2)$$

where the asterisk denotes dimensionless variables and Re is the Reynolds number ($\text{Re} = Uh/\nu$). In the limit of $\text{Re} \rightarrow 0$, the momentum equation can be simplified as

$$\frac{\partial \mathbf{u}}{\partial t} = -\frac{1}{\rho} \nabla p + \nu \nabla^2 \mathbf{u}, \quad (4.3)$$

which is the so-called Stokes equation. Liquid flow in nanochannels is also expected to behave as such Stokes (or Hele-Shaw-type) flow, provided that boundary layers (BLs) at the channel walls develop entirely across the channel height. But even under such small confinement, there exists finite time until the BLs are fully developed. This suggests that the Navier-Stokes Eq. (4.1), not the Stokes Eq. (4.3), needs to be considered in order to resolve the entire evolution of the unsteady flow. In what follows, the radial motion of a cylindrical bubble in nanochannels is investigated, starting from the Navier-Stokes equation. The goal is to derive the Rayleigh-Plesset-type equation that accounts for drag forces at channel walls. For simplicity, the flow is assumed to be axisymmetric ($\partial/\partial\theta = 0$) with no swirl ($u_\theta = 0$) and aligned with the radial axis ($u_z = 0$). That is, the nonzero velocity component is the radial velocity $u_r(r, z, t)$ only. In this case, the continuity equation is written as

$$\nabla \cdot \mathbf{u} = \frac{1}{r} \frac{\partial}{\partial r} (ru_r) = 0. \quad (4.4)$$

It follows that the velocity has the form

$$u_r = \frac{G(z, t)}{r}. \quad (4.5)$$

According to Hele-Shaw analyses, the depth-averaged velocity is defined as

$$\bar{u}_r(r, t) = \frac{1}{h} \int_{-h/2}^{h/2} u_r(r, z, t) dz. \quad (4.6)$$

It can also be written as

$$\bar{u}_r(r, t) = \frac{1}{hr} \int_{-h/2}^{h/2} G(z, t) dz = \frac{F(t)}{r}. \quad (4.7)$$

With the boundary condition at the bubble wall (i.e. $\bar{u}_r(R, t) = \dot{R}$), it is easy to find that $F(t) = R\dot{R}$ and then

$$\bar{u}_r(r, t) = \frac{R\dot{R}}{r}. \quad (4.8)$$

Similarly, the depth-averaged velocity squared can be given by

$$\overline{u_r^2}(r, t) = \frac{R^2 \dot{R}^2}{r^2}. \quad (4.9)$$

The Navier-Stokes equation dealing with the radial components can be expressed as

$$\rho \left(\frac{\partial u_r}{\partial t} + u_r \frac{\partial u_r}{\partial r} \right) = -\frac{\partial p}{\partial r} + \mu \left[\frac{1}{r} \frac{\partial}{\partial r} \left(r \frac{\partial u_r}{\partial r} \right) + \frac{\partial^2 u_r}{\partial z^2} - \frac{u_r}{r^2} \right], \quad (4.10)$$

where $p = p(r, t)$ from the z momentum equation. With the aid of Eq. (4.5), the above equation is further simplified as

$$\rho \left(\frac{\partial u_r}{\partial t} - \frac{u_r^2}{r} \right) = -\frac{\partial p}{\partial r} + \mu \frac{\partial^2 u_r}{\partial z^2}. \quad (4.11)$$

Integrating this over the channel height, it is obtained as

$$\rho \left(\frac{\partial \bar{u}_r}{\partial t} - \frac{\bar{u}_r^2}{r} \right) = -\frac{\partial p}{\partial r} + \frac{2\tau_w}{h}, \quad (4.12)$$

where τ_w is the shear stress at the channel wall

$$\tau_w = \mu \left. \frac{\partial u_r}{\partial z} \right|_{z=h/2}. \quad (4.13)$$

Substitution of Eqs. (4.8) and (4.9) into Eq. (4.12) yields

$$\frac{\rho}{r} (R\ddot{R} + \dot{R}^2) - \frac{\rho}{r^3} R^2 \dot{R}^2 = -\frac{\partial p}{\partial r} + \frac{2\tau_w}{h}. \quad (4.14)$$

Integrating the above equation in the radial direction from R_∞ to R , it is finally expressed as

$$(R\ddot{R} + \dot{R}^2) \ln \frac{R}{R_\infty} + \frac{\dot{R}^2}{2} \left(1 - \frac{R^2}{R_\infty^2} \right) = \frac{p(R_\infty) - p(R)}{\rho} + \frac{2}{h\rho} \int_{R_\infty}^R \tau_w dr, \quad (4.15)$$

where $p(R)$ is the bubble wall pressure at the liquid side. To avoid the logarithmic singularity, finite value of R_∞ is selected for which the velocity is effectively zero (i.e. $R \ll R_\infty < \infty$).

The last step is to explicitly specify the wall shear stress in Eq. (4.15). The velocity profile is assumed as Poiseuille-type with no-slip surfaces at the channel walls,

$$u_r = \frac{f(r,t)}{2\mu} \left(z^2 - \frac{h^2}{4} \right), \quad (4.16)$$

where the function f has the units of pressure gradients. The depth-averaged velocity is therefore given by $\bar{u}_r = -f(r,t)h^2/(12\mu)$. Based on the mass conservation

$$2\pi R h \dot{R} = 2\pi r h \left(-\frac{f(r,t)h^2}{12\mu} \right), \quad (4.17)$$

the function f can be written as

$$f(r,t) = -\frac{12\mu R \dot{R}}{r h^2}. \quad (4.18)$$

Hence, the velocity profile is given by

$$u_r = \frac{3R \dot{R}}{2r} \left[1 - \left(\frac{2z}{h} \right)^2 \right]. \quad (4.19)$$

The corresponding shear stress Eq. (4.13) at the channel wall is obtained as

$$\tau_w = -\frac{6\mu R \dot{R}}{hr}. \quad (4.20)$$

Substitution of this shear stress into Eq. (4.15) finally leads to

$$\left(R\ddot{R} + \dot{R}^2 + \frac{12\nu}{h^2} R\dot{R} \right) \ln \frac{R}{R_\infty} + \frac{\dot{R}^2}{2} \left(1 - \frac{R^2}{R_\infty^2} \right) = \frac{p(R_\infty) - p(R)}{\rho}. \quad (4.21)$$

The third term inside the parentheses on the left-hand side arises from drag forces at the channel walls, which will come into play particularly in extended nanochannels. It should be noted that the viscous Rayleigh-Plesset-type Eq. (4.21) approaches the inviscid version in the limit of infinite channel height ($h \rightarrow \infty$). Now that normal stress associated with liquid viscosity may be negligible compared to the channel wall stress Eq. (4.20). The bubble wall pressure is expressed as

$$p(R) = p_v + p_g - \Delta p = p_v + p_{g0} \left(\frac{R_0}{R} \right)^{2\kappa} - \sigma \left(\frac{1}{R} + \frac{2 \cos \theta}{h} \right), \quad (4.22)$$

where p_v is the vapor pressure, p_g is the partial pressure of noncondensable gases with polytropic index κ , p_{g0} is the initial partial pressure of noncondensable gases when the bubble radius is R_0 , and Δp denotes the Laplace pressure that depends on the surface tension σ and the contact angle θ . Here, it is assumed that the mass of gases in the bubble is unchanged.

It is noted that the assumption of fully developed BLs (in deriving the Rayleigh-Plesset model) needs to be relaxed to account for the inertial collapse/growth of bubbles in the initial stage when the BLs is under development and viscous effects on the bubble dynamics are less important. To do so, the viscous Rayleigh-Plesset model (4.21) is corrected as

$$\left(R\ddot{R} + \dot{R}^2 + \phi(\delta^*) \frac{12\nu}{h^2} R\dot{R} \right) \ln \frac{R}{R_\infty} + \frac{\dot{R}^2}{2} \left(1 - \frac{R^2}{R_\infty^2} \right) = \frac{p(R_\infty) - p(R)}{\rho}, \quad (4.23)$$

where ϕ is the correction factor that depends on the BL thickness δ^* , normalized by the channel height. Since the BL thickness at the top and bottom of the channel is approximated by $2\sqrt{\nu t}$, the dimensionless BL thickness may be given by

$$\delta^* = \frac{4\sqrt{\nu t}}{h}. \quad (4.24)$$

To regulate the viscous contribution, the correction factor can be defined as a step function

$$\phi(\delta^*) = \begin{cases} 0 & \text{if } 0 \leq \delta^* < 1, \\ 1 & \text{if } \delta^* \geq 1, \end{cases} \quad (4.25)$$

or through a linearly increasing function

$$\phi(\delta^*) = \begin{cases} \delta^* & \text{if } 0 \leq \delta^* < 1, \\ 1 & \text{if } \delta^* \geq 1. \end{cases} \quad (4.26)$$

Both viscous corrections, Eqs. (4.25) and (4.26), lead to visually indistinguishable results.

It is found that the viscous correction for water has an effect for channels larger than several micrometers, while for the extended nanochannels it has little effect. This suggests that boundary layer growth in extended nanochannels is considerably faster than the bubble collapse time. Therefore, for predicting the dynamics in extended nanochannels, the assumption of a fully developed boundary layer is reasonable, while the viscous correction Eq. (4.25) is suitable for microchannels.

4.1.2 Mass diffusion on bubble surface

While the collapse time of vapor bubbles in nanochannels is at most on the order of milliseconds, the overall collapse time in our experiment is on the order of seconds. The discrepancy leads to the conjecture that the bubble also contains noncondensable gases whose mass diffusion may be sufficiently slow to account for the experimental observation. The gas contents can possibly come from mass diffusion during the expansion phase of laser-induced bubbles or air trapped on channel surfaces.

Analyses of the dissolution of spherical bubbles are found in the work of Epstein and Plesset [286]. Here, their analyses are extended to two-dimensional, cylindrical gas bubbles that are fixed in space (no translation). Even when the liquid is saturated with gases, the bubble can dissolve into the liquid. To be specific, the Laplace pressure creates higher gas concentrations at the bubble wall according to Henry's law, and then the mass flux follows Fick's law. For cylindrical bubbles in channels, the Laplace pressure is

$$\Delta p = \sigma \left(\frac{1}{R} + \frac{2 \cos \theta}{h} \right). \quad (4.27)$$

Hence, for cases with hydrophilic channel walls ($\theta < 90^\circ$), the overpressure in the gas phase is always positive so that bubble dissolution will be observed.

If one ignores convection induced by the radial motion of shrinking cylindrical bubbles, the mass diffusion obeys

$$\frac{\partial c}{\partial t} = \frac{D}{r} \frac{\partial}{\partial r} \left(r \frac{\partial c}{\partial r} \right), \quad (4.28)$$

where c is the mass concentration of the gas and D is the diffusion coefficient. The concentration field is assumed initially to be uniform with $c(r, 0) = c_i$ for $r > R$. The concentration at the bubble wall obeys Henry's law

$$c(R, t) = c_s(p_g), \quad (4.29)$$

where c_s is the concentration at saturation and p_g is the gas pressure ($p_g \approx p_0 + \Delta p$; p_0 is the ambient pressure or one atmosphere). The concentration at the far field is

$$\lim_{r \rightarrow \infty} c(r, t) = c_i. \quad (4.30)$$

The corresponding concentration fields is described as [287, 288]

$$\frac{c(r, t) - c_i}{c_s(p_g) - c_i} = 1 + \frac{2}{\pi} \int_0^\infty \exp(-D\xi^2 t) \frac{J_0(\xi r) Y_0(\xi R) - Y_0(\xi r) J_0(\xi R)}{J_0^2(\xi R) + Y_0^2(\xi R)} \frac{d\xi}{\xi}, \quad (4.31)$$

where J_0 and Y_0 are the Bessel functions of the first and second kinds, respectively.

The mass flux at the bubble wall is then given by

$$m_g'' = -D \frac{\partial c}{\partial r} \Big|_{r=R} = \frac{4D}{\pi^2} \frac{c_s(p_g) - c_i}{R} \int_0^\infty \frac{\exp(-D\xi^2 t)}{J_0^2(\xi R) + Y_0^2(\xi R)} \frac{d\xi}{\xi}, \quad (4.32)$$

Hence, the rate of change in the mass of bubble contents is written as

$$\dot{m}_g = -A(R, \theta) \dot{m}_g'', \quad (4.33)$$

where A is the area of the gas-liquid interfaces and approximated by $(\pi - 2\theta)\pi Rh / \cos \theta$. The mass conservation also requires

$$\dot{m}_g = A(R, \theta) \rho_g(p_g) \dot{R}, \quad (4.34)$$

where ρ_g is the gas density within the bubble. For isothermal gases, $\rho_g = \rho_{g0} p_g / p_{g0}$. With Eqs. (4.29) and (4.30), the evolution of the bubble dissolution can be expressed as

$$\dot{R} = \frac{4D}{\pi^2} \frac{c_i - c_s(p_g)}{\rho_g(p_g)R} \int_0^\infty \frac{\exp(-D\xi^2 t)}{J_0^2(\xi R) + Y_0^2(\xi R)} \frac{d\xi}{\xi}. \quad (4.35)$$

4.2 Fabrication processes and experimental setups

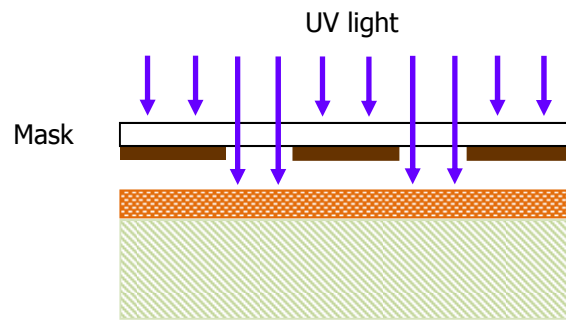
4.2.1 Glass chip fabrication process flow

The micro/nanochannel is fabricated in a $25 \times 45 \times 0.07$ mm borosilicate glass (Pyrex 7740) using standard photolithography and wet chemical etching processes as shown in Fig. 4.2. Because of its low coefficient of thermal expansion, the borosilicate glass is useful in high temperature application and suitable for thermal bonding.

The design layout of the optofluidic chip is drawn a computer-aided design (CAD) program (L-Edit 12.0). A dark field clear feature chrome mask is commercially fabricated on a piece of sodalime glass based on the drawing. For the microchannel and nanochannel combined chip, the masks for microchannel and nanochannel are separated and share the same marks for alignment.

The glass plate is bathed in acetone and sonicated for 20 min. After that, the glass is rinsed by DI water and dried with nitrogen. It is baked on a hot plate at 105°C for 5 min before the spin coating. A thin layer of photoresist (AZ9260) is spun coated on the wafer at 2000 rpm for 60 s (spin coater: CEE, 200). The resist coated glass is soft baked on the hot plate at 105°C for 3 min. After that, it is exposed to UV light for 80 s under the soda lime glass mask (mask aligner: Karl Suss MJB4). The exposed glass is put into AZ developer for 2 min to develop the pattern, and rinsed by DI water and dried with nitrogen gas. Then, the glass is hard baked at 105 °C for 60 min.

 Borosilicate glass
  AZ 9260
  Chrome
  Sodalime glass



(a) Patterning



(b) Developing



(c) Etching



(d) Bonding

Figure 4.2: Fabrication process flow of glass chip.

The structure on the glass is etched by HF/HCl solution. The wet etching of glasses is mainly performed in HF solutions. The etching depth increases with the etching time and the concentration of HF. Adding HCl could improve the quality of the etching process and make the etched surface much smoother [22]. For the etching of microchannel and nanochannel, different compositions of HF/HCl solution are used. Microchannels with the height of 3 to 10 μm are etched by using an HF/HCl/H₂O ratio of 10:6:10 (volumetric ratio). Nanochannels with the height of 100 to 900 nm are etched by using an HF/HCl/H₂O ratio of 1:6:10. The etching time is always controlled within 5 min. After the patterned glass being etched, the photoresist is removed by acetone and the glass is rinsed by IPA and water. When the nanochannels and microchannels are designed on the same chip, the microchannels are etched first. Then the cleaned glass with microchannels is coated by the photoresist again. The nanochannels are fabricated following the standard lithography and etching steps.

Inlets and outlets are drilled by an ultrasonic driller (Drill Master, SOM-121) after the etching process, followed by bonding. The etched glass substrate and another cover glass are cleaned in a fresh Piranha solution (H₂SO₄(%):H₂O₂(%) = 3:1) for 45 min, then rinsed 5 times by DI water in an ultrasonic bath for 1 min each. The two pieces of glass are carefully aligned and clung to each other by pressing by hands. The two glass plates are hold tightly after the intimate contact. Strong bonding is performed by fusing the two glass plates in a furnace at 625°C for 2 hours with a ramp rate of 5 °C min⁻¹. A sealed micro/nanofluidic chip can be formed after the bonding.

4.2.2 Surface treatment of the glass channel

The optofluidic chips for bubble experiments are made of Pyrex (borosilicate glass), which had a hydrophilic surface. A silanization treatment with 1H,1H,2H,2H- perfluorodecyltrichlorosilane (FDTS, $C_{10}H_4C_{13}F_{17}Si$, 97%, Gelest Inc., USA) can make the surface becomes hydrophobic [289]. The organosilane molecules absorb onto the surface of the wafer and a Si-Cl group of each organosilane reacts with a surface of OH group to form Si-O-Si bonds. The remaining Si-Cl bonds on each molecule react with neighboring organosilane molecules in the presence of trace preadsorbed water molecules to form a network of Si-O-Si bonds over the surface. The presence of a long hydrocarbon chain and fluorine atoms in the organosilane compound causes the treated surface to repel water and makes the surface hydrophobic. The FDTS treated surface is stable and can withstand for a long time, high temperature and different chemical treatments [290].

DI water is pumped into the channels and flushed for 15 min, then clean nitrogen gas is blown into the channels for drying. Next, the channels are pretreated by isopropyl alcohol (IPA) and 30% H_2O_2 for 15 min each and then dried by nitrogen. A solution of isooctane containing 2 v/v% FDTS is pumped into the channels for 15 min and dried by nitrogen. After that, the channels are rinsed by fresh isooctane solvent, ethanol and IPA for 10 min each, and dried by nitrogen after being rinsed by each solution. Finally, the glass chip is annealed in an oven at 100°C for 30 min.

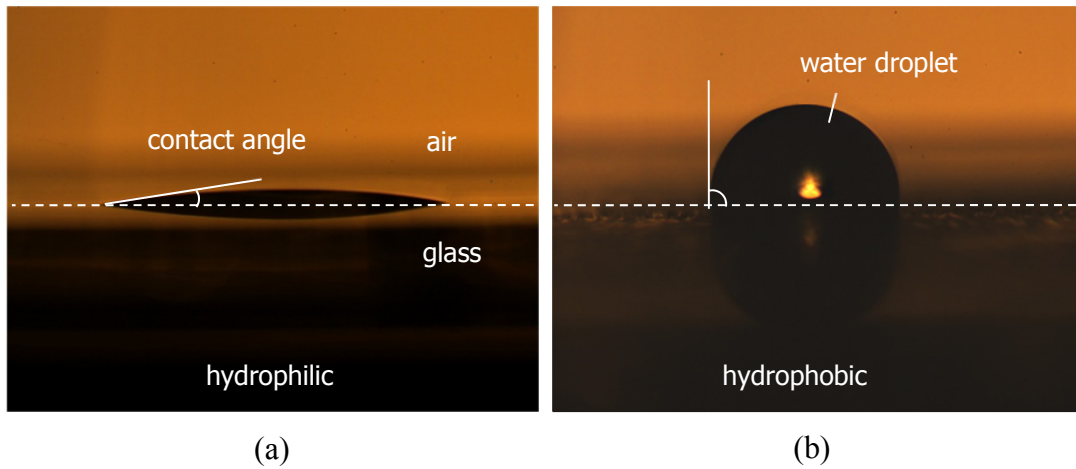


Figure 4.3: Photograph of the water droplet on a glass substrate (a) before the surface treatment and (b) after the surface treatment.

In order to characterize the surface modification results, the contact angle is measured. A water droplet is gently placed on the glass surface, and a photograph of the side view of the droplet is taken using a CCD camera as shown in Fig. 4.3. Without any surface treatment, the hydrophilic borosilicate glass has a contact angle of 9° . A silanization treatment with FDTs creates a hydrophobic surface with a contact angle of 90° .

4.2.3 Experimental setup

Figure 4.4 shows the experimental setup which consists of a pulsed Nd:YAG laser (Orion, New Wave Research, Fremont, 532-nm, pulse duration approximately 6 ns), a digital delay generator (model 575, BNC, USA), an inverted microscope (IX-71, Olympus, Japan) and a high speed camera (SA-1.1, Photron,

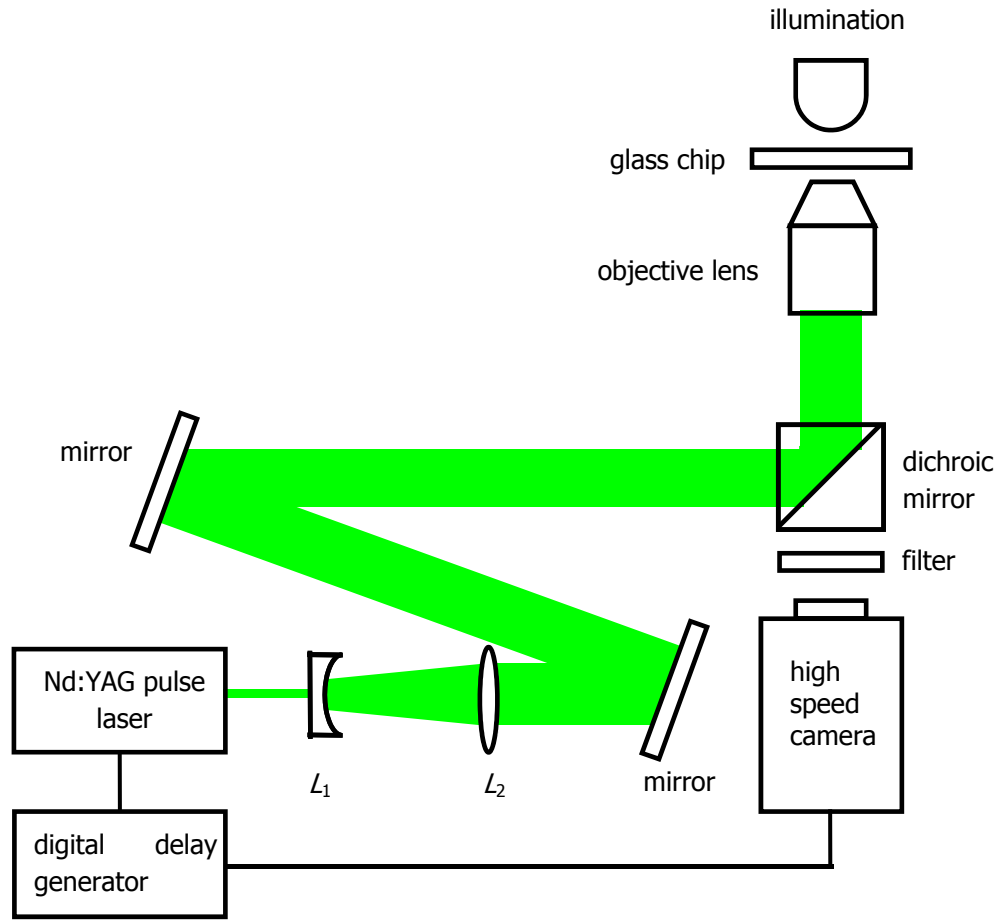


Figure 4.4: Schematics of the experimental setup for laser-induced bubbles.

USA). The laser beam is expanded by the lenses L_1 ($f = -30$ mm) and L_2 ($f = 400$ mm), and reflected from mirrors into the microscope. The bubble is generated by focusing the laser pulse with the microscope objective (Olympus, water immersion, $20\times$, $NA = 0.5$). The energy of the laser pulse is controlled by delaying the interval between the flash lamp and the Q-switch trigger. The micro/nano-structured channel is filled with blue ink (Maxtec Inc., Hongkong), which strongly absorbs the green light and yields a good contrast for the bright field illumination. High-speed

recording is done at framing rates between 450 000 – 675 000 frame/s with the lowest possible exposure time of 370 ns.

4.3 Experimental results of microbubble

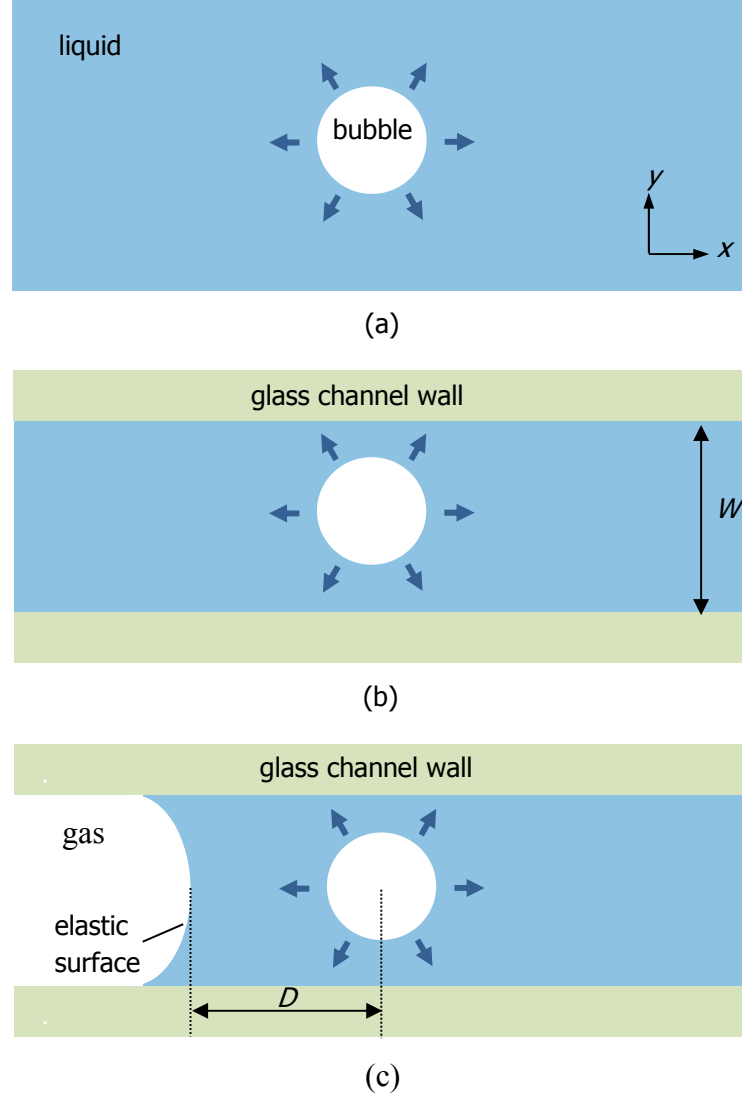


Figure 4.5: Schematic of the laser-induced microbubble on different boundary conditions: (a) 1D confined channel, (b) 2D confined channel, and (c) near an elastic surface.

In this section, the microbubble dynamics are investigated on three different boundary conditions as shown in Fig. 4.5. The bubble is generated by the pulsed

laser in the channel with a height of several micrometers. When the channel length (L) and width (W) are much larger than the bubble size (e.g. $L = W = 1$ mm), the microbubble is only confined in the z direction. In other words, the microbubble is in a 1D confined channel as shown in Fig. 4.5 (a). When the channel width is comparable with the bubble size and the channel length is still sufficiently long, the boundaries on the y and z direction will affect the bubble dynamics as shown in Fig. 4.5 (b). It is called 2D confined channel. When the bubble is generated close to a gas/liquid interface which is an elastic surface, the bubble dynamics will be affected on the x direction as shown in Fig. 4.5 (c). The details are discussed in the following sections.

4.3.1 Microbubble in a 1D confined channel

Figure 4.6 shows the microbubble evolution in an 8- μm high, 1-mm wide and 3-mm long microchannel. Sudden absorption of the pulsed laser energy vaporizes the liquid. The hot vapor expands rapidly and reaches the maximum size of the microbubble in 2 μs . When the temperature of the vapor decreases, its pressure eventually drops to a level lower than that of the outside liquid. The unbalanced pressure between the inside and outside of the bubble causes the collapse, which is finished within 6 μs . The dynamics are undisturbed by other boundaries due to the large distance between the bubble and side walls. Therefore, the radial evolution of the microbubble is symmetrical. Since the microbubble radius (the maximum value is 22.5 μm) is much larger than the channel height, it

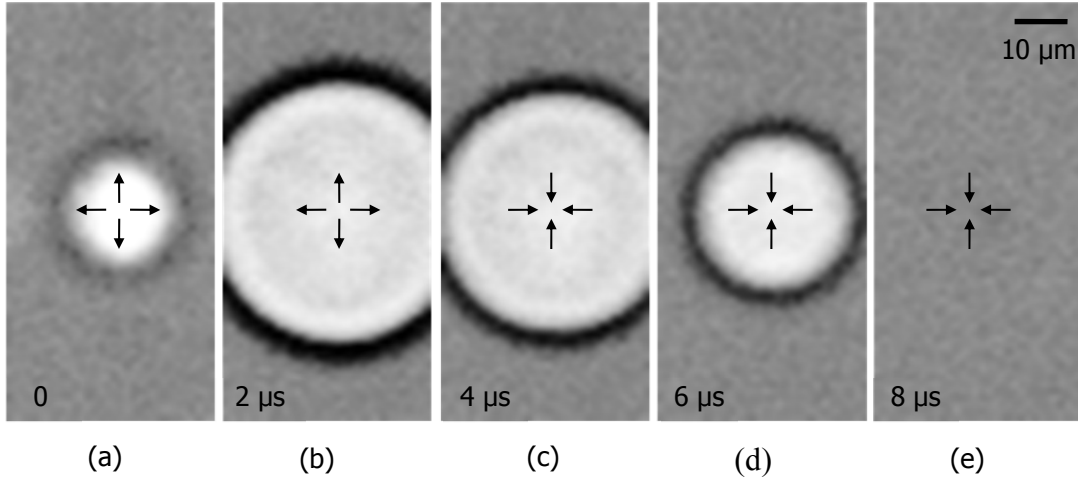


Figure 4.6: Photographs of microbubble evolution in a 1D confined channel.

shows a cylindrical shape as confined by the top and bottom channel walls. Planar bubble dynamics can be described as [291]

$$\left(R\ddot{R} + \dot{R}^2\right) \log \frac{R}{R_\infty} + \frac{1}{2} \dot{R}^2 = \frac{p}{\rho}, \quad (4.35)$$

where R is the bubble radius, ρ is the liquid density, p is the pressure in the liquid far from the bubble, and R_∞ is the distance at which the velocity in the fluid has dropped to zero. Here R_∞ is identified as half of the channel width, since the bubble is generated at the center of the channel. Figure 4.7 shows the measured bubble radius agrees well with the calculated dynamics from Eq. (4.35). The experimental results are also compared with the Rayleigh equation [168], which can be expressed as

$$R\ddot{R} + \frac{3}{2} \dot{R}^2 = \frac{p}{\rho}. \quad (4.36)$$

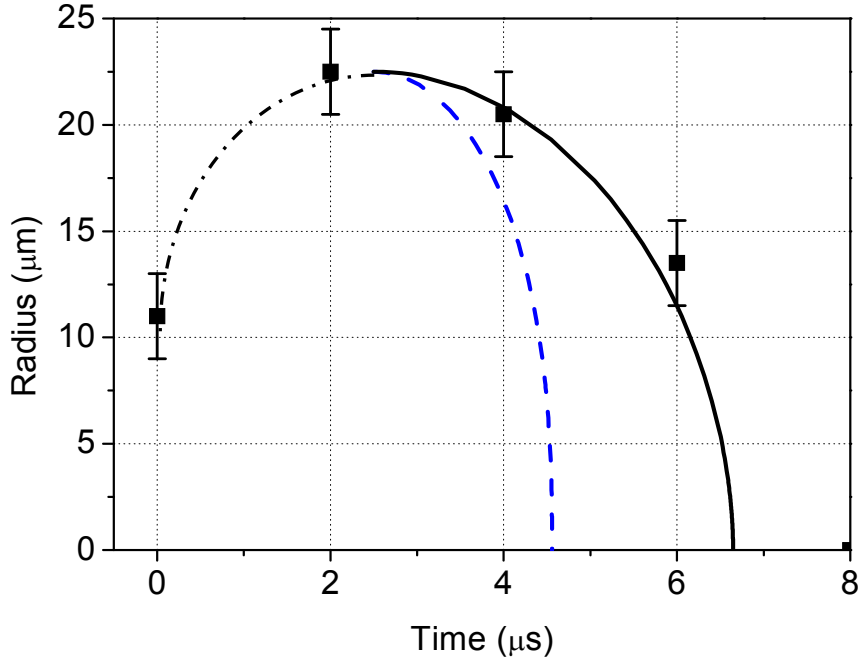


Figure 4.7: Comparison of the measured bubble radii (square) and the model predictions for the 3D Rayleigh collapse (dashed line) and 2D inviscid Rayleigh type collapse (solid line). The dash-dot line is used to illustrate the bubble expansion tendency.

As depicted by the dashed line in Fig.4.7, the 3D bubble model predicts a much faster collapse than that observed in the experiments.

In both models described in Eqs. (4.34) and (4.35), the viscosity is neglected. The time scale for the diffusive growth of the viscous boundary layer can be given by

$$t = y^2 / \nu, \quad (4.37)$$

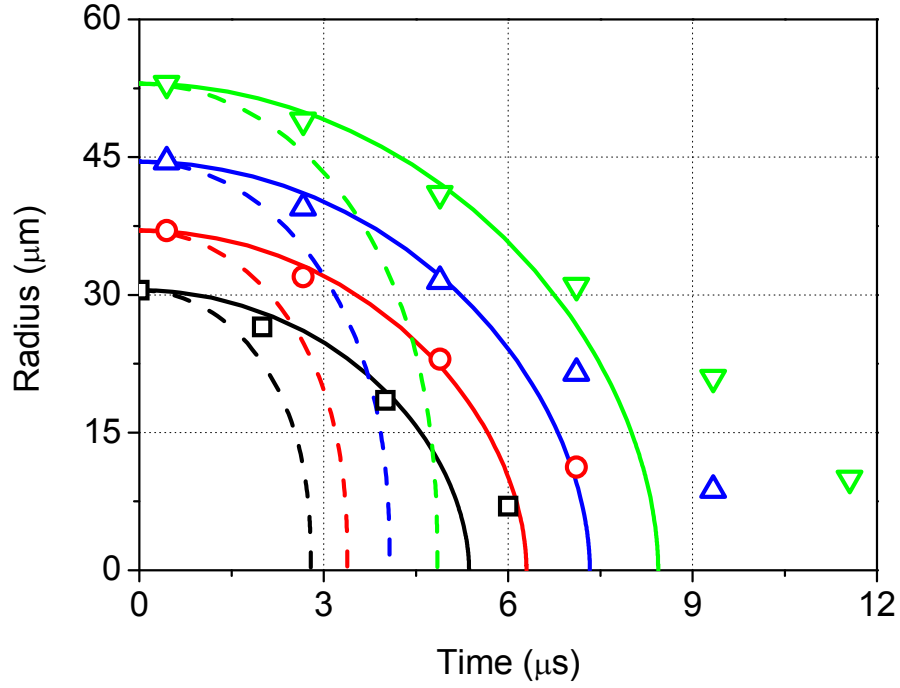


Figure 4.8: Comparison of the bubble dynamics for different sized bubbles with a 2D inviscid (solid line) and 3D Rayleigh model (dashed line).

where y is the distance that the vorticity can grow from the wall into the channel, ν is the kinematic viscosity of the liquid. It roughly takes $16 \mu\text{s}$ for the boundary layer to grow to the center of an $8\text{-}\mu\text{m}$ height channel with $\nu = 10^{-6} \text{ m}^2/\text{s}$. In Fig. 4.7, the bubble life time is $7 \mu\text{s}$ approximately, thus y is estimated as $2.6 \mu\text{m}$ that is far from the center of the channel. Therefore, the measured bubble dynamics shows good agreement with the inviscid model.

However, the dynamics for larger bubbles can no longer be described with a simple inertia driven model, i.e. Eq. (4.35). Figure 4.8 shows that the good agreement between the 2D inviscid model and experimental results is eventually

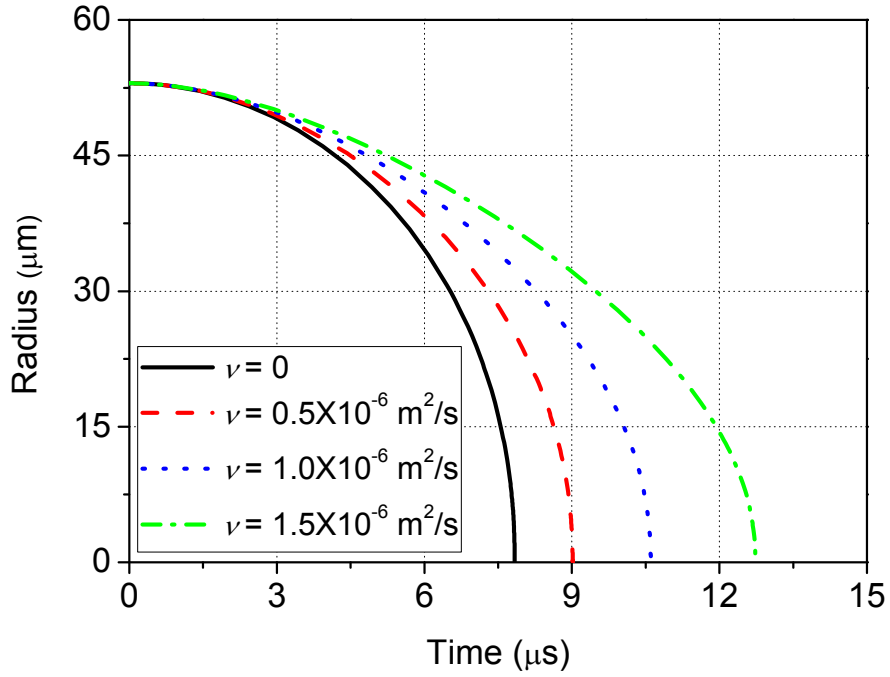


Figure 4.9: Simulation results for 2D viscous Rayleigh-Plesset-type model with different viscosities in a microchannel ($h = 8 \mu\text{m}$).

lost when the bubble radius becomes larger and larger. This is due to the fact that the larger bubble has a longer life time, which gives more time for the boundary layer to diffuse from the channel wall and affects the inflow. Another reason is that the larger bubble is generated with a higher laser energy, which can bring more noncondensable gas into the bubble. The collapse process of the microbubble can be hindered by the effects of viscosity or increased gas pressure.

The 2D viscous Rayleigh-Plesset-type model derived in section 4.1 has considered the viscosity as well as the noncondensable gas pressure. Figure 4.9 shows the microbubble radius changes as a function of time when the bubble

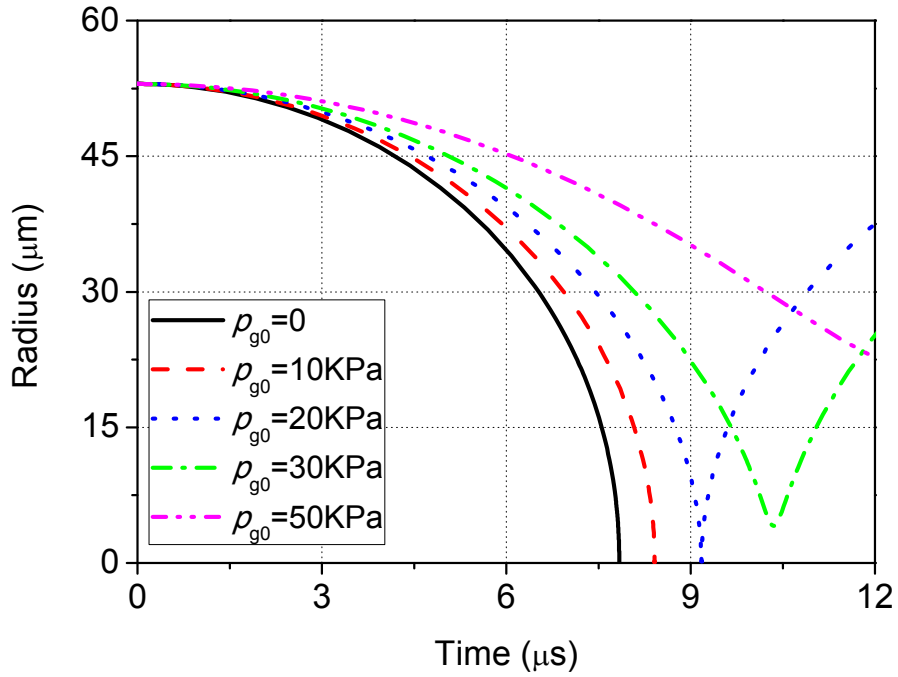


Figure 4.10: Simulation results for 2D viscous Rayleigh-Plesset-type model with different gas pressure in a microchannel ($h = 8 \mu\text{m}$).

content is vapor only. The simulation is based on Eq. (4.21) while the bubble pressure $p(R)$ is set as zero. As shown in Fig. 4.9, the collapse rate slows down with increasing viscosity. When the viscosity is increased from 0 to $1.5 \times 10^{-6} \text{ m}^2/\text{s}$, the collapse time is increased from 7.8 to 12.7 μs . That means the viscous force hinders the bubble collapse. The collapse dynamics can also be altered by including noncondensable gases into the microbubble. Figure 4.10 shows the effect of including polytropic gases ($\kappa = 1.0$) within the microbubble. The viscosity is ignored here. When the initial partial pressure of gases (p_{g0}) is quite small, i.e. $p_{g0} < 5 \text{ KPa}$, the bubble collapse is almost the same as a pure vapour bubble. As the gas amount increases, the overall decay rate is hindered by compression of the gases. It

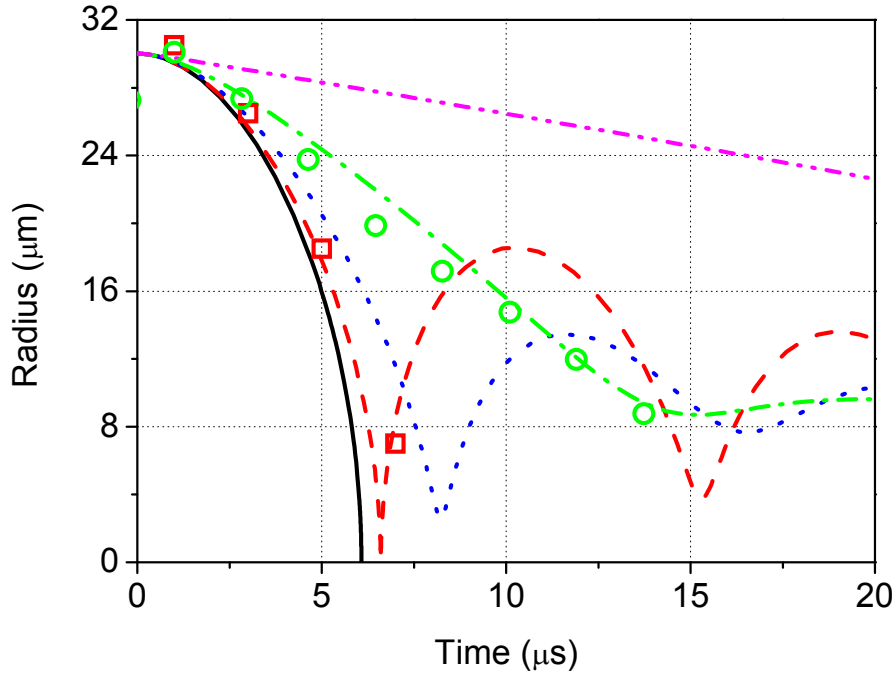


Figure 4.11: Bubble dynamics for 2D viscous Rayleigh-Plesset-type model with simulation results in different channel heights: 10 μm (solid), 8 μm (dash), 6 μm (dot), 4 μm (dash dot) and 2 μm (dash dot dot), and experiments results in 8 μm and 4 μm channel.

is noted that the simulations show an oscillation after the initial collapse when p_{g0} is larger than 20 KPa (see Fig. 4.10). However, it is not observable in the experiments as shown in Fig.4.11.

Figure 4.11 shows the simulated and experimented bubble collapse with different channel heights. In the simulation, the viscosity is set as $1 \times 10^{-6} \text{ m}^2/\text{s}$, and the initial gas pressure is 15 KPa. With the decrease of channel height, the bubble collapse time is prolonged. For instance, when a bubble with the radius of 30 μm is in the 10- μm microchannel, its collapse time is 6 μs ; when the bubble is in the 4- μm

microchannel, its collapse time is longer than 15 μs . In addition, the bubble oscillation occurs with the noncondensable gas, which is especially obvious in the 8- μm and 6- μm microchannel. The oscillation is not observed in the 10- μm channel due to the larger volume of the bubble, which makes the gas pressure being ignored. The oscillation is gradually damped with decreasing channel height as in the 2- μm channel as shown in Fig. 4.11. The experimental results in the 8- μm and 4- μm channels show the same collapse tendency with the simulation results. However, no oscillation is observed. The oscillation is possibly affected by the drag force due to the wall shear stress. It is expected that in smaller scale confinements, such as the nanochannels, the surface forces are going to play a more important role in the bubble dynamics.

In addition, different contact angles have been considered in the simulation. A contact angle of 0° and 90° is used to represent hydrophilic and hydrophobic surface, respectively. However, the simulation results do not show any difference in the bubbles dynamics. As a result, the effect of surface hydrophobicity on microbubbles dynamics can be ignored.

4.3.2 Microbubble in a 2D confined channel

In the previous section, the bubble is only confined in the z direction (channel height h), the microchannel width and length are sufficiently large to ignore the boundary effect in the x - y plane. In the following parts, the bubble dynamics is investigated in a rectangular microchannel, which offers confinement in the y and z direction.

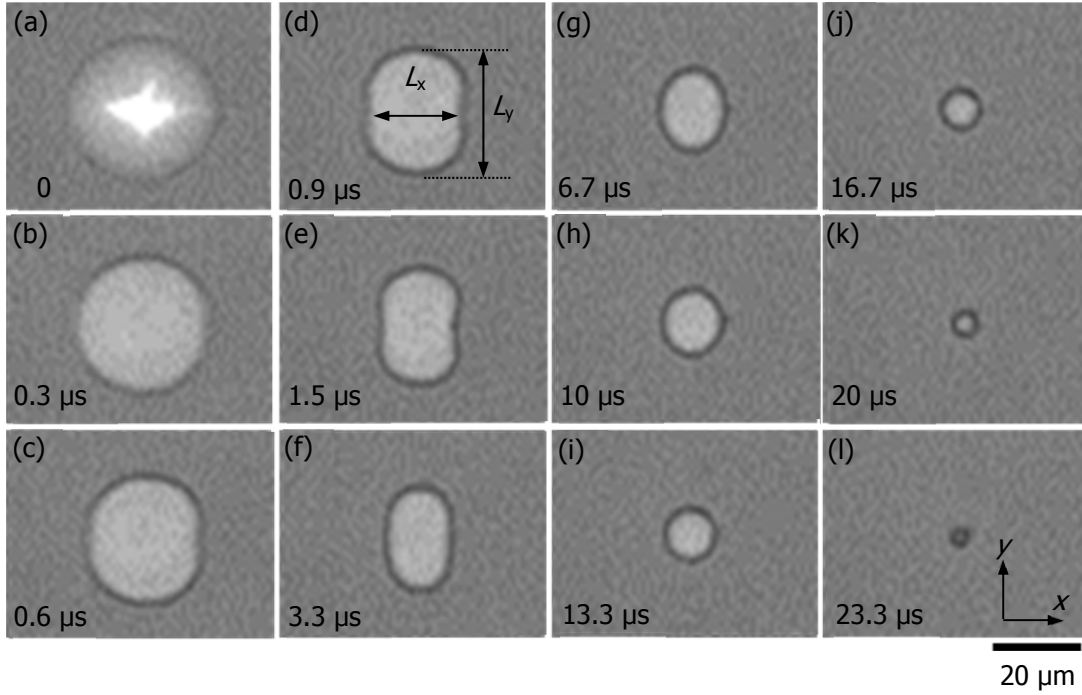


Figure 4.12: Sequential snapshots of a microbubble in the microchannel with the height of $4\ \mu\text{m}$ and the width of $140\ \mu\text{m}$.

Bubbles in a 2D confined channel have received increasingly attentions due to their application in the medical fields, such as cavitation therapy in vessels [292]. In this type of microchannel, the largely expanding bubble is ellipsoidal and the motion remains nearly one-dimensional [293]. However, the experiments have not shown a stretch of the bubble in this project. On the contrary, the bubble expansion is impeded along the channel.

Figure 4.12 shows the bubble evolution in a 2D confined microchannel with the height of $4\ \mu\text{m}$. The photographs are taken by the high speed camera from the top of channel. The experimental condition is shown in Fig. 4.5 (b), with $W = 140\ \mu\text{m}$ and $L = 3\ \text{mm}$. The vapor microbubble appears soon after the laser shooting ($t =$

0). It expands spherically and reaches its maximum radius within 370 ns as shown in Fig. 4.12 (a). Instead of growing along the channel, the microbubble constricts in this direction as shown in Fig. 4.12 (b)-(e). This is because the liquid is pushed towards the channel wall and reflected during the microbubble expansion, which causes the transport of vortices to the microbubble boundary along x axis. That makes the microbubble boundary to move towards the center of the microbubble as shown in Fig. 4.12 (e). When the effect of the vortices fades, the microbubble shows an oval shape (Fig. 4.12 (f)). It is noted that the collapse of the microbubble in the 2D confined microchannel is asymmetric. The distance between the right and left edges of the microbubble (L_x) is decreased faster than the distance between the upper and lower edges of the microbubble (L_y) due to the vortices at the beginning as indicated in Fig.4.12 (d). The decrease of L_x slows down after 3.3 μ s. The decrease rate of L_x catches up that of L_y until the microbubble becomes a round-shape again as shown in Fig. 4.12 (h)-(l).

Time evolutions of L_x and L_y are shown in Fig. 4.13. L_x decreases faster than L_y in the first 2 μ s and stay constant until L_x eventually reaches the same value as L_y . Since that, the bubble collapses symmetrically. This process is affected by the surface tension. At $t = 2 \mu$ s, the surfaces on the right and left edges of the bubble are almost flat, while radii of curvature on the upper and lower edges are much smaller. It results in higher Laplace pressure on the upper/lower edge and causes asymmetrical collapse. For comparison, another microbubble is created in a 1D confined microchannel with the same height and laser energy. Figure 4.14 plots out the radial evolution of the 1D confined microbubble (R_0). The 1D confined microbubble reaches its maximum radius in 2 μ s, which is twice as large as the

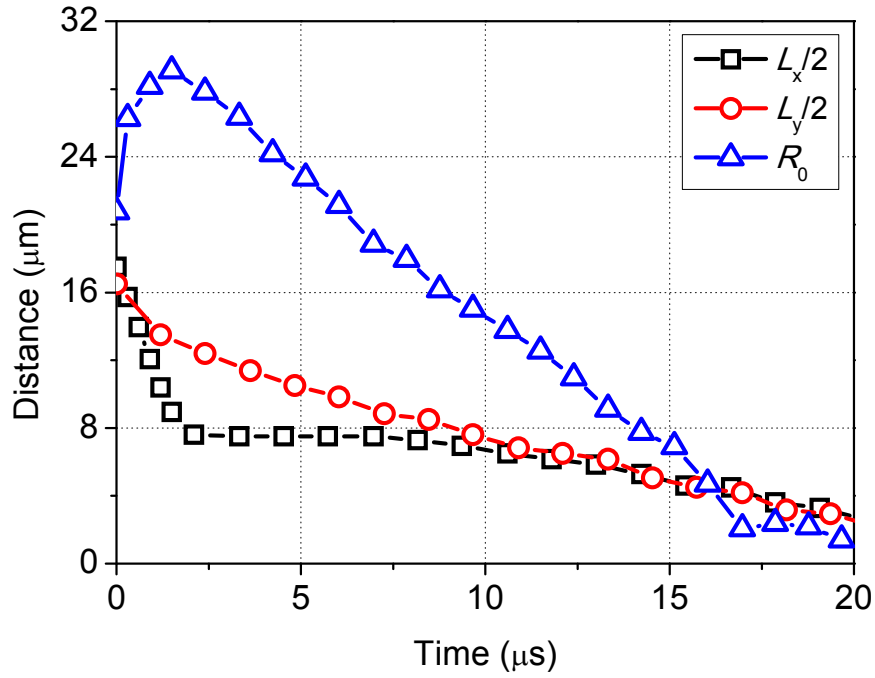


Figure 4.13: Distances between the right and left edges (L_x), and upper and lower edges (L_y) of the bubble in the 2D confined microchannel are depicted as a function of time, and compared with the radial revolution of a 1D confined bubble (R_0).

maximum radius of the 2D confined microbubble. However, the microbubble life times are almost the same. The collapse time of the 2D confined microbubble is much longer than the expected one from Eq. (4.21). It indicates that the confinement along the y axis also hinders the bubble collapse rate.

Figure 4.14 shows the volume evolution of the microbubble in the 2D microchannel at different laser energies. The bubble size is increased with the laser energy. The initial expansion is always stopped within the first 370 ns. Thereafter, the bubble volume decreases fast due to the vortices from the channel walls. The

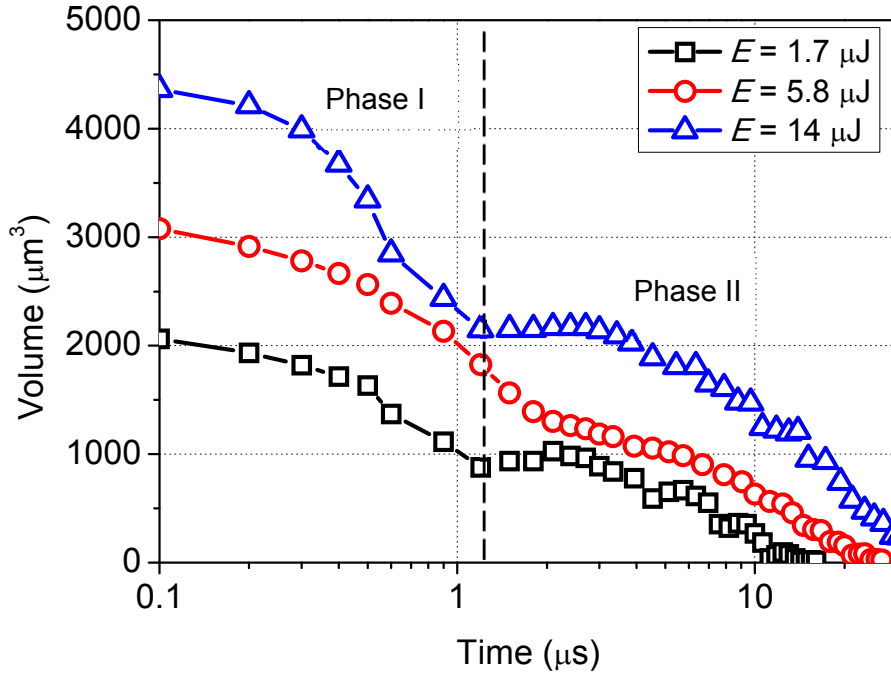


Figure 4.14: Volume evolution of the 2D confined microbubble at laser energies of 1.7, 5.8 and 14 μJ .

collapse slows down after a turnover at 1.2 μs approximately. Larger bubble volume results in longer collapse time. It takes 12 and 34 μs to collapse at laser energies of 1.7 and 14 μJ , respectively. In addition, the laser energy also has great influence on the collapse rate of the microbubble. The collapse rate can be divided into two phases as shown in Fig. 4.14. The collapse is affected by the vortices from channel walls in phase I, while the collapse is dominated by inertia in phase II. When the laser energy is increased from 1.7 to 14 μJ , the collapse rate in phase I is increased from 1×10^{-3} to $2 \times 10^{-3} \mu\text{m}^3/\text{s}$. However, the collapse rate is not changed with the laser energy in phase II, and almost fixed at $7.5 \times 10^{-5} \mu\text{m}^3/\text{s}$ approximately. It is because higher laser energy will accelerate more flows to compress the microbubble in phase I, while the collapse is not affected by the laser in phase II.

4.3.3 Microbubble near an elastic surface

The two previous sections have demonstrated that the microbubble dynamics are prominently affected by the restricted solid boundaries. Next, a microbubble is generated near an elastic surface in a 2D confined microchannel, and its dynamics are studied in details.

The experiments are done in the same microchannel as in Section 4.3.2. A long gas bubble is trapped inside the microchannel while a cavitation bubble is generated by the laser on a nearby location as shown in Fig. 4.5 (c). The gas/liquid interface can be considered as an elastic surface, which significantly affects the dynamics of the laser-induced bubble. Figure 4.15 shows the evolution of the laser-induced bubble, which is on the left side of the static gas bubble. The distance between the laser spot and the adjacent gas/liquid surface (D) is 85 μm . The bubble

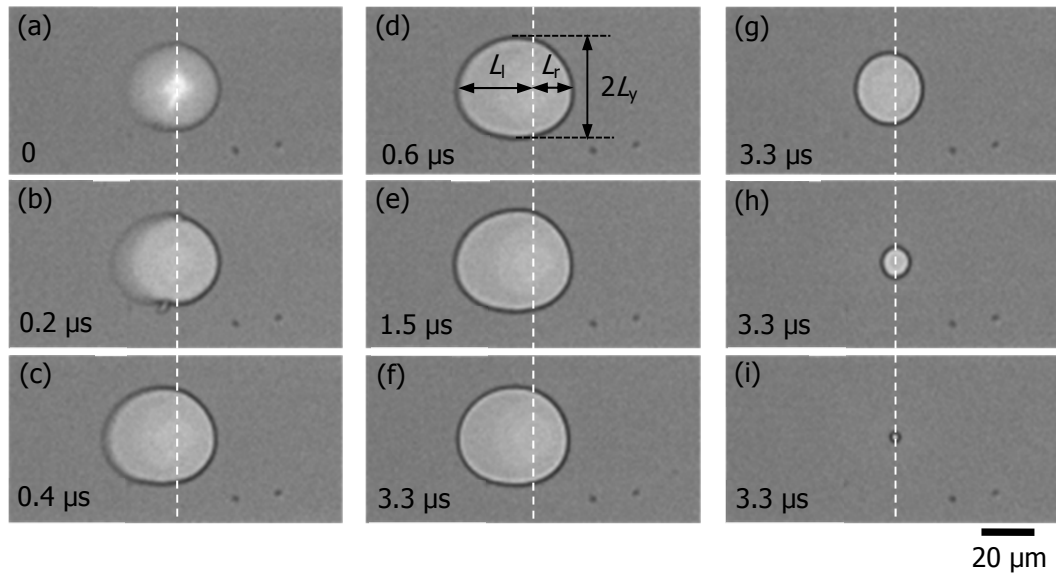


Figure 4.15: Sequential snapshots of a bubble in a tube microchannel with a distance of 85 μm away from a gas/liquid surface.

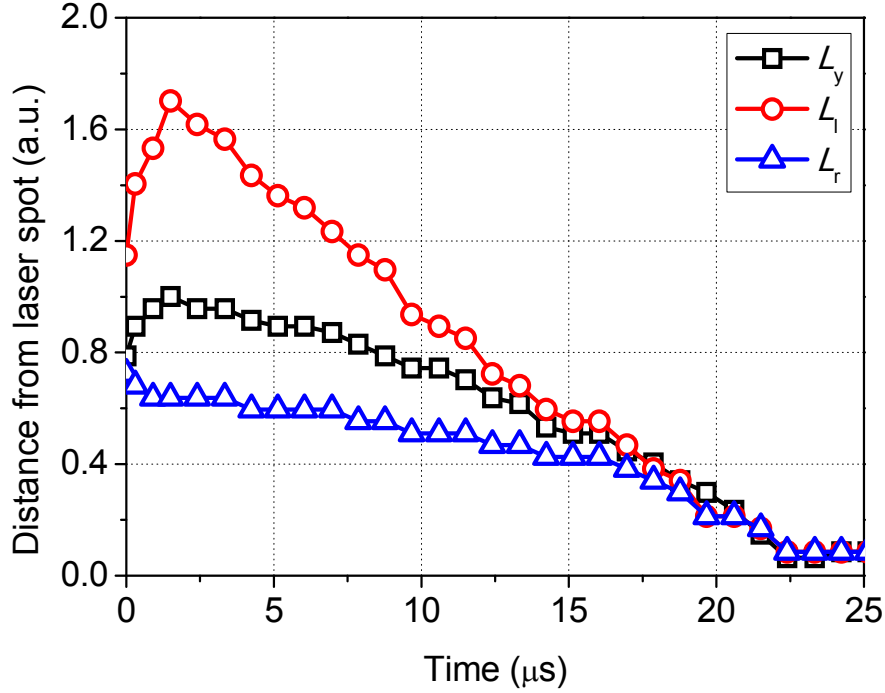


Figure 4.16: Evolution of the length between the laser spot and the bubble edges.

grows and reaches its maximum radius at about 1.5 μs . It is obviously expanding towards the elastic surface, i.e. the gas/liquid interface. Figure 4.16 shows the evolution of the length between the laser spot and each edge as indicated in Fig. 4.15 (d). The plotted data are normalized by the maximum value of L_y . Here, $L_{y\text{max}} = 23.5 \mu\text{m}$. Although the bubble growth on the y axis is still symmetrical, the evolutions of the left and right parts of the bubble are much different. L_l has a vigorous expansion and recession process, while L_r is decreasing gradually. When the microbubble reaches its maximum size, L_l is 2.7 times longer than L_r . This asymmetrical expansion is due to the low inertia value of the surface. A rigid boundary and a free surface are the examples with different inertia for the extreme limits. Whereas a rigid boundary may be regarded as the infinite-inertia limit for a

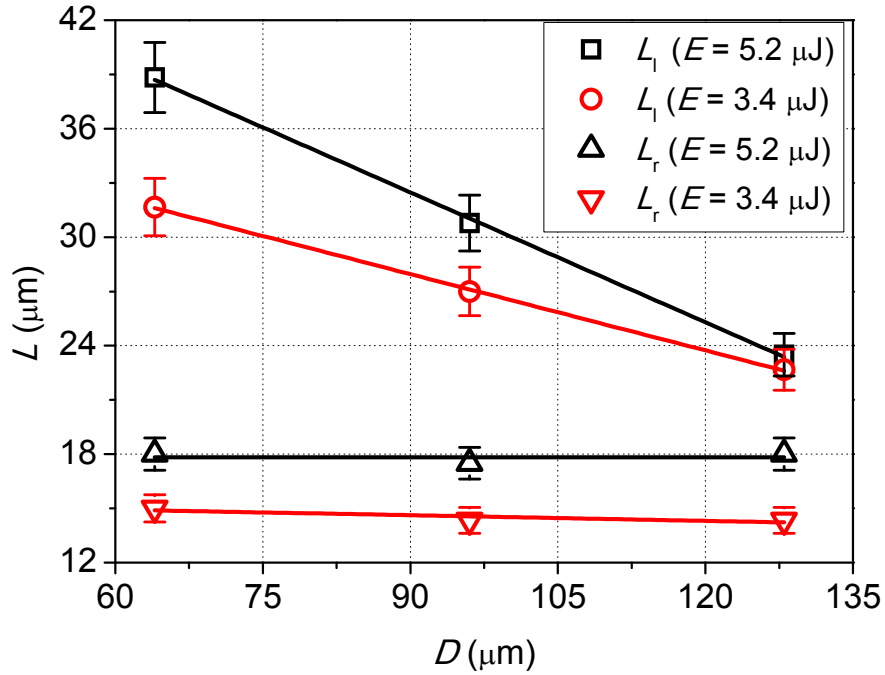


Figure 4.17: Maximum length of L_l and L_r with different distances when $E = 5.2$ and $3.4 \mu\text{J}$.

boundary, a free surface (i.e. interface between the sea and air) corresponds to the exact opposite, being the zero-inertia limit. As a consequence, fluid motion is directed towards the surface with low inertia during the growth, inducing net cavity migration towards the elastic surface.

Figure 4.17 shows the maximum length of L_l and L_r changes as a function of the distance D with different laser energies E . When the laser energy E is increased, L_l and L_r are both increased. When the distance D is increased, L_l is rapidly decreased, but L_r is not varied. In other words, the distortion of the microbubble becomes larger when the distance between the microbubble and the elastic surface is shorter. For example, when D is changed from 128 to 64 μm , the difference

between L_l and L_r is increased from 5.4 to 20.8 μm , with $E = 5.2 \mu\text{J}$. In some situations, the existence of another bubble may compress the expansion of the cavitation bubble. Increasing D can increase the maximum volume of the bubble. However, in this experiment, the expansion of the cavitation bubble has already been compressed by the side channel walls in the microchannel as discussed in Section 4.3.2. When another bubble serving as an elastic surface is nearby, the bubble will be expanded towards it. According to Bernoulli's principle, high fluid velocity creates a low pressure zone. Since the fluid particle is set into motion by the impulse pressure due to laser shooting, the fluid velocity is related to the laser energy E and distance D from the laser spot. Decreasing D or increasing E can increase the fluid velocity, thus decrease the pressure gradient. Therefore, greater elongation of the bubble can be achieved at shorter distance D and higher energy E as shown in Fig. 4.17.

Figure 4.18 shows the volume evolution of the microbubble near an elastic surface with different laser energies at $D = 64 \pm 3 \mu\text{m}$. With higher laser energy, the bubble has larger maximum volume and longer life time as expected. When the laser energy E is increased from 1.3 to 5.0 μJ , the maximum volume of the microbubble is increased from 5.2×10^3 to $7.3 \times 10^3 \mu\text{m}^3$, and the collapse time is increased from 14 to 20 μs . Figure 4.19 shows the volume evolution of the microbubble near an elastic surface with different distances at $E = 5 \pm 0.4 \mu\text{J}$. Although the volume of the microbubble is also varied with the distance D , it does not affect the collapse time. When the distance D is decreased from 128 to 64 μm , the maximum volume of the microbubble is increased from 4×10^3 to $7.5 \times 10^3 \mu\text{m}^3$.

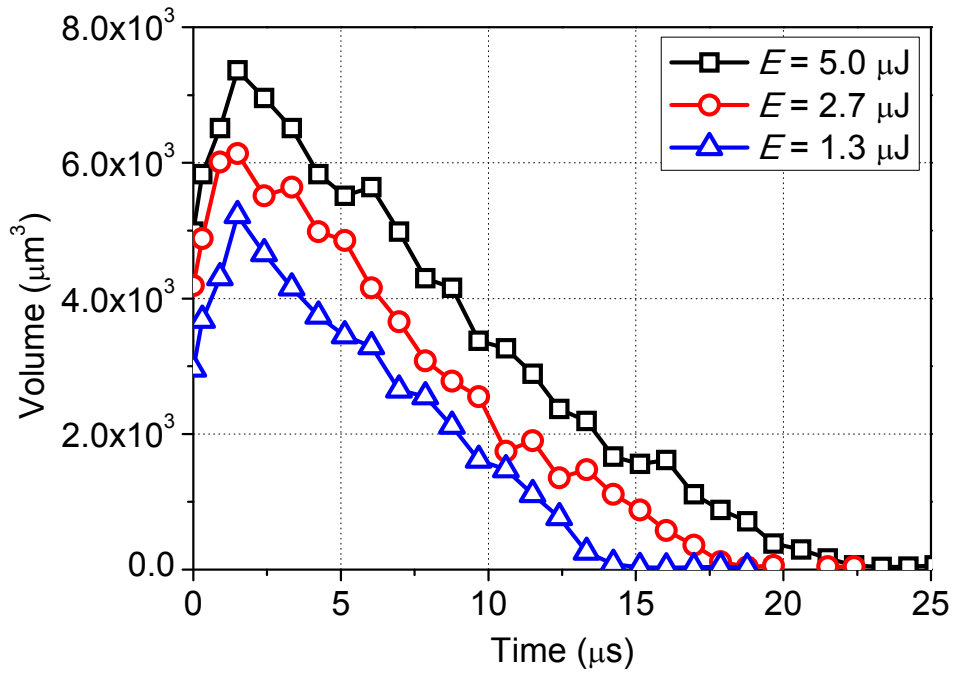


Figure 4.18: Volume evolution of the microbubble near an elastic surface with different laser energies at $D = 64 \pm 3 \mu\text{m}$.

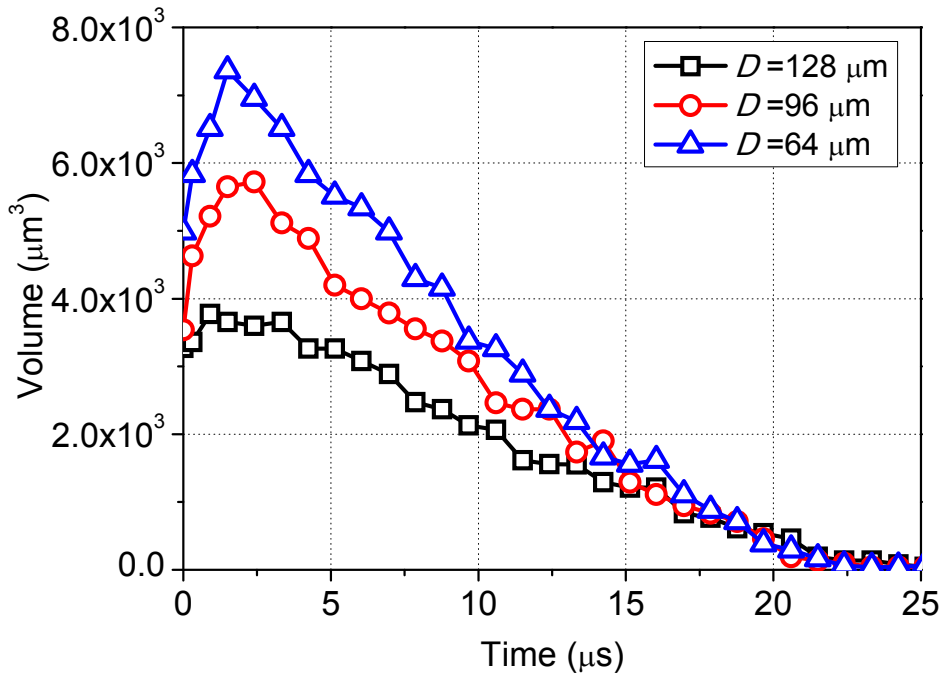


Figure 4.19: Volume evolution of the microbubble near an elastic surface with different distances at $E = 5 \pm 0.4 \mu\text{J}$.

However, the collapse time is almost the same, i.e. 20 μs . It indicates that a fast compression is followed by the expansion.

As discussed for bubble collapse near a free surface, there should be a jet that moves in the opposite direction to the growing free-surface spike [186]. Although no liquid jet is observed, the movement of the fluid can still be indicated from the evolution of the bubble volume. As shown in Fig. 4.19, although the bubble maximum volume increases with decreasing distance D , the collapse time is almost the same. It means that the bubble collapses faster with shorter distance D . Besides inertia, there must be other force to accelerate the bubble collapse [186]. It can also be explained as the energy transfer and oscillation.

Unlike other reported works, vigorous compression and reexpansion of the cavitation bubble is not observed during the rebound period of the elastic surface. It means that the pressure is damped rapidly in the microchannel as well as the energy in this oscillating system. When the microbubble grows, the initial kinetic energy gradually changes to the potential energy. The residual kinetic energy in the fluid depends on the initial location of the microbubble from the elastic surface. There is a steep rise in the residual kinetic energy as the distance decreases. Further analysis on the microbubble may give a picture about the energy transfer between the microbubble and fluids.

4.4 Experimental results of nanobubble

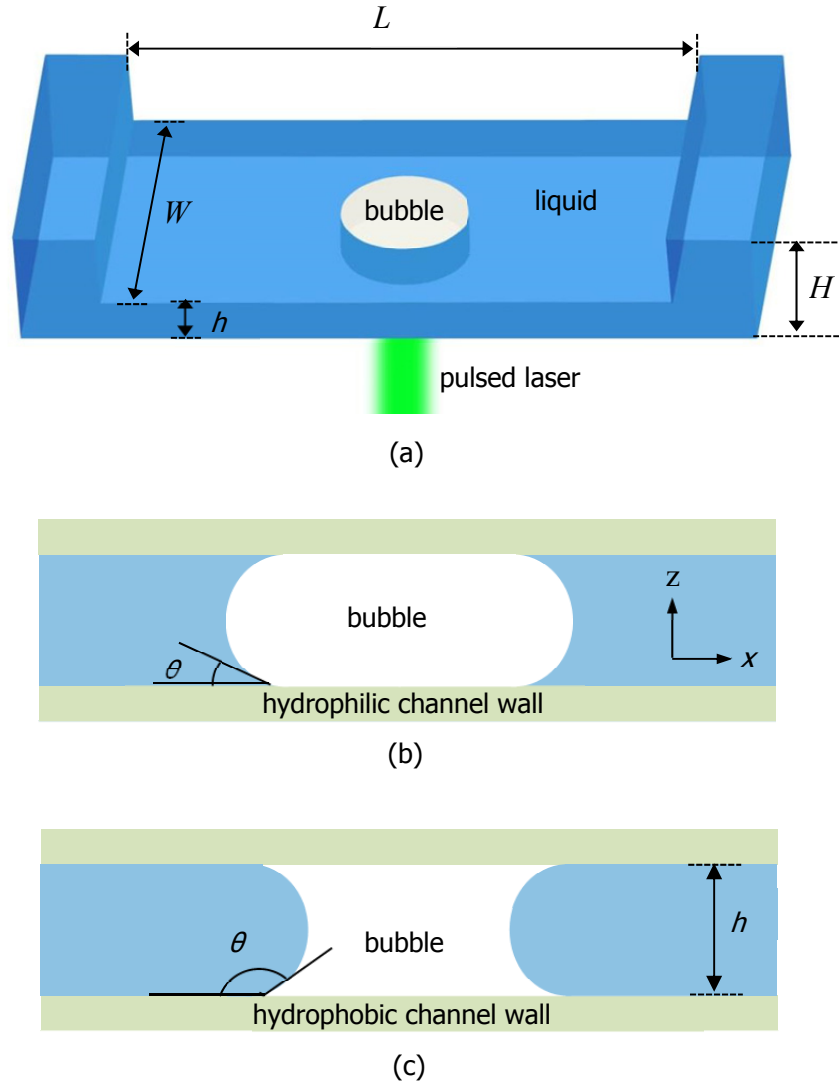


Figure 4.20: (a) Schematics of the laser-induced nanobubble in the micro-nanofluidic channel. Side view of the nanobubble in the (b) hydrophilic and (c) hydrophobic channel.

In this section, the nanobubble dynamics are investigated in nanochannels with the height (h) of 300 to 900 nm. The experiments are conducted in a micro-nanofluidic chip as shown in Fig. 4.20 (a). The liquid is injected through microchannels into the nanochannel whose length (L) is 3 mm and width (W) is 1 mm. The bubble is generated in the centre of the nanochannel. The discussions are focused on the effect of the channel height and surface wetting condition (Fig. 4.20 (b)-(c)).

4.4.1 Effect of channel height

Figure 4.21 compares the dynamics of bubbles generated in channels with heights of 8 μm and 700 nm at the same laser energy in the lateral center of the channel. Linear absorption of the laser energy leads to the explosive vaporization of the liquid and the rapid expansion of a bubble centered around the focal spot. The bubble is constrained into an approximately cylindrical shape by the top and bottom surfaces of the channel. After expansion, the pressure imbalance between the inside and outside of the bubble causes it to collapse. Although the laser energy for both cases in Fig. 4.21 is very similar, a much smaller bubble radius is obtained in the nanochannel than that in the microchannel. This is likely caused by the fact that much less liquid is available for vaporization in the nanochannel as well as the largely different viscous pressure head in both channels. While the expansion phase is resolved with two frames for the microchannel, the bubble reaches its maximum size within less than 0.4 μs . The comparable collapse times with rather different maximum bubble radii indicates that the collapse is strongly hindered by the

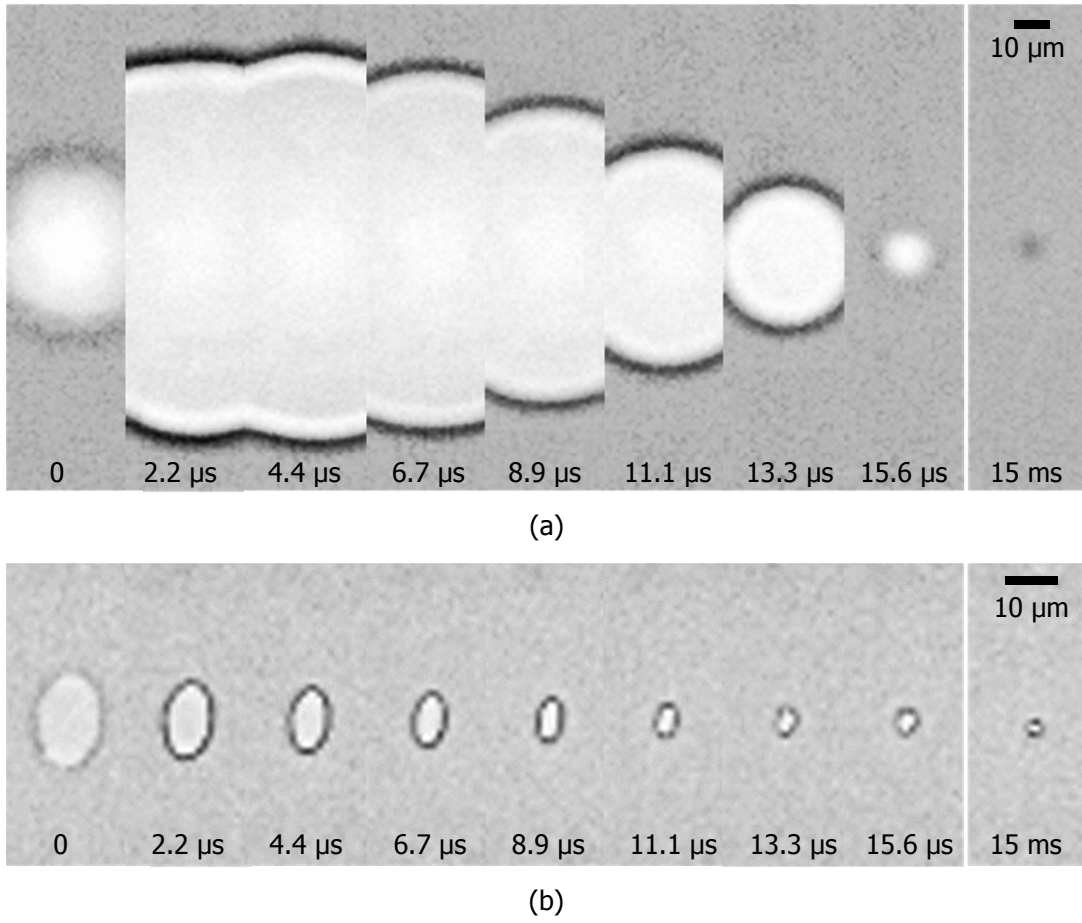


Figure 4.21: Cavitation bubble evolution in (a) microchannel ($h = 8 \mu\text{m}$) and (b) nanochannel ($h = 700 \text{ nm}$).

confinement. It is also noteworthy that even after the vapor-bubble-type collapse (the so-called Rayleigh collapse), a residual bubble remains for some longer time (here depicted after 15 ms). As discussed further below this is a slowly diffusing gas bubble. Due to the small channel height, even minute gas bubbles remain visible. A model to account for the fast dynamics is first discussed and then the dissolution of the bubble is modeled.

Due to the taller channels, previous studies ignore viscosity and surface tension on the bubble dynamics. However, the duration, δt , for a boundary layer to

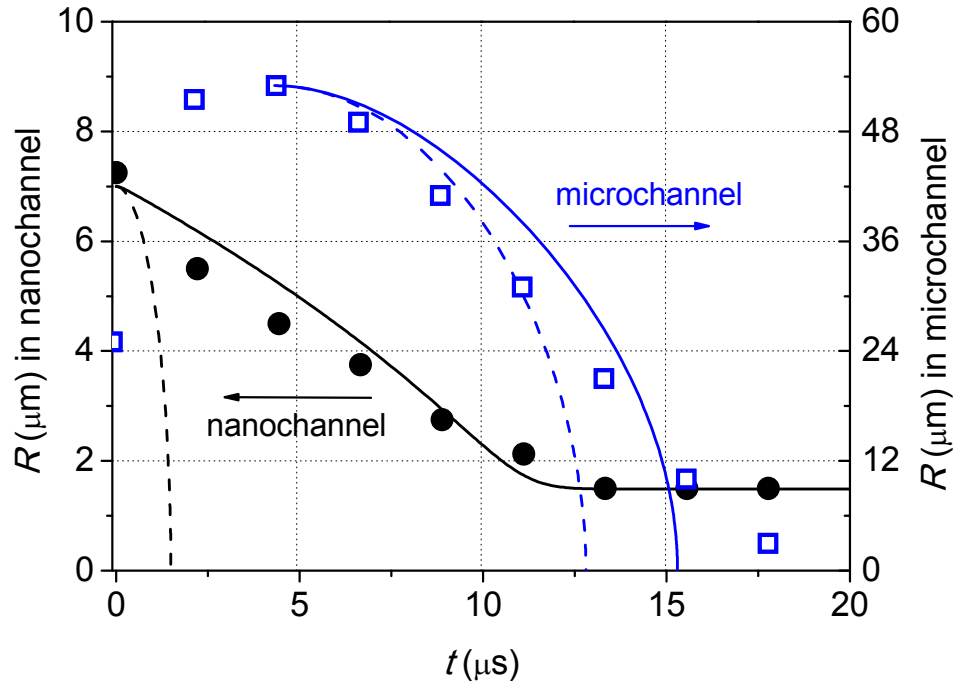


Figure 4.22: Comparing the radial dynamics of a bubble in nanochannel with $h = 700$ nm (circle) and microchannel with $h = 8$ μm (hollow square) with a viscous 2D model (solid line) and inviscid 2D model (dashed line). Left axis is for the bubble in nanochannel and right one is for the bubble in microchannel.

grow in the vertical direction, z , can be approximated with $\delta t \approx z^2 / \nu$. Thus the boundary layer reaches the center of the nanochannel within less than a microsecond for all nanochannels studied in this work.

Figure 4.22 demonstrates the importance of the viscosity on the bubble dynamics in the extended nanochannel. The measured (circles) and calculated (solid line) bubble dynamics including viscous effects, Eq. (4.21), shows a good agreement. In contrast, the inviscid model (dashed line), Eq. (4.35), predicts a much faster shrinkage in the nanochannel, but is still applicable in the microchannel

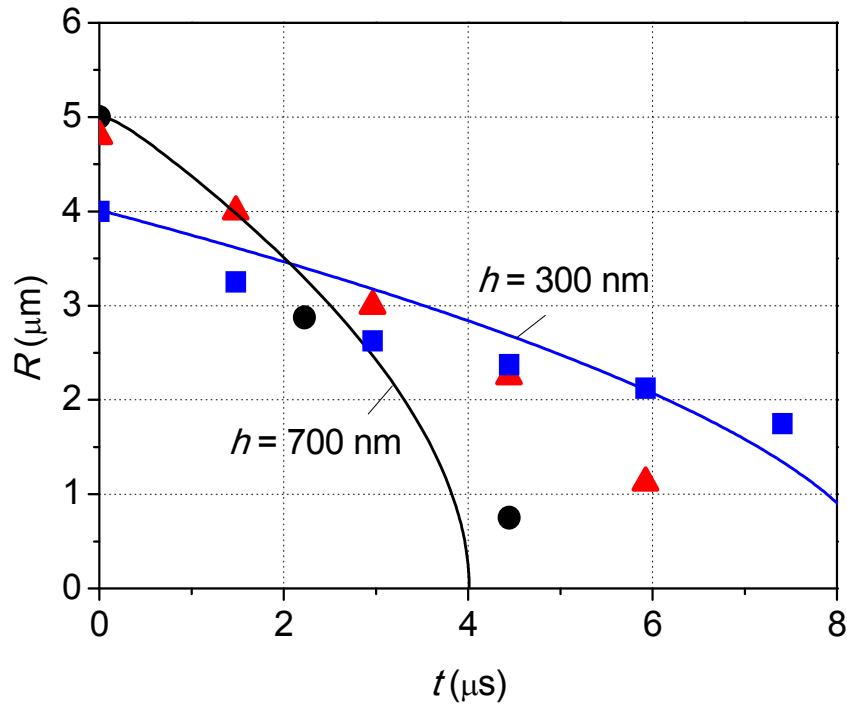


Figure 4.23: Dynamics of cavitation bubble in nanochannels of variable heights: 700 nm (circle), 500 nm (triangle) and 300 nm (square).

(square symbols). Moreover, the initial collapse of a vapor bubbles with an initial radius of about $5 \mu\text{m}$ in the extended nanochannels with heights between 300 nm and 700 nm is examined in Fig. 4.23. It is clearly seen that the rate of bubble collapse slows down in the thinner channel due to an increase in the wall shear stress. The same trend is also well predicted by the viscous Rayleigh-Plesset-type model.

4.4.2 Effect of surface hydrophilicity

Both for the diffusion dominated shrinkage of the remaining gas bubble as well as for the inertial bubble dynamics, the contact angle θ is important. To demonstrate this feature of extended nanochannels, the inertial collapse time and the succeeding diffusion governed shrinkage are compared for hydrophilic and hydrophobic channels. The last term in Eq. (4.22) serves as a constant driving pressure accelerating the collapse. This speeds up the bubble collapse in the hydrophilic channels. Fig. 4.24 depicts the inertial collapse time of bubbles of different maximum radii in an extended nanochannel of height $h = 800$ nm. The

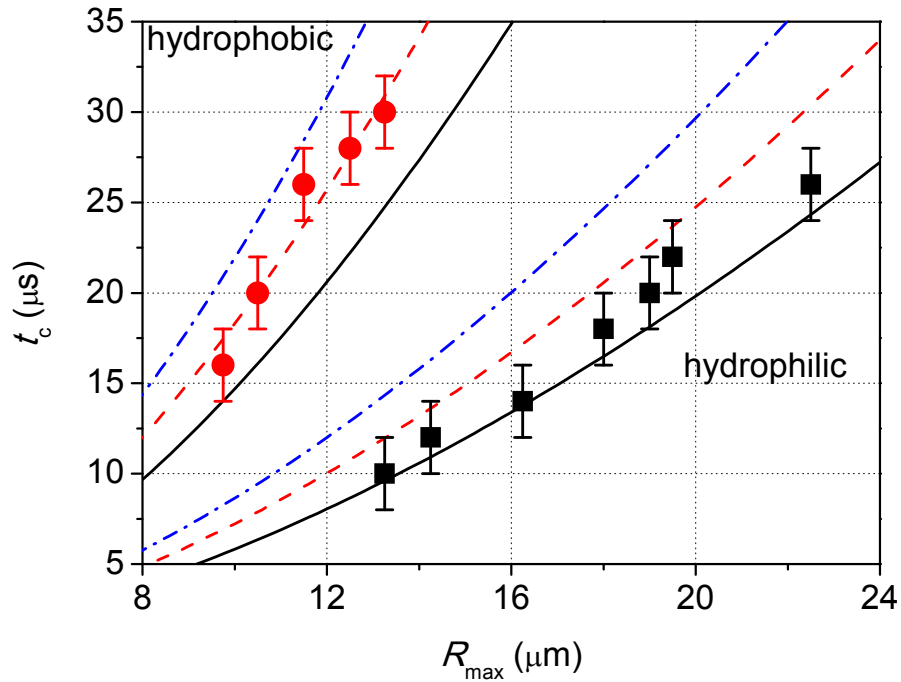


Figure 4.24: Collapse time as a function of the maximum radius of bubble in the hydrophilic (square) and hydrophobic (circle) nanochannels. The lines show the predicted effective viscosities as $0.4 \times 10^{-6} \text{ m}^2/\text{s}$ (solid line), $0.5 \times 10^{-6} \text{ m}^2/\text{s}$ (dashed line) and $0.6 \times 10^{-6} \text{ m}^2/\text{s}$ (dashed-dotted line).

slopes for the hydrophobic and hydrophilic cases are markedly different; and as expected, bubbles in the hydrophilic channel collapse in a 1/3 of the time as compared to those in a hydrophobic channel (9 μs as compared to 29 μs for a 13- μm radius bubble). Interestingly, for the same laser energy, much larger bubbles can be generated in hydrophobic channels. It is speculated that the rapid expansion process a three phase contact line is formed, whereas a thin water film remains on the surface in the hydrophilic case. Yet, the temporal and spatial resolutions of the current equipment cannot test this hypothesis. The dynamics are also compared with the model and a reasonable agreement is found. The initial partial pressure of the gas is unknown and the viscous Rayleigh model is integrated by neglecting for an empty void. Further, some heating of the liquid is expected due to the laser pulse and the illumination. To account for the temperature dependent viscosity, the results for the range from $\nu = 0.4 \times 10^{-6}$ to $0.6 \times 10^{-6} \text{ m}^2/\text{s}$ are shown.

Next, the gross bubble dynamics are compared including the slow diffusion of the bubble, Eq. (4.34), see Fig. 4.25. The fast inertial dynamics for the hydrophobic and hydrophilic surfaces agrees nicely with the model. The experiment shows that the bubble lifetime of the remaining bubble in the hydrophobic channel is about thirty times longer than that in the hydrophilic channel, i.e. 1.2 s and 40 ms, respectively. Note that the assumption of 2D concentration fields is valid only for cylindrical bubbles ($\theta = 90^\circ$), thus in the hydrophobic channels where a good agreement is obtained. Hydrophilic channels cause a height dependent concentration field due to the small contact angle and can therefore not be described with Eq. (4.34). This may explain the difference between the model and the hydrophilic channel experiments.

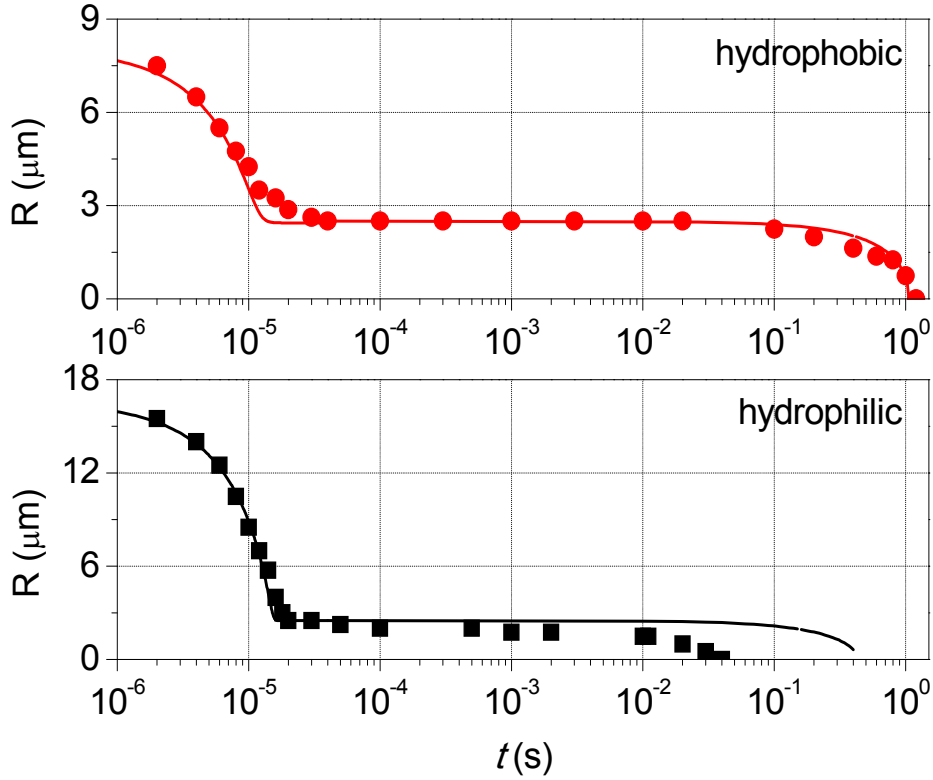


Figure 4.25: Comparison of the bubble dynamics in the hydrophilic and hydrophobic nanochannels together with the model predictions.

Here, a static contact angle is used as a representative value in the calculations for the moving contact line, because the (advancing) dynamic contact angle, which is larger than the static one, is unknown in the experiment. The difference between the static and dynamic contact angles (i.e. contact angle hysteresis) depends on the roughness of material surfaces and the velocity of moving contact lines [23]. For bubble dissolution driven by mass diffusion, the bubble collapse rate is sufficiently slow to expect negligible hysteresis effect. However, the vapor collapse rate is rather fast so that such effect may come into

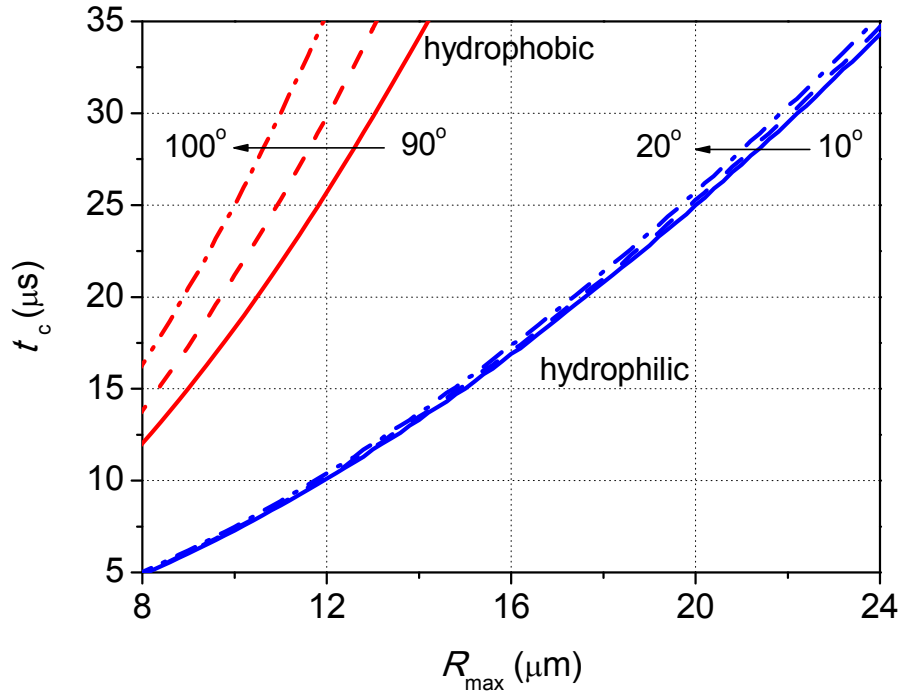


Figure 4.26: Simulation of the collapse time as a function of the maximum radius for varying contact angles in an 800-nm high extended nanochannel and viscosity of $\nu = 0.5 \times 10^{-6} \text{ m}^2/\text{s}$.

play. However, the surface roughness of the channel created by wet etching is at most 5 nm, which is much smaller than the channel dimensions. It is thus expected that calculation errors due to the variation of the contact angle are less than or comparable to those from the uncertainty in liquid viscosity. In Fig. 4.26, the effect of increasing the contact angle by 10° is examined. While very little effect is seen for the hydrophilic case, the variation gives rise to 30% error in predicting the collapse time of the vapor bubbles for hydrophobic surfaces.

4.5 Summary

This chapter focuses on the study of bubble dynamics in a confined environment: from microscale to nanoscale, and from 1D to 2D confinement. The theoretical analysis investigates the radial motion of a cylindrical vapor bubble starting from the Navier-Stokes equation. A Rayleigh-Plesset-type equation that accounts for the shear stress from channel walls and surface tension is derived. Moreover, the dynamics of a cylindrical gas bubble due to mass diffusion is explored. The theoretical models are verified in a micro/nanofluidic chip, which is designed and fabricated by using borosilicate glass. Experimental results demonstrate that the viscosity and surface tension play important roles on the bubble dynamics in the confined channels. With the decreasing of channel height, the bubble life time is prolonged. This study provides new insights in the cavitation dynamics especially for these practical situations where the fluid dynamics is severely affected by confinement.

The innovation of the study on the bubble dynamics in micro/nanochannels is summarized as follow,

- a) A theoretical model is derived to describe the dynamics of a confined cavitation bubble. This model considers the channel height as a critical factor, and including the effects of the surface tension and viscosity. Therefore, it is applicable for both microchannel and nanochannel, overcoming the shortages of other models, which diverge from the experimental data when the channel dimension decreases.

- b) Different boundary conditions are experimentally realized on the microbubbles. These experiments do not only verify the applicability of the theoretical model for the 1D confined microbubble, but also demonstrate the bubble behavior under 2D confinement with/without an elastic surface nearby.
- c) The nanofluidic dynamics is approaching by using an extended nanochannel which has only one dimension in the nanometer scale, i.e. hundreds nanometer height. It lowers the request for the fabrication techniques. In addition, the cavitation bubble created in the extended nanochannel reaches lateral extension of several micrometers that is sufficiently large to observe with standard high-speed photography. Previous studies on nanobubbles seldom use this kind of direct observation methods.

CHAPTER 5

JETS PENETRATION BY TWO BUBBLE INTERACTION

This chapter presents the dynamics of micro/nano-jet that is generated when a static gas bubble is impacted by a laser-induced cavitation bubble in a micro/nanochannel. In the microbubble interaction, the whole process of the microjet is theoretically and experimentally studied, which includes the flow focusing, jet penetration and retraction. High shear stress causes rupture of the gas bubble during the jetting in the confined environment. The breakup mechanism of the pinched-off microbubbles is analyzed based on the Plateau-Rayleigh instability. Based on the experimental results of the nanobubble interaction, it shows that the fast jetting process is in a much shorter time than that occurs in the microbubble interaction. The nanojet is in the shape of a thin sheet that is much thinner than the channel height. New phenomena with the rupture of the thin liquid sheet are experimentally presented and discussed.

5.1 Theoretical modeling

In this chapter, the liquid jet dynamics are studied with the transient bubble-bubble interaction in a confined channel whose height is changed from microscale to nanoscale. The dynamics are highly depending on the dimension of the thin film.

5.1.1 Cavitation induced jet

The asymmetric collapse of a cavitation bubble near a rigid boundary is always accompanied with a high-speed liquid jet directed towards the boundary [187, 226]. On the contrary, the jet is directed away from a free surface [294]. It has been demonstrated that the movement of the liquid jet depends on the physical properties of the boundary condition and that the energy is transferred from the bubble to liquid. In this section, the jet is analyzed using an impulse pressure description, and the jet velocity and the control parameters are studied.

Laser induced pressure wave

Optical breakdown leads to a plasma formation by the absorption of a focused laser pulse in the liquid. The plasma formation is accompanied with the generation of shock wave and cavitation bubble expansion. In order to characterize the shock wave propagation, the pressure amplitude at the shock front is investigated.

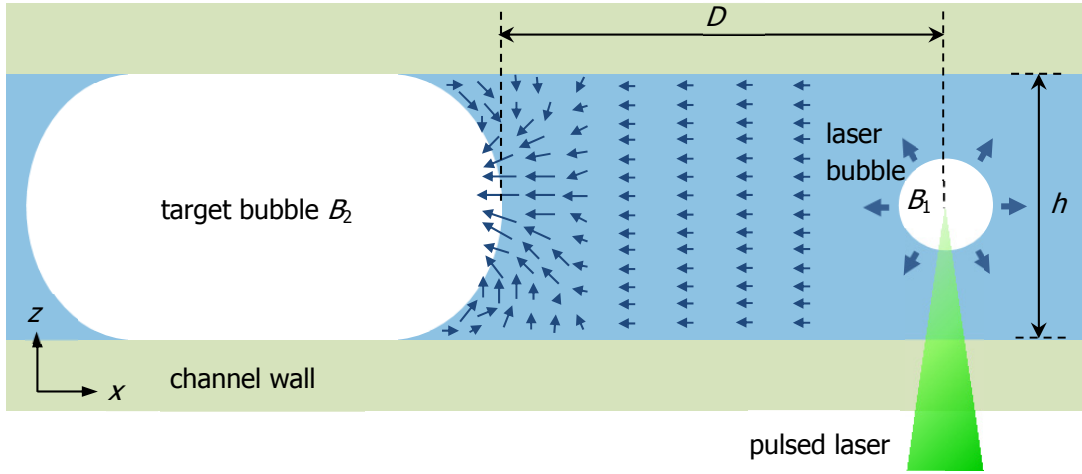


Figure 5.1: Schematic illustration of the jet formation induced by a laser bubble in a micro/nanochannel.

For incompressible and irrotational flow, the velocity vector in the function of a potential ϕ can be described as

$$\mathbf{u} = \nabla \phi, \quad (5.1)$$

which satisfies the Laplace equation

$$\nabla^2 \phi = 0. \quad (5.2)$$

The velocity potential for the motion of the liquid with spherical symmetry can be expressed as

$$\phi = \frac{R^2 \dot{R}}{r}. \quad (5.3)$$

where R is the bubble radius, r is the distance from bubble center. The pressure in the liquid found from the Bernoulli equation is

$$P = -\rho \frac{\partial \phi}{\partial t} - \frac{1}{2} |\nabla \phi|^2 + P_0, \quad (5.4)$$

where ρ is the liquid density, and P_0 is the hydrostatic pressure. In far field, the quadratic term is negligible. The shock wave pressure can be expressed as

$$P = -\rho \frac{\partial \phi}{\partial t}. \quad (5.5)$$

From Eqs. (5.3) and (3.5), it is found that the pressure amplitude decreases inversely with the distance, and can be stated as

$$P \propto \frac{1}{r}. \quad (5.6)$$

As discussed in Ref [16], the energy dissipated by the shock wave at points beyond a surface must be equal to the work done in the displacement of this surface by the shock wave. The work done on a surface having a radius r_0 before the arrival of the shock front at time $t(r_0)$ is given by

$$W = 4\pi \int_{t(r_0)}^{\infty} r_0^2 P u dt. \quad (5.7)$$

The liquid particle velocity u can be expressed as

$$u = \frac{P - P_0}{\rho c}, \quad (5.8)$$

where c is the speed of sound in the liquid. The shock wave energy can be estimated from Eqs. (5.7) and (5.8) as

$$E_{sw} = W = \frac{4\pi r_0^2}{\rho c} \int_{t(r_0)}^{\infty} P^2 dt, \quad (5.9)$$

when the hydrostatic pressure P_0 is neglected. It is known that most of the injected laser energy serves to heat the liquid while the remains is dissipated by the emitted pressure wave, and the shock wave energy is proportional to the laser energy E

[295]. The relationship between the laser energy and pressure difference can be expressed as

$$P \propto E^{\frac{1}{2}}. \quad (5.10)$$

Flow focusing

The pressure wave travels for a distance D and reflects on the surface of the gas bubble. The reflections of the pressure wave on the gas/liquid interface result in a pressure gradient ΔP between the cavitation bubble and the surface of the gas bubble as shown in Fig. 5.2. When the liquid is set into motion, the curved surface converges the liquid towards the center of the curvature. With the impulsive pressure shown in Fig. 5.2, each fluid particle is supposed to acquire a velocity U_0 before reaching the gas bubble surface. The fluid particles move towards the center of the curvature with the velocity of U_n , which is expressed as

$$U_n = U_0 (\hat{j} \cdot \hat{n}), \quad (5.11)$$

where \hat{j} is the unit vector in the x direction, and \hat{n} is the normal unit vector which is perpendicular to the tangent line on the bubble surface. Figure 5.3 illustrates the distribution that is considered as an equal momentum distribution within the liquid. The bubble surface evolution is only considering the displacement in x direction. After Δt , the point (x_i, y_i) on the bubble surface moves to $(x_i - \Delta x, y_i)$. The displacement can be expressed as

$$\Delta x = U_n \Delta t = U_0 (\hat{j} \cdot \hat{n}) \Delta t. \quad (5.12)$$

It demonstrates that the flow is focused on the axial of the bubble in the x -direction. However, it is hard to estimate the accurate axial jet velocity in a simple simulation

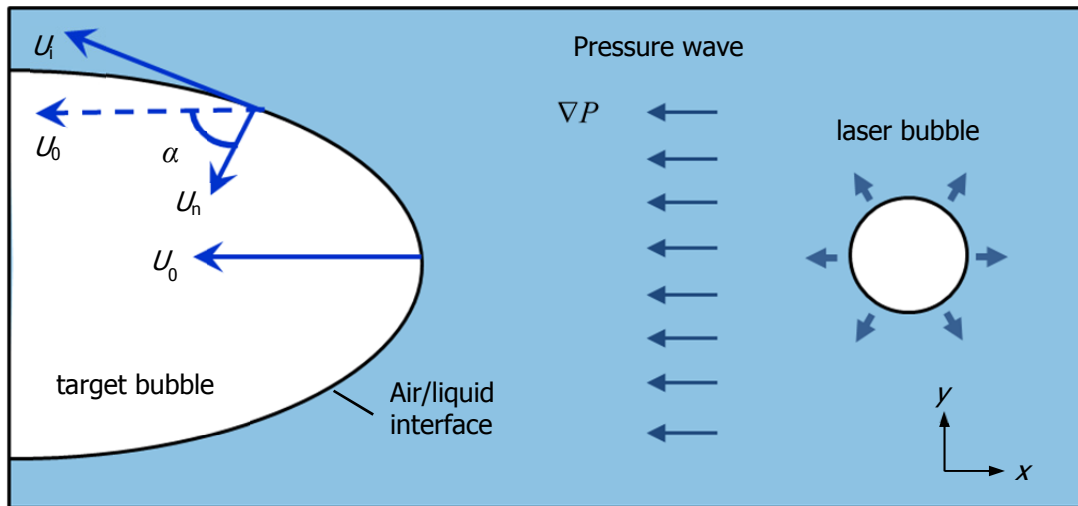


Figure 5.2: Schematic of flow focusing on the target bubble surface that is impacted by the pressure wave generated from the laser-induced bubble.

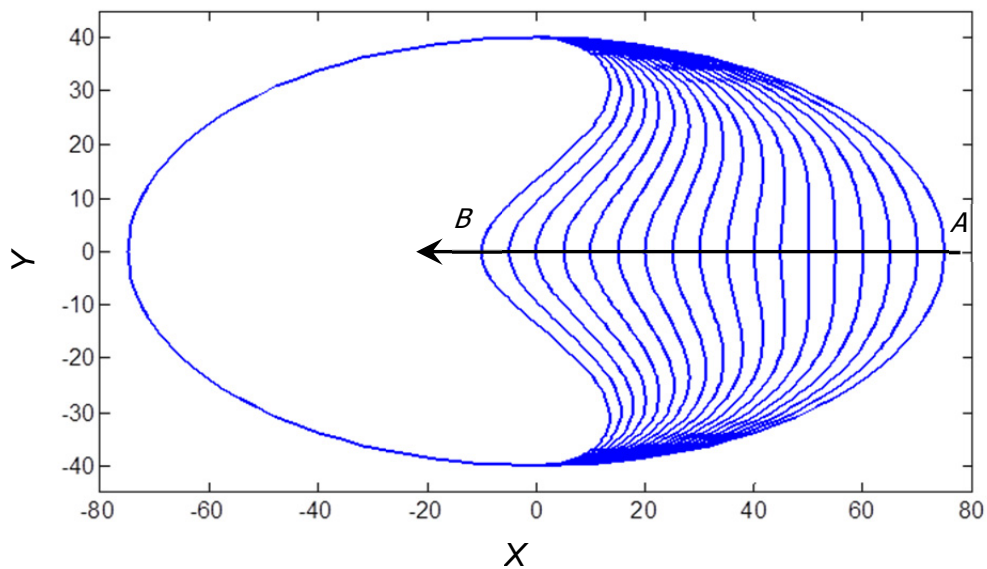


Figure 5.3: Simulation of shape change of the target bubble due to the flow focusing. The bubble surface is concaved from point A to B .

without considering the tangential components of the flow.

Jet penetration

In the case of jetting caused by the reflection of a shock wave from the gas/liquid interface, the velocity of the liquid jet U_{j0} is twice the liquid velocity U_p caused by the shock wave. From the conservation of momentum, the pressure wave strength can be estimated as

$$\Delta P \approx \frac{1}{2} \rho c U_{j0}, \quad (5.13)$$

where c is the speed of sound in the liquid.

When only considering the dependency of the jet velocity on the pressure wave strength, the jet velocity in a function of energy E and travel distance D of the shock wave can be described as

$$U_{j0} \approx C_0 \frac{(E - E_{th})^{\frac{1}{2}}}{D}, \quad (5.14)$$

where C_0 is a constant factor, and E_{th} is the energy threshold.

Jet retraction

When the jet reaches its maximum length, the retracting process begins as shown in Fig. 5.4. While the initial jet penetrating process is dominated by inertia, the jet retracting process is controlled by the viscosity and surface tension force. The velocity distribution of the flow is supposed to be parabolic with the maximum velocity U_m at the center and can be described as

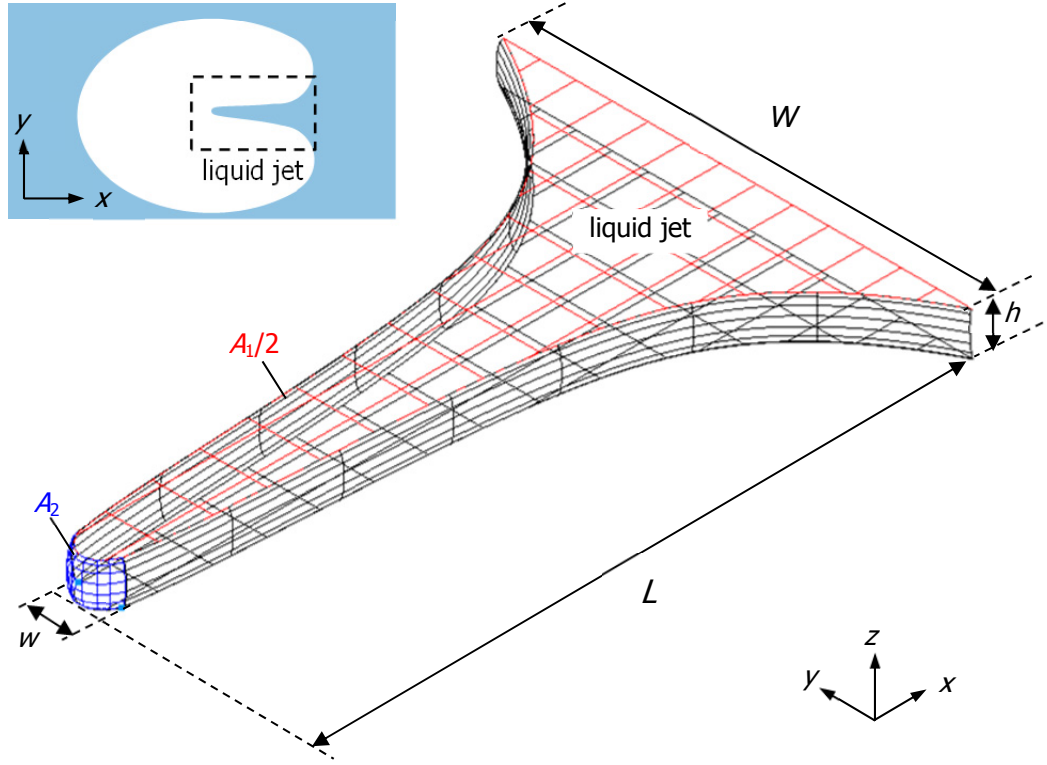


Figure 5.4: Schematic geometry of the liquid jet, which is the zoom-in view of the framed part in the inset.

$$U(z) = \frac{4U_m}{h^2} \left(\frac{h^2}{4} - z^2 \right), \quad (5.15)$$

where h is the channel height. The shear velocity is

$$\frac{dU}{dz} = -\frac{8z}{h^2} U_m. \quad (5.16)$$

The viscous force is expressed as

$$F_\mu = A_1 \mu \left| \frac{dU}{dz} \right|_{z=\frac{h}{2}} = A_1 \mu \frac{4U_m}{h}, \quad (5.17)$$

where A_l is the area of jet contacted with the channel wall. Suppose W is the width of the liquid jet and L is the jet length, then

$$A_l \approx LW. \quad (5.18)$$

The surface tension force is expressed as

$$F_\sigma = A_2 \sigma \left(\frac{1}{R_1} + \frac{1}{R_2} \right) = A_2 \sigma \left(\frac{2}{h} + \frac{2}{w} \right), \quad (5.19)$$

where A_2 is the surface area of the jet tip and can be approximately expressed as

$$A_2 \approx \pi h w. \quad (5.20)$$

By balancing the viscous force and surface tension force $F_\mu = F_\sigma$, the jet retracting velocity can be deduced from Eqs. (5.15) and (5.17) as

$$U_r \approx U_m = \frac{\pi h^2 w \sigma \left(\frac{1}{h} + \frac{1}{w} \right)}{2 \mu L W}. \quad (5.21)$$

When the jet is moving, the advanced contact angle could be 90° . In that case, the surface tension force is

$$F_\sigma = \frac{2 A_2 \sigma}{w}. \quad (5.22)$$

Then, the jet retracting velocity can be simplified as

$$U_r \approx \frac{\pi h^2 \sigma}{2 \mu L W}. \quad (5.23)$$

5.1.2 Transient plane Poiseuille flow

As discussed in the flow focusing section, the displacement of the gas/liquid interface is different in the vertical direction due to the high shear stress near the channel wall. A very small fraction of the liquid receiving the initial impulse and focusing into the jet is in contact with the wall, and therefore its motion is not significantly affected by the pressure wave. The velocity profile in the channel is discussed here.

In the case of rectilinear flow along the x axis, the y and z components of the equation of motion are satisfied by the pressure distribution as

$$p = -\chi(t)x + \rho(g_y y + g_z z) + p_0, \quad (5.24)$$

where $-\chi = \partial p / \partial x$ is the streamwise pressure gradient. The x component of the equation of motion provides an unsteady conduction equation for the streamwise velocity component u_x ,

$$\rho \frac{\partial u_x}{\partial t} = \chi(t) + \mu \left(\frac{\partial^2 u_x}{\partial y^2} + \frac{\partial^2 u_x}{\partial z^2} \right) + \rho g_x. \quad (5.25)$$

Time-dependent pressure-driven (Poiseuille) flow is in a channel confined between two parallel walls located at $z = 0$ and h . The unidirectional flow is due to the application of a constant pressure gradient. After separation of variables and using Fourier expansions, the velocity profile is obtained as [296]

$$u_x(z, t) = \frac{\chi}{2\nu\rho} \left[z(h-z) - \frac{8}{\pi^3} h^2 \sum_{n=1,3,\dots}^{\infty} \frac{1}{n^3} \exp\left(-\frac{n^2 \pi^2 \nu}{h^2} t\right) \sin \frac{n\pi z}{h} \right]. \quad (5.26)$$

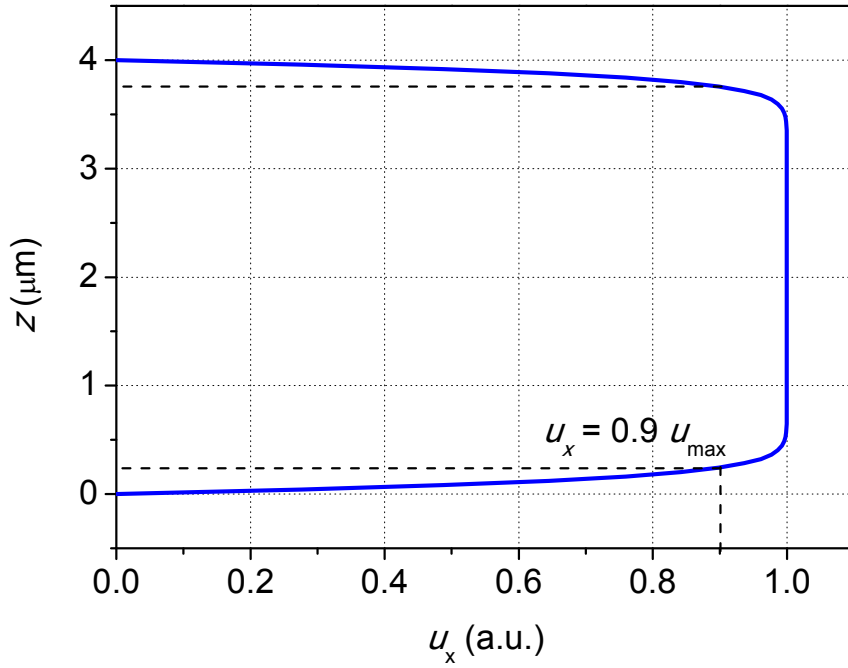


Figure 5.5: Velocity profile of Poiseuille flow in a microchannel.

The velocity vanishes at the initial instant, $t = 0$. At long times, it recovers the Hagen-Poiseuille parabolic profile.

Figure 5.5 shows the simulation result of the velocity profile in a microchannel with the height of $4 \mu\text{m}$. The source of the impulsive pressure is $100 \mu\text{m}$ away and the pressure gradient is 15 MPa . The liquid in the microchannel is water ($\rho=1 \times 10^{-3} \text{ kg/m}^3$, $\nu=1 \times 10^{-6} \text{ m}^2/\text{s}$). The flow velocity is almost the same except a small part of flow near the channel wall. Due to the non-slip boundary condition, the velocity is zero on the channel wall, and increases to 90% of the maximum velocity when the flow is 240 nm away from the wall as shown in Fig. 5.5. That means the plane pressure wave assumption is applicable in most part of the channel. However, a thin layer near the channel has a relative low velocity. It

makes the acceleration of the interface to be affected by the velocity profile. When the gas in the center of the channel is moved with the velocity of u_{\max} , the gas close to the channel wall is almost static. Therefore, a thin layer of gas with the thickness of hundreds nanometer is attached to the channel wall.

5.1.3 Jet break up and instability

The deformation of the existing gas bubble is amplified by the Richtmyer-Meshkov instability, which arises when a shock wave interacts with an interface separating two different fluids. The basic mechanism for the amplification of perturbations at the interface is baroclinic vorticity generation resulting from the misalignment of the pressure gradient of the shock and the local density gradient across the interface [297]. Therefore, a thin layer of gas attached to the channel wall is pinched off from the main part of the gas bubble.

When surface tension changes the remained gas layer into a thin cylinder, it subsequently breaks up into small bubbles due to Rayleigh-Plateau instability. Figure 5.6 shows the cylindrical column which is comprised of the fluid of density ρ and bound by surface tension σ . The stability of the column is broken by random perturbations, which are resolved into sinusoidal components. When the effect of the surrounding fluid is neglected, the wavelength of the varicosity corresponding to the mode of maximum instability is found to be [246]

$$\lambda = 4.51 \times 2a, \quad (5.27)$$

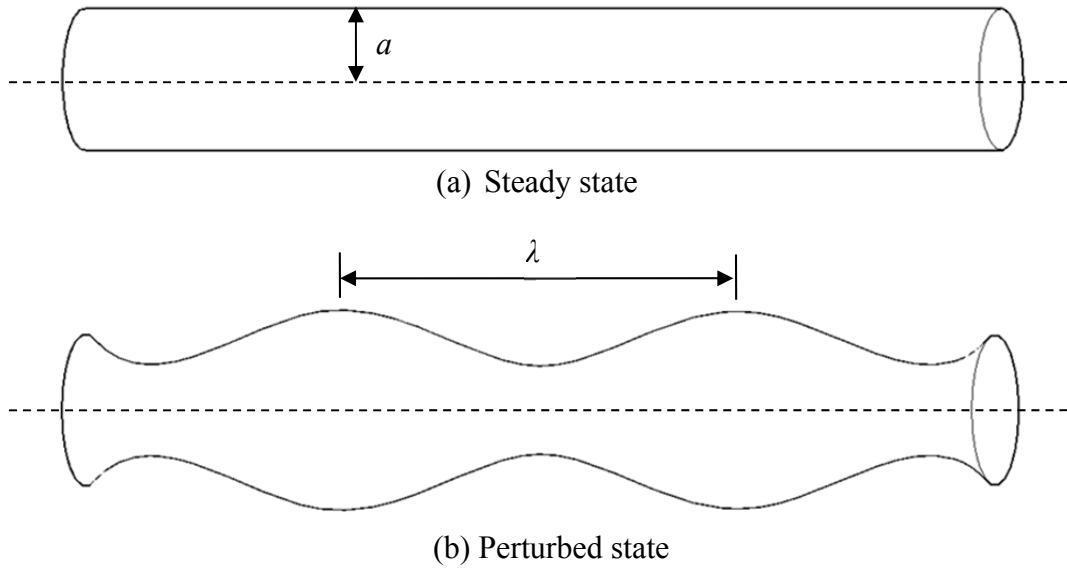


Figure 5.6: Schematics of the cylindrical column in (a) steady state and (b) perturbed state.

where a is the radius of the cylinder. However, the viscosity (μ) is not negligible in practical situations. The classical stability analysis of Tomotika [256] for a viscous cylinder jet predicts that the unstable mode with the largest growth rate corresponds to

$$\frac{2\pi a}{\lambda} = 0.47, \quad (5.28)$$

for $\mu_i/\mu_o=0.02$, assuming the cylinder is air ($\mu_i = 1.78 \times 10^{-5}$ Pa s) and surrounded by water ($\mu_o = 1 \times 10^{-3}$ Pa s). The maximum instability is given by

$$\lambda = 6.68 \times 2a. \quad (5.29)$$

The characteristic break up time scale can be estimate as [298]

$$t_{breakup} \approx \sqrt{\frac{\rho a^3}{\sigma}}, \quad (5.30)$$

where ρ is the density of the cylinder and σ is the surface tension. When $a = 1 \text{ } \mu\text{m}$, $t_{breakup}$ is 120 ns, which means that the breakup process is too fast to be recorded by the current high speed camera (exposure limitation is 370 ns).

5.2 Experimental results of microjet

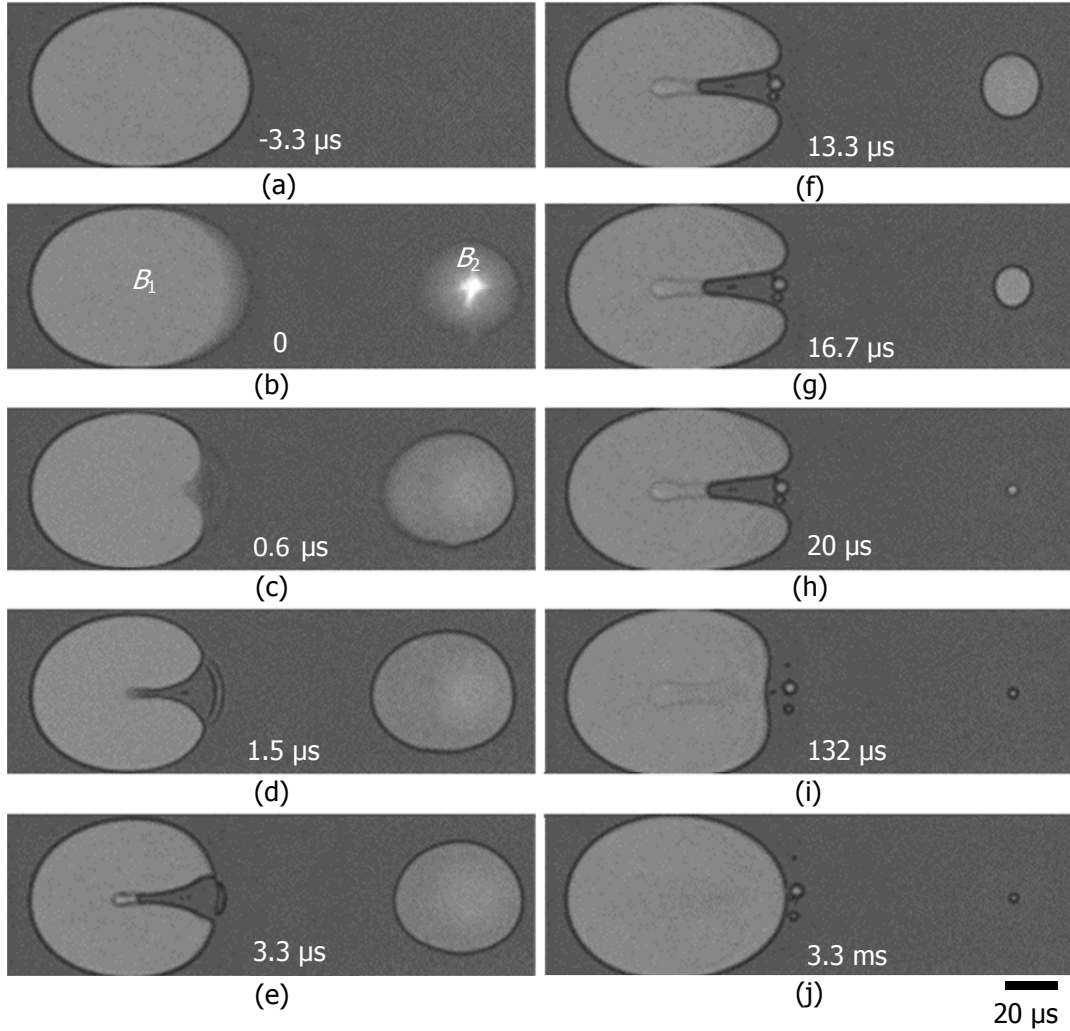


Figure 5.7: Sequential snapshots showing the interaction between a laser-induced cavitation bubble and a nearby gas bubble.

The microjet is generated in a microchannel with the height of $4\ \mu\text{m}$, and the width of $140\ \mu\text{m}$. The fabrication processes and experimental setup are the same as discussed in Chapter 4.

Figure 5.7 shows the dynamical evolution of an initially stationary bubble (B_1) perturbed by a nearby laser-induced bubble (B_2) at $E = 4.1 \mu\text{J}$ and $D = 85 \mu\text{m}$. The laser bubble reaches its maximum volume at $1.5 \mu\text{s}$ and collapses in $20 \mu\text{s}$. It expands towards the target bubble due to the easier displacement of the flow fields near a gas/liquid interface. This boundary can be regarded as the zero-inertia limit. Boundary on the opposite direction is far enough (i.e. 1 mm) for not perturbing the flow motion. The maximum volume of the bubble ($150 \times 10^3 \mu\text{m}^3$) near the gas/liquid interface is much larger than the single bubble expansion with the same energy ($\sim 2.5 \times 10^3 \mu\text{m}^3$) as discussed in chapter 4. At the same time as the laser bubble expansion, a strong pressure gradient causes the gas bubble to deform leftward as shown in Fig. 5.7 (c). An axial liquid jet is formed and starts to retract just after the laser bubble reaching its maximum volume as shown in Fig. 5.7 (d). During this two bubble interaction, a part of the gas bubble is pinched off from the main body (Fig. 5.7 (e)), and forms small bubbles in front of the jet (Fig. 5.7 f)). The jetting process, laser bubble revolution and shattered bubbles are discussed in details separately.

5.2.1 Jetting process

The whole jetting process is divided into three parts: flow focusing, jet penetration and retraction as shown in Fig. 5.8. When the laser bubble expands, a pressure wave is propagating towards the target bubble, and the flow is focused by the bubble surface as shown in Fig.5.8 (a)-(d). When the bubble surface becomes almost flat, the flow focusing leads the liquids to be converged to the axial of the

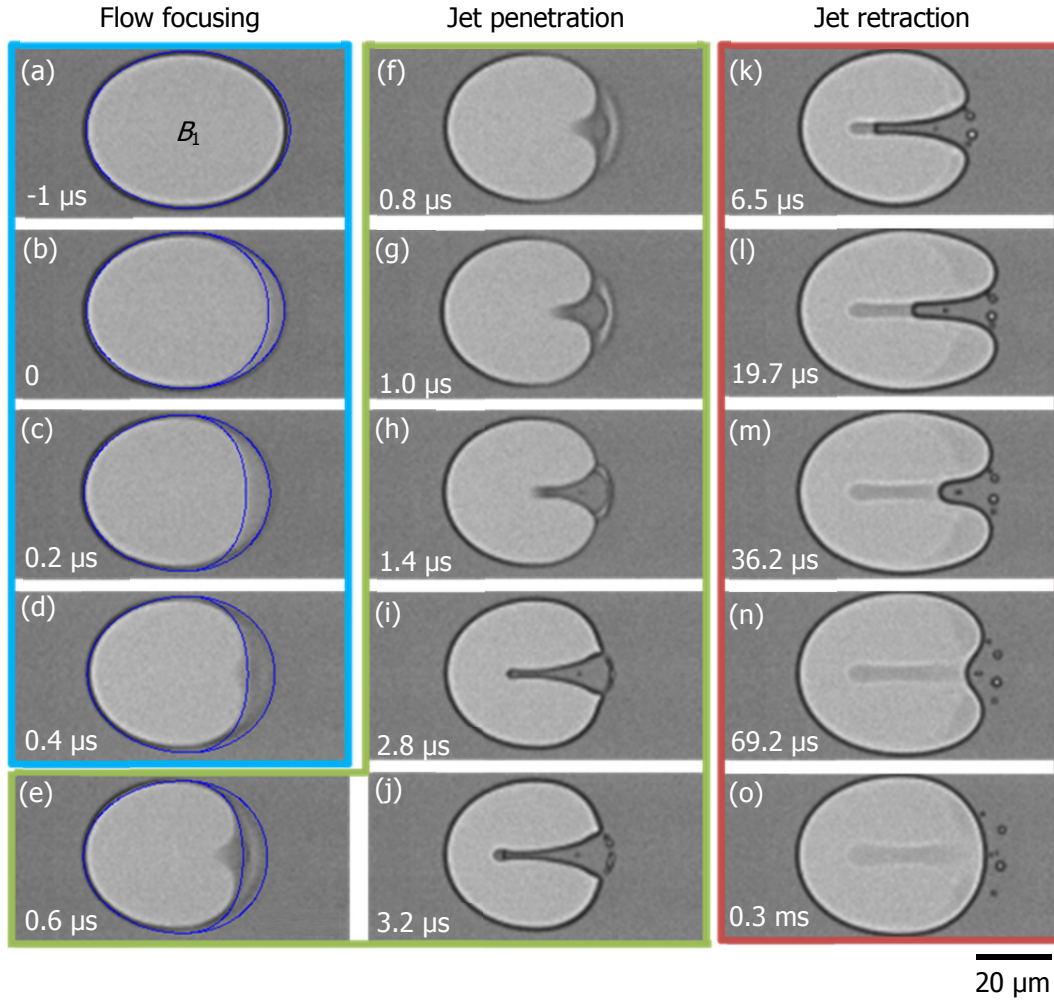


Figure 5.8: Sequential snapshots showing evolution of the target bubble when a cavitation bubble is generated nearby at $t = 0$.

bubble as shown in Fig.5.8 (e). The jet keeps penetrating into the target bubble and reaches its maximum length at $3.2 \mu s$ approximately (Fig. 5.8 (j)). Thereafter, the jet slowly retracts and the bubble returns into the elliptical shape as shown in Fig. 5.8 (k)-(o).

Figure 5.8 (a)-(e) show the simulated bubble shapes (blue lines), which are only considering the x-axis component of the liquid velocity (as described in Eq. (5.12)). In a thin channel, the fluid velocity in the center of the channel is larger

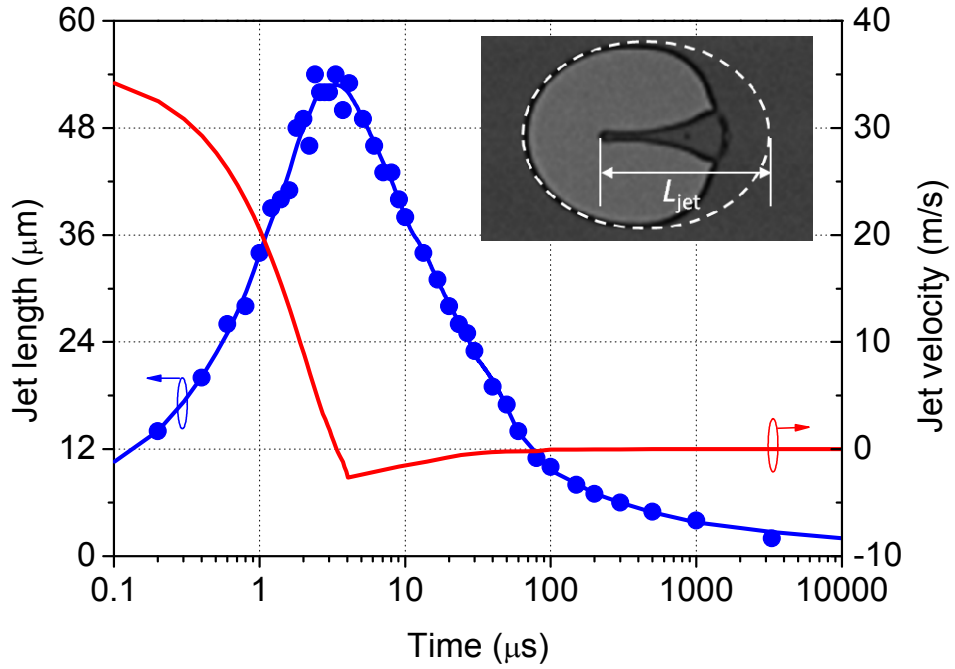


Figure 5.9: Evolution of the jet length (blue line) and jet velocity (red line). Inset is the definition of the parameter.

than that near the channel wall due to the high shear stress. It makes the bubble surface displacement to be different along z direction. Here, two curves are simulated at $z = 0$ and $z = h/2$, which are corresponding to the bubble surface deformation in the center of the channel and near the channel wall, respectively. The simulated result agrees well with the real bubble deformation in the initial $0.4 \mu\text{s}$. When the interface becomes almost flat, the tangential components of the flow focus on the center and form a jet with high velocity.

Figure 5.9 shows the temporal evolution of the jet velocity and jet length which is the distance between the original position of the bubble surface and the jet tip. The velocity acceleration is not observed in the experiments. That means the

flow focusing has not increased the velocity but just concentrated the liquid particles. The initial jet velocity depends on the pressure wave strength. The initial jet velocity is 35 m/s approximately as shown in Fig. 5.9. The relative high Reynolds number (~ 130) indicates the initial jet penetrating process is dominated by inertia. The thickness of the boundary layer gradually increases with decreasing flow velocity. From $\delta t \approx y^2 / \nu$ (δt is the boundary diffusion time, y is the thickness of boundary layer, the kinematic viscosity $\nu = 1 \times 10^{-6} \text{ m}^2/\text{s}$), the boundary layer is estimated to reach the center of the channel in the initial 2 μs . That means the viscosity and surface tension become important after 2 μs . When the jet reaches its maximum length around 3 μs , the surface tension begins to drive the jet to retract. The jet velocity increases to 2.5 m/s in 1 μs in the retracting process, The corresponding Capillary number is 0.03 and Weber number is 0.3. That means the jet retracting process is dominant by surface tension force. The retracting velocity is estimated as 2 m/s approximately by putting the experimental parameters into the Eq. (5.23). It demonstrates that the jet retraction mainly controlled by the surface tension and viscous force. Figure 5.9 shows the velocity slowly decreases after the first 1 μs , because the surface tension force gradually decreases when the jet tip becomes smooth and wider.

The strength of the jet impact is increased by increasing the energy or decreasing the distance between the two bubbles. The former increases the pressure and the velocity of the laser-induced flow front, and the total duration for the expansion stage of laser bubble. The latter increases the initial impact. Figure 5.10 demonstrates the transient stages at 3.3 μs with the same distance $D = 90 \pm 3 \mu\text{m}$, when the laser energy E is 1.7, 3.6, 5.4 and 6.5 μJ , respectively. When the energy is

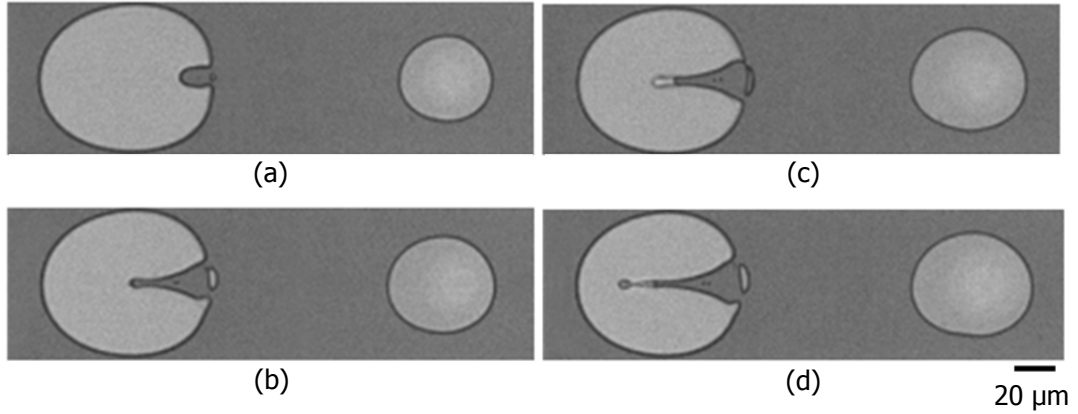


Figure 5.10: Photographs of the microjets with varied laser energies E : (a) $1.7 \mu\text{J}$, (b) $3.6 \mu\text{J}$, (c) $5.4 \mu\text{J}$ and (d) $6.5 \mu\text{J}$, when $D = 90 \pm 3 \mu\text{m}$ at $t = 3.3 \mu\text{s}$.

$1.7 \mu\text{J}$, a weak axial jet only forms a nipple on the right edge of the target bubble. The average penetration of the jet into the target bubble increases with the laser energy. The jet length increases from 25 to $64 \mu\text{m}$ when the energy is changed from 1.7 to $6.5 \mu\text{J}$. Figure 5.11 shows the transient stages at $3.3 \mu\text{s}$ with fixed laser energy $E = 6.0 \pm 0.4 \mu\text{J}$, when the distance D is 158 , 130 , 90 and $55 \mu\text{m}$, respectively. The results show that the jet penetration increases with the decreasing distance D . In addition, the jet impact is more vigorous at shorter distance as shown in Fig. 5.11 (a).

Figure 5.12 shows the jet velocity as a function of laser energy E for different distance D . The plotted jet velocity is the slope of jet length versus time curve in the first $1 \mu\text{s}$. It can be considered as the initial jet velocity U_{j0} . The jet velocity is increased with the laser energy, and the increase rate is higher with a shorter distance D . For instance, when the laser energy is increased from 3 to $6 \mu\text{J}$, the jet velocity is increased from 14 to 23 m/s at $D = 128 \mu\text{m}$, while from 72 to 115

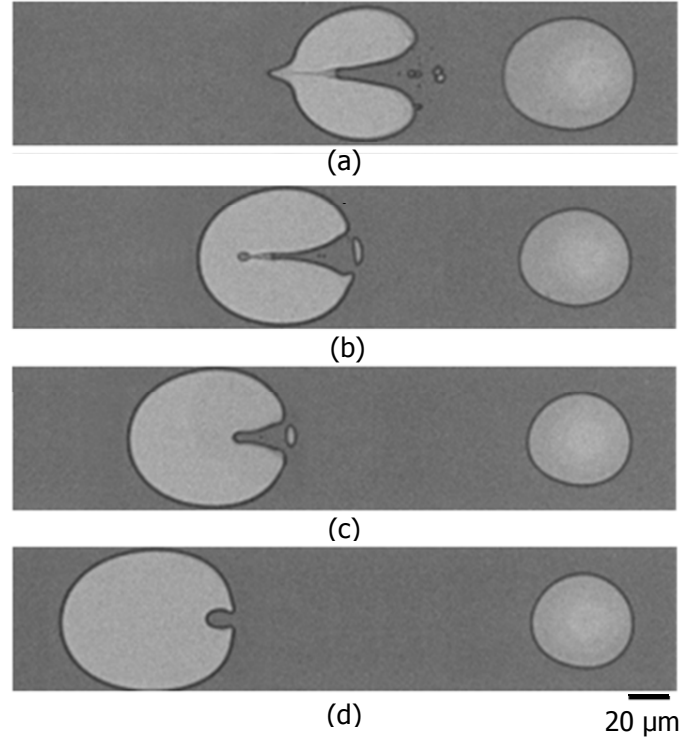


Figure 5.11: Photographs of the microjets with varied distances D : (a) 55 μm , (b) 90 μm , (c) 130 μm and (d) 158 μm , when $E = 6.0 \pm 0.4 \mu\text{J}$ at $t = 3.3 \mu\text{s}$.

m/s at $D = 32 \mu\text{m}$. The corresponding increase rates are 3 and 14 m/s· μJ , respectively.

As discussed previously, the jet penetrating velocity only depends on the pressure wave strength. Considering the Eq. (5.14), the dependency of the jet velocity on the energy can be expressed as

$$U_{j0} \approx f(D)(E - E_{th})^{\frac{1}{2}}. \quad (5.32)$$

The factor $f(D)$ embodies the dependence on the distance D . E_{th} is determined as 1 μJ from Fig. 5.12. The value of $f(D)$ for a certain distance D can be obtained from the fitting curve.

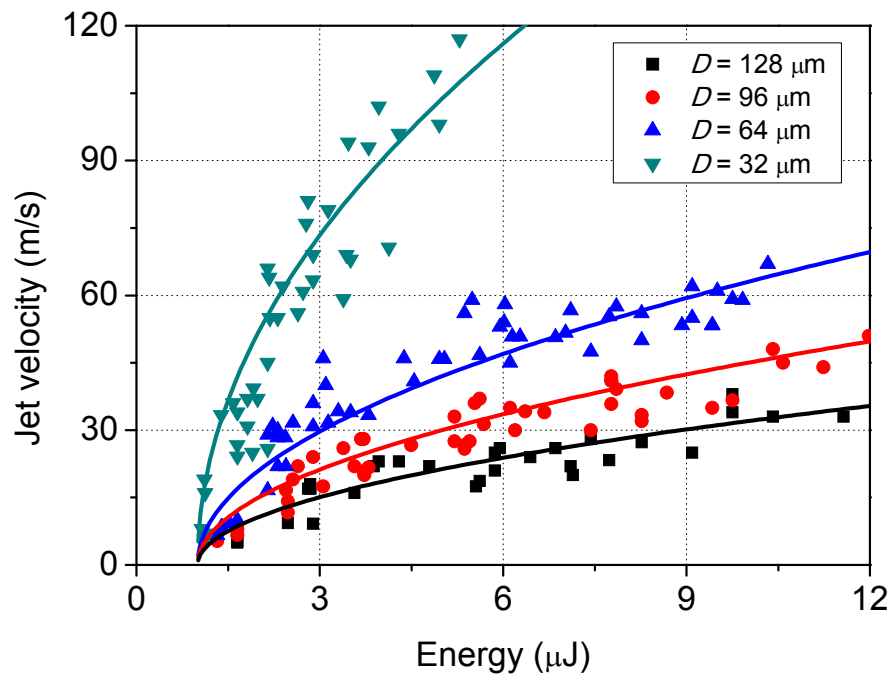


Figure 5.12: Jet velocity as a function of the laser energy with different distances.

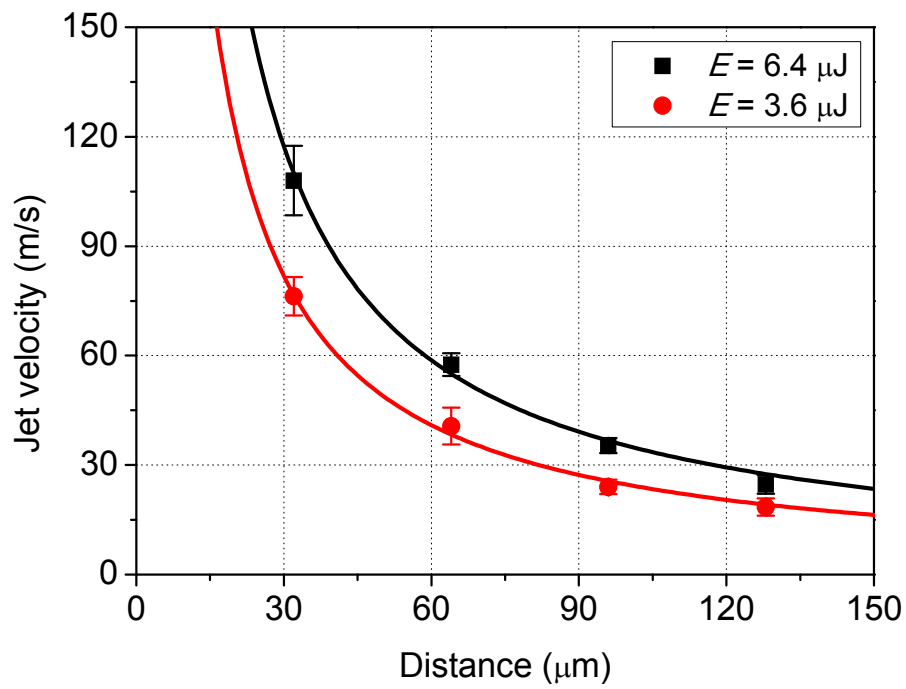


Figure 5.13: Jet velocity as a function of the distance with different laser energies.

Figure 5.13 shows that the jet velocity is inversely proportional to the distance under certain laser energy. When the distance is increased from 32 to 128 μm , the jet velocity is decreased from 76 to 18 m/s at $E = 3.6 \mu\text{J}$, and 108 to 25 m/s at $E = 6.4 \mu\text{J}$. The relationship between the jet velocity and the distance can be described as

$$U_{j0} \approx \frac{g(E)}{D} . \quad (5.33)$$

C_0 in Eq. (5.14) can be expressed as

$$C_0 \approx f_i D_i \approx \frac{g_i}{(E_i - E_{th})^{\frac{1}{2}}} . \quad (5.34)$$

A group of $f_i(D_i)$ and $g_i(E_i)$ are obtained from the fitting data in Fig. 5.12 and Fig. 5.13. Based on Eq (5.34), C_0 is calculated as $1.475 \pm 0.12 \text{ kg/s}$. Therefore, the jet can be reproducible and controllable by using the empirical equation, which can be described as

$$U_{j0} \approx 1.475 \frac{(E-1)^{\frac{1}{2}}}{D} . \quad (5.35)$$

5.2.2 Shattered bubbles

The most interesting part of our experiments is the shattered bubbles. This phenomenon is not reported in other bubble interactions in the bulk liquid or channel with larger diameter. Figure 5.13 demonstrates the typical consequence snapshots of the fragmentation of the front part of the target bubble with different

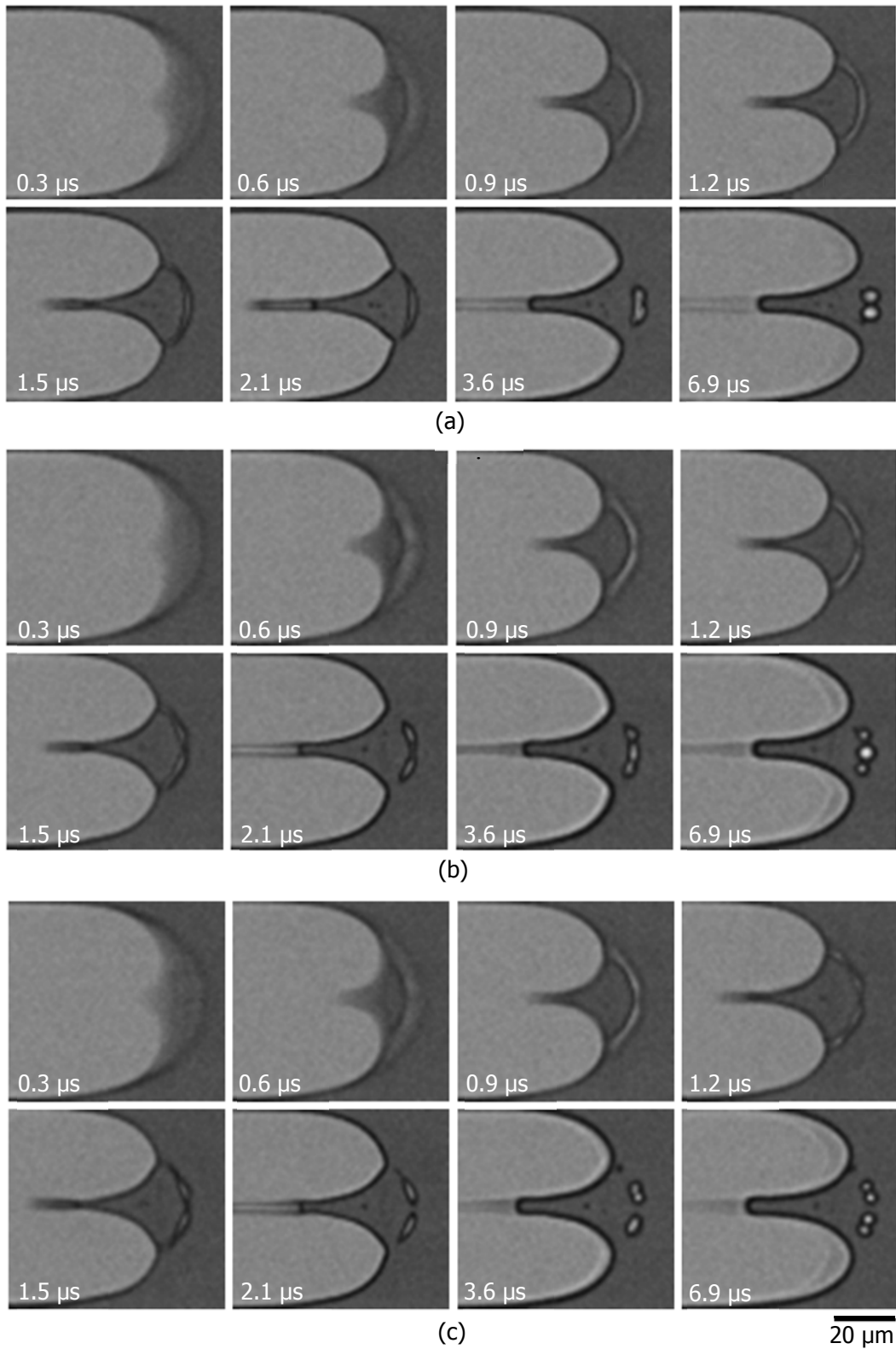


Figure 5.14: Typical sequence snapshots with (a) $E = 4.9 \pm 0.5 \mu\text{J}$, (b) $E = 6.0 \pm 0.5 \mu\text{J}$ and (c) $E = 7.1 \pm 0.5 \mu\text{J}$, when $D = 64 \pm 3 \mu\text{m}$.

laser energies. The beginnings are similar for the three consequences. However, when the laser energy is increased from 4.9 to 7.1 μJ , the number of shattered bubbles is increased from 2 to 4, as shown in Fig.5.14 (a) and (c). The pressure wave generated by the laser bubble pushes the target bubble surface towards its center. A thin layer of gas is attached to the channel wall due to the shear stress from the wall, as shown in the frame of 0.3 μs , Fig. 5.14. The thin layer is pinched off from the target bubble and constricted into curved gas cylinder from 0.6 to 1.2 μs . At about 1.5 μs , tiny perturbations caused instability waves appear. With further evolution of the instability, the neck between each two segments breaks up and the gas cylinder is shattered into small bubbles as shown in the frame of 2.1 to 6.9 μs . In this process, classical hydrodynamic instability caused breakup competes with a shrinkage mechanism in order to reduce the surface energy. The breakup of the curved cylindrical gas does not like a falling stream which can be considered as infinite long [246], or a liquid toroid whose wavelength of the instability must be commensurate with the tube's circumference [24, 25]. The curved gas cylinder is affected by the connecting points with the main part of B_1 . From the frame of 1.2 μs in Fig. 14 (c), it is seen that the cylindrical gas is separated into four segments. However, the segment number reduces to two due to the boundary condition affected by the ends of the curved cylinder. Although the wavelength of instability depends on the radius of the cylindrical, the wavelength can be changed resulting from environmental perturbation (i.e. nozzle of jets) [252].

It is astonishing that the two segments finally are divided into four small bubbles as shown in Fig. 5.14 (c). A reasonable explanation is that there are two layers of remaining gas attached to the top and bottom channel wall respectively

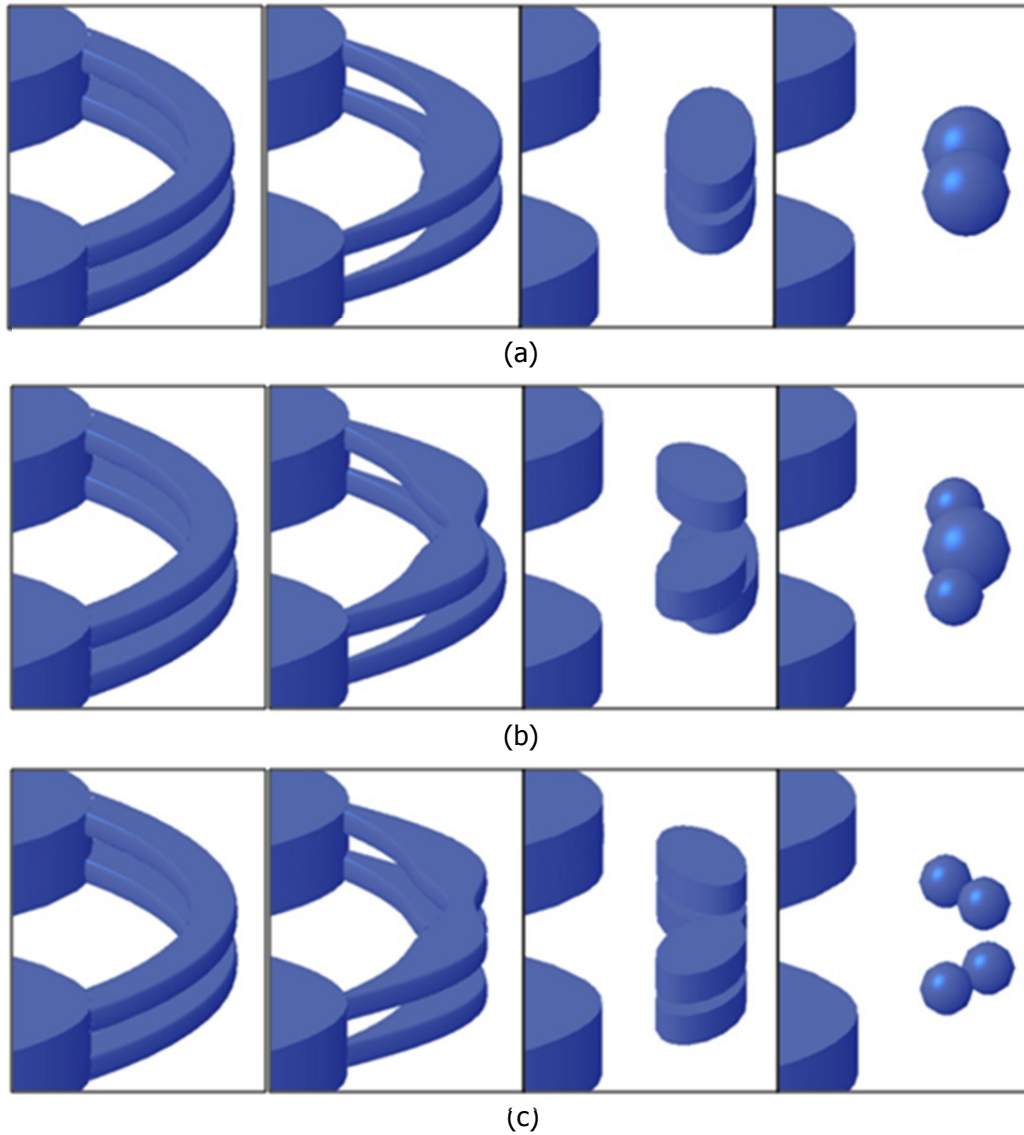


Figure 5.15: Sketch for breaking up of the gas cylinders with different numbers of shattered bubble.

and each layer is divided into two bubbles as shown in the frame of $3.6 \mu\text{s}$, Fig. 5.14 (c). If the two layers do not break up, each cylinder shrinks into one bubble, as depicted in Fig. 5.15 (a), and the final number of the shattered bubbles should be two. If one layer of gas breaks into two bubbles while another layer turn into one bubble, the final bubble number is three as shown in Fig. 5.15 (b). Based on the

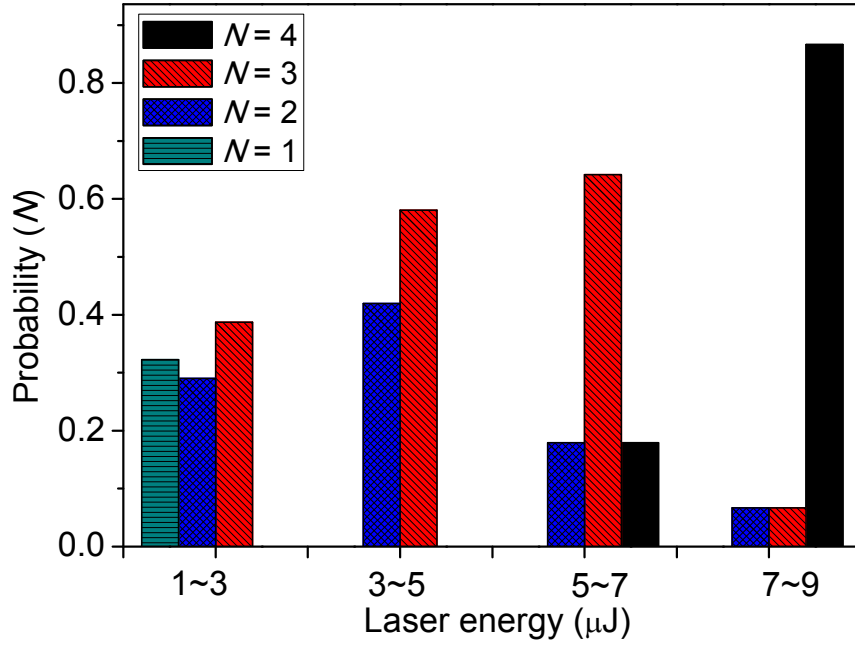


Figure 5.16: Histogram of the number of shattered bubbles for different energies with $D = 64 \pm 3 \mu\text{m}$.

double layer assumption, the thickness of each gas layer can be estimated by assuming the volume of the shattered bubbles to be the same as the ruptured gas. The average thickness of the gas layer is 200 nm at 0.3 μs in Fig.14. It agrees with the measured value by taking advantage of the relationship between the thickness of the gas layer and the gray value in the figures.

In Fig. 5.14, the number of the shattered bubbles is two, three and four, and the corresponding average laser energy is 4.9, 6 and 7.1 μJ , respectively. It illustrates that the fragmentation number of the shattered bubbles is associated with the laser energy. For lower laser energy, the shrinkage of the cylinder width is slow and its length keeps shortened as the connecting points between the main part and

the cylinder are pushed to the axis. For such short cylinder, only the shrinkage of the cylinder causes the subsequent shape transformation. Figure 5.16 depicts the statistical results for the fragmentation number of the shattered bubbles with varied laser energy and fixed distance $D = 64 \text{ } \mu\text{m}$. Those data are collected from 250 groups of experiments. When the laser energy is lower than $1 \text{ } \mu\text{J}$, the shattered bubble is seldom observed. Even if one bubble is remained after the impact, it is quite small and diffuses into the liquid quickly. With the increasing energy, the probability for a higher number of shattered bubbles increases. In most case, the pinched-off part will be shattered into 2 or 3 bubbles. The probability is as high as 91% when the laser energy is between 3 to $7 \text{ } \mu\text{J}$. However, the appearance of 4 bubbles is dominant ($P = 87\%$) as the laser energy is higher than $7 \text{ } \mu\text{J}$. Since the surface tension takes over after the jet reaches its maximum length, the connecting points between the main part of gas bubble and the thin thread are pushed towards the axis. At the same time, the cylinder gradually becomes shorter. With higher laser energy, the jetting process is longer and the thread is longer when the break up happens. That makes the thread to be broken into more bubbles when the laser energy is higher.

The classical stability analysis of Tomotika for a viscous cylinder jet predicts that the unstable mode with the largest growth rate corresponds to $(2\pi/\lambda)a = 0.47$ for $\mu_i/\mu_o=0.02$, ($\mu_i = 1.78 \times 10^{-5} \text{ Pa s}$, $\mu_o = 0.89 \times 10^{-3} \text{ Pa s}$) [256]. The radius of the gas cylinder a is about $1 \text{ } \mu\text{m}$, the estimated wavelength λ is $13 \text{ } \mu\text{m}$. The measured wavelength is $11 \text{ } \mu\text{m}$. In these experiments, the thread length is no longer than $42 \text{ } \mu\text{m}$. Therefore, it is hard to observe shattered pattern with more than 4 bubbles.

5.3 Experimental results of nanojet

5.3.1 Jetting process

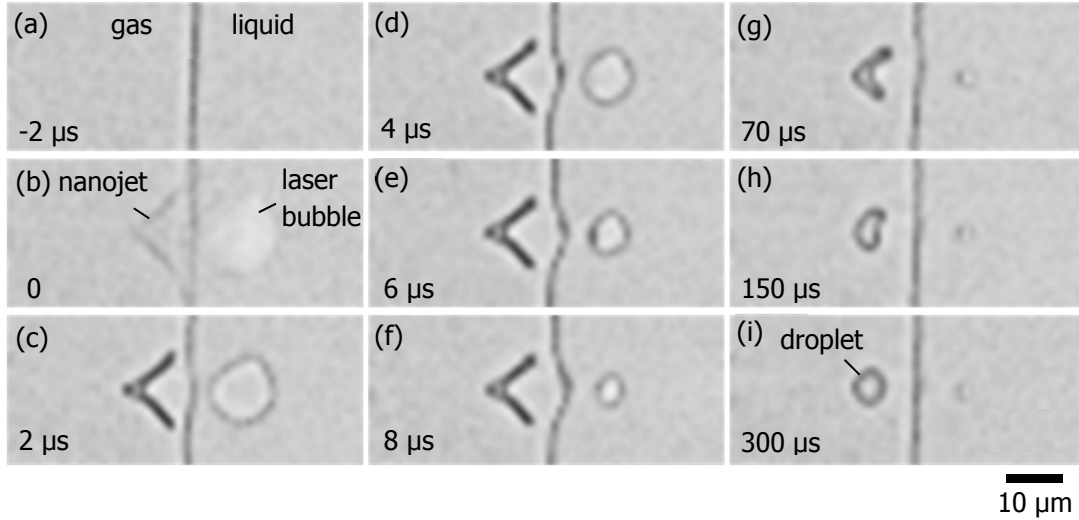


Figure 5.17: Photographs of nanojet in a nanochannel ($h = 550$ nm).

Recent molecular dynamics simulations report that even stable nanometer sized gas bubbles jet when they are impacted by a sufficiently strong shock wave [196]. In confined nanochannels, it is expected that for timescales shorter than the vortex diffusion time of approximately $t < h^2/\nu$, inertial dominated dynamics prevails, which is necessary for flow focusing. Thus, fast jetting may occur within $0.3 \mu\text{s}$ for $h = 550$ nm and $\nu = 10^{-6} \text{ m}^2\text{s}^{-1}$. Here, the pressure transient from the explosive vaporization induced by the laser pulse is used to generate nanojet. The laser is focused very close to a gas/liquid interface in the nanochannel. Figure 5.17 shows the liquid jetting into the gas phase for a stand-off distance of $10 \mu\text{m}$. At $t = 0$, the gas/liquid interface is rapidly accelerated towards the left (within the 370 ns exposure time of the camera), which gives a lower estimate of the jet velocity of 30

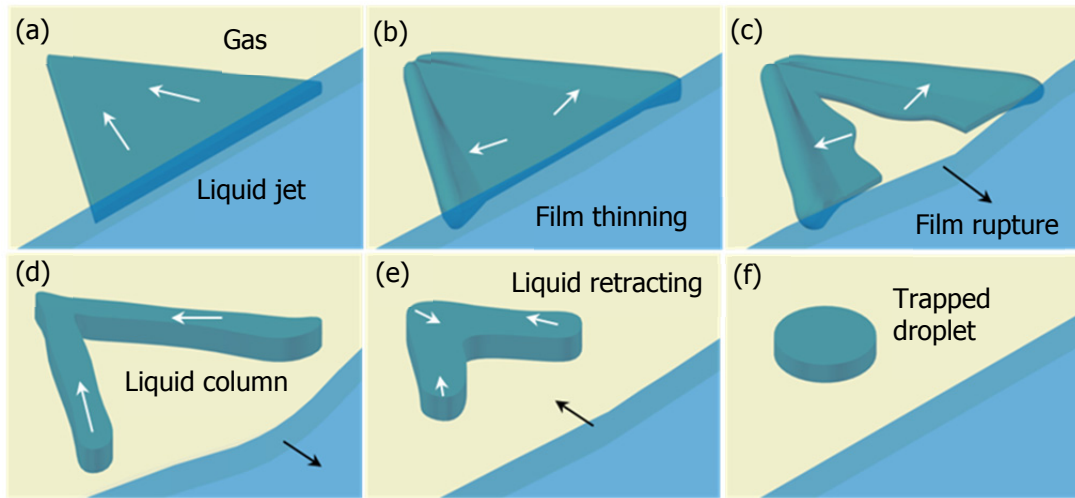


Figure 5.18: Sketches for the typical evolution of the thin liquid film generated in the nanojetting process.

m/s. A triangular shape on the gas side is formed at $t = 2 \mu\text{s}$ as shown in Fig. 5.17 (c). Two sides of the triangular are formed by two connected liquid columns. The dynamics after $t = 2 \mu\text{s}$ is relatively slow. The gas/liquid interface moves outwards due to the collapse of the nanobubble, as shown in Fig. 5.17 (c)-(f). As a result, the liquid columns lost their connection with the outside pool and contract into a droplet as shown in Fig. 5.17 (i).

These “stationary” liquid columns are formed from the breakup of the liquid nanojet. Figure 5.18 presents a sketch of the dynamics leading to these structures: First, a thin triangular liquid jet sheet is formed (Fig. 5.18 (a)). The extensional flow, vortices, and/or capillary forces may cause a thinning of the film, which eventually ruptures and leaves two liquid columns on its edges as shown in Fig. 5.18 (b)-(d). This process happens within 370 ns, and is not resolved due to the limitation of the imaging system. Surface tension further minimizes the surface area,

thus the liquid columns slowly retracts (Fig. 5.18 (e)). Finally, the liquid columns forms a droplet trapped in the gas phase (Fig. 5.18 (f)).

In Fig. 5.17 (i), the droplet volume is estimated as 18 femtoliter by using the measured diameter and the channel height of 550 nm. Assuming the conservation of mass and comparing the jet area in Fig. 5.17 (b) and the droplet volume in Fig. 5.17 (i), a homogeneous jet with thickness of 160 ± 30 nm is estimated, which is considerably thinner than the 550-nm thick confinement. Although the nanojet is much milder due to the viscous effect, it offers more precise control over the jetting location with high speed velocity.

The nanojet velocity is also sensitive to the laser energy and the distance. Figure 5.19 shows the nanojet velocity as a function of the distances between the laser focus and bubble surface when the laser energy is 6 μJ . The power of the nanojet attenuates faster with increasing distance. The jet velocity decreases from 32 to 3 m/s while the distance is only reduced by 6 μm as shown in Fig. 5.19. Figure 5.20 shows the nanojet velocity as a function of laser energy when D is 9 and 13 μm . The experimental results indicate that the laser power has a much greater effect when the distance is shorter. When the laser energy changes from 7.5 μJ to 11.5 μJ , the jet velocity is increased by 140% for $D = 9$ μm , while by 40% for $D = 13$ μm . No obvious effect can be observed when the distance is increased to 20 μm .

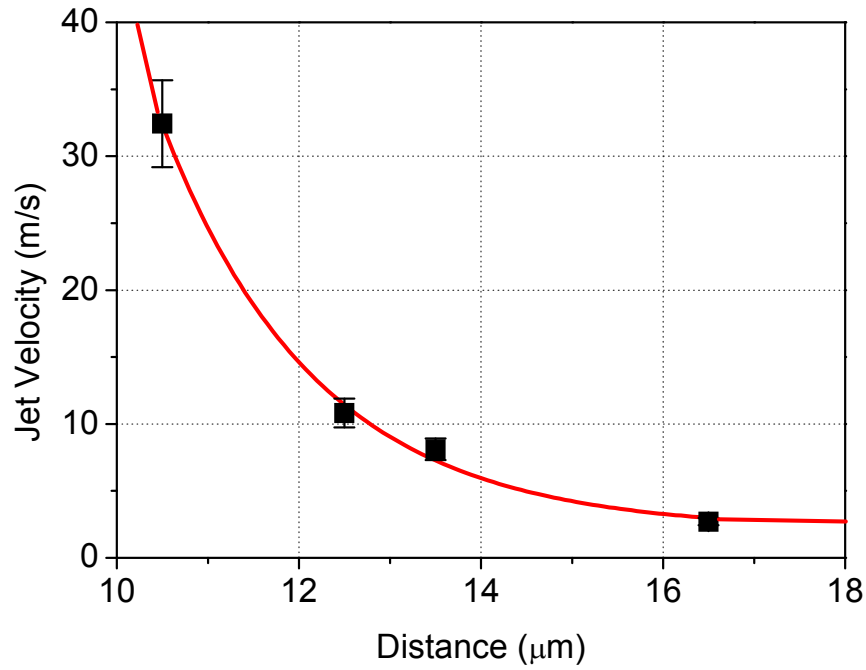


Figure 5.19: Nanojet velocity as a function of the distance between the laser focus and bubble surface when the laser energy is 6 μJ .

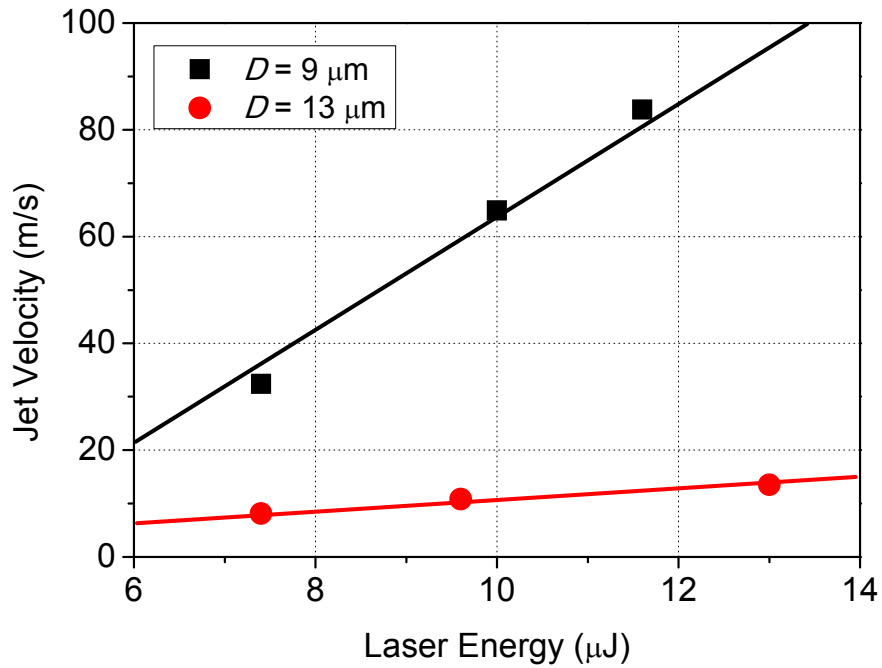


Figure 5.20: Nanojet velocity as a function of the laser energy with different distances between the laser focus and bubble surface

5.3.2 Breaking pattern and surface instability

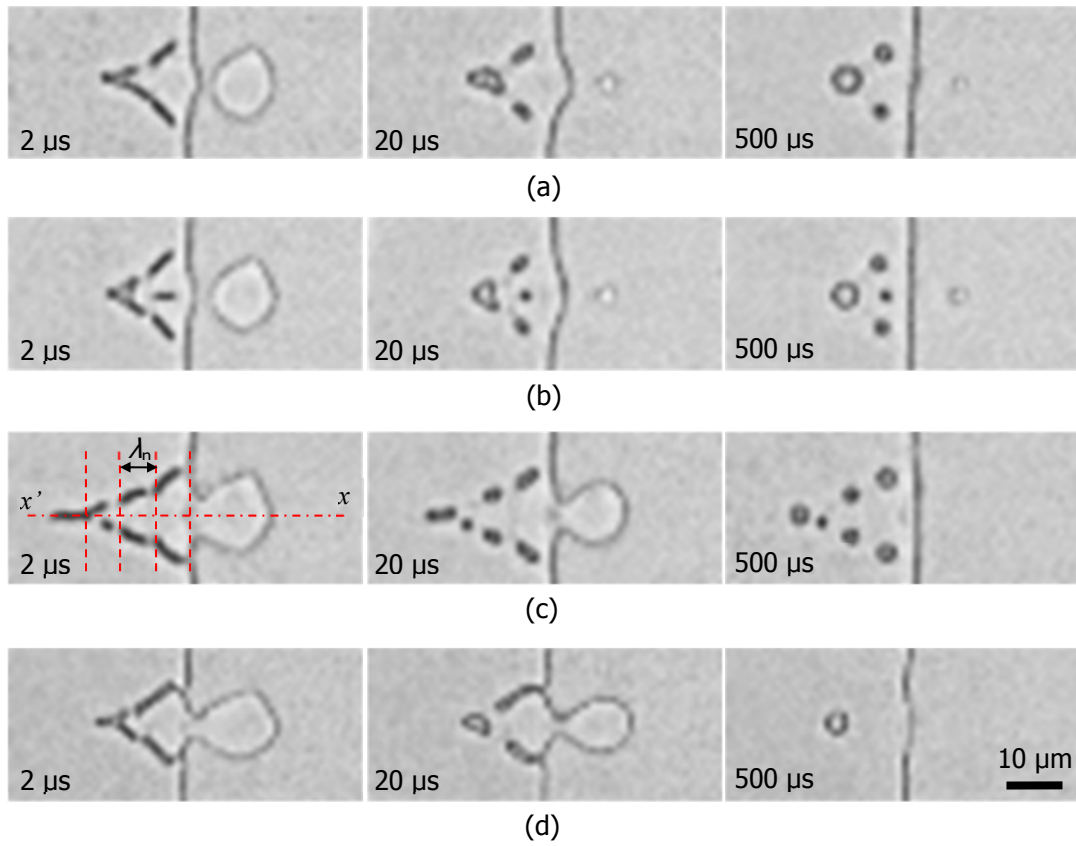


Figure 5.21: Photographs showing different breakup patterns of the nanojets.

In the previous section, the thin liquid jet is trapped in the gas phase and contracts into a droplet. Moreover, the thinning of the liquid film can lead to more complex breakup scenario. Figure 5.21 (a) shows the liquid columns break up and contract into three droplets. In some case, a satellite droplet in the centre of the film is formed as shown in Fig. 5.21 (b). It is likely that the larger opening angle of the triangular jet affects the film drainage, resulting in four distinct and symmetrically placed droplets. When the jet is longer, the liquid columns will break into more droplets.

Figure 5.21 (c) demonstrates a clearer case to illustrate the breakup of the nanojet due to instability. The thin film breaking pattern is symmetrical along the xx' axis. However, the droplet size decreases towards the jet penetrating direction as shown in the 3rd frame of Fig. 5.21 (c). These droplets are developed from liquid plugs on the contour of the original thin liquid film. It is interesting to find that the plugs can be divided into four parts, and the horizontal distance between each breaking position is the same, i.e. λ_n . In addition, the curves of the plugs are not continuous. From the current evidence, it is reasonable to deduce that the drainage is followed by the breakup of the thin film.

As a result of a shear instability properties with the surrounding medium, a thin liquid sheet destabilizes when the Weber number $We_h = \rho U_0^2 h / \sigma$ is larger than 2 [299]. From the previous section, the thickness of the liquid sheet h is estimated as 200 nm, and the jet velocity U_0 is 86 m/s (supposing the jet penetrating time is 300 ns). Thus, the Weber number is approximately 20. This condition implies that the liquid sheet is unstable. By balancing the destabilizing pressure and the curvature restoration constraint due to capillarity, the wavelength can be expressed as

$$\lambda \sim \frac{\sigma}{\rho_a U_0^2}, \quad (5.35)$$

where ρ_a is the density of the surrounding gas. The measured wavelength λ_n is 6.5 μm approximately as shown in the first frame of Fig. 5.21 (c). From Eq. (5.35), the jet velocity should be 96 m/s. This value confirms our hypothesis that the fast

jetting occurs when $t < 300$ ns. The sheet disintegration happens when the amplitude of the undulation keeps increasing. It breaks at the troughs.

At the same time, the rim of the liquid sheet is recessing due to the Laplace-Young force that is inversely proportional to the radius of curvature of the rim ($\sim h/2$). Then the rim agglomerates liquid during its recession. Consequently, the films that feed the rims drain and the rims progressively contracts into liquid plugs. The whole process is finished within 2 μ s. Then, it takes approximately 200 μ s for the surface tension to further modify the liquid plugs into spherical shape droplets.

In Figure 5.21 (a)-(c), the liquid sheet is immediately cut off from the main part of the liquid by the gas/liquid interface. However, in some cases, the liquid columns are always connected with the liquid pool. Thus, the connected liquid columns would recess into the main parts and left one droplets in the gas phase as shown in Fig. 5.21 (d).

5.3.3 “Soap bubble” in nanochannels

A soap bubble is a thin film of water enclosing air that forms a hollow sphere. The film usually consists of a thin sheet of water being sandwiched between two layers of soap molecules. One end of each soap molecule is hydrophilic, and another is hydrophobic. Liquid films can also be produced from highly viscous liquids (e.g. silicone oil, molten glass) in the absence of surfactant, which are called “bare films” [300]. This section presents air bubbles collected in the gas phase

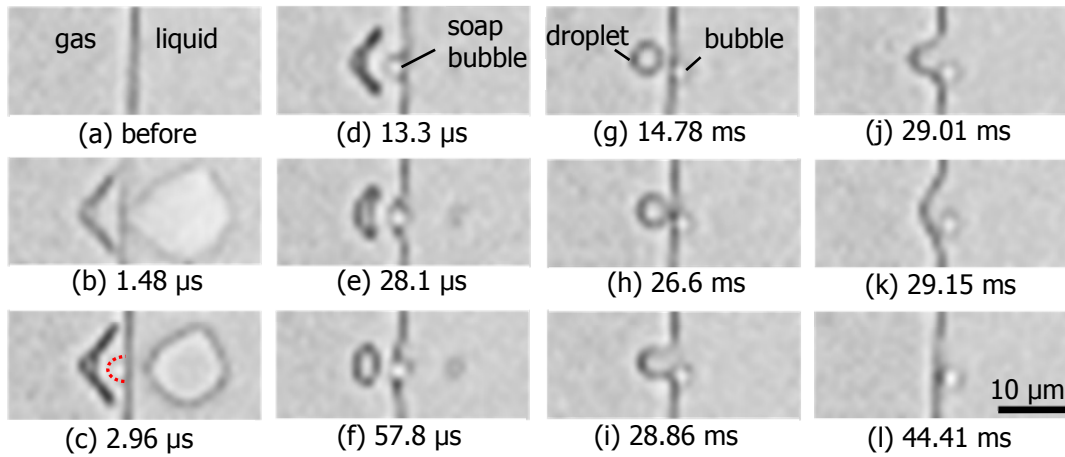


Figure 5.22: Photographs showing a soap bubble formed in the gas phase accompanied with the nanojet. Dot line highlights the thin liquid layer that forms the soap bubble.

during the jetting in a nanochannel. The liquid film separating the bubble from the bulk air is not protected by a surfactant and with low viscosity coefficient.

Figure 5.22 shows a typical case for the “soap bubble” generated in a 550-nm nanochannel. The jetting process is similar to the one analyzed in section 5.4.1, which also results in a trapped droplet in the gas phase. However, there is a thin layer of liquid, which is trapped near the interface between gas and liquid as marked in dot line in Fig. 5.22 (c). This thin layer is formed due to the instable drainage of the jetting film. The liquid layer connects with the outer pool, and a small quantity of gas is enclosed by the liquids. Hence, a “soap bubble” is attached to the gas/liquid interface as shown in Fig. 5.22 (d). The surface tension pushes the bubble into the pool before the bubble wall breaks as shown in Fig.5.22 (e)-(g). Not as the gas bubble, when the droplet moves towards the interface, the gas layer between the droplet and the bulk liquid becomes thinner and finally breaks up as shown in Fig.

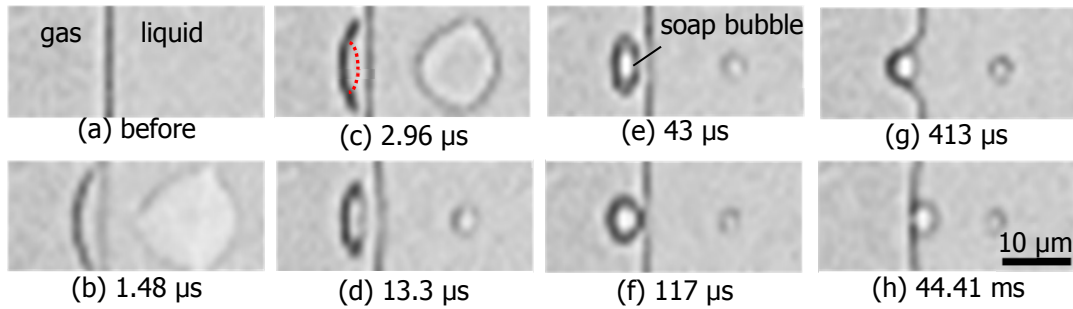


Figure 5.23: Photographs showing a soap bubble formed with thick wall accompanied with the nanojet. Dot line highlights the thin liquid layer that is critical for forming the soap bubble.

5.22 (h)-(j). The different behavior near the interface can be used to identify the trapped matter as gas or liquid (i.e. bubble or droplet). The bubble is attached to the interface until it slowly collapses due to mass diffusion as shown in Fig. 5.22 (i).

Sometimes the thin liquid layer does not connect with the outer pool as shown in Fig. 5.23 (c). The thin layer connects with the trapped liquid column, and a certain volume of gas is enclosed by the liquids. In this closed film, the fluid will redistribute to minimize the surface area (Fig. 5.23 (c)-(e)). Hence, a symmetric cylinder bubble is eventually formed as shown in Fig. 5.23 (e). Because the liquid that constitutes the bubble wall is more than that in the previously discussed case, the bubble wall is much thicker. When the “thick soap bubble” touches the gas/liquid interface, the liquid wall integrates into the pool as shown in Fig. 5.23 (f)-(g). Consequently, the bubble is released and transported from the gas phase to the liquid phase as shown in Fig. 5.23 (h).

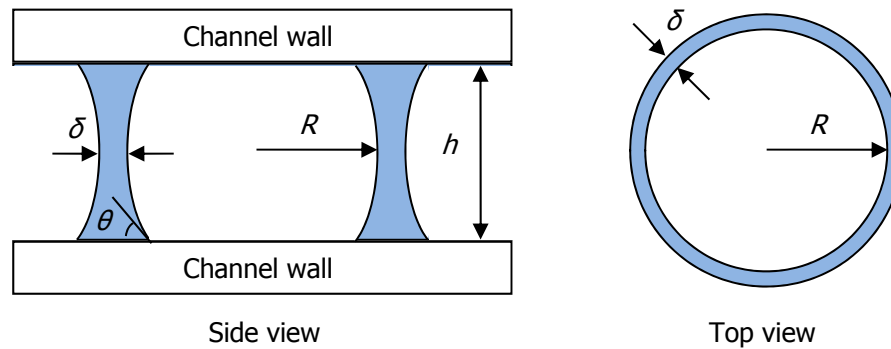


Figure 5.24: Schematics of the soap bubble in a nanochannel.

Figure 5.24 shows the schematic of a soap bubble in the nanochannel. In the experiments, the thickness of the bubble wall (δ) is $0.5\sim 2\text{ }\mu\text{m}$ approximately, the radius of the soap bubble (R) is changed from 2 to $5\text{ }\mu\text{m}$. The longevity of a soap bubble is limited by the rupture of the thin layer of water which constitutes its surface. For a traditional soap bubble, the soapy film is very thin, i.e. δ is comparable with the visible light wavelength. The rupture of the film could be caused by the gravity, evaporation or dirt. In the nanochannel, the gravity and evaporation can be ignored. When the bubble reaches its minimal surface, the pressure is equal inside and outside the bubble. That makes the bubble in a very stable state. The only problem is that the bubble is closed to the gas/liquid interface. The bubble gradually migrates towards the interface due to Bjerknes force. When the liquid bubble wall touches the interface, the pressure balance of the bubble surface is broken. Although the liquid wall of the bubble is ruptured, the gas bubble is still surrounded by liquid. As a result, it is changed from a “soap bubble” into a gas bubble immersed in liquid.

The constricted geometry of the nanochannel offers an opportunity to study the “soap bubble” constituted by bare wall and low viscosity liquid. However, the mechanism of the formation of the critical thin liquid layer is not well understood. More work will be done on this part in the future.

5.5 Summary

This chapter focuses on the theoretical analysis and experiments of jets in the micro/nanochannel. The jet is generated when a laser-induced cavitation bubble is formed near another gas bubble. The experiments are done in channels with heights of several micrometer and hundreds of nanometer. In a microchannel, the jetting process is sufficiently long to obtain a thorough analysis. An empirical equation is derived to describe the dependence of the jet velocity on the laser energy and the distance between the two bubbles. Moreover, the instability induced shattered bubbles are statistically analyzed. They are formed from the thin gas layers, which are ruptured from the gas bubble due to the shear stress. In a nanochannel, the fast jets are obtained within hundreds of nanoseconds. The nanojet is in the shape of a thin sheet, which has the thickness of 200 nm approximately. The breakup patterns of the thin liquid sheet are discussed. In addition, “soap bubbles” are generated during the jetting process.

The innovation of the study on jets during two bubble interaction is summarized as follow,

- e) Jets in a confined channel is studied with the high speed camera and digital trigger controller, which make the time step between each frame as short as 0.2 μ s. Therefore, the jetting process can be studied in details.
- f) Pinch-off of microbubbles from the accelerated bubble wall is observed. This new phenomenon is not reported before. It calls attention to the fluidic instability in a confined geometry.

- g) This is the first effort to experimentally illustrate the nanojets. It is demonstrated that inertia dominated dynamics is still possible for sufficient short times. Fast liquid jets with a thickness of 160 nm can be observed within 300 ns following the cavitation event.
- h) A “soap bubble” accompanied with the nanojet is demonstrated. The bubble is constituted by a layer of low viscosity liquid without surfactant. The confined channel keeps the bubble wall in the stable state, which makes the surfactant to be not necessary for the formation of a soap bubble in the nanochannel.

CHAPTER 6

CONCLUSIONS

6.1 Conclusions

Different optofluidic devices which can be integrated on the lab-on-a-chip and micro/nanofluidic systems have been theoretically and experimentally investigated, i.e. optofluidic prism, laser-induced micro/nanobubble and micro/nano liquid jets. Various aspects, including theoretical studies, system designs, fabrication technologies and experimental characterizations have been presented. The contents cover mainly the innovation of on-chip optical devices constructed by fluids with high degrees of tunability, and exploration of the optical manipulation on fluidic flows through the laser-induced cavitation. The major conclusions drawn are listed here.

The optofluidic prism is studied theoretically, fabricated and experimented. A simple theoretical model has been used to predict the apex angle of the prism, the deviation angle and the position of the output light beam. The tunability of the optofluidic prism has been experimentally proved. In addition, the dispersion of light with different wavelengths has been demonstrated. The experiment results also illustrate the possibility to use the optofluidic prism as an on-chip refractometer.

- (i) This is the first effort demonstrated to design a prism with two flows in a microfluidic chip. This apex angle of the prism and the deviation angle of the output light beam can be tuned continuously with a larger variation range than the previous methods. The apex angle of the prism was tuned from 75° to 135° . The deviation angle of the output light beam can be tuned by the prism from -13.5° to 22° .
- (ii) One of the new features of this optofluidic prism is its capability to transform from symmetric to asymmetric prism with the assistance of a third flow. Parallel light beam scanning is achieved with a constant deviation angle of 10° and tuning range of $60\text{ }\mu\text{m}$ using the asymmetric prism. The maximum intensity obtained by the asymmetric prism was increased by 65.7% compared to that of the symmetric prism.
- (iii) Light dispersion is experimentally demonstrated using 488-nm and 633-nm laser beams. The two laser beams become distinguishable with a deviation angle difference of 2.5° when the apex angle of the prism reaches 116° .
- (iv) The optofluidic prism is used to measure the refractive index of small quantity of liquid by detecting the output beam position. Based on our experimental condition, a sensitivity of 2×10^{-4} RIU/pixel is estimated.

Single micro/nanobubble created by focusing a pulsed laser into a micro/nanochannel filled with a light-absorbing liquid is studied theoretically and experimentally. A viscous Rayleigh-Plesset-type model of a cylindrical cavitation bubble is proposed. Glass chip fabrication technology is developed for generating

the micro/nanobubbles. The bubble dynamics is examined with different channel heights, boundary condition and surface hydrophobicities.

- (i) This is the first effort to derive a theoretical model for describing the dynamics of a cylindered cavitation nanobubble. This model considers the channel height as a critical factor, and including the effects of the surface tension and viscosity. Therefore, it is applicable for both microchannel and nanochannel, overcoming the shortages of other models which diverge from the experimental data when the channel dimension decreases.
- (ii) Different boundary conditions are experimentally realized on the microbubbles. These experiments not only verify the applicability of the theoretical model for the 1D confined microbubble, but also demonstrates the bubble behavior under 2D confinement without/with an elastic surface nearby.
- (iii) The nanofluidic dynamics is approached by using an extended nanochannel, which has only one dimension in the nanometer scale, i.e. hundreds nanometer height. It lowers the request for the fabrication techniques. In addition, the cavitation bubble created in the extended nanochannel reaches lateral extension of several micrometers that is sufficiently large to observe with standard high-speed photography. Previous studies on nanobubbles seldom use this kind of direct observation methods.

Micro/nanojets generated during two bubble interaction are studied theoretically and experimentally. The whole process of the microjet is demonstrated

and discussed into separated phases. The jet velocity is discussed based on its dependence on the laser energy and distance between the two bubbles. The fast nanojets are obtained in the shape of a thin sheet within hundreds of nanoseconds. New phenomena with the rupture of the thin liquid sheet are experimentally presented and discussed with fluidic instabilities.

- (i) Jets in a confined channel is studied with the high speed camera and digital trigger controller, which make the time step between each frame as short as 0.2 μs . Therefore the jetting process can be studied in details.
- (ii) Pinch-off of microbubbles from the accelerated bubble wall is observed. This new phenomenon is not reported before. It calls attention to the fluidic instability in a confined geometry.
- (iii) This is the first effort to experimentally illustrate the nanojets. It is demonstrated that inertia dominated dynamics is still possible for sufficiently short times. Fast liquid jets with a thickness of 160 nm can be observed within 300 ns following the cavitation event.
- (iv) A “soap bubble” accompanied with the nanojet is demonstrated. The bubble is constituted by a layer of low viscosity liquid without surfactant. The confined channel keeps the bubble wall in the stable status, which makes the surfactant unnecessary for the formation of a soap bubble in the nanochannel.

Optofluidic technology holds promise for increasing portability and sensitivity of the lab-on-a-chip systems, and offering tunable optical devices to

improve their robustness, flexibility and operator-independence in a variety of applications. Controlling optofluidics with light is the requirement for realizing the all-optical system. This thesis thoroughly studied the optofluidic components from the fundamental theory to engineering applications, aims to innovate and gain a new insight into the optofluidic technology. In addition, the optofluidics is extended to nanoscales that allows the testing of fundamental assumptions in nanofluidic systems, broadens its applications and prompts the miniaturization.

To further improve the development of optofluidic devices, several future works with relevant recommendations are described in the following section.

6.2 Recommendations

Recommendations for future research are summarized as follows

- a) In the development of the optofluidic prism, its optical characteristics with different refractive indices are examined using benzyl alcohol and deionized (DI) water as the inner liquids, respectively. Integrating a mixer on the chip can obtain any specific refractive index from the mixture solution, and achieve a continuous modulation of the refractive index of the inner liquid. Consequently, the light beam can smoothly shift from downwards to upwards refraction. Hence, the tuning range and modulation speed of the optofluidic prism is significantly increased, and it promises for the real-time detection.
- b) The optical analysis for the optofluidic prism in this thesis is in the context of geometry optics, which ignores the diffusion between the laminar flows. Novel phenomena such as chirped focusing and interference have been demonstrated in an optofluidic waveguide underpinned by a bi-directional refractive index gradient profile caused by diffusion. Inspired by that, the diffusion caused refractive index gradient in the optofluidic prism and the consequently fluid-light interaction would be an attractive topic for future study.
- c) In this thesis, the optofluidic prism has been used for the measurement of solution refractive index. It is highly recommended to incorporate biochemical analyses to explore its applications in lab-on-a-chip system. For

instance, the optofluidic prism may be used for surface plasmonic resonance technology for biomolecule detection.

- d) In the study of nanobubbles, the experiments have been carried out in the extended nanochannels, in which only the height is submicrometer and the width is several hundred micrometers. It is recommended to further reduce the dimension of channel into a real nanochannel, in which the width and height are both tens of nanometers. The e-beam technology should be helpful in making patterns with nanostructures.
- e) The expansion of nanobubble has not been recorded due to the limitation of the high speed camera, i.e. the lowest possible exposure time of 370 ns. In order to get more information about the beginning of the cavitation, a camera with short exposure time is needed. For instance, the intensified CCD (ICCD) camera is highly sensitive, and its exposure time can be as low as 1-2 ns.
- f) In the study of nanojets, the fluidic instability caused new phenomena have been discussed. However, the physical understanding of the nano-film breakups is still not satisfactory. It is highly recommended to do further theoretical analysis incorporated with fluidic modeling. This will extend the study of fluidic instabilities into the confined boundary condition, especially the nanofluidic fields.

AUTHOR'S PUBLICATIONS

Journal papers

1. S. Xiong, A. Q. Liu, L. K. Chin and Y. Yang, "An optofluidic prism tuned by two laminar flows," *Lab on a Chip*, 11, 1864 (2011).
2. S. Xiong, K. Ando, T. Tandiono, C. D. Ohl and A. Q. Liu, "Cavitation bubble dynamics insub-micrometer thin films," *Soft Matters*, (submitted).
3. S. Xiong, K. Ando, T. Tandiono, C. D. Ohl and A. Q. Liu, "Bubble pinch-off in confined jetting," *Lab on a Chip*, (submitted).

Conference papers (selected)

1. S. Xiong, T. Tandiono, C. D. Ohl and A. Q. Liu, "Study of nano/micro jets generated by laser-induced bubbles in thin films", MEMS 2013, Taiwan, pp.213-216 (**Oral**).
2. S. Xiong, L. K. Chin, Y. Yang, Y. H. Fu, Y. Chen and A. Q. Liu, "A tunable optofluidic prism for optical switch," MEMS2011, Mexico, pp. 5-8 (**Oral**).
3. S. Xiong, T. Tandiono, C. D. Ohl and A. Q. Liu, "Bubble pinch-off and breakup due to instability in microjetting," μ TAS2013, Germany, pp.71-73.
4. S. Xiong, K. Ando, Tandiono, C. D. Ohl and A. Q. Liu, "Nano/micro jets in thin films for biomaterial manipulation and characterization," μ TAS2012, Japan, pp.371-373.
5. S. Xiong, Y. Yang, K. Mawatari, T. Kitamori and A. Q. Liu, "Nano-optofluidic droplet via photonic crystal characters for bio-imaging and detection applications", μ TAS2011, USA, pp.407-409.
6. S. Xiong, L. K. Chin, Y. F. Yu, J. Q. Yu, Y. Chen, G. J. Zhang, G. Q. Lo and A. Q. Liu, "Multi-size droplets generation via side-branch microfluidic channels," μ TAS2010, The Netherlands, pp. 1109-1111.
7. S. Xiong, Y. Yang and A. Q. Liu, "A liquid optical coupler for refractive index measurement," μ TAS2009, South Korea, pp. 995-997.

BIBLIOGRAPHY

1. C. Monat, P. Domachuk and B. J. Eggleton, "Integrated optofluidics: A new river of light," *Nature Photonics*. **1**(2): pp. 106-114 (2007).
2. F. K. Balagadde, L. C. You, C. L. Hansen, F. H. Arnold and S. R. Quake, "Long-term monitoring of bacteria undergoing programmed population control in a microchemostat," *Science*. **309**(5731): pp. 137-140 (2005).
3. H. C. Hunt and J. S. Wilkinson, "Optofluidic integration for microanalysis," *Microfluidics and Nanofluidics*. **4**(1-2): pp. 53-79 (2008).
4. S. H. Cho, J. M. Godin, C. H. Chen, W. Qiao, H. Lee and Y. H. Lo, "Review article: Recent advancements in optofluidic flow cytometer," *Biomicrofluidics*. **4**(4): 43001 (2010).
5. J. W. Hong, V. Studer, G. Hang, W. F. Anderson and S. R. Quake, "A nanoliter-scale nucleic acid processor with parallel architecture," *Nature Biotechnology*. **22**(4): pp. 435-439 (2004).
6. C. Monat, P. Domachuk, C. Grillet, M. Collins, B. J. Eggleton, M. Cronin-Golomb, S. Mutzenich, T. Mahmud, G. Rosengarten and A. Mitchell, "Optofluidics: a novel generation of reconfigurable and adaptive compact architectures," *Microfluidics and Nanofluidics*. **4**(1-2): pp. 81-95 (2008).
7. U. Levy and R. Shamaï, "Tunable optofluidic devices," *Microfluidics and Nanofluidics*. **4**(1-2): pp. 97-105 (2008).
8. D. B. Wolfe, R. S. Conroy, P. Garstecki, B. T. Mayers, M. A. Fischbach, K. E. Paul, M. Prentiss and G. M. Whitesides, "Dynamic control of liquid-core/liquid-cladding optical waveguides," *Proceedings of the National Academy of Sciences of the United States of America*. **101**(34): pp. 12434-12438 (2004).
9. A. Werber and H. Zappe, "Tunable microfluidic microlenses," *Applied Optics*. **44**(16): pp. 3238-3245 (2005).
10. D. V. Vezenov, B. T. Mayers, R. S. Conroy, G. M. Whitesides, P. T. Snee, Y. Chan, D. G. Nocera and M. G. Bawendi, "A low-threshold, high-

- efficiency microfluidic waveguide laser," *Journal of the American Chemical Society*. **127**(25): pp. 8952-8953 (2005).
11. P. Domachuk, C. Grillet, V. Ta'eed, E. Magi, J. Bolger, B. J. Eggleton, L. E. Rodd and J. Cooper-White, " Compact tunable microfluidic interferometer," *Applied Physics Letters*. **86**(2): 024103 (2005).
 12. C. Grillet, P. Domachuk, V. Ta'eed, E. Magi, J. A. Bolger, B. J. Eggleton, L. E. Rodd and J. Cooper-White, "Compact tunable microfluidic interferometer," *Optics Express*. **12**(22): pp. 5440-5447 (2004).
 13. M. Godin, A. K. Bryan, T. P. Burg, K. Babcock and S. R. Manalis, "Measuring the mass, density, and size of particles and cells using a suspended microchannel resonator," *Applied Physics Letters*. **91**(12): 123121 (2007).
 14. X. Heng, D. Erickson, L. R. Baugh, Z. Yaqoob, P. W. Sternberg, D. Psaltis and C. H. Yang, "Optofluidic microscopy - a method for implementing a high resolution optical microscope on a chip," *Lab on a Chip*. **6**(10): pp. 1274-1276 (2006).
 15. W. Liang, Y. Y. Huang, Y. Xu, R. K. Lee and A. Yariv, "Highly sensitive fiber Bragg grating refractive index sensors," *Applied Physics Letters*. **86**(15): 151122 (2005).
 16. D. Erickson, D. Sinton and D. Psaltis, "Optofluidics for energy applications," *Nature Photonics*. **5**(10): pp. 583-590 (2011).
 17. M. Ozkan, M. Wang, C. Ozkan, R. Flynn, A. Birkbeck and S. Esener, "Optical manipulation of objects and biological cells in microfluidic devices," *Biomedical Microdevices*. **5**(1): pp. 61-67 (2003).
 18. S. Maruo and H. Inoue, "Optically driven micropump produced by three-dimensional two-photon microfabrication," *Applied Physics Letters*. **89**(14): 144101 (2006).
 19. R. Dijkink and C. D. Ohl, "Laser-induced cavitation based micropump," *Lab on a Chip*. **8**(10): pp. 1676-1681 (2008).

20. L. Lei, N. Wang, X. M. Zhang, Q. D. Tai, D. P. Tsai and H. L. W. Chan, "Optofluidic planar reactors for photocatalytic water treatment using solar energy," *Biomicrofluidics*. **4**(4): 043004 (2010).
21. N. T. Nguyen, "Micro-optofluidic Lenses: A review," *Biomicrofluidics*. **4**(3): 031501 (2010).
22. T. V. Starkey, "A variable-angle liquid-prism spectrometer," *Journal of Scientific Instruments*. **15**(9): pp. 290 (1938).
23. B. Stanislaw, "Prism with a variable refraction angle and refractive index," *Physics Education*. **28**(4): pp. 256 (1993).
24. Y. Yoshihata, A. Takei, N. Binh-Khiem, T. Kan, E. Iwase, K. Matsumoto and I. Shimoyama. *Micro liquid prism*. in *Micro Electro Mechanical Systems, 2009. MEMS 2009. IEEE 22nd International Conference on*. 2009.
25. A. Takei, E. Iwase, K. Hoshino, K. Matsumoto and I. Shimoyama, "Angle-tunable liquid wedge prism driven by electrowetting," *Journal of Microelectromechanical Systems*. **16**(6): pp. 1537-1542 (2007).
26. C. L. Song, N. T. Nguyen, A. K. Asundi and S. H. Tan, "Tunable micro-optofluidic prism based on liquid-core liquid-cladding configuration," *Optics Letters*. **35**(3): pp. 327-329 (2010).
27. G. L. Liu, J. Kim, Y. Lu and L. P. Lee, "Optofluidic control using photothermal nanoparticles," *Nature Materials*. **5**(1): pp. 27-32 (2006).
28. T. Asshauer, K. Rink and G. Delacretaz, "Acoustic transient generation by holmium-laser-induced cavitation bubbles," *Journal of Applied Physics*. **76**(9): pp. 5007-5013 (1994).
29. E. A. Brujan, K. Nahen, P. Schmidt and A. Vogel, "Dynamics of laser-induced cavitation bubbles near an elastic boundary," *Journal of Fluid Mechanics*. **433**: pp. 251-281 (2001).
30. Lauterbo.W, "Laser-induced cavitation," *Acustica*. **31**(2): pp. 51-78 (1974).
31. J. Leach, H. Mushfique, R. di Leonardo, M. Padgett and J. Cooper, "An optically driven pump for microfluidics," *Lab on a Chip*. **6**(6): pp. 735-739 (2006).

32. A. Terray, J. Oakey and D. W. M. Marr, "Microfluidic control using colloidal devices," *Science*. **296**(5574): pp. 1841-1844 (2002).
33. D. Erickson, S. Mandal, A. H. J. Yang and B. Cordovez, "Nanobiosensors: optofluidic, electrical and mechanical approaches to biomolecular detection at the nanoscale," *Microfluidics and Nanofluidics*. **4**(1-2): pp. 33-52 (2008).
34. A. Meister, M. Gabi, P. Behr, P. Studer, J. Voros, P. Niedermann, J. Bitterli, J. Polesel-Maris, M. Liley, H. Heinzelmann and T. Zambelli, "FluidFM: combining atomic force microscopy and nanofluidics in a universal liquid delivery system for single cell applications and beyond," *Nano Letters*. **9**(6): pp. 2501-2507 (2009).
35. P. S. Dittrich and A. Manz, "Single-molecule fluorescence detection in microfluidic channels - the Holy Grail in μ TAS?," *Analytical and Bioanalytical Chemistry*. **382**(8): pp. 1771-1782 (2005).
36. E. T. Lagally, I. Medintz and R. A. Mathies, "Single-molecule DNA amplification and analysis in an integrated microfluidic device," *Analytical Chemistry*. **73**(3): pp. 565-570 (2001).
37. G. M. Whitesides, "The origins and the future of microfluidics," *Nature*. **442**(7101): pp. 368-373 (2006).
38. A. C. R. Grayson, R. S. Shawgo, A. M. Johnson, N. T. Flynn, Y. W. Li, M. J. Cima and R. Langer, "A BioMEMS review: MEMS technology for physiologically integrated devices," *Proceedings of the Ieee*. **92**(1): pp. 6-21 (2004).
39. J. M. K. Ng, I. Gitlin, A. D. Stroock and G. M. Whitesides, "Components for integrated poly(dimethylsiloxane) microfluidic systems," *Electrophoresis*. **23**(20): pp. 3461-3473 (2002).
40. G. M. Whitesides and A. D. Stroock, "Flexible methods for microfluidics," *Physics Today*. **54**(6): pp. 42-48 (2001).
41. K. Mawatari, S. Kubota, Y. Xu, C. Priest, R. Sedev, J. Ralston and T. Kitamori, "Femtoliter droplet handling in nanofluidic channels: A Laplace nanovalve," *Analytical Chemistry*. **84**(24): pp. 10812-10816 (2012).

42. Y. Xu, C. X. Wang, L. X. Li, N. Matsumoto, K. Jang, Y. Y. Dong, K. Mawatari, T. Suga and T. Kitamori, "Bonding of glass nanofluidic chips at room temperature by a one-step surface activation using an O-2/CF₄ plasma treatment dagger," *Lab on a Chip*. **13**(6): pp. 1048-1052 (2013).
43. N. R. Pollock, J. P. Rolland, S. Kumar, P. D. Beattie, S. Jain, F. Noubary, V. L. Wong, R. A. Pohlmann, U. S. Ryan and G. M. Whitesides, "A paper-based multiplexed transaminase test for low-cost, point-of-care liver function testing," *Science Translational Medicine*. **4**(152): 152ra129 (2012).
44. A. D. Mazzeo, W. B. Kalb, L. Chan, M. G. Killian, J. F. Bloch, B. A. Mazzeo and G. M. Whitesides, "Paper-based, capacitive touch pads," *Advanced Materials*. **24**(21): pp. 2850-2856 (2012).
45. N. Pamme, R. Koyama and A. Manz, "Counting and sizing of particles and particle agglomerates in a microfluidic device using laser light scattering: application to a particle-enhanced immunoassay," *Lab on a Chip*. **3**(3): pp. 187-192 (2003).
46. N. Pamme, J. C. T. Eijkel and A. Manz, "On-chip free-flow magnetophoresis: Separation and detection of mixtures of magnetic particles in continuous flow," *Journal of Magnetism and Magnetic Materials*. **307**(2): pp. 237-244 (2006).
47. D. P. Schrum, C. T. Culbertson, S. C. Jacobson and J. M. Ramsey, "Microchip flow cytometry using electrokinetic focusing," *Analytical Chemistry*. **71**(19): pp. 4173-4177 (1999).
48. Z. H. Liang, N. Chiem, G. Ocirk, T. Tang, K. Fluri and D. J. Harrison, "Microfabrication of a planar absorbance and fluorescence cell for integrated capillary electrophoresis devices," *Analytical Chemistry*. **68**(6): pp. 1040-1046 (1996).
49. G. J. Veldhuis, O. Parriaux, H. Hoekstra and P. V. Lambeck, "Sensitivity enhancement in evanescent optical waveguide sensors," *Journal of Lightwave Technology*. **18**(5): pp. 677-682 (2000).

50. M. A. McClain, C. T. Culbertson, S. C. Jacobson and J. M. Ramsey, "Flow cytometry of Escherichia coli on microfluidic devices," *Analytical Chemistry*. **73**(21): pp. 5334-5338 (2001).
51. C. W. Hollars, J. Puls, O. Bakajin, B. Olsan, C. E. Talley, S. M. Lane and T. Huser, "Bio-assay based on single molecule fluorescence detection in microfluidic channels," *Analytical and Bioanalytical Chemistry*. **385**(8): pp. 1384-1388 (2006).
52. H. C. Yeh, C. M. Puleo, T. C. Lim, Y. P. Ho, P. E. Giza, R. C. C. Huang and T. H. Wang, "A microfluidic-FCS platform for investigation on the dissociation of Sp1-DNA complex by doxorubicin," *Nucleic Acids Research*. **34**(21): e144 (2006).
53. Y. X. Zhang, J. T. Bahns, Q. L. Jin, R. Divan and L. H. Chen, "Toward the detection of single virus particle in serum," *Analytical Biochemistry*. **356**(2): pp. 161-170 (2006).
54. D. C. Pregibon, M. Toner and P. S. Doyle, "Multifunctional encoded particles for high-throughput biomolecule analysis," *Science*. **315**(5817): pp. 1393-1396 (2007).
55. R. Barer and S. Joseph, "Refractometry of living cells. 1. Basic principles," *Quarterly Journal of Microscopical Science*. **95**(4): pp. 399-423 (1954).
56. R. Barer, K. F. A. Ross and S. Tkaczyk, "Refractometry of living cells," *Nature*. **171**(4356): pp. 720-724 (1953).
57. X. J. Liang, A. Q. Liu, C. S. Lim, T. C. Ayi and P. H. Yap, "Determining refractive index of single living cell using an integrated microchip," *Sensors and Actuators a-Physical*. **133**(2): pp. 349-354 (2007).
58. P. B. Liu, H. Huang, T. Cao, Z. A. Tang, X. Y. Liu, Z. B. Qi, M. K. Ren and H. B. Wu, "An optofluidics biosensor consisted of high-finesse Fabry-Perot resonator and micro-fluidic channel," *Applied Physics Letters*. **100**(23): 233705 (2012).

59. L. K. Chin, A. Q. Liu, C. S. Lim, C. L. Lin, T. C. Ayi and P. H. Yap, "An optofluidic volume refractometer using Fabry-Perot resonator with tunable liquid microlenses," *Biomicrofluidics*. **4**(2): 024107 (2010).
60. T. Wei, Y. K. Han, Y. J. Li, H. L. Tsai and H. Xiao, "Temperature-insensitive miniaturized fiber inline Fabry-Perot interferometer for highly sensitive refractive index measurement," *Optics Express*. **16**(8): pp. 5764-5769 (2008).
61. H. Li and X. D. Fan, "Characterization of sensing capability of optofluidic ring resonator biosensors," *Applied Physics Letters*. **97**(1): 011105 (2010).
62. H. Y. Zhu, P. S. Dale, C. W. Caldwell and X. D. Fan, "Rapid and label-free detection of breast cancer biomarker CA15-3 in clinical human serum samples with optofluidic ring resonator sensors," *Analytical Chemistry*. **81**(24): pp. 9858-9865 (2009).
63. H. Y. Zhu, I. M. White, J. D. Suter, P. S. Dale and X. D. Fan, "Analysis of biomolecule detection with optofluidic ring resonator sensors," *Optics Express*. **15**(15): pp. 9139-9146 (2007).
64. W. Z. Song, X. M. Zhang, A. Q. Liu, C. S. Lim, P. H. Yap and H. M. M. Hosseini, "Refractive index measurement of single living cells using on-chip Fabry-Perot cavity," *Applied Physics Letters*. **89**(20): 203901 (2006).
65. G. R. Quigley, R. D. Harris and J. S. Wilkinson, "Sensitivity enhancement of integrated optical sensors by use of thin high-index films," *Applied Optics*. **38**(28): pp. 6036-6039 (1999).
66. R. G. Heideman and P. V. Lambeck, "Remote opto-chemical sensing with extreme sensitivity: design, fabrication and performance of a pigtailed integrated optical phase-modulated Mach-Zehnder interferometer system," *Sensors and Actuators B-Chemical*. **61**(1-3): pp. 100-127 (1999).
67. F. J. Blanco, M. Agirregabiria, J. Berganzo, K. Mayora, J. Elizalde, A. Calle, C. Dominguez and L. M. Lechuga, "Microfluidic-optical integrated CMOS compatible devices for label-free biochemical sensing," *Journal of Micromechanics and Microengineering*. **16**(5): pp. 1006-1016 (2006).

68. P. Lu, L. Q. Men, K. Sooley and Q. Y. Chen, "Tapered fiber Mach-Zehnder interferometer for simultaneous measurement of refractive index and temperature," *Applied Physics Letters*. **94**(13): 131110 (2009).
69. Z. B. Tian, S. S. H. Yam, J. Barnes, W. Bock, P. Greig, J. M. Fraser, H. P. Loock and R. D. Oleschuk, "Refractive index sensing with Mach-Zehnder interferometer based on concatenating two single-mode fiber tapers," *Ieee Photonics Technology Letters*. **20**(5-8): pp. 626-628 (2008).
70. A. Ymeti, J. Greve, P. V. Lambeck, T. Wink, S. van Hovell, T. A. M. Beumer, R. R. Wijn, R. G. Heideman, V. Subramaniam and J. S. Kanger, "Fast, ultrasensitive virus detection using a young interferometer sensor," *Nano Letters*. **7**(2): pp. 394-397 (2007).
71. A. Ymeti, J. S. Kanger, J. Greve, G. A. J. Besselink, P. V. Lambeck, R. Wijn and R. G. Heideman, "Integration of microfluidics with a four-channel integrated optical Young interferometer immunosensor," *Biosensors & Bioelectronics*. **20**(7): pp. 1417-1421 (2005).
72. M. Brown, T. Vestad, J. Oakey and D. W. M. Marr, "Optical waveguides via viscosity-mismatched microfluidic flows," *Applied Physics Letters*. **88**(13): 134109 (2006).
73. R. S. Conroy, B. T. Mayers, D. V. Vezenov, D. B. Wolfe, M. G. Prentiss and G. M. Whitesides, "Optical waveguiding in suspensions of dielectric particles," *Applied Optics*. **44**(36): pp. 7853-7857 (2005).
74. S. K. Y. Tang, B. T. Mayers, D. V. Vezenov and G. M. Whitesides, "Optical waveguiding using thermal gradients across homogeneous liquids in microfluidic channels," *Applied Physics Letters*. **88**(6): 061112 (2006).
75. D. B. Wolfe, D. V. Vezenov, B. T. Mayers, G. M. Whitesides, R. S. Conroy and M. G. Prentiss, "Diffusion-controlled optical elements for optofluidics," *Applied Physics Letters*. **87**(18): 181105 (2005).
76. Y. Yang, A. Q. Liu, L. K. Chin, X. M. Zhang, D. P. Tsai, C. L. Lin, C. Lu, G. P. Wang and N. I. Zheludev, "Optofluidic waveguide as a transformation optics device for lightwave bending and manipulation," *Nature Communications*. **3**: 651 (2012).

77. J. Godin, V. Lien and Y. H. Lo, "Demonstration of two-dimensional fluidic lens for integration into microfluidic flow cytometers," *Applied Physics Letters*. **89**(6): 061106 (2006).
78. S. Camou, H. Fujita and T. Fujii, "PDMS 2D optical lens integrated with microfluidic channels: principle and characterization," *Lab on a Chip*. **3**(1): pp. 40-45 (2003).
79. Z. Wang, J. El-Ali, M. Englund, T. Gotsaed, I. R. Perch-Nielsen, K. B. Mogensen, D. Snakenborg, J. P. Kutter and A. Wolff, "Measurements of scattered light on a microchip flow cytometer with integrated polymer based optical elements," *Lab on a Chip*. **4**(4): pp. 372-377 (2004).
80. L. Pang, U. Levy, K. Campbell, A. Groisman and Y. Fainman, "Set of two orthogonal adaptive cylindrical lenses in a monolith elastomer device," *Optics Express*. **13**(22): pp. 9003-9013 (2005).
81. S. K. Y. Tang, C. A. Stan and G. M. Whitesides, "Dynamically reconfigurable liquid-core liquid-cladding lens in a microfluidic channel," *Lab on a Chip*. **8**(3): pp. 395-401 (2008).
82. Y. C. Seow, A. Q. Liu, L. K. Chin, X. C. Li, H. J. Huang, T. H. Cheng and X. Q. Zhou, "Different curvatures of tunable liquid microlens via the control of laminar flow rate," *Applied Physics Letters*. **93**(8): 084101 (2008).
83. C. Song, N. T. Nguyen, S. H. Tan and A. K. Asundi, "Modelling and optimization of micro optofluidic lenses," *Lab on a Chip*. **9**(9): pp. 1178-1184 (2009).
84. X. L. Mao, J. R. Waldeisen, B. K. Juluri and T. J. Huang, "Hydrodynamically tunable optofluidic cylindrical microlens," *Lab on a Chip*. **7**(10): pp. 1303-1308 (2007).
85. M. Rosenauer and M. J. Vellekoop, "3D fluidic lens shaping-A multiconvex hydrodynamically adjustable optofluidic microlens," *Lab on a Chip*. **9**(8): pp. 1040-1042 (2009).

86. H. Huang, X. L. Mao, S. C. S. Lin, B. Kiraly, Y. P. Huang and T. J. Huang, "Tunable two-dimensional liquid gradient refractive index (L-GRIN) lens for variable light focusing," *Lab on a Chip*. **10**(18): pp. 2387-2393 (2010).
87. X. L. Mao, S. C. S. Lin, M. I. Lapsley, J. J. Shi, B. K. Juluri and T. J. Huang, "Tunable Liquid Gradient Refractive Index (L-GRIN) lens with two degrees of freedom," *Lab on a Chip*. **9**(14): pp. 2050-2058 (2009).
88. Z. G. Li, Y. Yang, X. M. Zhang, A. Q. Liu, J. B. Zhang, L. Cheng and Z. H. Li, "Tunable visual color filter using microfluidic grating," *Biomicrofluidics*. **4**(4): 043013 (2010).
89. M. Hashimoto, B. Mayers, P. Garstecki and G. M. Whitesides, "Flowing lattices of bubbles as tunable, self-assembled diffraction gratings," *Small*. **2**(11): pp. 1292-1298 (2006).
90. J. Q. Yu, Y. Yang, A. Q. Liu, L. K. Chin and X. M. Zhang, "Microfluidic droplet grating for reconfigurable optical diffraction," *Optics Letters*. **35**(11): pp. 1890-1892 (2010).
91. L. K. Chin, A. Q. Liu, J. B. Zhang, C. S. Lim and Y. C. Soh, "An on-chip liquid tunable grating using multiphase droplet microfluidics," *Applied Physics Letters*. **93**(16): 164107 (2008).
92. L. K. Chin, A. Q. Liu, Y. C. Soh, C. S. Lim and C. L. Lin, "A reconfigurable optofluidic Michelson interferometer using tunable droplet grating," *Lab on a Chip*. **10**(8): pp. 1072-1078 (2010).
93. B. Helbo, A. Kristensen and A. Menon, "A micro-cavity fluidic dye laser," *Journal of Micromechanics and Microengineering*. **13**(2): pp. 307-311 (2003).
94. J. C. Galas, J. Torres, M. Belotti, Q. Kou and Y. Chen, "Microfluidic tunable dye laser with integrated mixer and ring resonator," *Applied Physics Letters*. **86**(26): 264101 (2005).
95. Q. Kou, I. Yesilyurt and Y. Chen, "Collinear dual-color laser emission from a microfluidic dye laser," *Applied Physics Letters*. **88**(9): 091101 (2006).

96. M. Gersborg-Hansen, S. Balslev, N. A. Mortensen and A. Kristensen, "A coupled cavity micro-fluidic dye ring laser," *Microelectronic Engineering*. **78-79**: pp. 185-189 (2005).
97. S. Balslev and A. Kristensen, "Microfluidic single-mode laser using high-order Bragg grating and antiguiding segments," *Optics Express*. **13**(1): pp. 344-351 (2005).
98. Z. Y. Li, Z. Y. Zhang, A. Scherer and D. Psaltis, "Mechanically tunable optofluidic distributed feedback dye laser," *Optics Express*. **14**(22): pp. 10494-10499 (2006).
99. D. V. Vezenov, B. T. Mayers, D. B. Wolfe and G. M. Whitesides, "Integrated fluorescent light source for optofluidic applications," *Applied Physics Letters*. **86**(4): 041104 (2005).
100. B. T. Mayers, D. V. Vezenov, V. I. Vullev and G. M. Whitesides, "Arrays and cascades of fluorescent liquid-liquid waveguides: Broadband light sources for spectroscopy in microchannels," *Analytical Chemistry*. **77**(5): pp. 1310-1316 (2005).
101. Y. Yang, A. Q. Liu, L. Lei, L. K. Chin, C. D. Ohl, Q. J. Wang and H. S. Yoon, "A tunable 3D optofluidic waveguide dye laser via two centrifugal Dean flow streams," *Lab on a Chip*. **11**(18): pp. 3182-3187 (2011).
102. M. Tanyeri, R. Perron and I. M. Kennedy, "Lasing droplets in a microfabricated channel," *Optics Letters*. **32**(17): pp. 2529-2531 (2007).
103. S. K. Y. Tang, R. Derda, Q. M. Quan, M. Loncar and G. M. Whitesides, "Continuously tunable microdroplet-laser in a microfluidic channel," *Optics Express*. **19**(3): pp. 2204-2215 (2011).
104. S. K. Y. Tang, Z. Y. Li, A. R. Abate, J. J. Agresti, D. A. Weitz, D. Psaltis and G. M. Whitesides, "A multi-color fast-switching microfluidic droplet dye laser," *Lab on a Chip*. **9**(19): pp. 2767-2771 (2009).
105. W. Lee, Y. Z. Sun, H. Li, K. Reddy, M. Sumetsky and X. D. Fan, "A quasi-droplet optofluidic ring resonator laser using a micro-bubble," *Applied Physics Letters*. **99**(9): 091102 (2011).

106. Q. Kou, I. Yesilyurt, V. Studer, M. Belotti, E. Cambril and Y. Chen, "On-chip optical components and microfluidic systems," *Microelectronic Engineering*. **73-4**: pp. 876-880 (2004).
107. A. Llobera, R. Wilke and S. Buttgenbach, "Poly(dimethylsiloxane) hollow Abbe prism with microlenses for detection based on absorption and refractive index shift," *Lab on a Chip*. **4**(1): pp. 24-27 (2004).
108. A. Llobera, R. Wilke and S. Buttgenbach, "Optimization of poly(dimethylsiloxane) hollow prisms for optical sensing," *Lab on a Chip*. **5**(5): pp. 506-511 (2005).
109. B. Yao, G. Luo, L. D. Wang, Y. D. Gao, G. T. Lei, K. N. Ren, L. X. Chen, Y. M. Wang, Y. Hu and Y. Qiu, "A microfluidic device using a green organic light emitting diode as an integrated excitation source," *Lab on a Chip*. **5**(10): pp. 1041-1047 (2005).
110. K. Dholakia and P. Reece, "Optical micromanipulation takes hold," *Nano Today*. **1**(1): pp. 18-27 (2006).
111. A. Terray, J. Arnold and S. J. Hart, "Enhanced optical chromatography in a PDMS microfluidic system," *Optics Express*. **13**(25): pp. 10406-10415 (2005).
112. S. J. Hart, A. Terray, T. A. Leski, J. Arnold and R. Stroud, "Discovery of a significant optical chromatographic difference between spores of *Bacillus anthracis* and its close relative, *Bacillus thuringiensis*," *Analytical Chemistry*. **78**(9): pp. 3221-3225 (2006).
113. S. J. Hart, A. Terray, J. Arnold and T. A. Leski, "Sample concentration using optical chromatography," *Optics Express*. **15**(5): pp. 2724-2731 (2007).
114. K. Cheng, X. Q. Zhong and A. P. Xiang, "Optical trapping of metallic Rayleigh particles by using coherently and incoherently combined beams," *Acta Physica Sinica*. **61**(7) (2012).
115. R. A. Flynn, A. L. Birkbeck, M. Gross, M. Ozkan, B. Shao, M. M. Wang and S. C. Esener, "Parallel transport of biological cells using individually

- addressable VCSEL arrays as optical tweezers," *Sensors and Actuators B-Chemical*. **87**(2): pp. 239-243 (2002).
116. J. Prikulis, F. Svedberg, M. Kall, J. Enger, K. Ramser, M. Goksor and D. Hanstorp, "Optical spectroscopy of single trapped metal nanoparticles in solution," *Nano Letters*. **4**(1): pp. 115-118 (2004).
 117. K. Ramser, J. Enger, M. Goksor, D. Hanstorp, K. Logg and M. Kall, "A microfluidic system enabling Raman measurements of the oxygenation cycle in single optically trapped red blood cells," *Lab on a Chip*. **5**(4): pp. 431-436 (2005).
 118. T. N. Buican, M. J. Smyth, H. A. Crissman, G. C. Salzman, C. C. Stewart and J. C. Martin, "Automated single-cell manipulation and sorting by light trapping," *Applied Optics*. **26**(24): pp. 5311-5316 (1987).
 119. A. Constable, J. Kim, J. Mervis, F. Zarinetchi and M. Prentiss, "Demonstration of a fiber-optical light-force trap," *Optics Letters*. **18**(21): pp. 1867-1869 (1993).
 120. P. R. T. Jess, V. Garces-Chavez, D. Smith, M. Mazilu, L. Paterson, A. Riches, C. S. Herrington, W. Sibbett and K. Dholakia, "Dual beam fibre trap for Raman microspectroscopy of single cells," *Optics Express*. **14**(12): pp. 5779-5791 (2006).
 121. P. T. Korda, G. C. Spalding and D. G. Grier, "Evolution of a colloidal critical state in an optical pinning potential landscape," *Physical Review B*. **66**(2): 024504 (2002).
 122. L. Paterson, E. Papagiakoumou, G. Milne, V. Garces-Chavez, S. A. Tatarkova, W. Sibbett, F. J. Gunn-Moore, P. E. Bryant, A. C. Riches and K. Dholakia, "Light-induced cell separation in a tailored optical landscape," *Applied Physics Letters*. **87**(12): 123901 (2005).
 123. Y. Y. Sun, L. S. Ong and X. C. Yuan, "Composite-microlens-array-enabled microfluidic sorting," *Applied Physics Letters*. **89**(14): 141108 (2006).

124. G. Milne, D. Rhodes, M. MacDonald and K. Dholakia, "Fractionation of polydisperse colloid with acousto-optically generated potential energy landscapes," *Optics Letters*. **32**(9): pp. 1144-1146 (2007).
125. S. Kawata and T. Tani, "Optically driven Mie particles in an evanescent field along a channeled waveguide," *Optics Letters*. **21**(21): pp. 1768-1770 (1996).
126. J. P. Hole, J. S. Wilkinson, K. Grujic and O. G. Hellesø, "Velocity distribution of Gold nanoparticles trapped on an optical waveguide," *Optics Express*. **13**(10): pp. 3896-3901 (2005).
127. A. H. J. Yang, S. D. Moore, B. S. Schmidt, M. Klug, M. Lipson and D. Erickson, "Optical manipulation of nanoparticles and biomolecules in sub-wavelength slot waveguides," *Nature*. **457**(7225): pp. 71-75 (2009).
128. S. L. Neale, M. P. Macdonald, K. Dholakia and T. F. Krauss, "All-optical control of microfluidic components using form birefringence," *Nature Materials*. **4**(7): pp. 530-533 (2005).
129. L. Kelemen, S. Valkai and P. Ormos, "Integrated optical motor," *Applied Optics*. **45**(12): pp. 2777-2780 (2006).
130. D. Boyer, P. Tamarat, A. Maali, B. Lounis and M. Orrit, "Photothermal imaging of nanometer-sized metal particles among scatterers," *Science*. **297**(5584): pp. 1160-1163 (2002).
131. S. R. Sershen, S. L. Westcott, N. J. Halas and J. L. West, "Independent optically addressable nanoparticle-polymer optomechanical composites," *Applied Physics Letters*. **80**(24): pp. 4609-4611 (2002).
132. R. D. Schroll, R. Wunenburger, A. Casner, W. W. Zhang and J. P. Delville, "Liquid transport due to light scattering," *Physical Review Letters*. **98**(13): 133601 (2007).
133. A. N. Hellman, K. R. Rau, H. H. Yoon, S. Bae, J. F. Palmer, K. S. Phillips, N. L. Allbritton and V. Venugopalan, "Laser-induced mixing in microfluidic channels," *Analytical Chemistry*. **79**(12): pp. 4484-4492 (2007).

134. S. R. Gonzalez-Avila, X. H. Huang, P. A. Quinto-Su, T. Wu and C. D. Ohl, "Motion of Micrometer Sized Spherical Particles Exposed to a Transient Radial Flow: Attraction, Repulsion, and Rotation," *Physical Review Letters*. **107**(7): 074503 (2011).
135. X. H. Huang, P. A. Quinto-Su, S. R. Gonzalez-Avila, T. Wu and C. D. Ohl, "Controlled manipulation and in situ mechanical measurement of single Co nanowire with a laser-induced cavitation bubble," *Nano Letters*. **10**(10): pp. 3846-3851 (2010).
136. S. Koch, P. Pohl, U. Cobet and N. G. Rainov, "Ultrasound enhancement of liposome-mediated cell transfection is caused by cavitation effects," *Ultrasound in Medicine and Biology*. **26**(5): pp. 897-903 (2000).
137. T. Kondo and E. Kano, "Effect of free-radicals induced by ultrasonic cavitation on cell killing," *International Journal of Radiation Biology*. **54**(3): pp. 475-486 (1988).
138. J. Wu and W. L. Nyborg, "Ultrasound, cavitation bubbles and their interaction with cells," *Advanced Drug Delivery Reviews*. **60**(10): pp. 1103-1116 (2008).
139. A. J. Coleman, M. Whitlock, T. Leighton and J. E. Saunders, "The spatial-distribution of cavitation induced acoustic-emission, sonoluminescence and cell-lysis in the field of a shock-wave lithotripter," *Physics in Medicine and Biology*. **38**(11): pp. 1545-1560 (1993).
140. M. O. Lamminen, H. W. Walker and L. K. Weavers, "Mechanisms and factors influencing the ultrasonic cleaning of particle-fouled ceramic membranes," *Journal of Membrane Science*. **237**(1-2): pp. 213-223 (2004).
141. E. Maisonhaute, C. Prado, P. C. White and R. G. Compton, "Surface acoustic cavitation understood via nanosecond electrochemistry. Part III: shear stress in ultrasonic cleaning," *Ultrasonics Sonochemistry*. **9**(6): pp. 297-303 (2002).
142. B. Niemczewski, "Observations of water cavitation intensity under practical ultrasonic cleaning conditions," *Ultrasonics Sonochemistry*. **14**(1): pp. 13-18 (2007).

143. T. J. Mason, *Sonochemistry*. Oxford chemistry primers: 70. 1999: Oxford ; New York : Oxford University Press.
144. K. S. Suslick, "Sonochemistry," *Science*. **247**(4949): pp. 1439-1445 (1990).
145. E. B. Flint and K. S. Suslick, "The temperature of cavitation," *Science*. **253**(5026): pp. 1397-1399 (1991).
146. K. S. Suslick, S. B. Choe, A. A. Cichowlas and M. W. Grinstaff, "Sonochemical synthesis of amorphous iron," *Nature*. **353**(6343): pp. 414-416 (1991).
147. Z. Z. Yin and A. Prosperetti, "A microfluidic 'blinking bubble' pump," *Journal of Micromechanics and Microengineering*. **15**(3): pp. 643-651 (2005).
148. J. H. Tsai and L. W. Lin, "Active microfluidic mixer and gas bubble filter driven by thermal bubble micropump," *Sensors and Actuators a-Physical*. **97-8**: pp. 665-671 (2002).
149. P. Marmottant and S. Hilgenfeldt, "A bubble-driven microfluidic transport element for bioengineering," *Proceedings of the National Academy of Sciences of the United States of America*. **101**(26): pp. 9523-9527 (2004).
150. P. Marmottant, T. Biben and S. Hilgenfeldt, "Deformation and rupture of lipid vesicles in the strong shear flow generated by ultrasound-driven microbubbles," *Proceedings of the Royal Society a-Mathematical Physical and Engineering Sciences*. **464**(2095): pp. 1781-1800 (2008).
151. P. Marmottant and S. Hilgenfeldt, "Controlled vesicle deformation and lysis by single oscillating bubbles," *Nature*. **423**(6936): pp. 153-156 (2003).
152. Z. G. Li, A. Q. Liu, E. Klaseboer, J. B. Zhang and C. D. Ohl, "Single cell membrane poration by bubble-induced microjets in a microfluidic chip dagger," *Lab on a Chip*. **13**(6): pp. 1144-1150 (2013).
153. P. A. Quinto-Su, C. Kuss, P. R. Preiser and C. D. Ohl, "Red blood cell rheology using single controlled laser-induced cavitation bubbles," *Lab on a Chip*. **11**(4): pp. 672-678 (2011).

154. S. D. Lubetkin, "The fundamentals of bubble evolution," *Chemical Society Reviews*. **24**(4): pp. 243-& (1995).
155. C. E. Brennen, *Cavitation and bubble dynamics*. Oxford engineering science series: 44. 1995: New York : Oxford University Press.
156. D. Lohse, "Bubble puzzles," *Physics Today*. **56**(2): pp. 36-41 (2003).
157. A. Philipp and W. Lauterborn, "Cavitation erosion by single laser-produced bubbles," *Journal of Fluid Mechanics*. **361**: pp. 75-116 (1998).
158. A. Vogel and W. Lauterborn, "Acoustic transient generation by laser-produced cavitation bubbles near solid boundaries," *Journal of the Acoustical Society of America*. **84**(2): pp. 719-731 (1988).
159. I. Akhatov, O. Lindau, A. Topolnikov, R. Mettin, N. Vakhitova and W. Lauterborn, "Collapse and rebound of a laser-induced cavitation bubble," *Physics of Fluids*. **13**(10): pp. 2805-2819 (2001).
160. A. Vogel, W. Lauterborn and R. Timm, "Optical and acoustic investigations of the dynamics of laser-produced cavitation bubble near a solid boundary," *Journal of Fluid Mechanics*. **206**: pp. 299-338 (1989).
161. C. D. Ohl, O. Lindau and W. Lauterborn, "Luminescence from spherically and aspherically collapsing laser induced bubbles," *Physical Review Letters*. **80**(2): pp. 393-396 (1998).
162. S. Buogo and G. B. Cannelli, "Implosion of an underwater spark-generated bubble and acoustic energy evaluation using the Rayleigh model," *Journal of the Acoustical Society of America*. **111**(6): pp. 2594-2600 (2002).
163. J. A. Cook, A. M. Gleeson, R. M. Roberts and R. L. Rogers, "A spark-generated bubble model with semi-empirical mass transport," *Journal of the Acoustical Society of America*. **101**(4): pp. 1908-1920 (1997).
164. S. W. Fong, D. Adhikari, E. Klaseboer and B. C. Khoo, "Interactions of multiple spark-generated bubbles with phase differences," *Experiments in Fluids*. **46**(4): pp. 705-724 (2009).

165. C. L. Kling and F. G. Hammitt, "Photographic study of spark-induced cavitation bubble collapse," *Journal of Basic Engineering*. **94**(4): pp. 825-833 (1972).
166. A. Shima, K. Takayama, Y. Tomita and N. Ohsawa, "Mechanism of impact pressure generation from spark-generated bubble collapse near a wall," *Aiaa Journal*. **21**(1): pp. 55-59 (1983).
167. A. Vogel, S. Busch and U. Parlitz, "Shock wave emission and cavitation bubble generation by picosecond and nanosecond optical breakdown in water," *Journal of the Acoustical Society of America*. **100**(1): pp. 148-165 (1996).
168. L. Rayleigh, "On the pressure developed in a liquid during the collapse of a spherical cavity," *Philosophical Magazine*. **34**(199-04): pp. 94-98 (1917).
169. M. S. Plesset, "The dynamics of cavitation bubbles," *Journal of Applied Mechanics-Transactions of the Asme*. **16**(3): pp. 277-282 (1949).
170. R. I. Nigmatulin, N. S. Khabeev and F. B. Nagiev, "Dynamics, heat and mass-transfer of vapor-gas bubbles in a liquid," *International Journal of Heat and Mass Transfer*. **24**(6): pp. 1033-1044 (1981).
171. J. W. Miles, "The collapse time of a closed cavity," *Journal of Fluid Mechanics*. **25** (4): pp. 743-760 (1966).
172. J. R. Blake, G. S. Keen, R. P. Tong and M. Wilson, "Acoustic cavitation: the fluid dynamics of non-spherical bubbles," *Philosophical Transactions of the Royal Society a-Mathematical Physical and Engineering Sciences*. **357**(1751): pp. 251-267 (1999).
173. V. S. Ajaev and G. M. Homsy, "Modeling shapes and dynamics of confined bubbles," *Annual Review of Fluid Mechanics*. **38**: pp. 277-307 (2006).
174. M. S. Plesset and A. Prosperetti, "Bubble dynamics and cavitation," *Annual Review of Fluid Mechanics*. **9**: pp. 145-85 (1977).
175. Z. C. Feng and L. G. Leal, "Nonlinear bubble dynamics," *Annual Review of Fluid Mechanics*. **29**: pp. 201-243 (1997).

176. H. G. Flynn, "Cavitation dynamics. 2. Free pulsations and models for cavitation bubbles," *Journal of the Acoustical Society of America*. **58**(6): pp. 1160-1170 (1975).
177. W. Lauterborn, T. Kurz, R. Mettin and C. D. Ohl, *Experimental and theoretical bubble dynamics*, in *Advances in Chemical Physics, Vol 110*, I. Prigogine and S.A. Rice, Editors. 1999. p. 295-380.
178. W. Lauterborn and T. Kurz, "Physics of bubble oscillations," *Reports on Progress in Physics*. **73**(10): pp. 106501 (2010).
179. T. G. Leighton, *The acoustic bubble*. 1994: London : Academic Press.
180. H. Frenzel and H. Schultes, "Luminescence in ultra-ray layered water. Short announcement," *Zeitschrift Fur Physikalische Chemie-Abteilung B-Chemie Der Elementarprozesse Aufbau Der Materie*. **27**(5/6): pp. 421-424 (1934).
181. M. P. Brenner, S. Hilgenfeldt and D. Lohse, "Single-bubble sonoluminescence," *Reviews of Modern Physics*. **74**(2): pp. 425-484 (2002).
182. D. F. Gaitan, L. A. Crum, C. C. Church and R. A. Roy, "Sonoluminescence and bubble dynamics for a single, stable, cavitation bubble," *Journal of the Acoustical Society of America*. **91**(6): pp. 3166-3183 (1992).
183. W. B. McNamara, Y. T. Didenko and K. S. Suslick, "Sonoluminescence temperatures during multi-bubble cavitation," *Nature*. **401**(6755): pp. 772-775 (1999).
184. Y. T. Didenko and K. S. Suslick, "The energy efficiency of formation of photons, radicals and ions during single-bubble cavitation," *Nature*. **418**(6896): pp. 394-397 (2002).
185. T. B. Benjamin and A. T. Ellis, "Collapse of cavitation bubbles and pressures thereby produced against solid boundaries," *Philosophical Transactions of the Royal Society of London Series a-Mathematical and Physical Sciences*. **260**(1110): pp. 221-240 (1966).
186. J. R. Blake and D. C. Gibson, "Cavitation bubbles near boundaries," *Annual Review of Fluid Mechanics*. **19**: pp. 99-123 (1987).

187. W. Lauterborn and H. Bolle, "Experimental investigations of cavitation-bubble collapse in neighborhood of a solid boundary," *Journal of Fluid Mechanics*. **72**: pp. 391-399 (1975).
188. A. Vogel, W. Lauterborn and R. Timm, "Optical and acoustic investigations of the dynamics of laser-produced cavitation bubbles near a solid boundary," *Journal of Fluid Mechanics*. **206**: pp. 299-338 (1989).
189. U. Parlitz, R. Mettin, S. Luther, I. Akhatov, M. Voss and W. Lauterborn, "Spatio-temporal dynamics of acoustic cavitation bubble clouds," *Philosophical Transactions of the Royal Society a-Mathematical Physical and Engineering Sciences*. **357**(1751): pp. 313-334 (1999).
190. G. Haussmann and W. Lauterborn, "Determination of size and position of fast moving gas bubbles in liquids by digital 3-D image processing of hologram reconstructions," *Applied Optics*. **19**(20): pp. 3529-3535 (1980).
191. R. Krishna, M. I. Urseanu, J. M. van Baten and J. Ellenberger, "Rise velocity of a swarm of large gas bubbles in liquids," *Chemical Engineering Science*. **54**(2): pp. 171-183 (1999).
192. G. Marrucci, "Rising velocity of a swarm of spherical bubbles," *Industrial & Engineering Chemistry Fundamentals*. **4**(2): pp. 224-225 (1965).
193. C. Xiao, D. M. Heyes and J. G. Powles, "The collapsing bubble in a liquid by molecular dynamics simulations," *Molecular Physics*. **100**(21): pp. 3451-3468 (2002).
194. F. Lugli, S. Hofinger and F. Zerbetto, "The collapse of nanobubbles in water," *Journal of the American Chemical Society*. **127**(22): pp. 8020-8021 (2005).
195. F. Lugli and F. Zerbetto, "Molecular dynamics of nanobubbles' collapse in ionic solutions," *Chemphyschem*. **8**(1): pp. 47-49 (2007).
196. M. Vedadi, A. Choubey, K. Nomura, R. K. Kalia, A. Nakano, P. Vashishta and A. C. T. van Duin, "Structure and dynamics of shock-induced nanobubble collapse in water," *Physical Review Letters*. **105**(1): 014503 (2010).

197. L. G. MacDowell, V. K. Shen and J. R. Errington, "Nucleation and cavitation of spherical, cylindrical, and slablike droplets and bubbles in small systems," *Journal of Chemical Physics*. **125**(3): 34705 (2006).
198. P. R. ten Wolde and D. Chandler, "Drying-induced hydrophobic polymer collapse," *Proceedings of the National Academy of Sciences of the United States of America*. **99**(10): pp. 6539-6543 (2002).
199. A. Vishnyakov and A. V. Neimark, "Nucleation of liquid bridges and bubbles in nanoscale capillaries," *Journal of Chemical Physics*. **119**(18): pp. 9755-9764 (2003).
200. J. L. Parker, P. M. Claesson and P. Attard, "Bubbles, cavities, and the long-ranged attraction between hydrophobic surfaces," *Journal of Physical Chemistry*. **98**(34): pp. 8468-8480 (1994).
201. M. Switkes and J. W. Ruberti, "Rapid cryofixation/freeze fracture for the study of nanobubbles at solid-liquid interfaces," *Applied Physics Letters*. **84**(23): pp. 4759-4761 (2004).
202. R. Steitz, T. Gutberlet, T. Hauss, B. Klosgen, R. Krastev, S. Schemmel, A. C. Simonsen and G. H. Findenegg, "Nanobubbles and their precursor layer at the interface of water against a hydrophobic substrate," *Langmuir*. **19**(6): pp. 2409-2418 (2003).
203. C. U. Chan and C. D. Ohl, "Total-Internal-Reflection-Fluorescence Microscopy for the Study of Nanobubble Dynamics," *Physical Review Letters*. **109**(17): 174501 (2012).
204. X. H. Zhang, X. D. Zhang, S. T. Lou, Z. X. Zhang, J. L. Sun and J. Hu, "Degassing and temperature effects on the formation of nanobubbles at the mica/water interface," *Langmuir*. **20**(9): pp. 3813-3815 (2004).
205. S. J. Yang, S. M. Dammer, N. Bremond, H. J. W. Zandvliet, E. S. Kooij and D. Lohse, "Characterization of nanobubbles on hydrophobic surfaces in water," *Langmuir*. **23**(13): pp. 7072-7077 (2007).

206. X. H. Zhang, G. Li, N. Maeda and J. Hu, "Removal of induced nanobubbles from water/graphite interfaces by partial degassing," *Langmuir*. **22**(22): pp. 9238-9243 (2006).
207. B. M. Borkent, S. de Beer, F. Mugele and D. Lohse, "On the shape of surface nanobubbles," *Langmuir*. **26**(1): pp. 260-268 (2010).
208. W. A. Ducker, "Contact angle and stability of interfacial nanobubbles," *Langmuir*. **25**(16): pp. 8907-8910 (2009).
209. M. P. Brenner and D. Lohse, "Dynamic equilibrium mechanism for surface nanobubble stabilization," *Physical Review Letters*. **101**(21): 214505 (2008).
210. J. H. Weijs and D. Lohse, "Why surface nanobubbles live for hours," *Physical Review Letters*. **110**(5): 054501 (2013).
211. J. Noack, D. X. Hammer, G. D. Noojin, B. A. Rockwell and A. Vogel, "Influence of pulse duration on mechanical effects after laser-induced breakdown in water," *Journal of Applied Physics*. **83**(12): pp. 7488-7495 (1998).
212. S. B. Kiselev, "Kinetic boundary of metastable states in superheated and stretched liquids," *Physica A*. **269**(2-4): pp. 252-268 (1999).
213. C. B. Schaffer, N. Nishimura, E. N. Glezer, A. M. T. Kim and E. Mazur, "Dynamics of femtosecond laser-induced breakdown in water from femtoseconds to microseconds," *Optics Express*. **10**(3): pp. 196-203 (2002).
214. A. Vogel, N. Linz, S. Freidank and G. Paltauf, "Femtosecond-laser-induced nanocavitation in water: Implications for optical breakdown threshold and cell surgery," *Physical Review Letters*. **100**(3): 038102 (2008).
215. V. Kotaidis and A. Plech, "Cavitation dynamics on the nanoscale," *Applied Physics Letters*. **87**(21): 213102 (2005).
216. V. Kotaidis, C. Dahmen, G. von Plessen, F. Springer and A. Plech, "Excitation of nanoscale vapor bubbles at the surface of gold nanoparticles in water," *Journal of Chemical Physics*. **124**(18): 184702 (2006).
217. E. Y. Lukianova-Hleb, X. Y. Ren, J. A. Zasadzinski, X. W. Wu and D. O. Lapotko, "Plasmonic nanobubbles enhance efficacy and selectivity of

- chemotherapy against drug-resistant cancer cells," *Advanced Materials*. **24**(28): pp. 3831-3837 (2012).
218. D. Lapotko, "Plasmonic nanoparticle-generated photothermal bubbles and their biomedical applications," *Nanomedicine*. **4**(7): pp. 813-845 (2009).
 219. C. Duan, R. Karnik, M. C. Lu and A. Majumdar, "Evaporation-induced cavitation in nanofluidic channels," *Proceedings of the National Academy of Sciences of the United States of America*. **109**(10): pp. 3688-3693 (2012).
 220. J. Eggers and E. Villermaux, "Physics of liquid jets," *Reports on Progress in Physics*. **71**(3): 036601 (2008).
 221. J. J. Quirk and S. Karni, "On the dynamics of a shock-bubble interaction," *Journal of Fluid Mechanics*. **318**: pp. 129-163 (1996).
 222. T. B. Benjamin and A. T. Ellis, "The collapse of cavitation bubbles and the pressures thereby produced against solid boundaries," *Philosophical Transactions of the Royal Society of London Series a-Mathematical and Physical Sciences*. **260**(1110): pp. 221-240 (1966).
 223. D. C. Gibson. *Cavitation adjacent to plane boundaries*. in *Third Australasian Conference of Hydraulics & Fluid Mechanics*. 1968. Sydney, Australia.
 224. W. Lauterborn and H. Bolle, "Experimental investigations of cavitation-bubble collapse in neighborhood of a solid boundary," *Journal of Fluid Mechanics*. **72**(NOV25): pp. 391-399 (1975).
 225. A. Shima, K. Takayama, Y. Tomita and N. Miura, "An experimental-study on effects of a solid wall on the motion of bubbles and shock-waves in bubble collapse," *Acustica*. **48**(5): pp. 293-301 (1981).
 226. J. R. Blake, B. B. Taib and G. Doherty, "Transient cavities near boundaries. Part 1. Rigid boundary," *Journal of Fluid Mechanics*. **170**: pp. 479-497 (1986).
 227. Y. Tomita and A. Shima, "High-speed Photographic observations of laser-induced cavitation bubbles in water," *Acustica*. **71**(3): pp. 161-171 (1990).

228. Y. Tomita, A. Shima and K. Sato, "Dynamic behavior of 2-laser-induced bubbles in water," *Applied Physics Letters*. **57**(3): pp. 234-236 (1990).
229. V. V. Kucherenko and V. V. Shamko, "Dynamics of electric-explosion cavities between two solid parallel walls," *Journal of Applied Mechanics and Technical Physics*. **27**(1): pp. 112-115 (1986).
230. J. R. Blake, B. B. Taib and G. Doherty, "Transient cavities near boundaries. Part 2. Free surface," *Journal of Fluid Mechanics*. **181**: pp. 197-212 (1987).
231. L. Duchemin, S. Popinet, C. Josserand and S. Zaleski, "Jet formation in bubbles bursting at a free surface," *Physics of Fluids*. **14**(9): pp. 3000-3008 (2002).
232. Q. X. Wang, K. S. Yeo, B. C. Khoo and K. Y. Lam, "Strong interaction between a buoyancy bubble and a free surface," *Theoretical and Computational Fluid Dynamics*. **8**(1): pp. 73-88 (1996).
233. A. Pearson, E. Cox, J. R. Blake and S. R. Otto, "Bubble interactions near a free surface," *Engineering Analysis with Boundary Elements*. **28**(4): pp. 295-313 (2004).
234. Q. X. Wang, K. S. Yeo, B. C. Khoo and K. Y. Lam, "Nonlinear interaction between gas bubble and free surface," *Computers & Fluids*. **25**(7): pp. 607-628 (1996).
235. D. C. Gibson and J. R. Blake, "The growth and collapse of bubbles near deformable surfaces," *Applied Scientific Research*. **38**: pp. 215-224 (1982).
236. E. Klaseboer and B. C. Khoo, "An oscillating bubble near an elastic material," *Journal of Applied Physics*. **96**(10): pp. 5808-5818 (2004).
237. S. W. Gong, S. W. Ohl, E. Klaseboer and B. C. Khoo, "Scaling law for bubbles induced by different external sources: Theoretical and experimental study," *Physical Review E*. **81**(5): 056317 (2010).
238. D. Obreschkow, M. Tinguely, N. Dorsaz, P. Kobel, A. de Bosset and M. Farhat, "Universal scaling law for jets of collapsing bubbles," *Physical Review Letters*. **107**(20): 204501 (2011).

239. T. Kodama and Y. Tomita, "Cavitation bubble behavior and bubble-shock wave interaction near a gelatin surface as a study of in vivo bubble dynamics," *Applied Physics B-Lasers and Optics*. **70**(1): pp. 139-149 (2000).
240. C. D. Ohl and R. Ikink, "Shock-wave-induced jetting of micron-size bubbles," *Physical Review Letters*. **90**(21): 214502 (2003).
241. Y. H. Chen and I. Lin, "Dynamics of impacting a bubble by another pulsed-laser-induced bubble: Jetting, fragmentation, and entanglement," *Physical Review E*. **77**(2): 026304 (2008).
242. Y. H. Chen, H. Y. Chu and L. I, "Interaction and fragmentation of pulsed laser induced microbubbles in a narrow gap," *Physical Review Letters*. **96**(3): 034505 (2006).
243. G. N. Sankin, F. Yuan and P. Zhong, "Pulsating tandem microbubble for localized and directional single-cell membrane poration," *Physical Review Letters*. **105**(7): 078101 (2010).
244. T. Young, "An essay on the cohesion of fluids," *Philosophical Transactions of the Royal Society of London*. **95**: pp. 65-87 (1805).
245. F. Savart, "Mémoire sur la constitution des veines liquides lancées par des orifices circulaires en mince paroi," *Annales de Chimie et de Physique*. **53**: pp. 337-386 (1833).
246. L. Rayleigh, "On the instability of jets " *Proceedings of the London mathematical society* **10**: pp. 4-13 (1878).
247. J. Eggers, "Universal pinching of 3D axisymmetrical free-surface flow," *Physical Review Letters*. **71**(21): pp. 3458-3460 (1993).
248. M. Moseler and U. Landman, "Formation, stability, and breakup of nanojets," *Science*. **289**(5482): pp. 1165-1169 (2000).
249. Y. Hennequin, D. Aarts, J. H. van der Wiel, G. Wegdam, J. Eggers, H. N. W. Lekkerkerker and D. Bonn, "Drop formation by thermal fluctuations at an ultralow surface tension," *Physical Review Letters*. **97**(24): 244502 (2006).

250. L. Rayleigh, "On the instability of a cylinder of viscous liquid under capillary force," *Philosophical Magazine*. **34**(207): pp. 145-154 (1892).
251. S. Tomotika, "On the instability of a cylindrical thread of a viscous liquid surrounded by another viscous fluid," *Proceedings of the Royal Society of London. Series A, Mathematical and Physical Sciences*. **150**(870): pp. 322-337 (1935).
252. P. Lafrance and R. C. Ritter, "Capillary breakup of a liquid jet with a random initial perturbation," *Journal of Applied Mechanics-Transactions of the Asme*. **44**(3): pp. 385-388 (1977).
253. L. N. Howard and A. S. Gupta, "On the hydrodynamic and hydromagnetic stability of swirling flows," *Journal of Fluid Mechanics*. **14**(3): pp. 463-476 (1962).
254. L. Rayleigh, "Some applications of photography," *nature*. **44**: pp. 249-254 (1891).
255. C. V. Boys, "Notes on photographs of rapidly moving objects, and on the oscillating electric spark," *Philosophical Magazine*. **30**(184): pp. 248-260 (1890).
256. S. Tomotika, "Breaking up of a drop of viscous liquid immersed in another viscous fluid which is extending at a uniform rate," *Proceedings of the Royal Society of London Series a-Mathematical and Physical Sciences*. **153**(A879): pp. 0302-0318 (1936).
257. G. E. A. Meier, A. Klopper and G. Grabitz, "The influence of kinematic waves on jet break down," *Experiments in Fluids*. **12**(3): pp. 173-180 (1992).
258. T. Grumstrup, J. B. Keller and A. Belmonte, "Cavity ripples observed during the impact of solid objects into liquids," *Physical Review Letters*. **99**(11): 114502 (2007).
259. M. R. Loewen, M. A. Odor and M. G. Skafel, "Bubbles entrained by mechanically generated breaking waves," *Journal of Geophysical Research-Oceans*. **101**(C9): pp. 20759-20769 (1996).

260. G. B. Deane and M. D. Stokes, "Scale dependence of bubble creation mechanisms in breaking waves," *Nature*. **418**(6900): pp. 839-844 (2002).
261. G. D. Crapper, N. Dombrowski, W. P. Jepson and G. A. D. Pyott, "A note on the growth of Kelvin-Helmholtz waves on thin liquid sheets," *Journal of Fluid Mechanics*. **57**: pp. 671-672 (1973).
262. J. Park, K. Y. Huh, X. G. Li and M. Renksizbulut, "Experimental investigation on cellular breakup of a planar liquid sheet from an air-blast nozzle," *Physics of Fluids*. **16**(3): pp. 625-632 (2004).
263. N. Bremond and E. Villermaux, "Atomization by jet impact," *Journal of Fluid Mechanics*. **549**: pp. 273-306 (2006).
264. G. Taylor, "The dynamics of thin sheets of fluid.1.Water bells," *Proceedings of the Royal Society of London Series a-Mathematical and Physical Sciences*. **253**(1274): pp. 289-295 (1959).
265. G. Taylor, "The dynamics of thin sheets of fluid. 2. Waves on fluid sheets," *Proceedings of the Royal Society of London Series a-Mathematical and Physical Sciences*. **253**(1274): pp. 296-& (1959).
266. G. Taylor, "The dynamics of thin sheets of fluid. 3. Disintegration of fluid sheets," *Proceedings of the Royal Society of London Series a-Mathematical and Physical Sciences*. **253**(1274): pp. 313-& (1959).
267. J. C. P. Huang, "The break-up of axisymmetric liquid sheets," *Journal of Fluid Mechanics*. **43**(2): pp. 305-319 (1970).
268. C. J. Clark and Dombrowski, N, "Aerodynamic instability and disintegration of inviscid liquid sheets," *Proceedings of the Royal Society of London Series a-Mathematical and Physical Sciences*. **329**(1579): pp. 467-& (1972).
269. S. P. Lin, Z. W. Lian and B. J. Creighton, "Absolute and convective instability of a liquid sheet," *Journal of Fluid Mechanics*. **220**: pp. 673-689 (1990).
270. A. Lozano, F. Barreras, G. Hauke and C. Dopazo, "Longitudinal instabilities in an air-blasted liquid sheet," *Journal of Fluid Mechanics*. **437**: pp. 143-173 (2001).

271. S. P. Lin, *Breakup of liquid sheets and jets*. 2003: Cambridge ; New York : Cambridge University Press.
272. W. Thomson, "Hydrokinetic solutions and observations," *Philosophical Magazine*. **42**(281): pp. 362-377 (1871).
273. Rayleigh, "Investigation of the character of the equilibrium of an incompressible heavy fluid of variable density," *Proceedings of the London Mathematical Society*. **s1-14**(1): pp. 170-177 (1882).
274. G. Taylor, "The instability of liquid surfaces when accelerated in a direction perpendicular to their planes I," *Proceedings of the Royal Society of London Series a-Mathematical and Physical Sciences*. **201**(1065): pp. 192-196 (1950).
275. D. J. Lewis, "The instability of liquid surfaces when accelerated in a direction perpendicular to their planes II," *Proceedings of the Royal Society of London Series a-Mathematical and Physical Sciences*. **202**(1068): pp. 81-& (1950).
276. J. B. Keller and I. Kolodner, "Instability of liquid surfaces and the formation of drops," *Journal of Applied Physics*. **25**(7): pp. 918-921 (1954).
277. N. Bremond and E. Villermaux, "Bursting thin liquid films," *Journal of Fluid Mechanics*. **524**: pp. 121-130 (2005).
278. E. E. Meshkov, "Instability of the interface of two gases accelerated by a shock wave," *Fluid Dynamics*. **4**(5): pp. 101-104 (1969).
279. G. Reiter, "Dewetting of thin polymer-films," *Physical Review Letters*. **68**(1): pp. 75-78 (1992).
280. M. Elbaum and S. G. Lipson, "How does a thin wetted film dry up," *Physical Review Letters*. **72**(22): pp. 3562-3565 (1994).
281. Z. G. Wu and N. T. Nguyen, "Convective-diffusive transport in parallel lamination micromixers," *Microfluidics and Nanofluidics*. **1**(3): pp. 208-217 (2005).

282. M. U. Larsen and N. C. Shapley, "Stream spreading in multilayer microfluidic flows of suspensions," *Analytical Chemistry*. **79**(5): pp. 1947-1953 (2007).
283. M. Born and E. Wolf, *Principles of optics*. 7th expanded ed. ed. 1999: New York : Cambridge University Press.
284. M. Daimon and A. Masumura, "Measurement of the refractive index of distilled water from the near-infrared region to the ultraviolet region," *Applied Optics*. **46**(18): pp. 3811-3820 (2007).
285. H. El-Kashef, "The necessary requirements imposed on polar dielectric laser dye solvents," *Physica B*. **279**(4): pp. 295-301 (2000).
286. P. S. Epstein and M. S. Plesset, "On the stability of gas bubbles in liquid-gas solutions," *Journal of Chemical Physics*. **18**(11): pp. 1505-1509 (1950).
287. P. A. Kottke, S. S. Bair and W. O. Winer, "Cavitation in creeping shear flows," *Aiche Journal*. **51**(8): pp. 2150-2170 (2005).
288. H. S. Carslaw and J. C. Jaeger, *Conduction of Heat in Solids*. 1959: Oxford University Press.
289. L. L. Shui, A. van den Berg and J. C. T. Eijkel, "Interfacial tension controlled W/O and O/W 2-phase flows in microchannel," *Lab on a Chip*. **9**(6): pp. 795-801 (2009).
290. K. Handique, D. T. Burke, C. H. Mastrangelo and M. A. Burns, "Nanoliter liquid metering in microchannels using hydrophobic patterns," *Analytical Chemistry*. **72**(17): pp. 4100-4109 (2000).
291. P. A. Quinto-Su, K. Y. Lim and C. D. Ohl, "Cavitation bubble dynamics in microfluidic gaps of variable height," *Physical Review E*. **80**(4): 047301 (2009).
292. N. Sheikov, N. McDannold, N. Vykhodtseva, F. Jolesz and K. Hynynen, "Cellular mechanisms of the blood-brain barrier opening induced by ultrasound in presence of microbubbles," *Ultrasound in Medicine and Biology*. **30**(7): pp. 979-989 (2004).

293. C. Sun, E. Can, R. Dijkink, D. Lohse and A. Prosperetti, "Growth and collapse of a vapour bubble in a microtube: the role of thermal effects," *Journal of Fluid Mechanics*. **632**: pp. 5-16 (2009).
294. J. R. Blake, B. B. Taib and G. Doherty, "Transient cavities near boundaries. Part 2. Free surface," *Journal of Fluid Mechanics*. **181**: pp. 197-212 (1986).
295. F. Aitken, F. M. J. McCluskey and A. Denat, "An energy model for artificially generated bubbles in liquids," *Journal of Fluid Mechanics*. **327**: pp. 373-392 (1996).
296. C. Pozrikidis, *Introduction to theoretical and computational fluid dynamics / C. Pozrikidis*. 2nd ed. ed. 2011: New York : Oxford University Press.
297. M. Brouillette, "The Richtmyer-Meshkov instability," *Annual Review of Fluid Mechanics*. **34**: pp. 445-468 (2002).
298. J. Eggers, "Nonlinear dynamics and breakup of free-surface flows," *Reviews of Modern Physics*. **69**(3): pp. 865-929 (1997).
299. E. Villermaux and C. Clanet, "Life of a flapping liquid sheet," *Journal of Fluid Mechanics*. **462**: pp. 341-363 (2002).
300. G. Debregeas, P. G. de Gennes and F. Brochard-Wyart, "The life and death of "bare" viscous bubbles," *Science*. **279**(5357): pp. 1704-1707 (1998).